

**A STUDY OF THE CHARGED TWO-BODY
DECAYS OF THE NEUTRAL D MESONS**

BY

KUANG-CHUNG (K.C.) PENG

Submitted in partial fulfillment of the
requirements for the degree of
Doctor of Philosophy in Physics
in the Graduate School of the
Illinois Institute of Technology

Approved _____

Adviser

Chicago, Illinois
December 1995

ACKNOWLEDGEMENT

I have to thank my parents and three younger brothers for everything. I also like to thank the parent-like love from Dr. H. Rubin, Dr. J. Appel, Dr. J. Slaughter, Dr. M. Sheaff, Dr. R. Burnstein, and L. Chen-Tokarek, the uncle-like patience from Dr. M. Purohit, Dr. L. Cremaldi, and Dr. M. Sokoloff, the cousin-like understanding from Dr. E. Cantoral, Dr. T. Carter, Dr. G. Blaylock, Dr. P. Kasper, Dr. C. James, Dr. A. Nguyen, and Dr. K. Thorne, the brother-like trust from Dr. S. Kwan, Dr. C. Zhang, Dr. S. Watanabe, Dr. S. Radeztsky, Dr. L. Perera, Dr. N. Witchey, Dr. A. Tripathi, Dr. K. Stenson, and Dr. L. Ho.

We have a popular article in our Chinese literature in junior high, and it is written by a Physicist. A few sentences I remember dearly are:

"We are given so much, but we give so little.

We don't know whom to thank for, but say 'Thank Heaven' after all."

Thank Heaven!

K.C.P.

三十功名塵與土
八千里路雲和月

"Three decades of harvest is nothing but dust & dirt;
Eight thousands of mileage is something of cloud & moon." — Chinese ancient poem.

TABLE OF CONTENTS

ACKNOWLEDGEMENT	Page iii
LIST OF TABLES	vii
LIST OF FIGURES	ix
ABSTRACT	xiii
CHAPTER	
I. INTRODUCTION	1
1.1 The Standard Model	1
1.2 The Branching Ratio $\frac{\Gamma(D^0 \rightarrow K^+ K^-)}{\Gamma(D^0 \rightarrow \pi^+ \pi^-)}$	5
1.3 CP Violation and Mixing in the D^0 - \bar{D}^0 System	15
II. THE E791 EXPERIMENT	31
2.1 The 500 GeV/c Negative Pion Incident Beam	31
2.2 Upstream Beam Tracking	33
2.3 Target Foils	33
2.4 Downstream Region One Tracking	33
2.5 Two Magnets	34
2.6 Drift Chambers	37
2.7 Čerenkov Counters	37
2.8 Calorimeters	38
2.9 The Muon Wall	40
2.10 Triggering and Data Acquisition	40
III. ALIGNMENT, RECONSTRUCTION AND SELECTION	43
3.1 Alignment	43
3.2 Event Reconstruction	45
3.3 Event Selection	50
IV. PHYSICS ANALYSIS PREPARATION	53
4.1 Monte Carlo Simulation	53
4.2 Tuning Analysis Cuts	54
4.3 Čerenkov ID Efficiency	59
4.4 Fitting Invariant Mass Plots	71
4.5 Reduced Proper Time	74

CHAPTER	Page
V. PHYSICS ANALYSIS	77
5.1 Relative Branching Ratios	77
5.2 Lifetime Difference	78
5.3 CP Asymmetry	95
VI. SYSTEMATIC ERROR	101
6.1 Uncertainty Due to Fitting Functions	101
6.2 Uncertainty Due to Weighting	105
6.3 Uncertainty Due to Cuts	108
6.4 Uncertainty Due to Fixed Widths	112
6.5 Uncertainty Due to Binned Lifetime Fitting	117
6.6 Uncertainty Due to MC Production Distribution	123
6.7 Uncertainty Due to Detection Bias on A_{CP}^{BR}	124
VII. COMPARISONS AND CONCLUSIONS	125
7.1 Comparison with Previous Measurements	125
7.2 Conclusions	130
APPENDIX	
A. LIFETIME DIFFERENCE VS. MEAN DECAY TIME DIFFERENCE	133
A.1 $\Delta\tau$ in the Case of Equal Acceptance	135
A.2 $\Delta\tau$ in the Case of Unequal Acceptance	136
A.3 Comments	139
B. CUT COMPARISONS OF MC AND DATA	141
REFERENCES	161

LIST OF TABLES

Table	Page
1.1. Amplitudes of $D \rightarrow PP$ Decays	14
2.1. E791 Upstream Tracking Configurations	33
2.2. E791 Target Configurations	34
2.3. E791 Downstream R1 Tracking Configurations	35
2.4. E791 Magnet Configurations	35
2.5. E791 Drift Chamber Configurations	37
2.6. E791 Čerenkov Counter Configurations	38
2.7. The SLIC Configuration	39
2.8. The Hadrometer Configurations	39
2.9. The Muon Wall Configurations	40
4.1. Summary of Analysis Cuts	56
4.2. Čerenkov ID Efficiency of Kaon and Pion Identification	70
5.1. Branching Ratios (Statistical Error Only)	78
5.2. Binned Method Lifetime (Statistical Error Only)	87
5.3. Binned $\Delta\gamma$ Mean Value (Statistical Error Only)	92
5.4. Result of Unbinned 2-D Maximum Likelihood Fit	96
5.5. A_{CP}^{BR} (Statistical Error Only)	99
6.1. Binned Method Lifetime (No ID Cut or Weighting)	108
6.2. List of Cut Variations	111
6.3. List of Different Bins Fitting	123

Table		Page
7.1.	Comparison of BR Measurements	125
7.2.	Comparison of BR $K3\pi$ Measurements	129
7.3.	Comparison of Lifetime Measurements	129
7.4.	Comparison of CP Asymmetry Measurements	129

LIST OF FIGURES

Figure		Page
1.1.	The Decay Diagrams for $D^0 \rightarrow K^+ K^-$ and $D^0 \rightarrow \pi^+ \pi^-$	2
1.2.	Six Possible Weak Quark-decay Diagrams.	12
2.1.	The E791 Spectrometer.	32
3.1.	The Beam Profile in x and y Views, in Terms of the Intercepts and Slopes of the Beam Line	46
3.2.	The Residual Alignments of Eight Upstream PWC Planes	47
3.3.	The Residual Alignments of Six Upstream SMD Planes	48
3.4.	Alignment for Five Target Foils and the Interaction Counter	49
4.1.	Tuning Cuts in the First Iteration Finds $PT2DK > 0.52$	57
4.2.	Tuning Cuts in the Second Iteration Finds $MNCHV > 6$	58
4.3.	K^+ Čerenkov Efficiency Study in the Momentum Range 21–24 GeV/c from the \bar{D}^0 Sample	63
4.4.	π^- Čerenkov Efficiency Study in the Momentum Range 6–9 GeV/c from the \bar{D}^0 Sample	64
4.5.	Track Momentum Spectra of DATA from $D^0 \rightarrow K^- \pi^+$	65
4.6.	Track Momentum Spectra of DATA from $D^+ \rightarrow K^- \pi^+ \pi^+$	66
4.7.	Track Momentum Spectra of MC from $D^0 \rightarrow K^- \pi^+$	67
4.8.	Track Čerenkov ID Efficiencies from $D^0 \rightarrow K^- \pi^+$	68
4.9.	Track Čerenkov ID Efficiencies from $D^+ \rightarrow K^- \pi^+ \pi^+$	69
4.10.	Study of Likely BG Under the $D^0 \rightarrow K^+ K^-$ Signal	72
4.11.	Fitting Functions for $K^\mp \pi^\pm$ $K^\pm K^\mp$ $\pi^\pm \pi^\mp$ and $K3\pi$	73
4.12.	Illustrations of (a) DIP and IMPACT Cuts and (b) Reduced Proper Decay Length, L_{min}^{SDZ}	76

Figure		Page
5.1.	MC Acceptance Study for Branching Ratios	79
5.2.	Fitting DATA for BR of $K^\mp\pi^\pm$, $K^\pm K^\mp$ and $\pi^\pm\pi^\mp$	80
5.3.	2-Dimensional View of D^0 Mass vs. Reduced Proper Time for (a) $K^\pm K^\mp$ and (b) $K^\mp\pi^\pm$	82
5.4.	$D^0 \rightarrow K^+ K^-$ Mass Plots After ID Cut But Unweighted, in 16 Bins of Reduced Proper Time.	83
5.5.	BG Subtraction from Čerenkov Corrected (Weighted) $D^0 \rightarrow K^+ K^-$ Mass Plots in 16 Bins of Reduced Proper Time.	84
5.6.	BG Subtraction from Čerenkov Corrected $D^0 \rightarrow K^- \pi^+$ Mass Plots in 16 Bins of Reduced Proper Time.	85
5.7.	BG Subtraction from MC for $D^0 \rightarrow K^+ K^-$ Mass Plots in 16 Bins of Reduced Proper Time	86
5.8.	MC Acceptance Functions for the Binned Reduced Proper Time Method	88
5.9.	Lifetime Fitting Result on a Semi-log Scale	90
5.10.	Lifetime Fitting and Δt_{mean} Results	91
5.11.	$A_{\text{CP}}^{\text{BR}}$ Study of DATA Plots for $K^\mp\pi^\pm$ and $K^\pm K^\mp$	97
5.12.	$A_{\text{CP}}^{\text{BR}}$ Study of DATA Plots for $\pi^\pm\pi^\mp$ and $K3\pi$	98
6.1.	Systematic Study of Different Fitting Functions for $K^\mp\pi^\pm$	102
6.2.	Systematic Study of Different Fitting Functions for $K^\pm K^\mp$	103
6.3.	Systematic Study of Different Fitting Functions for $\pi^\pm\pi^\mp$	104
6.4.	Uncertainty Due to Randomized Weighting.	107
6.5.	BG Subtraction from $D^0 \rightarrow K^+ K^-$ (Without ID Cut) Invariant Mass Plots in 16 Bins of Reduced Proper Time.	109
6.6.	Lifetime Fitting Result (Without ID Cut) on a Semi-log Scale	110

Figure	Page
6.7. Systematic Study of Varying Cuts for BR's	113
6.8. Systematic Study of Varying Cuts for τ_{KK} and $\tau_{K\pi}$	114
6.9. Systematic Study of Varying Cuts for $\Delta\gamma$'s	115
6.10. Systematic Study of Varying Cuts for A_{CP}^{BR} 's	116
6.11. Systematic Study of Varying Widths for BR's	118
6.12. Systematic Study of Varying Widths for SG's	119
6.13. Systematic Study of Varying Widths for τ_{KK} and $\tau_{K\pi}$	120
6.14. Systematic Study of Varying Widths for $\Delta\gamma$'s	121
6.15. Systematic Study of Varying Widths for A_{CP}^{BR} 's	122
7.1. E791 BR's Comparison with Previous Experiments	126
7.2. E791 BR's Comparison with Previous Experiments	127
7.3. E791 $\tau_{K\pi}$ and $A_{CP}^{BR}(K^{\pm}K^{\mp})$ Comparisons with Previous Experiments	128
B.1. Mass plots for cut comparisons between MC and DATA.	145
B.2. DIP cut comparisons between MC and DATA.	146
B.3. PISO cut comparisons between MC and DATA.	147
B.4. MNCHV cut comparisons between MC and DATA.	148
B.5. MNCHV (without 32) cut distribution comparisons between MC and DATA.	149
B.6. PT2DK cut comparisons between MC and DATA.	150
B.7. Decay Distance comparisons between MC and DATA.	151
B.8. SDZ cut comparisons between MC and DATA.	152
B.9. L_{min}^{SDZ} comparisons between MC and DATA.	153

Figure		Page
B.10.	PTBAL cut comparisons between MC and DATA.	154
B.11.	L_{min}^{PTBAL} comparisons between MC and DATA.	155
B.12.	Reduced Length comparisons between MC and DATA.	156
B.13.	D^0 Momentum comparisons between MC and DATA.	157
B.14.	K^- Momentum comparisons between MC and DATA.	158
B.15.	π^+ Momentum comparisons between MC and DATA.	159
B.16.	IMPACT cut comparisons between MC and DATA.	160

ABSTRACT

The charged two-body decays of D^0 mesons produced by 500 GeV/c π^- incident on platinum and carbon foil targets at the Fermilab Tagged Particle Laboratory have been analyzed. Three measurements are presented in this thesis: (1) Branching Ratios of Charged Two-body Decays: $\frac{\Gamma(D^0 \rightarrow K^+ K^-)}{\Gamma(D^0 \rightarrow K^- \pi^+)} = 0.107 \pm 0.003 \pm 0.003$, $\frac{\Gamma(D^0 \rightarrow \pi^+ \pi^-)}{\Gamma(D^0 \rightarrow K^- \pi^+)} = 0.040 \pm 0.002 \pm 0.002$, $\frac{\Gamma(D^0 \rightarrow K^+ K^-)}{\Gamma(D^0 \rightarrow \pi^+ \pi^-)} = 2.65 \pm 0.14 \pm 0.13$, and $\frac{\Gamma(D^0 \rightarrow K^- \pi^- \pi^+ \pi^+)}{\Gamma(D^0 \rightarrow K^- \pi^+)} = 2.19 \pm 0.03 \pm 0.08$; (2) Lifetime Difference: $\tau_{KK} = 0.414 \pm 0.012 \pm 0.014$, $\tau_{K\pi} = 0.409 \pm 0.003 \pm 0.004$, with $\Delta\gamma = -0.06 \pm 0.15 \pm 0.15$, or the upper limit of Mixing rate as $\mathcal{R}_{\text{mix}}^y < 0.00079$ (due to lifetime difference only) at 90% confidence level; and (3) CP Asymmetry Parameters: $A_{\text{CP}}^{\text{BR}}(K^\pm K^\mp) = -0.018 \pm 0.054 \pm 0.012$, $A_{\text{CP}}^{\text{BR}}(\pi^\pm \pi^\mp) = -0.053 \pm 0.093 \pm 0.029$, and $A_{\text{CP}}^{\text{BR}}(K3\pi) = -0.018 \pm 0.023 \pm 0.002$.

All measurements are consistent with most theoretical predictions and world average experimental values.

CHAPTER I

INTRODUCTION

This thesis focuses on three topics regarding the charged two-body singly Cabibbo suppressed decays (SCSD) of D^0 mesons, using a consistent analysis scheme. The topics are

1. the Branching Ratio (BR) $\frac{\Gamma(D^0 \rightarrow K^+ K^-)}{\Gamma(D^0 \rightarrow \pi^+ \pi^-)}$,
2. the Lifetime Difference between $D^0 \rightarrow K^- \pi^+$ and $D^0 \rightarrow K^+ K^-$, and
3. the CP Asymmetry between D^0 and \bar{D}^0 .

Measurements of these phenomena can yield sensitive tests of the Standard Model and various modifications to that model.

Unless noted otherwise throughout this thesis, particle symbols denote both particles and anti-particles.

The theoretical framework and how these measurements impact upon it will be presented in the following sections. Fig. 1.1 illustrates the quark contents, decay diagrams and decay amplitudes for $D^0 \rightarrow K^+ K^-$ and $D^0 \rightarrow \pi^+ \pi^-$.

1.1 The Standard Model

The Standard Model [Kane88][†] is the $SU_C(3) \times SU_L(2) \times U_Y(1)$ gauge theory with three families of fermions (spin = integer + $\frac{1}{2}$).

$$\begin{pmatrix} u & e \\ d & \nu_e \end{pmatrix} \quad \begin{pmatrix} c & \mu \\ d & \nu_\mu \end{pmatrix} \quad \begin{pmatrix} t & \tau \\ b & \nu_\tau \end{pmatrix}$$

[†]Code in square brackets refers to coded references in REFERENCE.

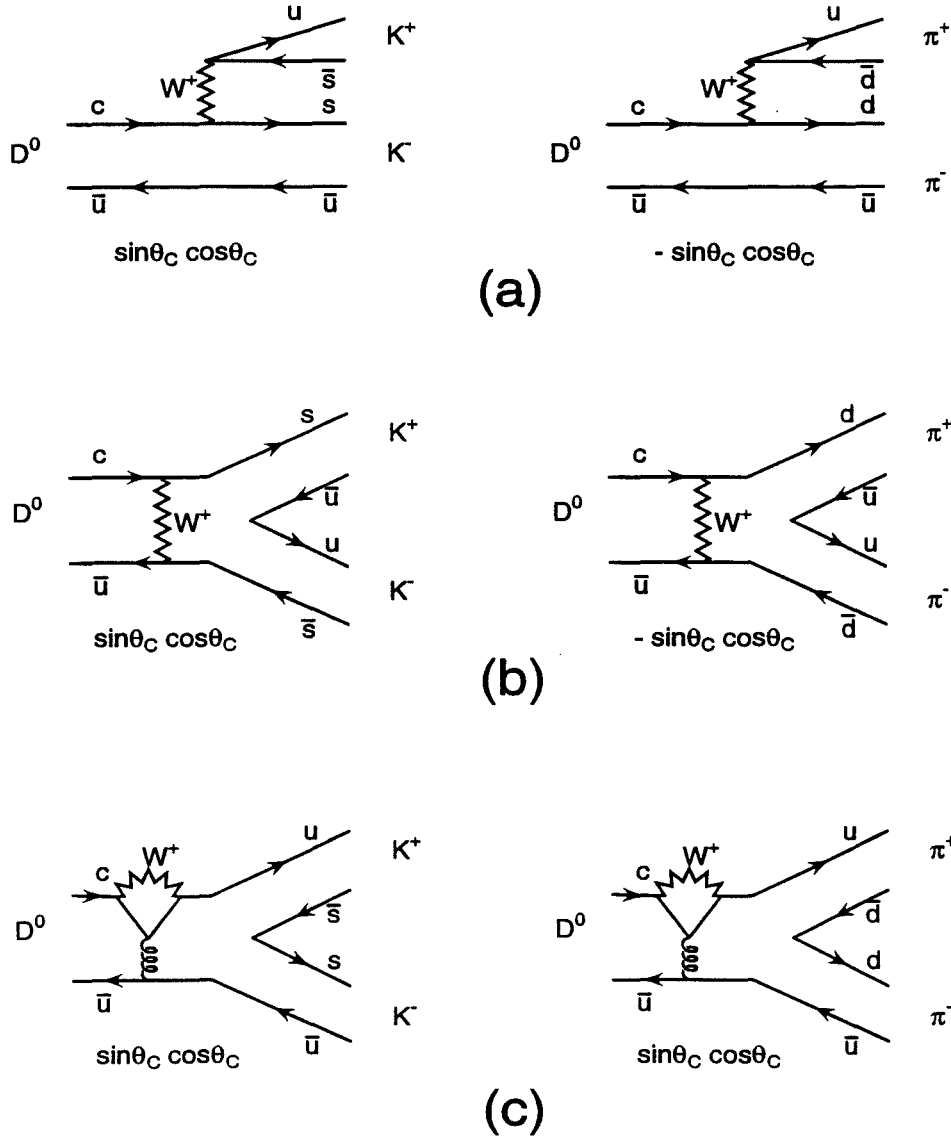


Figure 1.1. The Significant Decay Diagrams for $D^0 \rightarrow K^+ K^-$ and $D^0 \rightarrow \pi^+ \pi^-$:
 (a) spectator, (b) quark exchange and (c) penguin decays. The Cabibbo factors under $SU(3)$ symmetry, including signs, are indicated.

Each fermion family contains two quarks and two left-handed leptons, but isolated quarks are never observed. Instead they are always confined to be mesons ($q\bar{q}$ pairs) or baryons (qqq triplets). The symmetries of such a gauge group give rise to 12 gauge bosons (spin=integer): 8 gluons, the W^\pm , the Z^0 , and the photon (γ).

The $U_Y(1)$ electromagnetic symmetry is manifested by Quantum Electro-Dynamics (QED) where photons mediate interactions between electrically charged quarks and leptons.

The $SU_L(2)$ weak symmetry consists of both a flavor-changing charged current, mediated by the W^\pm , and a flavor-conserving neutral current, mediated by the Z^0 . The W^\pm 's are responsible for the SCSD in Fig. 1.1. The coupling of the charged current interaction is assumed to be universal, that is the decays

$$u \rightarrow d' \quad c \rightarrow s' \quad t \rightarrow b'$$

have the same strength. The Cabibbo-Kobayashi-Maskawa (CKM) matrix rotates the quark mass eigenstates into the weak decay eigenstates, Eq. (1.1). The lepton weak and mass eigenstates are identical, and their coupling to the W^\pm is 1.

$$\begin{pmatrix} d' \\ s' \\ b' \end{pmatrix} = \begin{pmatrix} V_{ud} & V_{us} & V_{ub} \\ V_{cd} & V_{cs} & V_{cb} \\ V_{td} & V_{ts} & V_{tb} \end{pmatrix} \begin{pmatrix} d \\ s \\ b \end{pmatrix} \quad (1.1)$$

The varying magnitudes of the CKM matrix elements imply that the strength of the rotations between the mass eigenstates is not universal.

In particular the (d, s) subspace can be parameterized by the Cabibbo angle ($\theta_C \approx 13^\circ$):

$$\begin{pmatrix} d' \\ s' \end{pmatrix} = \begin{pmatrix} \cos \theta_C & \sin \theta_C \\ -\sin \theta_C & \cos \theta_C \end{pmatrix} \begin{pmatrix} d \\ s \end{pmatrix} \quad (1.2)$$

Therefore, the decays involving $c \leftrightarrow d$ and $u \leftrightarrow s$ vertices are suppressed ($\sin \theta_C$) relative to $c \leftrightarrow s$ and $u \leftrightarrow d$ vertices ($\cos \theta_C$). The decays suppressed by one factor of $\sin \theta_C$ are called SCSD, indicated in Fig. 1.1.

The $SU_C(3)$ color symmetry consists of eight gluons mediating the strong interactions between the color carriers — the quarks and the gluons themselves. There have been many attempts to include strong interaction effects into weak decays. These includes the Penguin diagrams in Fig. 1.1 (e)(f), and the factorization approach of Bauer, Stech and Wirbel (BSW) [BSW87].

There is a special phenomenon, Mixing, in neutral meson systems. For example, in the $K^0 - \bar{K}^0$ system, one can delineate three sets of states:

- Strong or Quark eigenstates — (K^0, \bar{K}^0) ;
- CP eigenstates — (K_1^0, K_2^0) ;
- Weak or Mass eigenstates — (K_S^0, K_L^0) .

The rotations among these three states can be visualized as follows for the $D^0 - \bar{D}^0$ system (including Direct CP asymmetry):

Mass Eigenstate		CP Eigenstate		Quark Eigenstate	
$\begin{pmatrix} D_H^0 \\ D_L^0 \end{pmatrix}$	$\frac{1}{\sqrt{1- \epsilon ^2}} \begin{pmatrix} 1 & \epsilon \\ \epsilon & 1 \end{pmatrix}$	$\begin{pmatrix} D_1^0 \\ D_2^0 \end{pmatrix}$	$\frac{1}{\sqrt{2}} \begin{pmatrix} 1 & 1 \\ 1 & -1 \end{pmatrix}$	$\begin{pmatrix} D^0 \\ \bar{D}^0 \end{pmatrix}$	$\begin{matrix} \xrightarrow{\quad} f \\ \xrightarrow{\epsilon'} \bar{f} \end{matrix}$
	Indirect CP		Mixing		Direct CP

(1.3)

where ϵ is the Indirect (or Mixing-type) CP asymmetry parameter, and ϵ' is the Direct CP asymmetry parameter depending on the final state, f . The subscript notations H and L are chosen because we expect to observe a larger mass difference than lifetime

difference. Thus H and L stand for Heavy and Light, and 1 and 2 denote CP-odd and CP-even, respectively. If there is no Mass Mixing or no Indirect CP asymmetry, then the corresponding rotation in Eq. (1.3) would reduce to a unit matrix. One can easily derive the rotation between the quark eigenstates and the mass eigenstates by combining two rotations into one. [Commins]

$$\begin{array}{cc} \text{Mass} & \text{Quark} \\ \text{Eigenstate} & \text{Eigenstate} \end{array} \quad \begin{pmatrix} D_H^0 \\ D_L^0 \end{pmatrix} = \frac{1}{\sqrt{2(1-|\epsilon|^2)}} \begin{pmatrix} \begin{pmatrix} 1+\epsilon \\ 1+\epsilon \end{pmatrix} & \begin{pmatrix} 1-\epsilon \\ -(1-\epsilon) \end{pmatrix} \end{pmatrix} \begin{pmatrix} D^0 \\ \bar{D}^0 \end{pmatrix} \quad (1.4)$$

I will demonstrate how to construct the decay amplitudes, and thus the partial decay rates in Sec. 1.2. Then I will look in detail into CP asymmetry and D^0 - \bar{D}^0 Mixing in Sec. 1.3.

1.2 The Branching Ratio $\frac{\Gamma(D^0 \rightarrow K^+ K^-)}{\Gamma(D^0 \rightarrow \pi^+ \pi^-)}$

From naive SU(3) symmetry, one expects that $\frac{\Gamma(D^0 \rightarrow K^+ K^-)}{\Gamma(D^0 \rightarrow \pi^+ \pi^-)}$ would be 1 [EiQu75], because there is no difference between u, d, and s in the simple picture of Fig. 1.1. But in 1979 the first experimental data [mark-79] showed this ratio to be 3.4 ± 1.8 , and since then various models have been proposed to explain this result while experimental groups have improved the precision of this measurement. The most recent world average is $\frac{\Gamma(D^0 \rightarrow K^+ K^-)}{\Gamma(D^0 \rightarrow \pi^+ \pi^-)} = 2.86 \pm 0.28$ [PDG94]. To date, the phenomenological fitting model and the final state interaction (FSI) model can explain all the $D \rightarrow PP$ or PV (P =pseudoscalar, V =vector) hadronic 2-body decays of D mesons.

1.2.1 Effective Hamiltonian for Hadronic Charm Decays. The effective Hamiltonian for hadronic charm decays is given as [Bur86]

$$H_W^{\text{eff}} = \sqrt{\frac{1}{2}} G_F V_{cj}^* V_{kl} \{c_1 (\bar{k}l)_L (\bar{j}c)_L + c_2 (\bar{k}c)_L (\bar{j}l)_L\}, \quad (1.5)$$

where c_1 and c_2 are composed of short distance QCD coefficients (c_+ and c_-):

$$c_1 = \frac{1}{2}(c_+ + c_-), \quad c_2 = \frac{1}{2}(c_+ - c_-), \quad (1.6)$$

and V_{ij} are the elements of the CKM matrix with (c, k) and (j, l) standing for $+\frac{2}{3}$ charge (up-type) quarks and $-\frac{1}{3}$ charge (down-type) quarks, respectively. The $V - A$ weak interaction is

$$(\bar{k}l)_L \equiv \bar{k}_\alpha \gamma_\mu (1 - \gamma_5) l_\alpha, \quad (1.7)$$

with α being the color index. In Eq. (1.5), the first operator describes the usual charged current interactions. The second term is an effective neutral current interaction generated by short distance QCD effects and in the absence of these effects, *i.e.* $c_+ = c_- = 1$, the second term vanishes.

In particular the Cabibbo favored decay (CFD) of $D^0 \rightarrow K^- \pi^+$ is described by

$$H_W^{\text{eff}} = \sqrt{\frac{1}{2}} G_F V_{cs}^* V_{ud} \{ c_1 (\bar{u}d)_L (\bar{s}c)_L + c_2 (\bar{u}c)_L (\bar{s}d)_L \}. \quad (1.8)$$

To find the decay amplitude, one computes the matrix H_W^{eff} of Eq. (1.8) between the initial state $|D^0\rangle$, and the final state $|K^- \pi^+\rangle$:

$$A(D^0 \rightarrow K^- \pi^+) = \langle K^- \pi^+ | H_W^{\text{eff}} | D^0 \rangle. \quad (1.9)$$

1.2.2 Factorization Model. Continuing from Sec. 1.2.1, I factorize[†] the weak amplitude in all possible ways by performing appropriate Fierz transformations

[†]The factorization hypothesis means that the meson two-body decay amplitudes may be expressed as the product of two independent hadronic currents.

[BS85] — vacuum insertion — on the hadronic matrix elements. With this replacement of interacting fields by asymptotic fields, I neglect any initial or final state interaction of the corresponding particles for the moment [BSW87]. Then

$$A(D^0 \rightarrow K^- \pi^+) = \sqrt{\frac{1}{2}} G_F V_{cs}^* V_{ud} \{ a_1 \langle \pi^+ | (\bar{u}d)_L | 0 \rangle \langle K^- | (\bar{s}c)_L | D^0 \rangle + a_2 \langle K^- \pi^+ | (\bar{u}c)_L | 0 \rangle \langle 0 | (\bar{s}d)_L | D^0 \rangle \}, \quad (1.10)$$

where

$$a_1 = c_1 + \xi c_2, \quad a_2 = c_2 + \xi c_1. \quad (1.11)$$

It has been emphasized [Bur86] that factorization follows to leading order in a $1/N_c$ expansion, where N_c is the number of quark colors (3 in SU(3)). The color factor $\xi = 1/N_c$ arises from color mismatch in forming color singlets after Fierz transformation. After some phenomenological tests, it has been shown that ξ is not universal but channel or class dependent [Chen94]. The first term in Eq. (1.10) represents the spectator decay mechanism, and the second the quark annihilation decay contribution. Evaluating the corresponding matrix elements in Eq. (1.10) we find

$$A(D^0 \rightarrow K^- \pi^+) = a_1 \sqrt{\frac{1}{2}} G_F V_{cs}^* V_{ud} f_\pi \cdot (m_D^2 - m_K^2) \cdot F^{DK}(m_\pi^2, 0^+) \cdot h + a_2 \sqrt{\frac{1}{2}} G_F V_{cs}^* V_{ud} f_D \cdot (m_K^2 - m_\pi^2) \cdot F^{K\pi}(m_D^2, 0^+) \cdot h \quad (1.12)$$

where f_π and f_D are the decay constants, $F_{DK}(q^2, 0^+)$ and $F_{K\pi}(q^2, 0^+)$ are the form factors, and h is a reduction factor which has been introduced to account for an incomplete overlap of the relevant meson wave functions. From Eq. (1.12), annihilation is suppressed by a factor of $(a_2/a_1)(m_K^2/m_D^2)$ relative to the charm quark decay. The annihilation term in Eq. (1.12) can be neglected due to the conserved vector current (CVC) hypothesis [KaXu92], unless the annihilation form factor, $F_{K\pi}(m_D^2, 0^+)$, shows an unexpected large resonance effect.

Thus the partial decay width for $D^0 \rightarrow K^- \pi^+$ is

$$\Gamma(D^0 \rightarrow K^- \pi^+) \propto |A(D^0 \rightarrow K^- \pi^+)|^2 \propto |a_1|^2 \times \hat{\Gamma}_{K\pi} \quad (1.13)$$

Similar results [BSW87] can be obtained for other $D \rightarrow PP$ or PV decays. By this factorization approach, I can separate all the partial decay widths for $D \rightarrow PP$ or PV into three classes characterized by the QCD factors $|a_1|^2$ (e.g. $D^0 \rightarrow \pi^+ K^-$), $|a_2|^2$ (e.g. $D^0 \rightarrow \pi^0 K^0$) and $|a_1 + x a_2|^2$ (e.g. $D^+ \rightarrow \bar{K}^0 \pi^+$). The parameter x describes SU(3) breaking effects and is equal to 1 in the SU(3) limit. The success of the BSW model in the two-body nonleptonic decays indicates that, to leading order in $1/N_c$, quarks belonging to different color singlet currents do not form hadrons, or equivalently, color suppression is absolute [Bur86].

The decay amplitudes of both $D^0 \rightarrow K^+ K^-$ and $D^0 \rightarrow \pi^+ \pi^-$ fall into class a_1 :

$$A(D^0 \rightarrow K^+ K^-) = -a_1 \sqrt{\frac{1}{2}} G_F V_{cs}^* V_{us} f_K \cdot (m_D^2 - m_K^2) \cdot F^{DK}(m_K^2, 0^+) \cdot h \quad (1.14)$$

$$A(D^0 \rightarrow \pi^+ \pi^-) = a_1 \sqrt{\frac{1}{2}} G_F V_{cd}^* V_{ud} f_\pi \cdot (m_D^2 - m_\pi^2) \cdot F^{D\pi}(m_\pi^2, 0^+) \cdot h. \quad (1.15)$$

Some examples in other classes are:

$$\begin{aligned} A(D^0 \rightarrow \pi^0 \pi^0) &= -a_2 \sqrt{\frac{1}{2}} G_F V_{cd}^* V_{ud} f_\pi \cdot (m_D^2 - m_\pi^2) \cdot F_{D\pi}(m_\pi^2, 0^+) \cdot h \\ A(D^0 \rightarrow K^0 \bar{K}^0) &= 0 \\ A(D^+ \rightarrow \pi^0 \pi^+) &= -\frac{a_1 + a_2}{\sqrt{2}} G_F V_{cd}^* V_{ud} f_\pi \cdot (m_D^2 - m_\pi^2) \cdot F_{D\pi}(m_\pi^2, 0^+) \cdot h \end{aligned} \quad (1.16)$$

SU(3) symmetry breaking effects can be found in the straightforward comparison of Eq. (1.14) and Eq. (1.15). First, the deviation of $\frac{\Gamma(D^0 \rightarrow K^+ K^-)}{\Gamma(D^0 \rightarrow \pi^+ \pi^-)}$ from 1 is due to the slight difference between $|V_{cs}|$ and $|V_{ud}|$ ($\sim \cos \theta_C$), and $|V_{us}|$ and $|V_{cd}|$ ($\sim \sin \theta_C$). Second, the deviation from 1 of $F_0^{DK}(0)/F_0^{D\pi}(0)$ ($\sim 0.76/0.83$) [PDG94], f_K/f_π

($\sim 159.8/130.7$) [PDG94], and m_K/m_π ($\sim 493.7/139.6$) [PDG94]. The q^2 dependence of the form factor $F(q^2)$ is usually assumed to be governed by a single low-lying pole:

$$F(q^2) = \frac{F(0)}{1 - (q^2/m_\star^2)}, \quad (1.17)$$

where m_\star is the mass of the 0^+ pole, with $m_\star = 2.47 \text{ GeV}/c^2$ for $F_0^{D\pi}$ and $m_\star = 2.60 \text{ GeV}/c^2$ for F_0^{DK} [ChCh94].

Phenomenological approaches [BSW87] treat a_1 , a_2 , and x as the fitting parameters for available data, using them to predict other decay widths. Generally speaking, this factorization approach can fit most of the experimental decay widths of $D \rightarrow PP$ or PV , but some exceptions (e.g. $D^0 \rightarrow \pi^+\pi^-$) force us to other models, such as final state interactions (FSI), to decrease the discrepancy between experimental data and theoretical predictions.

1.2.3 Final State Interactions. Final state interactions (FSI) play an important role in processes where a number of hadrons are produced through a “basic” process and then allowed to interact strongly. Familiar examples are: [KaCo81]

- Electromagnetic (EM) form factors where the basic process is EM, and FSI endows the form factors with a momentum-transfer dependence;
- Weak decays of hadrons, for example $K \rightarrow 2\pi$ or 3π , $\Lambda \rightarrow p\pi^-$, etc., where the basic process is weak and FSI results in a phase to the amplitude;
- Particle production, for example $\pi N \rightarrow \pi\pi N$ and $KN \rightarrow \pi KN$, etc., where the basic process is a real Born amplitude followed by FSI in 2-body sub-systems of produced particles.

The D meson mass lies in a resonance region where strong rescattering effects of the outgoing mesons will be of particular importance. For the on-mass-shell FSI case, the bare amplitude A^0 should be corrected to [BSW87]

$$A = \sqrt{S} \cdot A^0, \quad (1.18)$$

where \sqrt{S} denotes the square root of the strong interaction S -matrix for hadron-hadron scattering. Inclusion of this correction results in the introduction of phase factors and mixing of channels. Since little is known about the many open channels, \sqrt{S} cannot be estimated.

Nevertheless, an isospin analysis gives some information about the effects of FSI. For such an analysis we borrow the concept of strong scattering with isospin decomposition to analyze $D \rightarrow \pi\pi, K\pi$, and $K\bar{K}$. In terms of isospin (I) amplitudes, the decay amplitudes are: [KaPh941]

- $D \rightarrow \pi\pi$; I = 0, 2 in the final state,

$$\begin{aligned} A(D^0 \rightarrow \pi^+\pi^-) &= \frac{1}{\sqrt{6}} A_0^{\pi\pi} e^{i\delta_0^{\pi\pi}} + \frac{1}{\sqrt{12}} A_2^{\pi\pi} e^{i\delta_2^{\pi\pi}} \\ A(D^0 \rightarrow \pi^0\pi^0) &= \frac{1}{\sqrt{6}} A_0^{\pi\pi} e^{i\delta_0^{\pi\pi}} - \frac{1}{\sqrt{3}} A_2^{\pi\pi} e^{i\delta_2^{\pi\pi}} \\ A(D^+ \rightarrow \pi^0\pi^+) &= -\frac{\sqrt{3}}{2\sqrt{2}} A_2^{\pi\pi} e^{i\delta_2^{\pi\pi}} \end{aligned} \quad (1.19)$$

- $D \rightarrow K\bar{K}$; I = 0, 1 in the final state,

$$\begin{aligned} A(D^0 \rightarrow K^+K^-) &= \frac{1}{\sqrt{2}} A_0^{K\bar{K}} e^{i\delta_0^{K\bar{K}}} + \frac{1}{\sqrt{2}} A_1^{K\bar{K}} e^{i\delta_1^{K\bar{K}}} \\ A(D^0 \rightarrow K^0\bar{K}^0) &= \frac{1}{\sqrt{2}} A_0^{K\bar{K}} e^{i\delta_0^{K\bar{K}}} - \frac{1}{\sqrt{2}} A_1^{K\bar{K}} e^{i\delta_1^{K\bar{K}}} \\ A(D^+ \rightarrow K^+\bar{K}^0) &= \sqrt{2} A_1^{K\bar{K}} e^{i\delta_1^{K\bar{K}}} \end{aligned} \quad (1.20)$$

- $D \rightarrow K\pi$; $I = \frac{1}{2}, \frac{3}{2}$ in the final state,

$$\begin{aligned}
A(D^0 \rightarrow K^- \pi^+) &= \frac{1}{\sqrt{3}} A_{3/2}^{K\pi} e^{i\delta_{3/2}^{K\pi}} + \sqrt{\frac{2}{3}} A_{1/2}^{K\pi} e^{i\delta_{1/2}^{K\pi}} \\
A(D^0 \rightarrow \bar{K}^0 \pi^0) &= \sqrt{\frac{2}{3}} A_{3/2}^{K\pi} e^{i\delta_{3/2}^{K\pi}} - \frac{1}{\sqrt{3}} A_{1/2}^{K\pi} e^{i\delta_{1/2}^{K\pi}} \\
A(D^+ \rightarrow \bar{K}^0 \pi^+) &= \sqrt{3} A_{3/2}^{K\pi} e^{i\delta_{3/2}^{K\pi}}
\end{aligned} \tag{1.21}$$

There are many more decay modes as well, and it is possible to use data from all of the different decay modes to fit these parameters simultaneously, and make predictions for other modes, in order to see if FSI can explain all the phenomena. In fact, the uncertainty of the FSI model is due to the arbitrary complex isospin phases.

An attempt to connect the FSI and BSW models (described in Sec. 1.2.2) is made by assuming that FSI simply rotates the decay amplitudes in the complex plane (in others words, assuming FSI is weak or elastic) [KaXu92], so that the isospin amplitudes can be evaluated by setting all the isospin phases equal to zero and equating the amplitudes in Sec. 1.2.3 with the amplitudes in Sec. 1.2.2. This allows a test of the consistency of the BSW model.

Alternatively, for example, one can avoid the complex FSI phases by comparing the phase-independent quantities (BR's): [KaPh941]

$$\Sigma \Gamma(D^0 \rightarrow K \bar{K}) \equiv \Gamma(D^0 \rightarrow K^+ K^-) + \Gamma(D^0 \rightarrow K^0 \bar{K}^0) \tag{1.22}$$

and $\Gamma(D^+ \rightarrow \bar{K}^0 K^+)$. Thus, without the uncertainty of unknown complex isospin phases, one can test the consistency of the BSW model and also estimate the strong interaction amplitudes.

1.2.4 Phenomenological Approach. There is another phenomenological approach using the model-independent quark-diagram scheme to assign decay amplitudes for all 2-body exclusive decays of D mesons. It has the 6 basic quark diagrams shown in Fig. 1.2: [ChCh87]

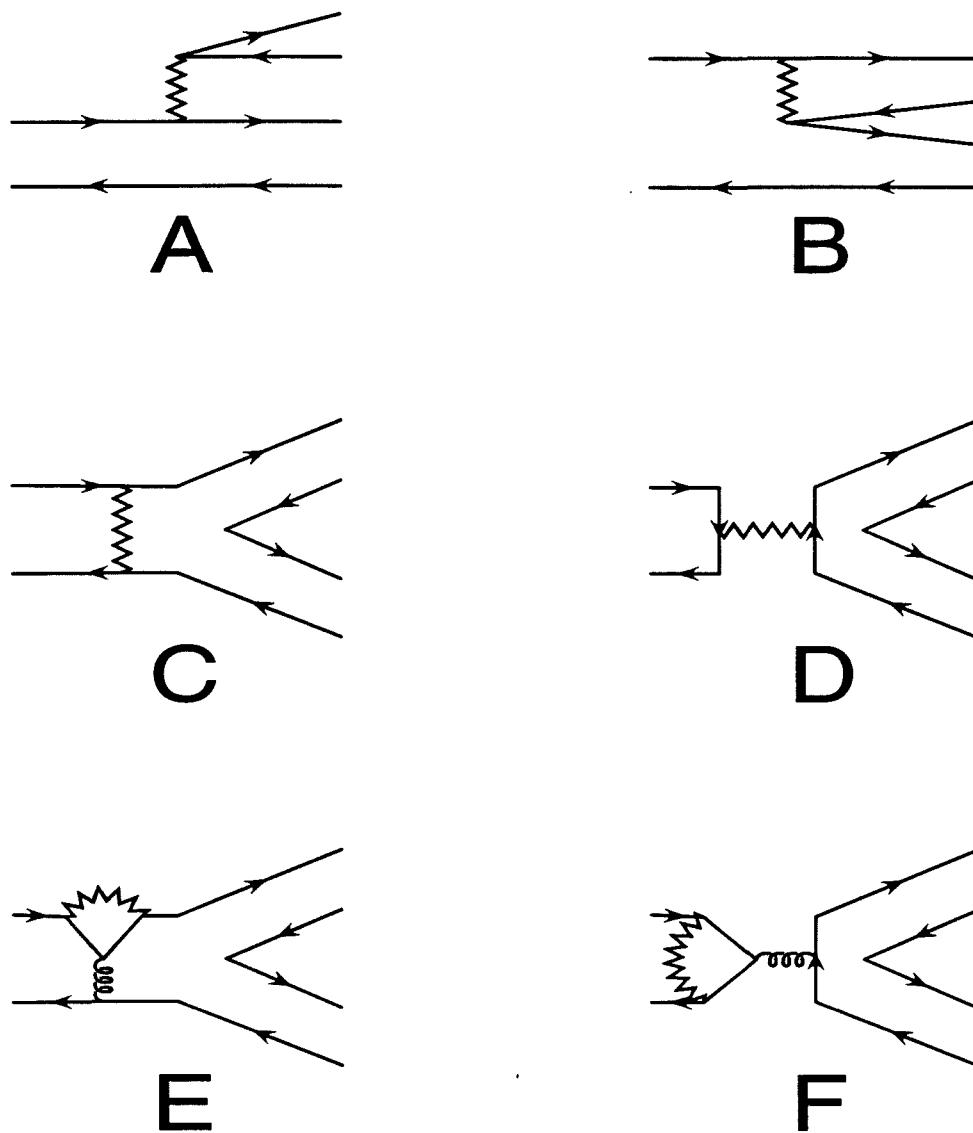


Figure 1.2. Six Possible Weak Quark-decay Diagrams in a Phenomenological Approach:

\mathcal{A} — The external W emission diagram; \mathcal{B} — The internal W emission diagram;
 \mathcal{C} — The W exchange diagram; \mathcal{D} — The W annihilation diagram;
 \mathcal{E} — The horizontal W loop diagram; \mathcal{F} — The vertical W loop diagram.

- External W emission (\mathcal{A}).
- Internal W emission (\mathcal{B}).
- W exchange (\mathcal{C}).
- W annihilation (\mathcal{D}).
- Horizontal W loop (\mathcal{E}).
- Vertical W loop (\mathcal{F}).

This classification is independent of the strong-interaction schemes, and can incorporate any specific strong-interaction-model calculations. Thus all the s , c , b , and t particle decays can be expressed in terms of these six types of quark diagrams and the quark mixing matrix. These quark diagrams are specific and well-defined physical quantities. They are classified according to the topology of first-order (e.g. one-gluon loop) weak interactions, but all QCD strong-interaction effects are included [ChCh892].

Table 1.1 [ChCh92] lists a few decay amplitudes of interest. The amplitudes with tildes ($\tilde{}$) denote the diagrams involving the creation of $s\bar{s}$; $\delta\mathcal{E} \equiv \tilde{\mathcal{E}} - \mathcal{E}$ and $\delta\mathcal{F} \equiv \tilde{\mathcal{F}} - \mathcal{F}$. These are SU(3) breaking. In addition, the difference of form factors and decay constants (discussed in Sec. 1.2.2) will further induce different \mathcal{A} 's for different decay modes. FSI is expressed by the phase shifts, the δ 's, which in general have both real and imaginary parts. The real parts are related to the elastic scattering effects while the imaginary parts indicate effects of inelasticity [ChCh94]. δ_I^{PP} (as mentioned in Sec. 1.2.3) is the FSI phase shift of isospin I in $D \rightarrow PP$ decay and Δ_{PP} is the phase difference between the two final isospin states.

In the case of $\Gamma(D^0 \rightarrow K^+ K^-)$ and $\Gamma(D^0 \rightarrow \pi^+ \pi^-)$, Table 1.1 shows two possible sources responsible for the deviation from the naive SU(3) symmetry prediction that $\frac{\Gamma(D^0 \rightarrow K^+ K^-)}{\Gamma(D^0 \rightarrow \pi^+ \pi^-)} = 1$.

Table 1.1. Amplitudes of $D \rightarrow PP$ Decays

Decay Mode	SU(3) symmetry $V_{us}V_{cs}^* \simeq -V_{ud}V_{cd}^* = s_1 c_1$	Amplitudes in { } are replaced due to SU(3) breaking and FSI
$D^+ \rightarrow$		
$\pi^0 \pi^+$	$\frac{1}{\sqrt{2}}(s_1 c_1)\{\mathcal{A} + \mathcal{B}\}$	$(\mathcal{A} + \mathcal{B})e^{i\delta_2^{\pi\pi}}$
$K^+ \bar{K}^0$	$(s_1 c_1)\{\mathcal{A} - \mathcal{D}\}$	$(\mathcal{A} - \tilde{\mathcal{D}} + \delta\mathcal{E})e^{i\delta_1^{KK}}$
$\bar{K}^0 \pi^+$	$(c_1)^2\{\mathcal{A} + \mathcal{B}\}$	$(\mathcal{A} + \mathcal{B})e^{i\delta_{3/2}^{K\pi}}$
$D^0 \rightarrow$		
$K^- \pi^+$	$(c_1)^2\{\mathcal{A} + \mathcal{C}\}$	$[(\mathcal{A} + \mathcal{C}) - \frac{1}{3}(\mathcal{A} + \mathcal{B})(1 - e^{i\Delta_{K\pi}})]e^{i\delta_{1/2}^{K\pi}}$
$K^- K^+$	$(s_1 c_1)\{\mathcal{A} + \mathcal{C}\}$	$[(\mathcal{A} + \mathcal{C}) + (\delta\mathcal{E} + 2\delta\mathcal{F}) - \frac{1}{2}(\mathcal{A} + \tilde{\mathcal{C}} + \delta\mathcal{E})(1 - e^{i\Delta_{KK}})]e^{i\delta_0^{KK}}$
$\pi^- \pi^+$	$-(s_1 c_1)\{\mathcal{A} + \mathcal{C}\}$	$[(\mathcal{A} + \mathcal{C}) - (\delta\mathcal{E} + 2\delta\mathcal{F}) - \frac{1}{3}(\mathcal{A} + \mathcal{B})(1 - e^{i\Delta_{\pi\pi}})]e^{i\delta_0^{\pi\pi}}$
$\bar{K}^0 \pi^0$	$\frac{1}{\sqrt{2}}(c_1)^2\{\mathcal{B} - \mathcal{C}\}$	$[(\mathcal{B} - \mathcal{C}) - \frac{2}{3}(\mathcal{A} + \mathcal{B})(1 - e^{i\Delta_{K\pi}})]e^{i\delta_{1/2}^{K\pi}}$
$K^0 \bar{K}^0$	$(s_1 c_1)\{0\}$	$[(\mathcal{C} - \tilde{\mathcal{C}} + 2\delta\mathcal{F}) + \frac{1}{2}(\mathcal{A} + \tilde{\mathcal{C}} + \delta\mathcal{E})(1 - e^{i\Delta_{KK}})]e^{i\delta_0^{KK}}$
$\pi^0 \pi^0$	$\frac{1}{\sqrt{2}}(s_1 c_1)\{\mathcal{B} - \mathcal{C}\}$	$[(\mathcal{B} - \mathcal{C}) + (\delta\mathcal{E} + 2\delta\mathcal{F}) - \frac{2}{3}(\mathcal{A} + \mathcal{B})(1 - e^{i\Delta_{\pi\pi}})]e^{i\delta_0^{\pi\pi}}$

- SU(3) symmetry breaking — Accumulations of small pieces of SU(3)-symmetry breaking effects, such as the decay constants, the form factors, and the mass-difference ratios (described in Sec. 1.2.2), lead to a deviation of $\frac{\Gamma(D^0 \rightarrow K^+ K^-)}{\Gamma(D^0 \rightarrow \pi^+ \pi^-)}$ from 1. However, SU(3) symmetry breaking is insufficient to explain all of the data.[†]
- Coupled Channel FSI — The $\pi\pi$ can rescatter into $\bar{K}K$ through the $I = 0$ channel by inelastic FSI [KaCo81, KaSi87]. In particular, there is a known 0^+ resonance ($f_0(1300)$) which couples to both $\pi\pi$ and $\bar{K}K$ by the $I = 0$ channel, as well as a resonance $a_0(980)$ which couples to both $\eta\pi$ and $\bar{K}K$ by the $I = 1$ channel.

[†]It has been suggested [Finj81, Pham86] that penguin contributions (Fig. 1.1(c) or \mathcal{E} & \mathcal{F} in Fig. 1.2) may help to explain the discrepancy between models and experiments. However, it is evident in Table 1.1 that including penguins contributions would only increase the deviation. Also, the penguin contributions are rather small, estimated to be $\mathcal{E}/\mathcal{A} \sim 1\%$. Kamal & Pham [KaPh94] conclude that the Penguin mechanism, which could solve some problems in isolation, is not the solution to the global problem in $D \rightarrow K\bar{K}$ and $D \rightarrow \pi\pi$ decay.

To summarize the BR study, I emphasize that $\frac{\Gamma(D^0 \rightarrow K^+ K^-)}{\Gamma(D^0 \rightarrow \pi^+ \pi^-)}$ is only one of many BR's. There are many models which calculate this particular BR relying on the apparent simplicity and similarity implied by Fig. 1.1. But few models can survive a global phenomenological test of all the two-body decay BR's. Our measurements narrow the experimental errors, so that further phenomenological tests can be made on different models and different decay modes.

So far, the BR's have been calculated by ignoring the tiny (10^{-4} or smaller) differences in decay rates between particles and anti-particles. The following section will discuss the effects of direct CP and Mixing phenomena resulting in different BR's for particles and anti-particles.

1.3 CP Violation and Mixing in the D^0 - \bar{D}^0 System

Looking at the simple picture in Eq. (1.3), another parameter is the direct CP asymmetry, ϵ' . This direct CP asymmetry would be reflected in a difference between the partial decay widths of any (charged or neutral) particle and its anti-particle, namely the asymmetry between $\langle f|H|D^0 \rangle$ and $\langle \bar{f}|H|\bar{D}^0 \rangle$. To complete the consideration of neutral mesons, there is

- Direct CP asymmetry, ϵ' ;
- Indirect CP asymmetry, ϵ ;
- Mass Mixing, γ , $\Delta\gamma$, and Δm .

The time evolution of the quark eigenstates (D^0 , \bar{D}^0) is described in terms of an effective Hamiltonian. That is, writing the wavefunction in the two-component form

$$\psi(t) = \begin{pmatrix} |D^0(t)\rangle \\ |\bar{D}^0(t)\rangle \end{pmatrix}, \quad (1.23)$$

with

$$\psi(0) = \begin{pmatrix} |D^0\rangle \\ |\bar{D}^0\rangle \end{pmatrix}, \quad (1.24)$$

we have

$$i \frac{d}{dt} \psi(t) = H_W^{\text{eff}} \psi(t) \quad (1.25)$$

$$= \begin{pmatrix} H_{11} & H_{12} \\ H_{21} & H_{22} \end{pmatrix} \psi(t) \quad (1.26)$$

$$= \left(\mathcal{M} - i \frac{1}{2} \mathcal{T} \right) \psi(t) \quad (1.27)$$

$$= \begin{pmatrix} M - i \frac{1}{2} \Gamma & M_{12} - i \frac{1}{2} \Gamma_{12} \\ M_{12}^* - i \frac{1}{2} \Gamma_{12}^* & M - i \frac{1}{2} \Gamma \end{pmatrix} \psi(t). \quad (1.28)$$

where \mathcal{M} and \mathcal{T} are the mass matrix and the decay matrix, respectively, and CPT is conserved for Eq. (1.28) [Commins, Na94].

Following Eq. (1.4), the Physical mass eigenstates D_H^0 and D_L^0 are found to be

$$|D_H^0\rangle = \frac{1}{\sqrt{2(1+|\epsilon|^2)}} [(1+\epsilon)|D^0\rangle + (1-\epsilon)|\bar{D}^0\rangle] \equiv p|D^0\rangle + q|\bar{D}^0\rangle \quad (1.29)$$

$$|D_L^0\rangle = \frac{1}{\sqrt{2(1+|\epsilon|^2)}} [(1+\epsilon)|D^0\rangle - (1-\epsilon)|\bar{D}^0\rangle] \equiv p|D^0\rangle - q|\bar{D}^0\rangle, \quad (1.30)$$

or by diagonalizing the mass matrix Eq. (1.28), and using different notation

$$\frac{p}{q} = \frac{1+\epsilon}{1-\epsilon} = \sqrt{\frac{H_{12}}{H_{21}}} = \sqrt{\frac{M_{12} - i \frac{1}{2} \Gamma_{12}}{M_{12}^* - i \frac{1}{2} \Gamma_{12}^*}}. \quad (1.31)$$

where $\epsilon = \frac{p-q}{p+q}$.

Let f denote the final decay state of the neutral meson and \bar{f} its charge conjugate state. Define 4 decay amplitudes for D^0 and \bar{D}^0 : [PaWu95]

$$g \equiv \langle f | H_W^{\text{eff}} | D^0 \rangle, \quad h \equiv \langle f | H_W^{\text{eff}} | \bar{D}^0 \rangle; \quad \bar{g} \equiv \langle \bar{f} | H_W^{\text{eff}} | \bar{D}^0 \rangle, \quad \bar{h} \equiv \langle \bar{f} | H_W^{\text{eff}} | D^0 \rangle. \quad (1.32)$$

Parameters containing direct CP violation are defined by

$$\epsilon' \equiv \frac{g-h}{g+h}, \quad \bar{\epsilon}' \equiv \frac{\bar{h}-\bar{g}}{\bar{h}+\bar{g}}, \quad \epsilon'' \equiv \frac{g-\bar{g}}{g+\bar{g}}, \quad \bar{\epsilon}'' \equiv \frac{h-\bar{h}}{h+\bar{h}}. \quad (1.33)$$

Note that the above parameters are not physical observables since they are from complex decay amplitudes, and thus are not rephase-invariant [PaWu95]. One can however define the CP-violating observables by considering the ratio,

$$\eta_f \equiv \frac{\langle f | H_W^{\text{eff}} | D_L^0 \rangle}{\langle f | H_W^{\text{eff}} | D_H^0 \rangle} = \frac{1 - r_f}{1 + r_f}, \quad (1.34)$$

with $r_f = \frac{q/p}{h/g}$ being rephase-invariant. It can be shown that[†]

$$\eta_f = \frac{a_\epsilon + a_{\epsilon'} + i a_{\epsilon+\epsilon'}}{2 + a_\epsilon a_{\epsilon'} + a_{\epsilon\epsilon'}} \quad (1.35)$$

with new rephase-invariant quantities

$$\begin{aligned} a_\epsilon &\equiv \frac{1 - |q/p|^2}{1 + |q/p|^2} = \frac{2\Re(\epsilon)}{1 + |\epsilon|^2}, \\ a_{\epsilon'} &\equiv \frac{1 - |h/g|^2}{1 + |h/g|^2} = \frac{2\Re(\epsilon')}{1 + |\epsilon'|^2}, \\ a_{\epsilon+\epsilon'} &\equiv \frac{-4\Im(qh/pg)}{(1 + |q/p|^2)(1 + |h/g|^2)} = \frac{2\Im(\epsilon)(1 - |\epsilon'|^2) + 2\Im(\epsilon')(1 - |\epsilon|^2)}{(1 + |\epsilon|^2)(1 + |\epsilon'|^2)}, \\ a_{\epsilon\epsilon'} &\equiv \frac{-4\Re(qh/pg)}{(1 + |q/p|^2)(1 + |h/g|^2)} - 1 = \frac{4\Im(\epsilon)\Im(\epsilon') - 2(|\epsilon|^2 + |\epsilon'|^2)}{(1 + |\epsilon|^2)(1 + |\epsilon'|^2)}. \end{aligned} \quad (1.36)$$

Only three of these are independent as $(1 - a_\epsilon^2)(1 - a_{\epsilon'}^2) = a_{\epsilon+\epsilon'}^2 + (1 + a_{\epsilon\epsilon'})^2$. Analogously, one has

$$\eta_f \equiv \frac{\langle \bar{f} | H_W^{\text{eff}} | D_L^0 \rangle}{\langle \bar{f} | H_W^{\text{eff}} | D_H^0 \rangle} = \frac{a_\epsilon + a_{\bar{\epsilon}'} + i a_{\epsilon+\bar{\epsilon}'}}{2 + a_\epsilon a_{\bar{\epsilon}'} + a_{\epsilon\bar{\epsilon}'}} \quad (1.37)$$

where $a_{\bar{\epsilon}'}$, $a_{\epsilon+\bar{\epsilon}'}$ and $a_{\epsilon\bar{\epsilon}'}$ are similar to $a_{\epsilon'}$, $a_{\epsilon+\epsilon'}$ and $a_{\epsilon\epsilon'}$ but with ϵ' being replaced by $\bar{\epsilon}'$. Two additional rephase-invariant quantities complete the set of observables,

$$a_{\epsilon''} \equiv \frac{1 - |\bar{g}/g|^2}{1 + |\bar{g}/g|^2} = \frac{2\Re(\epsilon'')}{1 + |\epsilon''|^2}, \quad a_{\bar{\epsilon}''} \equiv \frac{1 - |\bar{h}/h|^2}{1 + |\bar{h}/h|^2} = \frac{2\Re(\bar{\epsilon}'')}{1 + |\bar{\epsilon}''|^2}. \quad (1.38)$$

CP violation can be classified into three types:

[†]By using $1 - ab = [(1+a)(1-b) + (1-a)(1+b)]/2$ and $1 + ab = [(1+a)(1+b) + (1-a)(1-b)]/2$.

- pure indirect (Mixing-type) CP violation which is given by the rephase-invariant CP-violating observable a_ϵ ;
- pure direct CP violation which is characterized by the rephase-invariant CP-violating observables $a_{\epsilon''}$ and $a_{\bar{\epsilon}''}$ (plus $a_{\epsilon'}$ and $a_{\bar{\epsilon}'}$ for the following special cases);
- indirect-direct mixed CP violation which is described by the rephase-invariant CP-violating observables $a_{\epsilon+\epsilon'}$ & $a_{\epsilon+\bar{\epsilon}'}$ and $a_{\epsilon\bar{\epsilon}'}$ & $a_{\bar{\epsilon}\epsilon'}$.

In order to measure these rephase-invariant observables, consider the proper time evolution of the neutral mesons

$$|D^0(t)\rangle = \frac{1}{2p} e^{-i(m_H - i\gamma_H/2)t} |D_H^0\rangle + \frac{1}{2p} e^{-i(m_L - i\gamma_L/2)t} |D_L^0\rangle \quad (1.39)$$

$$|\bar{D}^0(t)\rangle = \frac{1}{2q} e^{-i(m_H - i\gamma_H/2)t} |D_H^0\rangle - \frac{1}{2q} e^{-i(m_L - i\gamma_L/2)t} |D_L^0\rangle \quad (1.40)$$

or

$$\begin{aligned} |D^0(t)\rangle &= f_+(t) |D^0\rangle + \frac{q}{p} \cdot f_-(t) |\bar{D}^0\rangle, \\ |\bar{D}^0(t)\rangle &= \frac{p}{q} \cdot f_-(t) |D^0\rangle + f_+(t) |\bar{D}^0\rangle, \end{aligned} \quad (1.41)$$

with

$$f_\pm = \frac{1}{2} \{ e^{i(-m_H + i\frac{\gamma_H}{2})t} \pm e^{i(-m_L + i\frac{\gamma_L}{2})t} \}, \quad (1.42)$$

$$\gamma \equiv \frac{\gamma_H + \gamma_L}{2}, \quad (1.43)$$

$$\Delta\gamma \equiv \gamma_L - \gamma_H = +4\Im \sqrt{(M_{12} - i\frac{\Gamma_{12}}{2})(M_{12}^* - i\frac{\Gamma_{12}^*}{2})}, \quad (1.44)$$

$$\Delta m \equiv m_L - m_H = -2\Re \sqrt{(M_{12} - i\frac{\Gamma_{12}}{2})(M_{12}^* - i\frac{\Gamma_{12}^*}{2})}. \quad (1.45)$$

The time-dependent decay rates are found to be [PaWu95]

$$\begin{aligned} \Gamma(D^0(t) \rightarrow f) \propto | \langle f | H_W^{\text{eff}} | D^0(t) \rangle |^2 &= \frac{1}{1 + a_\epsilon} \frac{|g|^2 + |h|^2}{2} e^{-\gamma t} \times \\ &\left\{ (1 + a_\epsilon a_{\epsilon'}) \cosh(\Delta\gamma t) + (1 + a_{\epsilon\bar{\epsilon}'}) \sinh(\Delta\gamma t) \right. \\ &\left. + (a_\epsilon + a_{\epsilon'}) \cos(\Delta m t) + a_{\epsilon+\epsilon'} \sin(\Delta m t) \right\} \end{aligned} \quad (1.46)$$

$$\begin{aligned} \Gamma(\bar{D}^0(t) \rightarrow \bar{f}) \propto | \langle \bar{f} | H_W^{\text{eff}} | \bar{D}^0(t) \rangle |^2 &= \frac{1}{1 - a_\epsilon} \frac{|\bar{g}|^2 + |\bar{h}|^2}{2} e^{-\gamma t} \times \\ &\left\{ (1 + a_\epsilon a_{\bar{\epsilon}'}) \cosh(\Delta\gamma t) + (1 + a_{\epsilon\bar{\epsilon}'}) \sinh(\Delta\gamma t) \right. \\ &\left. - (a_\epsilon + a_{\bar{\epsilon}'}) \cos(\Delta m t) - a_{\epsilon+\bar{\epsilon}'} \sin(\Delta m t) \right\}. \end{aligned} \quad (1.47)$$

1.3.1 Lifetime Difference for D^0 - \bar{D}^0 Mixing. Ordinarily, one measures the Mixing rate by the ratio of wrong sign signals to right sign signals

$$\mathcal{R}_{\text{mix}}(t) = \frac{\Gamma(D^0(t) \rightarrow \bar{f})}{\Gamma(D^0(t) \rightarrow f)} \quad (1.48)$$

$$\bar{\mathcal{R}}_{\text{mix}}(t) = \frac{\Gamma(\bar{D}^0(t) \rightarrow f)}{\Gamma(\bar{D}^0(t) \rightarrow \bar{f})}. \quad (1.49)$$

Note that $\mathcal{R}_{\text{mix}}(t)$ and $\bar{\mathcal{R}}_{\text{mix}}(t)$ would be the same only for CP invariance, *i.e.* $p = q$ in Eq. (1.41) or $\epsilon = 0$ in Eq. (1.4). See also the discussion of indirect-CP with Mixing in a first order approximation by L. Wolfenstein [Wolf95].

Assume CP invariance[†], *i.e.* $|\epsilon|$ and $|\epsilon''|$ are 0, $|g| = |\bar{g}|$, $|h| = |\bar{h}|$, and $p = q = 1$. Then directly from Eq. (1.3), the mass eigenstates are identical to the CP eigenstates. Obviously, $K^\pm K^\mp$ are the decay products of the CP-even eigenstate D_2^0 which has definite lifetime and mass, whereas $K^\mp \pi^\pm$ is not a decay product of a CP eigenstate but rather a mixture of CP-even and CP-odd states.

[†]Original idea by T. Liu [Liu94]

With the CP invariance assumption, we have $a_\epsilon = a_{\bar{\epsilon}} = 0$, $q/p = 1$, $g = \bar{g}$, $h = \bar{h}$, $a_\epsilon = a_{\bar{\epsilon}}$, $a_{\epsilon\epsilon'} = a_{\bar{\epsilon}\bar{\epsilon}'}$, and $a_{\epsilon+\epsilon'} = a_{\bar{\epsilon}+\bar{\epsilon}'}$. Eq. (1.46) and Eq. (1.47) lead to

$$\begin{aligned} \Gamma(D^0(t) \rightarrow f) &\propto |\langle f | H_W^{\text{eff}} | D^0(t) \rangle|^2 = \frac{|g|^2 + |h|^2}{2} e^{-\gamma t} \times \\ &\left\{ \cosh(\Delta\gamma t) + (1 + a_{\epsilon\epsilon'}) \sinh(\Delta\gamma t) \right. \\ &\quad \left. + a_{\epsilon'} \cos(\Delta mt) + a_{\epsilon+\epsilon'} \sin(\Delta mt) \right\} \end{aligned} \quad (1.50)$$

$$\begin{aligned} \Gamma(\bar{D}^0(t) \rightarrow \bar{f}) &\propto |\langle \bar{f} | H_W^{\text{eff}} | \bar{D}^0(t) \rangle|^2 = \frac{|g|^2 + |h|^2}{2} e^{-\gamma t} \times \\ &\left\{ \cosh(\Delta\gamma t) + (1 + a_{\epsilon\epsilon'}) \sinh(\Delta\gamma t) \right. \\ &\quad \left. - a_{\epsilon'} \cos(\Delta mt) - a_{\epsilon+\epsilon'} \sin(\Delta mt) \right\}. \end{aligned} \quad (1.51)$$

Combine Eq. 1.50 and Eq. 1.51 for $K^\mp \pi^\pm$:

$$\begin{aligned} \Gamma(D^0, \bar{D}^0 \rightarrow K^\mp \pi^\pm) &\propto (|g|^2 + |h|^2) e^{-\gamma t} \times \\ &\left\{ \cosh(\Delta\gamma t) + (1 + a_{\epsilon\epsilon'}) \sinh(\Delta\gamma t) \right\} \end{aligned} \quad (1.52)$$

which is not a pure exponential decay.

- For $K^\pm K^\mp$ being a CP-even eigenstate decay, which has definite mass and lifetime, τ_{KK} in $D_2^0 \rightarrow K^+ K^-$ is the inverse of γ_2 .
- For $K^\mp \pi^\pm$ case, h could be considered as the contribution from Doubly Cabibbo Suppressed Decay (DCSD). Obviously, Eq. 1.50 and Eq. 1.51 are not pure exponential decays. Even after the right sign tagging from the strong decay of $D^{\pm\pm} \rightarrow D^0(\bar{D}^0)\pi^\pm$, i.e. with $h = 0$, Eq. 1.50 and Eq. 1.51 still do not yield pure exponential decays:

$$\begin{aligned} \Gamma(D^0(t) \rightarrow K^- \pi^+) &\propto |\langle f | H_W^{\text{eff}} | D^0(t) \rangle|^2 \\ &= \frac{|g|^2}{2} e^{-\gamma t} \times [\cosh(\Delta\gamma t) + \cos(\Delta mt)] \\ \Gamma(\bar{D}^0(t) \rightarrow K^+ \pi^-) &\propto |\langle \bar{f} | H_W^{\text{eff}} | \bar{D}^0(t) \rangle|^2 \\ &= \frac{|g|^2}{2} e^{-\gamma t} \times [\cosh(\Delta\gamma t) - \cos(\Delta mt)]. \end{aligned} \quad (1.53)$$

But $\tau_{K\pi}$ in $D^0 \rightarrow K^- \pi^+$ can be approximated as the inverse of γ , and since only the exponential decay can be noticed easily, there is no need to separate D^0 and \bar{D}^0 to measure $\tau_{K\pi}$ [Liu95].

Thus, by studying the lifetime difference with the CP invariance assumption,

$$\Delta\gamma \equiv \gamma_{2(L)} - \gamma_{1(H)} \quad (1.54)$$

$$\doteq 2 \cdot \left(\frac{1}{\tau_{KK}} - \frac{1}{\tau_{K\pi}} \right) \quad (1.55)$$

$$\doteq 2 \cdot \frac{\tau_{K\pi} - \tau_{KK}}{\tau_{KK} \times \tau_{K\pi}} \quad (1.56)$$

$$\simeq 2 \cdot \frac{\tau_{K\pi} - \tau_{KK}}{(PDG\tau_{K\pi})^2}. \quad (1.57)$$

In Appendix A[†], I also adopt another approach by using the difference between two mean values of the proper decay time to estimate the lifetime difference ($\tau_{K\pi} - \tau_{KK}$) in terms of Eq. (1.57).

The Mixing rate can be parameterized, assuming CP invariance as

$$\mathcal{R}_{\text{mix}} = \bar{\mathcal{R}}_{\text{mix}} = \frac{x^2 + y^2}{2} \quad (1.58)$$

with $x = \frac{m_2 - m_1}{\gamma_2 + \gamma_1}$ and $y = \frac{\gamma_2 - \gamma_1}{\gamma_2 + \gamma_1}$, leading to

$$y \doteq \left(\frac{\tau_{K\pi}}{\tau_{KK}} - 1 \right) \quad (1.59)$$

for $\tau_{KK} = \frac{1}{\gamma_2}$ and $\tau_{K\pi} \doteq \frac{2}{\gamma_2 + \gamma_1}$. By studying the lifetime ratio, we can estimate the Mixing rate due to lifetime difference. Note that x and y is independent to each other (mass difference vs. lifetime difference). To have a complete estimate of Mixing

[†]Developed by Dr. M. Purohit

rate, we need to have both x and y . The Standard Model predicts that $\frac{\Delta\gamma}{\gamma} < \frac{\Delta m}{\gamma}$ in D^0 - \bar{D}^0 system. E791 measurement will be the first estimate of y in D^0 - \bar{D}^0 Mixing.

1.3.2 Direct CP Violation. Experimentally, define the CP asymmetry parameter from the comparison of the partial decay widths as

$$A_{\text{CP}} = \frac{\Gamma - \bar{\Gamma}}{\Gamma + \bar{\Gamma}}. \quad (1.60)$$

In general, one can represent the decay amplitude of a meson M (\bar{M}) decaying to a final state, f (\bar{f}), as

$$\begin{aligned} A(M \rightarrow f) &= W_1 e^{i\delta_1} + W_2 e^{i\delta_2} \\ \bar{A}(\bar{M} \rightarrow \bar{f}) &= W_1^* e^{i\delta_1} + W_2^* e^{i\delta_2} \end{aligned}$$

where W 's are the weak decay amplitudes and δ 's are the strong final state-interaction phases. Then

$$\begin{aligned} A_{\text{CP}}(M \rightarrow f) &= \frac{\Gamma - \bar{\Gamma}}{\Gamma + \bar{\Gamma}} \\ &= \frac{A^* A - \bar{A}^* \bar{A}}{A^* A + \bar{A}^* \bar{A}} \\ &= \frac{2\Im(W_1 W_2^*) \sin(\delta_2 - \delta_1)}{|B_1|^2 + |B_2|^2 + 2\Re(W_1 W_2^*) \cos(\delta_2 - \delta_1)}. \end{aligned} \quad (1.61)$$

Both factors in the numerator of Eq. (1.60) should be nonvanishing to have a nonzero effect. Moreover, to have a sizable asymmetry the moduli of the two amplitudes W_1 and W_2 should not differ by very much. From Table 1.1, note that the SCSD's, $D^0 \rightarrow K^+ K^-$ and $D^0 \rightarrow \pi^+ \pi^-$, look like candidates to observe Direct CP asymmetry, since they have two different weak amplitudes — $V_{us} V_{cs}^*$ from quark diagrams and $V_{ud} V_{cd}^*$ from penguin diagrams — as well as two different strong isospin final states. However, I will show below that $D^0 \rightarrow K^+ K^-$ and $D^0 \rightarrow \pi^+ \pi^-$ are not good candidates for observing pure direct CP asymmetry. Even $A_{\text{CP}}(K^\mp \pi^\pm)$ could be nonzero

resulting from unknown contributions of the beyond-Standard-Model (BSM) sector [YOR92], if any, and the well-known interference of FSI.

To measure the direct CP asymmetry [BeJa81, BuLu93], A_{CP} , for the charged mesons (without any neutral meson in the intermediate or final state), one can follow the definition described above. But for neutral mesons, as D^0 and \bar{D}^0 , indirect CP asymmetry is accompanied by D^0 - \bar{D}^0 Mixing.

Following Eq. (1.46) and Eq. (1.47), first define a time-dependent $A_{CP}(t)$ as

$$\begin{aligned} A_{CP}(t) &= \frac{\Gamma(t) - \bar{\Gamma}(t)}{\Gamma(t) + \bar{\Gamma}(t)} \\ &= \frac{\Gamma(D^0(t) \rightarrow f) - \Gamma(\bar{D}^0(t) \rightarrow \bar{f})}{\Gamma(D^0(t) \rightarrow f) + \Gamma(\bar{D}^0(t) \rightarrow \bar{f})} \end{aligned} \quad (1.62)$$

Consider two special cases: [PaWu95]

- $D^0 \rightarrow f(D^0 \not\rightarrow \bar{f}), \bar{D}^0 \rightarrow \bar{f}(\bar{D}^0 \not\rightarrow f)$, *i.e.* f or \bar{f} is not a common final state of D^0 and \bar{D}^0 . If one can rule out Doubly Cabibbo Suppressed Decay (DCSD) contamination[†] then $D^0 \rightarrow K^- \pi^+$ ($\bar{D}^0 \rightarrow K^+ \pi^-$) is such an example. Also I assume the “DCSD after Mixing,” *i.e.* $D^0 \xrightarrow{\text{Mixing}} \bar{D}^0 \xrightarrow{\text{DCSD}} K^- \pi^+$ is well below the order of A_{CP} . This case leads $h = \bar{h} = 0$, $a_{\epsilon'} = -a_{\bar{\epsilon}'} = 1$, $a_{\epsilon+\epsilon'} = a_{\epsilon+\bar{\epsilon}'} = 0$, and $a_{\epsilon\epsilon'} = a_{\epsilon\bar{\epsilon}'} = -1$ in Eq. (1.46) and Eq. (1.47). Then

$$A_{CP}(t) = a_{\epsilon''} \quad (1.63)$$

which is actually time-independent. Even though $D^0 \rightarrow K^- \pi^+$ is CFD, the measurement of nonzero $A_{CP}(D^0 \rightarrow K^- \pi^+)$ would indicate pure direct CP asymmetry from the interference of weak phases between the SM and BSM sectors [YOR92].

[†]DCSD is an order of $\tan^4 \theta_c$ (Cabibbo angle), and D^0 - \bar{D}^0 CP violation would be below this order, so DCSD is non-negligible in CP studies.

- $D^0 \rightarrow (f = \bar{f}, f^{\text{CP}} = f) \leftarrow \bar{D}^0$, *i.e.* the final states are CP eigenstates, such as $D^0 \rightarrow K^+ K^-$ and $D^0 \rightarrow \pi^+ \pi^-$. This case leads to $g = \bar{h}$, $h = \bar{g}$, $a_{\epsilon'} = a_{\epsilon''} = a_{\bar{\epsilon}'} = a_{\bar{\epsilon}''}$, $a_{\epsilon\epsilon'} = a_{\epsilon\bar{\epsilon}'}$ and $a_{\epsilon+\epsilon'} = a_{\epsilon+\bar{\epsilon}'}$ in Eq. (1.46) and Eq. (1.47). Thus,

$$A_{\text{CP}}(t) = \frac{\Delta_m(t) - a_{\epsilon}\Delta_{\gamma}(t)}{\Delta_{\gamma}(t) - a_{\epsilon}\Delta_m(t)} \quad (1.64)$$

where

$$\begin{aligned} \Delta_m(t) &= (a_{\epsilon} + a_{\epsilon'}) \cos(\Delta m t) + a_{\epsilon+\epsilon'} \sin(\Delta m t), \\ \Delta_{\gamma}(t) &= (1 + a_{\epsilon}a_{\epsilon'}) \cosh(\Delta \gamma t) + (1 + a_{\epsilon\epsilon'}) \sinh(\Delta \gamma t). \end{aligned} \quad (1.65)$$

$A_{\text{CP}}(t)$ is no longer a pure direct CP asymmetry parameter but a mixture of direct and indirect CP asymmetry parameters.

Ideally, by making A_{CP} measurements on different D decays, especially the time-dependent measurements, one can extract information about the multiple parameters of Direct and Indirect CP asymmetry and Mass Mixing.

$A_{\text{CP}}^{\text{BR}}$ for the E791 Experiment. For a collider experiment, the above theoretical discussion is sufficient, but in fixed target experiments, such as E791, the Leading Particle Effect[†] complicates D meson production studies.

In order to compensate for this production asymmetry, define a new CP asymmetry parameter using branching ratios:

$$A_{\text{CP}}^{\text{BR}}(K^{\pm} K^{\mp}) \equiv \frac{\frac{\Gamma(D^{*\pm} \rightarrow (D^0 \rightarrow K^+ K^-) \pi^{\pm})}{\Gamma(D^{*\pm} \rightarrow (D^0 \rightarrow K^- \pi^+) \pi^{\pm})} - \frac{\Gamma(D^{*\mp} \rightarrow (\bar{D}^0 \rightarrow K^- K^+) \pi^{\mp})}{\Gamma(D^{*\mp} \rightarrow (\bar{D}^0 \rightarrow K^+ \pi^-) \pi^{\mp})}{\frac{\Gamma(D^{*\pm} \rightarrow (D^0 \rightarrow K^+ K^-) \pi^{\pm})}{\Gamma(D^{*\pm} \rightarrow (D^0 \rightarrow K^- \pi^+) \pi^{\pm})} + \frac{\Gamma(D^{*\mp} \rightarrow (\bar{D}^0 \rightarrow K^- K^+) \pi^{\mp})}{\Gamma(D^{*\mp} \rightarrow (\bar{D}^0 \rightarrow K^+ \pi^-) \pi^{\mp})} \quad (1.66)$$

$$A_{\text{CP}}^{\text{BR}}(\pi^{\pm} \pi^{\mp}) \equiv \frac{\frac{\Gamma(D^{*\pm} \rightarrow (D^0 \rightarrow \pi^+ \pi^-) \pi^{\pm})}{\Gamma(D^{*\pm} \rightarrow (D^0 \rightarrow K^- \pi^+) \pi^{\pm})} - \frac{\Gamma(D^{*\mp} \rightarrow (\bar{D}^0 \rightarrow \pi^- \pi^+) \pi^{\mp})}{\Gamma(D^{*\mp} \rightarrow (\bar{D}^0 \rightarrow K^+ \pi^-) \pi^{\mp})}{\frac{\Gamma(D^{*\pm} \rightarrow (D^0 \rightarrow \pi^+ \pi^-) \pi^{\pm})}{\Gamma(D^{*\pm} \rightarrow (D^0 \rightarrow K^- \pi^+) \pi^{\pm})} + \frac{\Gamma(D^{*\mp} \rightarrow (\bar{D}^0 \rightarrow \pi^- \pi^+) \pi^{\mp})}{\Gamma(D^{*\mp} \rightarrow (\bar{D}^0 \rightarrow K^+ \pi^-) \pi^{\mp})} \quad (1.67)$$

[†]The leading particle is the charm particle carrying the valence quark from the incident $\pi^- (\bar{u}d)$, and its anti-particle is non-leading. So in fixed target experiments, we see more production of leading particles (e.g. $D^0(c\bar{u}) D^- (\bar{c}d)$) than non-leading (e.g. $\bar{D}^0(\bar{c}u) D^+(c\bar{d})$) in the forward direction (or the high x_F region). Also, fixed target experiments usually don't have good acceptance in the negative x_F region, enhancing the net production asymmetry between leading and non-leading particles.

where I utilize the strategy of identifying the bachelor π^\pm from the strong decay of $D^{*\pm} \rightarrow D^0(\bar{D}^0)\pi^\pm$ to tag $D^0(\bar{D}^0)$ production and decay. I use the $D^0 \rightarrow K^-\pi^+$ mode as the normalization mode.

Note that even in the simpler picture of Eq. (1.64) and Eq. (1.65) there are three factors — Direct CP asymmetry, Indirect CP asymmetry, and Mass Mixing. So from a naive approach, in order to study Direct CP asymmetry, I wish to cancel out (1) the huge production asymmetry (such as the Leading Particle Effect), (2) the tiny Mixing (causing the interference), and (3) the unknown Indirect CP asymmetry, by doing certain normalizations. My intention here is to deduce a prediction from theory for $A_{\text{CP}}^{\text{BR}}$.

First, the right sign[†] $D^{*\pm} \rightarrow D^0(\bar{D}^0)\pi^\pm$ tagging is necessary for $K^\mp\pi^\pm$ (and $K3\pi$), in order to eliminate or reduce DCSD contamination. In addition, the possibly different efficiencies for slow (or bachelor) π^\pm 's tagging in $D^{*+} \rightarrow (D^0 \rightarrow K^+K^-)\pi^+$ and $D^{*-} \rightarrow (\bar{D}^0 \rightarrow K^-K^+)\pi^-$ can be compensated for by normalizing to $D^{*+} \rightarrow (D^0 \rightarrow K^-\pi^+)\pi^+$ and $D^{*-} \rightarrow (\bar{D}^0 \rightarrow K^+\pi^-)\pi^-$. I do not induce more CP asymmetry from $D^{*\pm} \rightarrow D^0(\bar{D}^0)\pi^\pm$, since these are strong decays (but if strong CP asymmetry is of the same order there might be interference between strong and weak CP asymmetries). I do include the possible weak CP asymmetry from $D^0 \rightarrow K^-\pi^+$ and $\bar{D}^0 \rightarrow K^+\pi^-$ into Eq. (1.66) and Eq. (1.67).

[†]In $D^{*+} \rightarrow (D^0 \rightarrow K^-\pi^+)\pi^+$, events with two same-charged π 's are called right sign events, and those with opposite-signed π 's are called wrong sign. Similar notation applies to $D^{*-} \rightarrow (\bar{D}^0 \rightarrow K^+\pi^-)\pi^-$.

Second, due to the limited statistics, I measure the time-integrated $A_{\text{CP}}^{\text{BR}}$. Integrating the general forms of Eq. (1.46 and 1.47),

$$\begin{aligned} \int_0^\infty \Gamma(D^0(t) \rightarrow f) dt &\propto \frac{1}{[\gamma^2 - (\Delta\gamma)^2][\gamma^2 + (\Delta m)^2]} \times \frac{|g|^2 + |h|^2}{2(1 + a_\epsilon)} \times \\ &\left\{ (1 + a_\epsilon a_{\epsilon'})[\gamma^3 + \gamma(\Delta m)^2] + (1 + a_{\epsilon\epsilon'})[\gamma^2 \Delta\gamma + \Delta\gamma(\Delta m)^2] \right. \\ &\quad \left. - (a_\epsilon + a_{\epsilon'})[\gamma(\Delta\gamma)^2 - \gamma^3] - a_{\epsilon+\epsilon'}|\Delta m|[(\Delta\gamma)^2 - \gamma^2] \right\} \end{aligned} \quad (1.68)$$

$$\begin{aligned} \int_0^\infty \Gamma(\bar{D}^0(t) \rightarrow \bar{f}) dt &\propto \frac{1}{[\gamma^2 - (\Delta\gamma)^2][\gamma^2 + (\Delta m)^2]} \times \frac{|\bar{g}|^2 + |\bar{h}|^2}{2(1 - a_\epsilon)} \times \\ &\left\{ (1 + a_\epsilon a_{\bar{\epsilon}})[\gamma^3 + \gamma(\Delta m)^2] + (1 + a_{\epsilon\bar{\epsilon}})[\gamma^2 \Delta\gamma + \Delta\gamma(\Delta m)^2] \right. \\ &\quad \left. + (a_\epsilon + a_{\bar{\epsilon}})[\gamma(\Delta\gamma)^2 - \gamma^3] + a_{\epsilon+\bar{\epsilon}}|\Delta m|[(\Delta\gamma)^2 - \gamma^2] \right\}. \end{aligned} \quad (1.69)$$

Thus for the $D^0 \rightarrow K^+ K^-$ mode (according to the conditions mentioned above),

$$\begin{aligned} \Gamma(D^0 \rightarrow K^+ K^-) &\propto \frac{1}{[\gamma^2 - (\Delta\gamma)^2][\gamma^2 + (\Delta m)^2]} \times \frac{|g|^2 + |\bar{g}|^2}{2(1 + a_\epsilon)} \times \\ &\left\{ (1 + a_\epsilon a_{\epsilon'})[\gamma^3 + \gamma(\Delta m)^2] + (1 + a_{\epsilon\epsilon'})[\gamma^2 \Delta\gamma + \Delta\gamma(\Delta m)^2] \right. \\ &\quad \left. - (a_\epsilon + a_{\epsilon'})[\gamma(\Delta\gamma)^2 - \gamma^3] - a_{\epsilon+\epsilon'}|\Delta m|[(\Delta\gamma)^2 - \gamma^2] \right\} \end{aligned} \quad (1.70)$$

$$\begin{aligned} \Gamma(\bar{D}^0 \rightarrow K^- K^+) &\propto \frac{1}{[\gamma^2 - (\Delta\gamma)^2][\gamma^2 + (\Delta m)^2]} \times \frac{|\bar{g}|^2 + |g|^2}{2(1 - a_\epsilon)} \times \\ &\left\{ (1 + a_\epsilon a_{\bar{\epsilon}})[\gamma^3 + \gamma(\Delta m)^2] + (1 + a_{\epsilon\bar{\epsilon}})[\gamma^2 \Delta\gamma + \Delta\gamma(\Delta m)^2] \right. \\ &\quad \left. + (a_\epsilon + a_{\bar{\epsilon}})[\gamma(\Delta\gamma)^2 - \gamma^3] + a_{\epsilon+\bar{\epsilon}}|\Delta m|[(\Delta\gamma)^2 - \gamma^2] \right\}; \end{aligned} \quad (1.71)$$

and for the $D^0 \rightarrow K^- \pi^+$ mode,

$$\begin{aligned} \Gamma(D^0 \rightarrow K^- \pi^+) &\propto \frac{1}{[\gamma^2 - (\Delta\gamma)^2][\gamma^2 + (\Delta m)^2]} \times \frac{|g'|^2}{2(1 + a_\epsilon)} \times \\ &\left\{ (1 + a_\epsilon)[\gamma^3 + \gamma(\Delta m)^2] - (a_\epsilon + 1)[\gamma(\Delta\gamma)^2 - \gamma^3] \right\} \end{aligned} \quad (1.72)$$

$$\begin{aligned} \Gamma(\bar{D}^0 \rightarrow K^+ \pi^-) &\propto \frac{1}{[\gamma^2 - (\Delta\gamma)^2][\gamma^2 + (\Delta m)^2]} \times \frac{|\bar{g}'|^2}{2(1 - a_\epsilon)} \times \\ &\left\{ (1 + a_\epsilon)[\gamma^3 + \gamma(\Delta m)^2] + (a_\epsilon - 1)[\gamma(\Delta\gamma)^2 - \gamma^3] \right\}. \end{aligned} \quad (1.73)$$

Substituting Eqs. (1.70–1.73) into Eq. (1.66), two different decay modes share the same set of indirect CP rephase-invariant parameters, $\Delta\gamma$, Δm and γ — but different g and g' (the decay amplitude of the numerator and denominator, respectively), and different direct CP rephase-invariant parameters. Unfortunately, the calculation of $A_{\text{CP}}^{\text{BR}}$ cannot be simplified without further assumption, due to the complicated normalization of Eq. (1.72, 1.73) — the difference between $|g'|$ and $|\bar{g}'|$ and between $-(a_\epsilon + 1)$ and $+(a_\epsilon - 1)$. Also because each term in Eqs. (1.70–1.73) is additive, it makes cancellation difficult, especially the terms in the $K^\mp\pi^\pm$ mode.

Because both $K^\mp\pi^\pm$ and $K3\pi$ are in the same category (the final state is not a common state of D^0 and \bar{D}^0 , and both share the same Mixing parameters and Indirect CP parameters although not Direct CP parameters), without any assumption, the $A_{\text{CP}}^{\text{BR}}$ for right sign $K3\pi$ with the same normalization of right sign $K^\mp\pi^\pm$ shows a simple form:

$$A_{\text{CP}}^{\text{BR}}(K3\pi) = \frac{\frac{|g|^2}{|g'|^2} - \frac{|\bar{g}|^2}{|\bar{g}'|^2}}{\frac{|g|^2}{|g'|^2} + \frac{|\bar{g}|^2}{|\bar{g}'|^2}}. \quad (1.74)$$

This is an indication of direct CP asymmetry of the BR $\frac{\Gamma(D^0 \rightarrow K^- \pi^- \pi^+ \pi^+)}{\Gamma(D^0 \rightarrow K^- \pi^+)}.$

Applying assumptions in the order of their least effect on $A_{\text{CP}}^{\text{BR}}$,

- Assume Direct CP invariance in $D^0 \rightarrow K^- \pi^+$ and $\bar{D}^0 \rightarrow K^+ \pi^-$ — i.e. the unlikely weak phase from BSM [YOR92] sector is ruled out, thus $|g'| = |\bar{g}'|$ and

$$\begin{aligned} A_{\text{CP}}^{\text{BR}}(K^\pm K^\mp) \doteq & \left\{ a_\epsilon(1 + a_{\epsilon\epsilon'})\Delta\gamma[(\Delta m)^2 + \gamma^2][(\Delta\gamma)^2 - \gamma^2] + \right. \\ & a_\epsilon(1 + a_{\epsilon\epsilon'})\gamma[(\Delta m)^2 + \gamma^2][(\Delta\gamma)^2 - \gamma^2] - \\ & a_{\epsilon+\epsilon'}|\Delta m|[(\Delta\gamma)^2 - \gamma^2][-(\Delta\gamma)^2 + \gamma^2 + (1 + a_\epsilon)[(\Delta m)^2 + \gamma^2]] - \\ & \left. (a_\epsilon + a_{\epsilon'})\gamma[(\Delta\gamma)^2 - \gamma^2][-(\Delta\gamma)^2 + \gamma^2 + (1 + a_\epsilon)[(\Delta m)^2 + \gamma^2]] \right\} \div \end{aligned}$$

$$\left\{ -a_\epsilon a_{\epsilon'} |\Delta m| [(\Delta\gamma)^2 - \gamma^2]^2 - a_\epsilon (a_\epsilon + a_{\epsilon'}) [(\Delta\gamma)^2 - \gamma^2]^2 + \right. \\ \left. (1 + a_{\epsilon\epsilon'}) \Delta\gamma [(\Delta m)^2 + \gamma^2] [-(\Delta\gamma)^2 + \gamma^2 + (1 + a_\epsilon) [(\Delta m)^2 + \gamma^2]] \right. \\ \left. (1 + a_\epsilon a_{\epsilon'}) [(\Delta m)^2 + \gamma^2] [-(\Delta\gamma)^2 + \gamma^2 + (1 + a_\epsilon) [(\Delta m)^2 + \gamma^2]] \right\} \quad (1.75)$$

Also, in Eq. (1.74) $A_{\text{CP}}^{\text{BR}}(K3\pi)$ would be 0 (again because $K^\mp\pi^\pm$ and $K3\pi$ are in the same category).

- Assume no Indirect CP asymmetry — *i.e.* ϵ or $a_\epsilon \ll 1$, as $\Gamma(D^0 \rightarrow K^- \pi^+) = \Gamma(\bar{D}^0 \rightarrow K^+ \pi^-)$ in $A_{\text{CP}}^{\text{BR}}(K^\pm K^\mp)$. Thus, the ϵ and ϵ' interference terms will reduce to pure Direct CP asymmetry parameters:

$$a_{\epsilon+\epsilon'} \cong \frac{2\Im(\epsilon')}{1 + |\epsilon'|^2}, \quad a_{\epsilon\epsilon'} \cong \frac{-2|\epsilon'|^2}{1 + |\epsilon'|^2}; \quad (1.76)$$

$A_{\text{CP}}^{\text{BR}}$ of our SCSD modes under such assumptions would be simplified to

$$A_{\text{CP}}^{\text{BR}}(K^\pm K^\mp) \cong \frac{-a_{\epsilon'} [\gamma(\Delta\gamma)^2 - \gamma^3] - a_{\epsilon+\epsilon'} |\Delta m| [(\Delta\gamma)^2 - \gamma^2]}{[\gamma^3 + \gamma(\Delta m)^2] + (1 + a_{\epsilon\epsilon'}) [\gamma^2 \Delta\gamma + \Delta\gamma(\Delta m)^2]} \\ = \frac{-a_{\epsilon'} \gamma [(\Delta\gamma/\gamma)^2 - 1] - a_{\epsilon+\epsilon'} |\Delta m| [(\Delta\gamma/\gamma)^2 - 1]}{[\gamma + (\Delta m)^2/\gamma] + (1 + a_{\epsilon\epsilon'}) [\Delta\gamma + \Delta\gamma(\Delta m/\gamma)^2]}. \quad (1.77)$$

which is equivalent to no normalization in Eq. (1.66). If the measurement is non-zero it indicates that at least one of $a_{\epsilon'}$ and $a_{\epsilon+\epsilon'}$ has to be non-zero; *i.e.* $|\epsilon'| \neq 0$, an indication of Direct CP asymmetry.

- Neglect $(\Delta m/\gamma)^2$ and $(\Delta\gamma/\gamma)^2$ terms — *i.e.* $\Delta m, \Delta\gamma \ll \gamma$.

$$A_{\text{CP}}^{\text{BR}}(K^\pm K^\mp) \simeq \frac{a_{\epsilon'} \gamma + a_{\epsilon+\epsilon'} |\Delta m|}{\gamma + (1 + a_{\epsilon\epsilon'}) \Delta\gamma}. \quad (1.78)$$

If the measurement of $A_{\text{CP}}^{\text{BR}}(K^\pm K^\mp)$ is 0, then the following relationships hold:

$$a_{\epsilon'} \gamma \sim -a_{\epsilon+\epsilon'} |\Delta m| \quad (1.79)$$

$$2\Re(\epsilon') \gamma \sim -2\Im(\epsilon') |\Delta m| \quad (1.80)$$

$$-\frac{|\Delta m|}{\gamma} \sim \frac{\Re(\epsilon')}{\Im(\epsilon')} \quad \text{or} \quad \epsilon' = 0. \quad (1.81)$$

In this case, Direct CP invariance is not guaranteed by the measurement of $A_{\text{CP}}^{\text{BR}}(K^\pm K^\mp) = 0$.

Taking advantage of Eq. 1.74 (the CFD $K3\pi$ mode normalized to the CFD $K^\mp\pi^\pm$ mode), a simplification of the theory and an interpretation of experimental results can be achieved simultaneously by studying $A_{\text{CP}}^{\text{BR}}(\frac{\pi^\pm\pi^\mp}{K^\pm K^\mp})$, i.e. the SCSD $\pi^\pm\pi^\mp$ mode normalized to the SCSD $K^\pm K^\mp$ mode, which is also described by Eq. 1.74, since both are CP-even eigenstates. But the price is that a huge amount of data is necessary in order to study SCSD $A_{\text{CP}}^{\text{BR}}$. Also, if $|g| > |\bar{g}|$ and $|g'| > |\bar{g}'|$ or $|g| < |\bar{g}|$ and $|g'| < |\bar{g}'|$ then the direct CP asymmetry of $\pi^\pm\pi^\mp$ and $K^\pm K^\mp$ will be masked; but if $|g| > |\bar{g}|$ and $|g'| < |\bar{g}'|$ or $|g| < |\bar{g}|$ and $|g'| > |\bar{g}'|$ then the direct CP asymmetry of $\pi^\pm\pi^\mp$ and $K^\pm K^\mp$ will be enhanced.

CHAPTER II

THE E791 EXPERIMENT

The E791 collaboration took data over a 6-month period ending in January 1992 at the Tagged Particle Laboratory (TPL) at Fermilab. E791 was one of the second generation charm hadro-production experiments.

Fig. 2.1 shows the elements of the E791 spectrometer at TPL.

2.1 The 500 GeV/c Negative Pion Incident Beam

The source of the incident π^- was the 900 GeV/c Tevatron proton beam. Protons were extracted from the Tevatron and split into our P-East beam line, and then focused on a 30-cm beryllium target where the secondary 500 GeV/c π^- were created.

P-East received an average of 2×10^{12} protons per 22-second spill, resulting in about 10^7 π^- incident on E791 targets per spill, and about 200,000 events recorded per spill.

Define the $+z$ (longitudinal) axis from South to North, very close to the direction of the beam line, with $z = 0$ at the center of the E791 Interaction Counter located just downstream of the target foils. With a right-handed coordinate system, the x -axis is parallel to the ground (West) and the y -axis is vertical. Additionally, the u , v , w and w' directions are defined as follows: u and v are at an angle of $+20.5^\circ$ and -20.5° from the x -axis on the (x, y) plane, and w and w' are at $\pm 60^\circ$ on the same plane.

TAGGED PHOTON SPECTROMETER E791

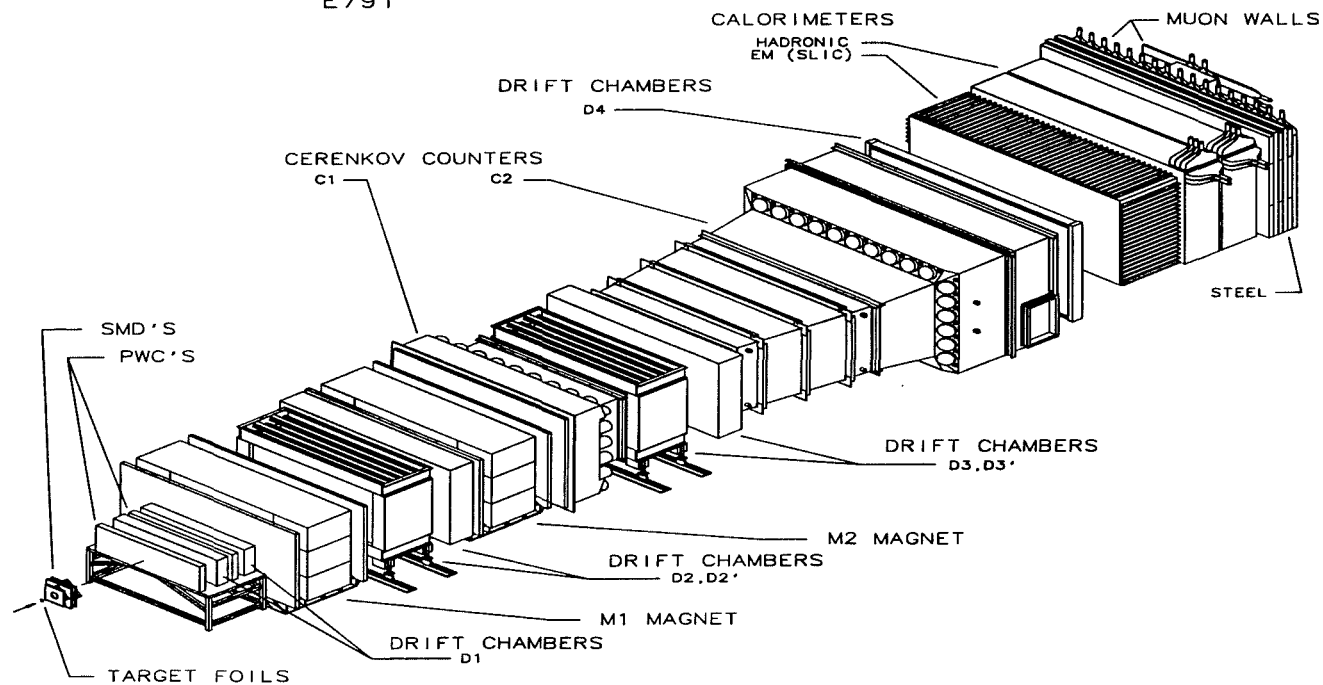


Figure 2.1. The E791 Spectrometer.

2.2 Upstream Beam Tracking

For upstream beam tracking, there were 8 planes of Proportional Wire Chambers (PWC's) and 6 planes of Silicon Microstrip Detectors (SMD's) before the target foils.

Table 2.1 shows the characteristics of the upstream tracking configuration.

Table 2.1. E791 Upstream Tracking Configurations

PWC	First Group	Second Group
Number of Planes	4	4
Dimension(cm)	6×3	6×3
View Ordering	x, x', y, w	x, x', y, w
Wire Spacing(mm)	1.0	1.0
Resolution(μm)	$145(x, x'), 289(y, w')$	$145(x, x'), 289(y, w')$
Z position(cm)	$-3117 - -3116$	$-1211 - -1209$
SMD	First Group	Second Group
Number of Planes	3	3
Dimension(cm)	5×5	5×5
View Ordering	y, x, w'	w', x, y
Strip Pitch(μm)	25	25
Resolution(μm)	7.2	7.2
Z position(cm)	$-80.25 - -74.52$	$-33.163 - -29.483$

2.3 Target Foils

The E791 target consisted of 5 foils. They were a platinum coin and 4 carbon (diamond) foils. The lifetime of the D^0 is 0.415 ps [PDG94], or about .667 cm for 100 GeV/c momentum, so the 1.5-cm spacing between center of each target foil is adequate for our lifetime study. Some details of the E791 targets are listed in Table 2.2. Using two different target materials makes possible a study of the A-dependence (A stands for the atomic number) of the production mechanism.

2.4 Downstream Region One Tracking

Separating the secondary decay vertices from the primary production vertex requires good spatial resolution and good solid angle coverage. Table 2.3 shows the

Table 2.2. E791 Target Configurations

Target Number	1	2	3	4	5
Material(Atomic number)	Pt(78)	C(12)	C(12)	C(12)	C(12)
Thickness(cm)	.052	.1572	.1567	.1530	.1584
Diameter(cm)	1.606	1.369	1.377	1.368	1.355
Proton Interaction					
Length(cm) [†]	.00584	.00590	.00585	.00582	.00587
Z position(cm)	-8.143	-6.663	-5.127	-3.588	-2.048

[†]The ratio of interaction length is $\pi : p = 2 : 3$.

characteristics of the downstream Region 1 (from target to the first magnet) tracking, consisting of 17 planes of SMD and 2 planes of PWC (Fig. 2.1). The angular acceptance of the SMD system is about ± 150 mrad around the beam axis and the per-plane efficiency is roughly 90% with 0.1% noise. The longitudinal resolution of the vertex is 300 to 400 μm , and the transverse resolution 15 μm . The resolution of our PWC detectors is approximately the wire spacing divided by $\sqrt{12}$.

2.5 Two Magnets

E791 used two large-aperture dipole magnets to reconstruct the momentum of the charged tracks (Fig. 2.1). Since different momenta yield different bending angles

$$\theta \simeq \frac{\int B \cdot dl}{3.33 p}$$

where p is track momentum, B the magnetic field and dl for the path integral, we measure momentum by tracking before and after the magnets and reconstructing the bend angle θ . Some characteristics of the two magnets are listed in Table 2.4.

Table 2.3. E791 Downstream R1 Tracking Configurations

SMD Plane	z position (cm)	Strip Pitch(μm) (inner;outer)	Box, View
1	0.670	(25;50)	(1, y)
2	1.000	(25;50)	(1, x)
3	1.931	(25;50)	(2, x)
4	3.015	(50;50)	(2, y)
5	6.684	(50;50)	(2, v)
6	11.046	(50;50)	(3, y)
7	11.342	(50;50)	(3, x)
8	14.956	(50;50)	(3, v)
9	19.915	(50;50)	(4, x)
10	20.254	(50;50)	(4, y)
11	23.878	(50;50)	(4, v)
12	27.558	(50;200)	(\star , v)
13	31.848	(50;200)	(\star , x)
14	34.548	(50;200)	(\star , y)
15	37.248	(50;200)	(\star , x)
16	39.948	(50;200)	(\star , y)
17	45.508	(50;200)	(\star , v)
PWC Plane	z position (cm)	Strip Pitch(mm)	View
1	118.10	2	y
2	164.40	2	y

\star Planes 12 – 17 were not grouped.

Table 2.4. E791 Magnet Configurations

Magnets	M1	M2
Center z (cm)	272.2	619.2
Length (cm)	165	208
Entrance Aperture	153.6×72.6	154.0×73.8
Exit Aperture (cm^2)	194.6×96.2	188.8×102.6
p_T Kick (GeV/c)	0.212	0.320
$\int B dl$ (T-m)	-0.71	-1.07

2.6 Drift Chambers

E791 was equipped with a total of 35 drift chamber (DC) planes grouped into 4 sets to measure 4 different views (Fig. 2.1). The x' view is offset from the x view in order to eliminate ambiguity in reconstructing tracks. Table 2.5 lists the DC configurations. The gas and field strength in our DC's resulted in a drift velocity of $50 \mu\text{m}/\text{ns}$. In each event, t_0 is chosen when the Interaction Counter is hit. An additional time offset corresponding to the distance of each plane from the Interaction Counter, and the electronic delay of each sense wire, is subtracted in order to measure the true drift time.

Table 2.5. E791 Drift Chamber Configurations

	D1	D2	D3	D4
Dimension (cm^2)	126×71	285×143	323×143	511×259
View ordering	$2(x, x', u, v)$	$4(x, u, v)$	$4(x, u, v)$	$1(x, u, v)$
Number of planes & channels	8 & 1536	12 & 2400	12 & 1952	3 & 416
x cell size (cm)	0.446	0.892	1.487	2.974
uv cell size (cm)	0.476	0.953	1.588	3.175
Resolution (μm)	400	300	300	450

2.7 Čerenkov Counters

E791 used two gas radiator Čerenkov counters for charged particle mass identification. The upstream counter (C1) was located just downstream of M2, actually partially inset into M2 due to space constraints. Thus, C1 had two-bounce optics to keep the photomultiplier tubes (PMT's) out of the magnetic field of M2. The other Čerenkov counter (C2) was located between D3 and D4 (Fig. 2.1), and it had only one primary mirror plane. Table 2.6 summarizes the Čerenkov counter configurations.

Table 2.6. E791 Čerenkov Counter Configurations

	C1	C2
Length (m)	3.7	6.6
Number of Mirrors	28	32
Gas Mixture	100% N ₂	80% He & 20% N ₂
π momentum threshold	6 GeV/c	11 GeV/c
K momentum threshold	20 GeV/c	36 GeV/c
p momentum threshold	38 GeV/c	69 GeV/c

The Čerenkov probability calculation proceeds as follows. For each track and mass hypothesis, a Poisson distribution with the predicted number of photons (μ) and the observed number of photons (n) was formed:

$$f_{i,j} = \frac{\mu^n}{n!} e^{-\mu}$$

where i stands for C1 or C2, and j for different particles. The final combined probability P_j used for particle identification was normalized by taking into account that there is an *a priori* expectation (A_j) based on the assumed natural occurrence of each type of particle:

$$P_j = \frac{f_{1,j} \times f_{2,j}}{\sum_{k=1}^5 f_k} \times A_k,$$

with *a priori* values of $A(e, \mu, \pi, K, p) = (0.02, 0.01, 0.81, 0.12, 0.04)$.

2.8 Calorimeters

TPL utilized two calorimeters, the Segmented Liquid Ionization Calorimeter (SLIC) and the Hadrometer. Both were used to enhance the particle identification capabilities for charged tracks, and to identify possible photon and neutral hadron candidates. Also, both were used as part of the transverse energy (E_T) trigger.

The SLIC consisted of 60 scintillation layers, and some of the characteristics of the SLIC are listed in Table 2.7. Electrons in matter can emit bremsstrahlung photons

and photons near nuclei may produce e^+e^- pairs. These two processes are responsible for the propagation of electromagnetic showers. This scintillation light is proportional to the energy of the incident particle.

Table 2.7. The SLIC Configuration

	u channel	v channel	y channel
Number of channels	109	109	116
Number of layers	20	20	20
Single channel width (cm)	3.17	3.17	3.17
Channel length (cm)	110.4	110.4	46.25
Radiating material		lead	
Scintillating material		plastic and mineral oil	
Total radiation length		20	
Total absorption length		1.5	
Position resolution (cm)		.65	

The Hadrometer was a steel and acrylic scintillator calorimeter located downstream of the SLIC. Hadrons can lose energy due to interactions with the nucleus via the strong interaction when traveling in a high density material. Less than 1% of the energy of electromagnetic showers reached the Hadrometer. Thus, charged hadrons could be identified as wide SLIC showers with significant hadronic energy. Neutral hadrons were also identified after all the hadronic energy associated with charged tracks was subtracted. Table 2.8 lists some information about the Hadrometer.

Table 2.8. The Hadrometer Configurations

	x channel	y channel
Number of channels	66	76
Number of layers	36	36
Single channel width (cm)	14.5	14.5
Interacting material		steel
Scintillating material		plastic
Total interaction length		6

2.9 The Muon Wall

E791 had two muon walls made of scintillating paddles placed directly behind a thick (106-cm) steel shielding wall. The steel wall blocked hadrons that had not deposited their complete energy in the SLIC and Hadrometer. Muons interact mainly through ionization and consequently retain most of their energy even after going through the calorimeters and steel wall. These minimum ionizing particles are easily detected with simple scintillating paddles. Table 2.9 summarizes our two muon walls.

Table 2.9. The Muon Wall Configurations

	x wall	y wall
Number of channels	15	16
Single channel width (cm)	40.6	14.2
Radiating material		lead
Scintillating material		plastic
Absorber thickness	11.6 interaction lengths	
Active dimension (cm ²)	300 × 224	

2.10 Triggering and Data Acquisition

E791 was designed to take data with a very open trigger and to prune events in offline software. The E791 trigger consisted of two parts: a pre-trigger based on the quality of the π^- beam and a secondary trigger based on the charm-like decay products. The pre-trigger required one and only one beam particle incident within the target cross section. The secondary trigger required an above-threshold (4-particle) signal from the Interaction Counter behind the target foils, plus a minimum total transverse energy for the event $E_T \geq 4.5$ GeV.

The E791 Data Acquisition (DA) system was designed to accept a large amount of data at the fastest rate allowing data to be fully processed. It then made use of the dead time in the beam delivery structure to process and record the data to tapes. The DA system read out 24000 channels in 50 μ s, and events were accepted at a rate

of 9000 events per second. Data was written continuously to a total of 42 Exabyte Model 8200 tape drives in 6 VME crates at a rate of 9.6 Mb/sec. It took an average of 2.5 hours to fill a set of 42 8-mm tapes. We successfully collected 20 billion Physics events with an average event size of 2500 bytes on 24,000 tapes.

CHAPTER III

ALIGNMENT, RECONSTRUCTION AND SELECTION

Each event was reconstructed, filtering charm candidate events from 24,000 raw data tapes onto 7,500 data summary tapes (DST's). To reconstruct hits in the detectors into tracks, and further to assign tracks to vertices, required good geometry constants to define the coordinates of each plane. The initial geometry constants were measured by a survey team, allowing rough reconstruction of tracks. The geometry constants were then fine tuned on a run-by-run basis. Production processing then could precisely reconstruct tracks using the refined alignment constants.

3.1 Alignment

IIT was responsible for SMD alignment for each run on an IBM RS-6000 single node UNIX machine. The algorithm used is described in E791 internal document 043.

The basic procedure was

- Reconstruction tracks: Choose the geometry file from the nearest earlier run as the starting point, in order to reconstruct tracks by knowing the approximate positions of hits.
- Selecting samples from raw data: The alignment was done in a multi-pass manner for each run. From each run two disk files were created:
 - E_T sample: A total of about 8800 events passing the Interaction trigger with $E_T \geq 3 \text{ GeV}/c^2$. There must be at least one good quality track having momentum $> 10 \text{ GeV}/c$, more than 11 hits in the SMD's, and a track slope $> 25 \text{ mrad}$.

- Beam sample: A total of 7000 events passing only the pre-scaled Beam trigger.

The E_T sample was used for aligning the 17 downstream SMD planes, and later was used again for locating the 5 targets and the Interaction Counter. The Beam sample was used for the 6 upstream SMD planes and the 8 upstream PWC planes.

- Downstream alignment: Define 5 alignment constants for each plane.
 - Δu — Offset of the central strip from the z -axis.
 - $\Delta\phi$ — Plane rotation around the z -axis.
 - Δz — Plane shift along the z -axis.
 - $\Delta\theta$ — Tilt around the strip direction.
 - $\Delta\psi$ — Tilt around the axis normal to the strip direction.

There were a total of 4 passes of minimizing the χ^2 for the final downstream alignment constants:

- 1st fit — Global fit of Δu and $\Delta\phi$ by fixing planes 9, 12, 15, and 16 for Δu , and planes 9 and 12 for $\Delta\phi$.
- 2nd fit — Global fit of Δu , $\Delta\phi$ and Δz by fixing planes 9, 12, 15, and 16 for Δu , planes 9 and 12 for $\Delta\phi$, and plane 9 and 15 for Δz
- 3rd fit — Using fitted values of Δu , $\Delta\phi$ and Δz , further global fit $\Delta\theta$.
- 4th fit — Using fitted values of Δu , $\Delta\phi$, Δz , and $\Delta\theta$, further global fit $\Delta\psi$.

- Upstream alignment: In the upstream alignment, only the accuracy of Δu is critical, in order to reconstruct a good straight beam track. So after the downstream planes was properly aligned, 7000 events of the Beam sample were projected from downstream to upstream. The mean residual values from these 7000 events for each of the upstream SMD's and PWC's were determined. In an example of upstream alignment for run 1500, Fig. 3.1 shows the beam profiles and beam slopes in two views. Fig. 3.2 shows the residual of each upstream PWC plane. Fig. 3.3 shows the residual of each upstream SMD plane.

Finally,

- Target alignment: After downstream and upstream alignments were done, the new geometry constants were used to re-reconstruct wide-angle and high momentum tracks plus the beam track to form a primary vertex for each event. By plotting more than 8000 primary vertices, each target foil was fit with a Gaussian distribution to get the z-position of each foil center. Fig. 3.4 shows the mean z-positions of 5 target foils and the Interaction Counter.

After SMD alignment was complete, by using a similar algorithm and multiple passes, the DC alignment was done. Then the new and complete geometry constants file was posted to all machines, and farm reconstruction of this run could proceed.

3.2 Event Reconstruction

The philosophy of charm candidate reconstruction is: from hits to form tracks, from tracks to form vertices, and then to separate secondary vertices from the primary vertex.

In E791, first a beam track is reconstructed from the best χ^2 fit of the hits in the upstream 6 SMD's and 8 PWC's. Then focus shifts to the downstream SMD

Beam Profile on Upstream Planes

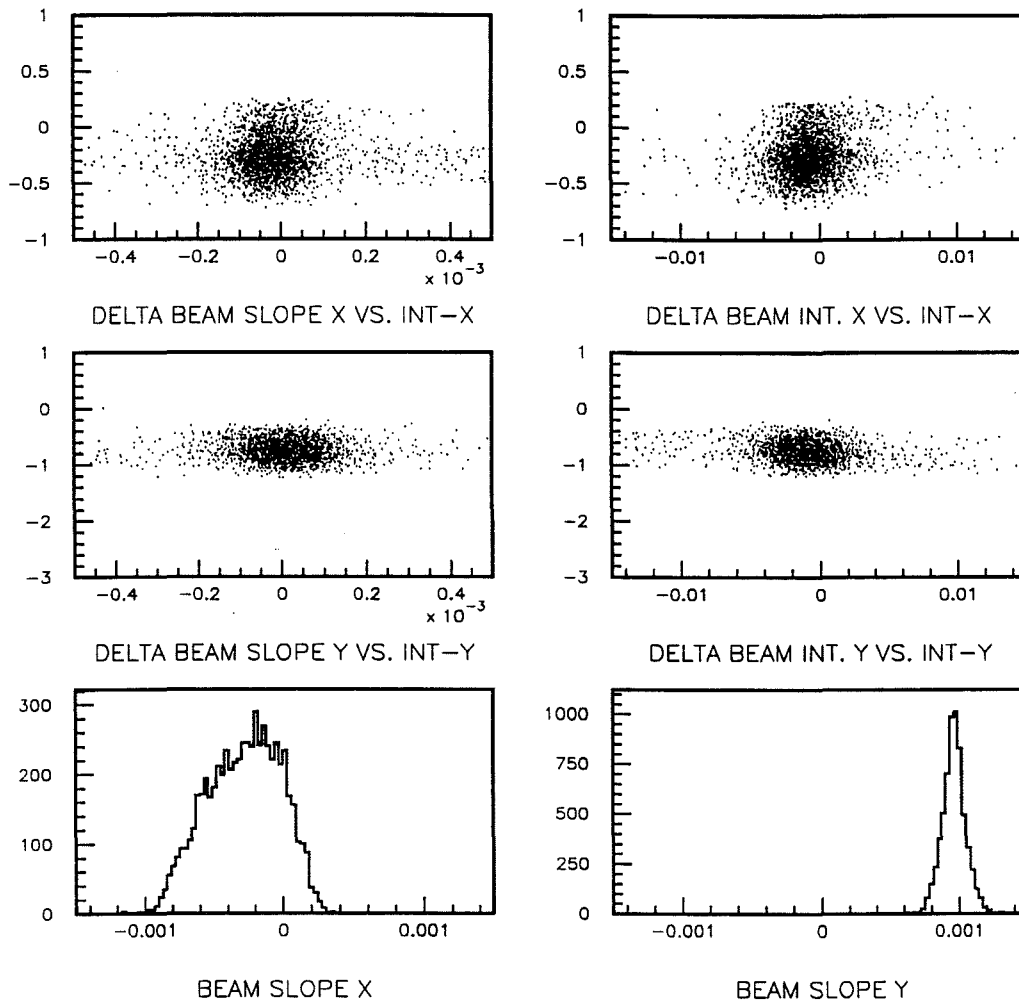


Figure 3.1. The Beam Profile in x and y Views, in Terms of the Intercepts and Slopes of the Beam Line

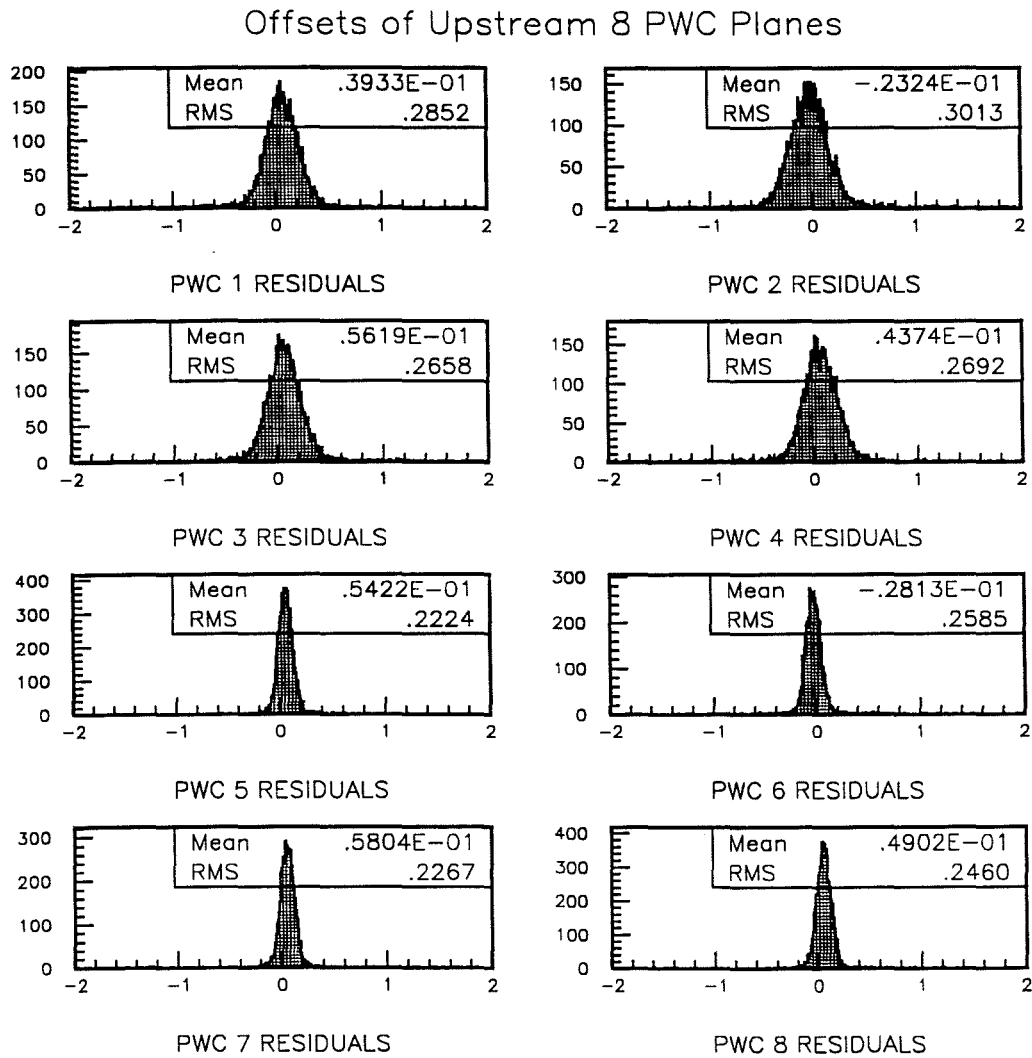


Figure 3.2. The Alignment Residuals of Eight Upstream PWC Planes: they are the offsets to their own view direction on vertical planes.

Offsets of Upstream 6 SMD Planes

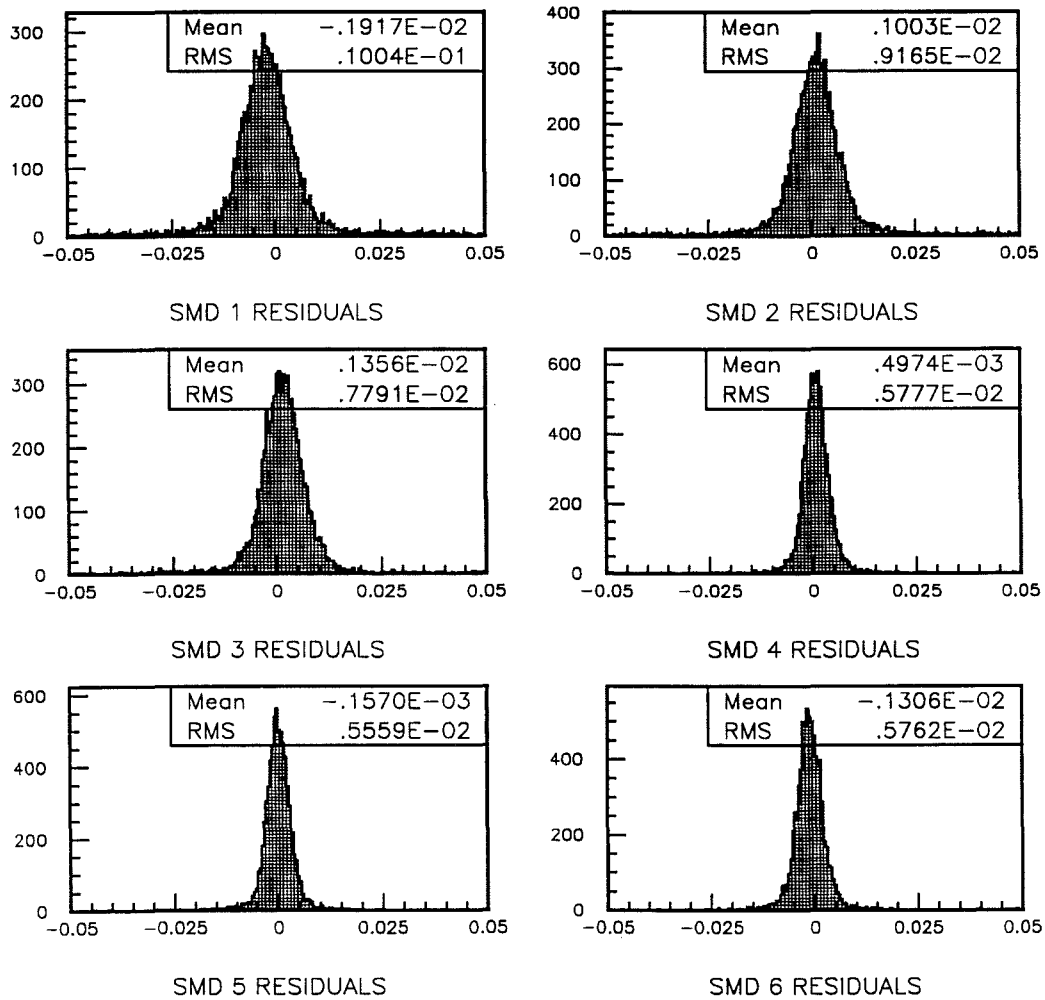


Figure 3.3. The Alignment Residuals of Six Upstream SMD Planes: they are the offsets to their own view direction on vertical planes.

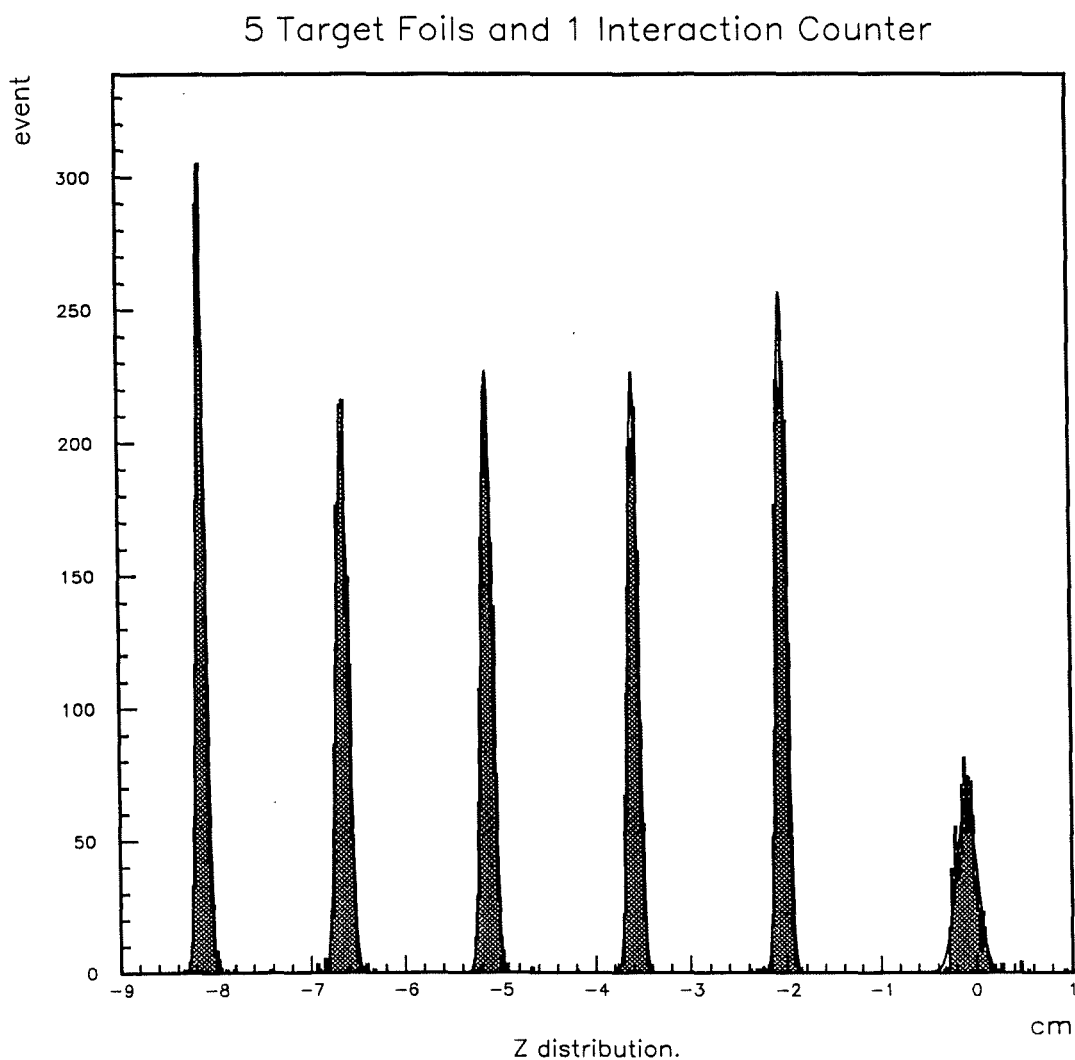


Figure 3.4. The z -position Alignments for Five Target Foils and the Interaction Counter: The first target foil is a Pt coin, and the other 4 are made of Carbon. The right-most peak is the Interaction Counter, a plastic scintillator in wrapping paper.

planes. Projections are formed in each view (x , y , and v). Tracks are formed from 3 views and compiled into a Track List. Independently, tracks are also formed in the DC system (downstream of magnets). Then the SMD tracks are linked with the single-bend hypothesis to the DC tracks. This yields intercepts and slopes on x and y , and the momentum for each track.

Using the Track List and the unique beam track, a 3-D reconstruction of the primary vertex is done. Finally from the remaining tracks, 2-prong, then 3-prong, 4-prong, and higher multiplicity secondary vertices are formed into a Vertex List. Each vertex has an associated χ^2 .

3.3 Event Selection

In order to prune the huge data set and improve signal to noise, certain criteria were added at each stage of Filtering, Stripping, Sub-stripping, KSU Micro-stripping, and Final analysis — due to huge amount of data, several stages of reduction are necessary to have a compact and manageable amount of data for different users and different topics. Most of our cuts have one goal: separating the secondary vertices from the primary vertex. I summarize my analysis cuts in Table 4.1, but let me define them here.

- **SDZ** - The longitudinal distance between the primary and the secondary vertices divided by their measurement errors added in quadrature. The higher the value of SDZ, the more significant is the separation between the primary and secondary vertices.
- **DIP** - The distance on the $x - y$ plane between the primary vertex and the line of flight of the reconstructed particles. Refer to Fig. 4.12 (a).

- **PT2DK** - The sum of the P_t^2 (in GeV^2/c^2) of all the secondary tracks with respect to the flight path of the reconstructed particles.
- **PT_BAL** - The absolute value of the vector sum of the \vec{P}_t (in GeV/c) of the secondary tracks with respect to the flight path of the reconstructed particles.
- **TARSIG** - The number of standard deviations in distance of the secondary vertex from the closest edge of target foil or Interaction Counter.
- **TAUDEC** - The roughly estimated decay proper time in ps for the reconstructed charm hypothesis.
- **MNCHV** - The least **CHVXTK** - the χ^2 for including this track into the primary vertex fit; the smaller the value of **MNCHV** is, the more likely is the track to come from the primary vertex.
- **IMPACT** - The intercept on the $x - y$ primary vertex plane of the bachelor pion candidate track from the D^* . Refer to Fig. 4.12 (a).
- **ASYM** - The asymmetry of two decay tracks' momenta: $\frac{|p_1 - p_2|}{p_1 + p_2}$ in the lab frame. It is correlated to the **COS θ** and **PT2DK** cuts.
- **COS θ** - The opening angle of one track along the parent line of flight. It is correlated to the **ASYM** and **PT2DK** cuts.
- **JCATSG** - E791 divides the detector geometry into 4 regions; for example, region 1 is the SMD area and region 2 is between the two magnets (refer to Fig. 2.1). Whether a given track has hits in each region is encoded into a computer word as a bit pattern: bit 1 is on if there are hits in region 1, etc. This encoded word for a track which is seen in all accessible regions then has possible values of 3 (0011), 7 (0111), or 15 (1111) depending on the track length.

CHAPTER IV

PHYSICS ANALYSIS PREPARATION

The strategy of my analysis follows. I use the Vertex List to analyze every 2-prong vertex. To improve statistical significance, I apply some tighter cuts for my final analysis sample. To categorize 2-prong vertices into K^-K^+ , $K^-\pi^+$, or $\pi^-\pi^+$, I rely on the Čerenkov particle identifications. To extract signal (SG), I use fitting functions to estimate the background (BG) under SG. I describe the preparation for the complete analysis in the following sections.

4.1 Monte Carlo Simulation

I use the Monte Carlo (MC) simulation for several purposes:

- To produce an unbiased set of the MC SG. I use this SG from the MC and BG from real DATA to tune the analysis cuts.
- To understand the acceptance of the detector geometry. I apply geometric corrections to observed data.
- To understand the efficiency of the chosen set of cuts. I apply an efficiency correction to the survival sample.

Usually, the last two items are combined into one study.

In addition, I use the well-known CFD $D^0 \rightarrow K^-\pi^-\pi^+\pi^+$ mode to check the consistency of my analysis Technique. Therefore I am dealing with 4 decay modes simultaneously, $D^0 \rightarrow K^+K^-$, $D^0 \rightarrow K^-\pi^+$, $D^0 \rightarrow \pi^+\pi^-$, and $D^0 \rightarrow K^-\pi^-\pi^+\pi^+$. I count the event numbers at the generator-level, so that more raw MC data events (800,000

events) can be saved on one tape without truth table information. Without applying the Čerenkov ID cut, it is not easy to distinguish $K^-\pi^+$ from $K^+\pi^-$, resulting in problems fitting the MC BG. Therefore, I generate four sets of MC samples: (1) $D^0 \rightarrow K^-\pi^+$ and $\bar{D}^0 \rightarrow K^+\pi^+\pi^-\pi^-$, (2) $D^0 \rightarrow K^-\pi^-\pi^+\pi^+$ and $\bar{D}^0 \rightarrow K^+\pi^-$, (3) $D^0 \rightarrow K^+K^-$ and $\bar{D}^0 \rightarrow K^-K^+$, and (4) $D^0 \rightarrow \pi^+\pi^-$ and $\bar{D}^0 \rightarrow \pi^-\pi^+$. D^0 and \bar{D}^0 are not forced to appear in the same event. There is no extra selection criteria on how D^0 and \bar{D}^0 are produced but only on the decay modes. Note that in (1) and (2) D^0 and \bar{D}^0 are easily distinguished without Čerenkov identification. I accumulate more than 7 million MC events for each decay mode at the generator-level.

4.2 Tuning Analysis Cuts

Since I have no *a priori* knowledge of what the best set of cuts is nor how the pure signal (SG) data distributes for each cut variable, to tune the cuts, I start with SG from a $D^0 \rightarrow K^-\pi^+$ MC simulation, and BG normalized by two sidebands of DATA ($D^0 \rightarrow K^-\pi^+$ hypothesis). I compare distributions of certain cut variable from the MC SG and from the DATA SG in order to understand which set of cuts has been well represented in the MC. Refer to Appendix B for details of these comparisons and specifications of signal and sideband regions.

A few things to be emphasized are:

- I consider only cuts which yield very similar distributions in DATA and MC; especially, there must be no shift of peak values between MC and DATA (refer to Appendix B).
- Among the chosen set of cuts, the first cut I adopt is the one giving the best optimization (statistical significance $\equiv \frac{SG}{\sqrt{SG+BG}}$). Fig. 4.1 (c) and (f) show the effect of using different optimizations ($\frac{SG}{\sqrt{BG}}$ and $\frac{SG^2}{\sqrt{BG}}$).

- Adding the best optimized cut at a time, I iterate the optimizing steps for the next best cut.

Fig. 4.1 shows the best cut to apply in the first iteration. After applying $PT2DK > 5.2$, I found the next best cut is $MNCHV > 6$ (Fig. 4.2). In the third iteration, there is no further improvement. Thus, I have completed the tuning cut process. Table 4.1 lists all the analysis cuts including the stages where they are applied. In my final analysis (refer to Chapter V), I apply all the cuts simultaneously. Because there is a small fraction of double-charm events (two charm mesons in the same event), all charm candidates are required to pass the same selection criteria. The same analysis is applied to the MC sample, and I don't need to worry whether MC has the correct double-charm production.

I apply the same set of cuts on $D^0 \rightarrow K^+ K^-$, $D^0 \rightarrow K^- \pi^+$, $D^0 \rightarrow \pi^+ \pi^-$, and $D^0 \rightarrow K^- \pi^- \pi^+ \pi^+$. Recall that I used MC ($K^\mp \pi^\pm$) SG and DATA ($K^\mp \pi^\pm$) BG to tune the cuts. If the MC ($D^0 \rightarrow K^- \pi^+$) can satisfactorily reproduce the effects of cuts on the DATA ($D^0 \rightarrow K^- \pi^+$), then there is no reason why the MC should not yield reliable cut distributions for $D^0 \rightarrow K^+ K^-$, and $D^0 \rightarrow \pi^+ \pi^-$. Applying the same set of cuts to each sample reduces the complexity of the systematic error study described in Sec. 6.3.

Table 4.1. Summary of Analysis Cuts

Name	Value	Comment
Cuts for D^0 candidates		
.NOT.Target	outside targets 0.1 cm or Int.Counter 0.5 cm	At Strip stage.
TAUDEC	< 2.5 ps	At Strip stage.
PSUM	> 25 GeV	At Strip stage.
$z_{\text{secondary}}$	< 3.0 cm	At Strip stage.
Charge	$= 0$	At Strip stage.
Track \vec{P}_z	15 — 500 GeV	At Strip stage.
ASYM	< 0.8	At Strip stage.
Mass	≥ 1.7 GeV	At Micro-strip stage.
SDZ	> 8.0	At Micro-strip stage.
PTBAL	< 0.40 GeV for 2-prong < 0.35 GeV for 4-prong	At Micro-strip stage.
z_{primary}	< -0.35 cm	At Micro-strip stage.
$ \cos \theta $	< 0.995	At Micro-strip stage.
JCATSG	$= 3, 7, \text{ or } 15$	At analysis stage (to have momentum).
Track χ^2	≤ 5.0 for 2-prong ≤ 6.0 for 4-prong	(very loose) At analysis stage.
PT2DK	> 0.52 GeV for 2-prong	At analysis stage.
MNCHV	> 6.0	At analysis stage.
Track $ \vec{P} $	6 — 80 GeV	At analysis stage, for the \check{C} ID.
Kaon	$K_{ID} \geq 0.16$ for 2-prong	
Pion	$K_{ID} < 0.16$ for 2-prong	At analysis stage.
Cuts for $D^{*\pm}$ tagging		
JCATSG	$= 3, 7, \text{ or } 15$	At analysis stage.
Track $ \vec{P} $	< 100 GeV	At analysis stage.
IMPACT	< 0.008 cm	At analysis stage.
Δm	0.1430 — 0.1480 GeV	At analysis stage.
ONLY π	To ensure 1 π for 1 vertex, at analysis stage.	

Cuts comparison for MC and DATA of mkpi2422

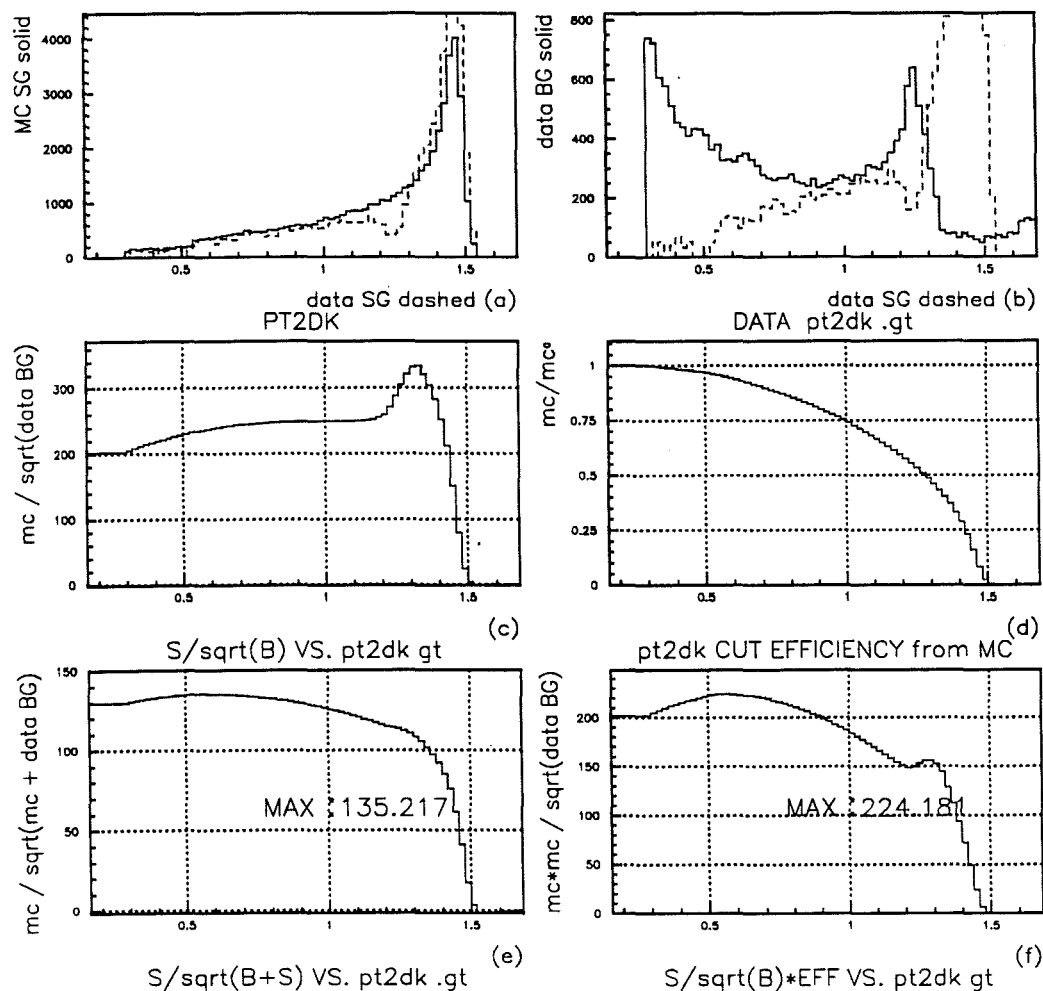


Figure 4.1. Tuning cut in the first iteration finds the best cut as $PT2DK > 0.52$ in (e). In (a), the solid line is the cut distribution from MC SG and the dashed line is from DATA SG; in (b), the solid line is the sideband to represent the DATA BG, and the dashed line is DATA SG. Focusing on two solid lines in (a) as SG and in (b) as BG, calculate the $SG/\sqrt{SG + BG}$ in (e), and estimate the cut value as 0.52 giving the maximum peak. (c) is SG/\sqrt{BG} (not a good criteria in this case), (d) the cut efficiency, and (f) another selection criteria of (c)*(d).

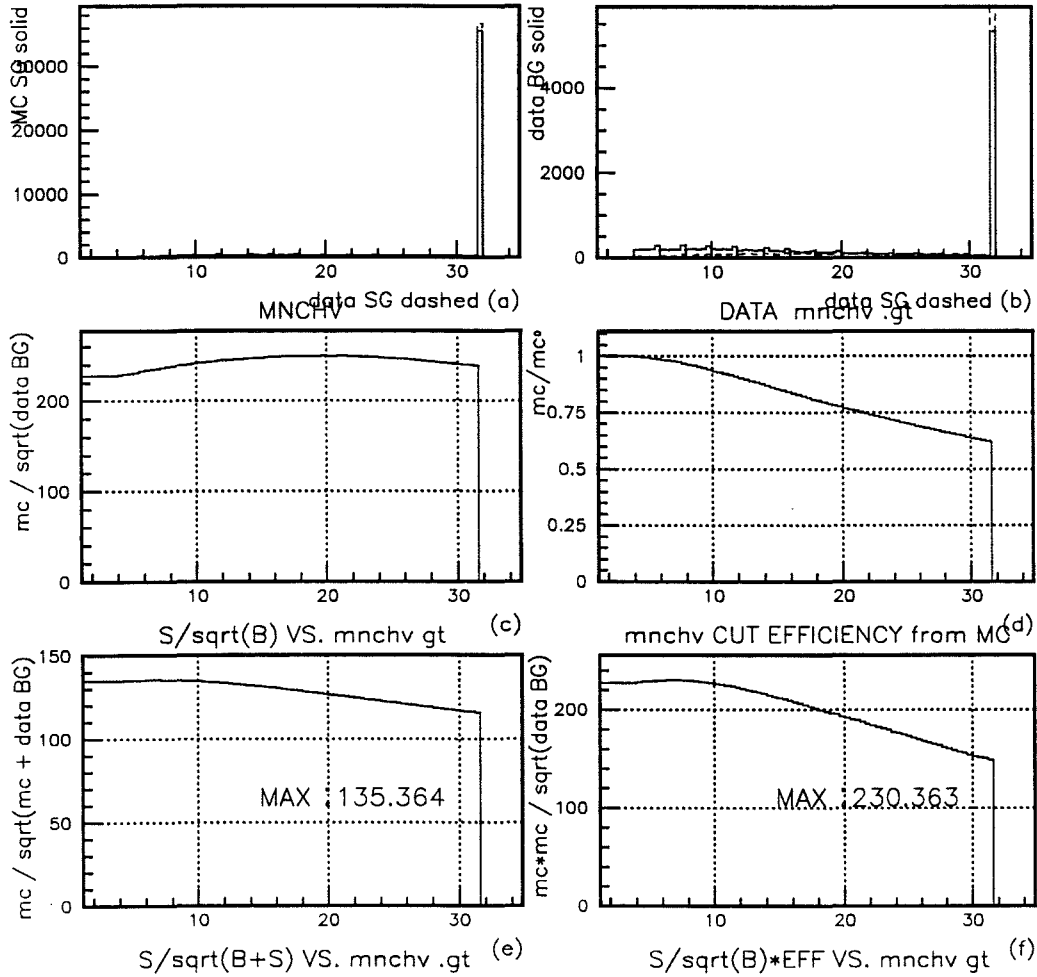


Figure 4.2. Tuning cut in the second iteration finds the best cut as $MNCHV > 6$ in (e). In (a), the solid line is the cut distribution from MC SG and the dashed line from DATA SG; in (b), the solid line is the sideband to represent the DATA BG, and the dashed line is DATA SG. Focusing on two solid lines in (a) as SG and in (b) as BG, calculate the $SG/\sqrt{SG + BG}$ in (e), and estimate the cut value as 0.52 giving the maximum peak. (c) is SG/\sqrt{BG} , (d) the cut efficiency, and (f) another selection criteria of (c)*(d).

4.3 Čerenkov ID Efficiency

In order to use Čerenkov identification to separate kaons from pions, I must determine the efficiency for kaons and pions as a function of their momenta and charges. Because the MC doesn't have accurate Čerenkov efficiencies (evidence in Fig. B.14), I can only use DATA to do this study.

I use the signals of decay particles themselves as evidence of the correct track assignment, and then I vary one ID cut for one track at a time, to get the efficiency from the ratio of the reduced SG number over the original SG number. For example, if I am interested in K^- ID efficiency, then using the $D^0 \rightarrow K^- \pi^+$ sample and hypothesis, I form an invariant mass plot, and the BG-subtracted D^0 SG number is then taken to be the number of K^- . In other words, no $D^{*\pm} \rightarrow D^0(\bar{D}^0)\pi^\pm$ tagging is required to distinguish $D^0 \rightarrow K^- \pi^+$ and $\bar{D}^0 \rightarrow K^+ \pi^-$. Using the $D^+ \rightarrow K^- \pi^+ \pi^+$ sample and hypothesis, the unlike charged track in the 3-prong vertex is the K^- . I assume that the DCSD contamination is tiny in either sample. I also study the $K_S^0 \rightarrow \pi^+ \pi^-$ sample for the π ID efficiency comparison.

Using 100% of the DATA sample of $D^0 \rightarrow K^- \pi^+$, I fix all other non-Čerenkov ID cuts (as listed in Table 4.1) — varying non-Čerenkov ID cuts only produces $< 1\%$ difference in the Čerenkov efficiencies. The ID cut efficiency as a function of momentum and charge is defined as

$$E \equiv \frac{A \equiv D^0 \text{ SG number after ID cut}}{T \equiv D^0 \text{ SG number without ID cut}} \quad (4.1)$$

I use two steps to determine the BG-subtracted D^0 SG numbers (contrary to use sidebands to do BG subtraction — fix sidebands and signal regions):

- Not fixing the sidebands: I don't assume the BG is a linear function, but rather a third order polynomial function ($p3$), because the reflections from $D^0 \rightarrow K^+ K^-$ and $D^0 \rightarrow K^- \pi^+ \pi^0$ appear in the low-mass region of the $D^0 \rightarrow K^- \pi^+$ hypothesis (Fig. 4.3).
- Not fixing the SG region: I let the Gaussian widths float, because the fitted widths of decay particles are a result of two track momenta. For instance, when I study π^- ID efficiency in low momentum bins, the partner K^+ tends to have lower momentum, when π^- is above *a priori* Čerenkov probability. In other words, the widths might be different after each Čerenkov ID cut (illustrated in Fig. 4.4).

I then apply the Čerenkov ID cut in 0.05 increments for each momentum bin for each charge. The momentum bins run from 6 to 66 GeV/c in 2 GeV/c steps, then 2 bins from 66 to 73 and 73 to 80 GeV/c, due to the lack of statistics in the high-momentum region.

As an example, Fig. 4.3 shows the efficiency study for K^+ with momentum 21–24 GeV/c from the $\bar{D}^0 \rightarrow K^+ \pi^-$ sample. The ID cut efficiency for $K_{ID}^+ \geq 0.20$ is $\frac{1867.2 \pm 50.6}{2325.7 \pm 69.6} = 0.8027 \pm 0.0171$. Fig. 4.4 shows the efficiency study for π^- with momentum 6–9 GeV/c from the $\bar{D}^0 \rightarrow K^+ \pi^-$ sample. Note that the widths are smaller above the *a priori* value of $\text{CPRB2}(\pi) = 0.81$. In this case, the ID cut efficiency of $\pi_{ID}^- \geq 0.90$ is $\frac{428.3 \pm 26.1}{1469.9 \pm 56.3} = 0.2912 \pm 0.0159$.

According to Eq. (4.1), the efficiency error is calculated not simply by assuming that numerator and denominator are uncorrelated, but by assuming that [the SG number of events above ID cut] and [the SG number of events under ID cut] are uncorrelated. Redefine the efficiency as:

$$E \equiv \frac{A \equiv D^0 \text{ SG number above ID cut}}{[A \equiv D^0 \text{ SG number above ID cut}] + [B \equiv D^0 \text{ SG number under ID cut}]}, \quad (4.2)$$

i.e.

$$E \equiv \frac{A}{A+B} = \frac{A}{T}$$

and the associated error is estimated as

$$\sigma_E = \left[\left(\sigma_A \cdot \frac{dE}{dA} \right)^2 + \left(\sigma_B \cdot \frac{dE}{dB} \right)^2 \right]^{\frac{1}{2}} \quad (4.3)$$

$$= \left[\left(\frac{\sigma_A \cdot B}{(A+B)^2} \right)^2 + \left(\frac{\sigma_B \cdot A}{(A+B)^2} \right)^2 \right]^{\frac{1}{2}}. \quad (4.4)$$

To return to Eq. (4.1), I can replace B by $T - A$ and σ_B by $\sqrt{\sigma_T^2 - \sigma_A^2}$, since I consistently estimate the SG errors (for A , B , and T) as the $\sqrt{SG + BG}$ in the SG region.

Note that using different samples ($D^0 \rightarrow K^- \pi^+$, $D^+ \rightarrow K^- \pi^+ \pi^+$, or $K^0 \rightarrow \pi^+ \pi^-$) yields 10% variations in some momentum bins (compare Fig. 4.8 and Fig. 4.9). The variations could arise because in order to get the SG number by BG subtraction in Eq. (4.1), I am actually measuring the average efficiency in a certain momentum bin:

$$E_i = \frac{\int_{p_{i-1}}^{p_i} [\epsilon_i(p) \cdot f(p)] dp}{\int_{p_{i-1}}^{p_i} f(p) dp} \quad (4.5)$$

where $f(p)$ is the momentum distribution of sample tracks. The kaons or pions from $D^0 \rightarrow K^- \pi^+$ and $D^+ \rightarrow K^- \pi^+ \pi^+$, each have their own distinctive momentum distributions, so the average Čerenkov efficiencies are not the same in bins of momentum:

$$E_i(K^-) D^0 \rightarrow K^- \pi^+ = \frac{\int_{p_{i-1}}^{p_i} [\epsilon_i(p) \cdot f_1(p)] dp}{\int_{p_{i-1}}^{p_i} f_1(p) dp}$$

$$E_i(K^-) D^+ \rightarrow K^- \pi^+ \pi^+ = \frac{\int_{p_{i-1}}^{p_i} [\epsilon_i(p) \cdot f_2(p)] dp}{\int_{p_{i-1}}^{p_i} f_2(p) dp}.$$

They would be the same only if $\epsilon_i(p)$ were a constant, or $f_1(p)$ and $f_2(p)$ were proportional to each other. Compare Fig. 4.5 with Fig. 4.6. In 3-prong vertex finding, we form a good 2-prong vertex first and then add the third track to form a 3-prong vertex, so index 3 in a 3-prong vertex list is usually a slower pion track. The different efficiencies between the two pions (with the same charges and birth points) from the same $D^+ \rightarrow K^- \pi^+ \pi^+$ (Fig. 4.9) in the low momentum bins offers support to my argument. Also, the different efficiencies between the kaon from $D^0 \rightarrow K^- \pi^+$ and the kaon from $D^+ \rightarrow K^- \pi^+ \pi^+$ is presented in Fig. 4.8 and Fig. 4.9. Thus, the difference of Čerenkov ID efficiencies from $D^0 \rightarrow K^- \pi^+$ and $D^+ \rightarrow K^- \pi^+ \pi^+$ samples can be explained as the difference of momentum spectra of decay tracks. This shows the need to be cautious in applying Čerenkov efficiencies based upon a sample with a similar momentum distribution.

After these comparisons, I am confident of using $D^0 \rightarrow K^- \pi^+$ for my final Čerenkov ID efficiency study, and the assumption here is that the kaons of $D^0 \rightarrow K^+ K^-$ and the pions of $D^0 \rightarrow \pi^+ \pi^-$ have similar momentum distributions to the kaons and pions from $D^0 \rightarrow K^- \pi^+$. I choose the analysis cut of $K_{ID} \geq 0.16$ (which gives the best statistical significance on $D^0 \rightarrow K^+ K^-$) to identify tracks as kaons. If $K_{ID} < 0.16$, tracks are assumed to be pions. Thus, each 2-prong vertex can be a candidate for one and only one of $D^0 \rightarrow K^+ K^-$, $D^0 \rightarrow \pi^+ \pi^-$, or $D^0 \rightarrow K^- \pi^+$. Table 4.2 lists the Čerenkov ID efficiencies I use for the final analysis.

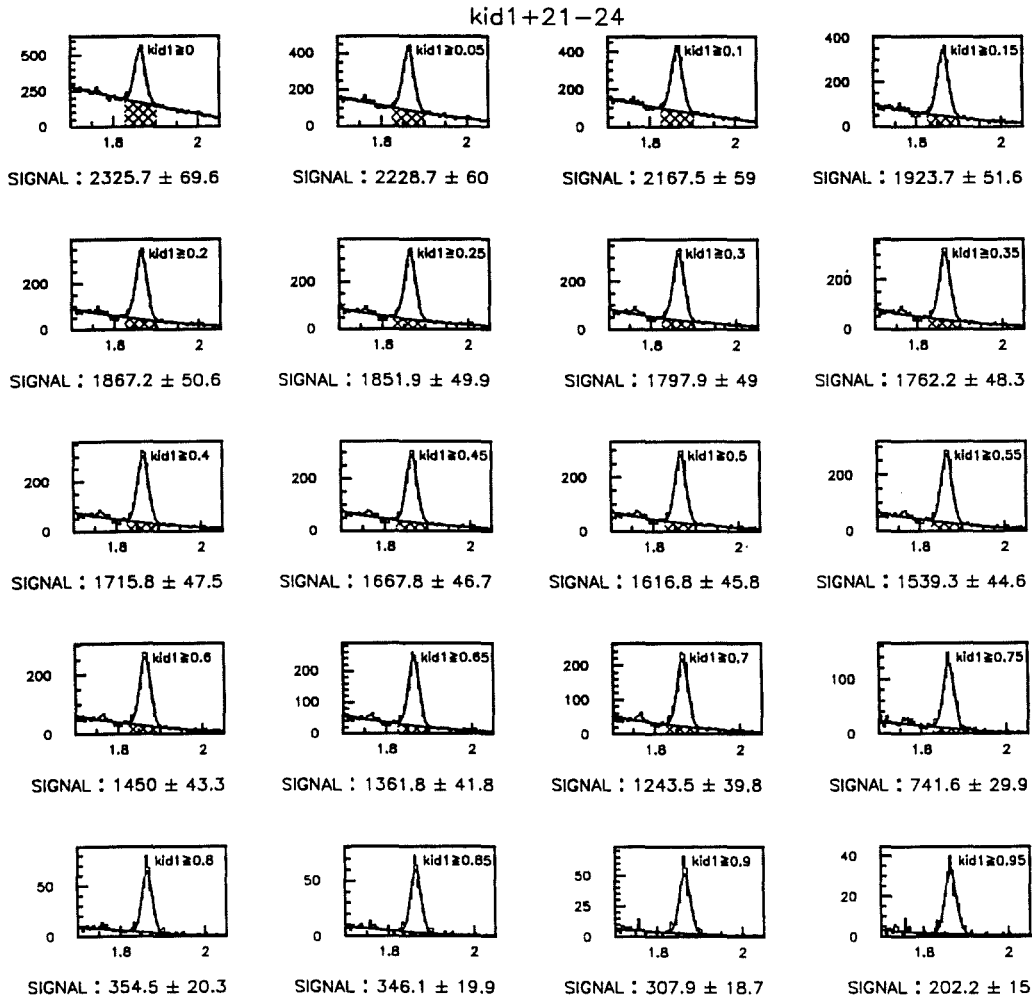


Figure 4.3. K^+ Čerenkov Efficiency Study in the Momentum Range 21-24 GeV/c from the \bar{D}^0 Sample:

20 plots represent 20 increments of K_{ID}^+ per 0.05. So for $K_{ID}^+ \geq 0.20$, the ID cut efficiency is $(1867.2 \pm 50.6)/(2325.7 \pm 69.6) = 0.8029 \pm 0.0043$.

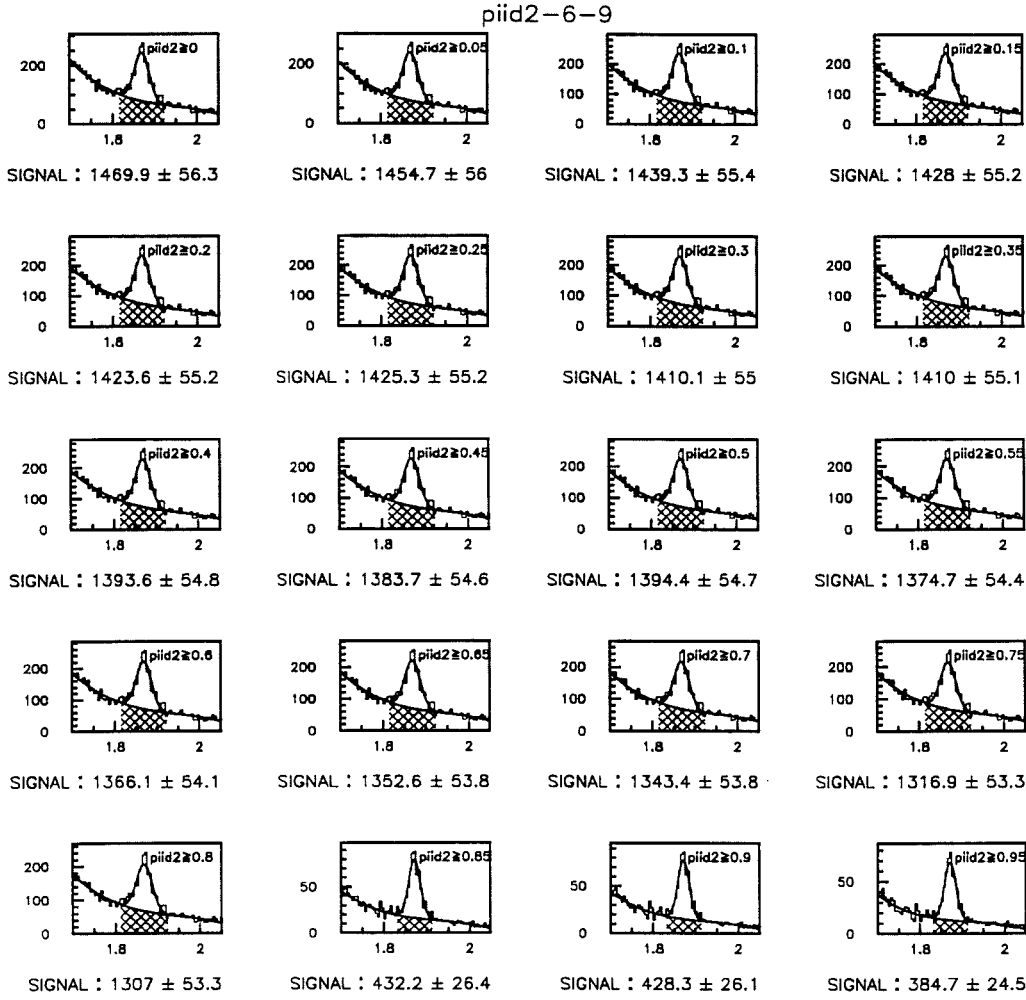


Figure 4.4. π^- Čerenkov Efficiency Study in the Momentum Range 6–9 GeV/c from the \bar{D}^0 Sample:

20 plots represent 20 increments of π_{ID} per 0.05. So for $\pi_{ID} \geq 0.90$, the ID cut efficiency is $(428.3 \pm 26.1 / 1469.9 \pm 56.3) = 0.2914 \pm 0.0125$. Notice that the widths are smaller in the last three plots.

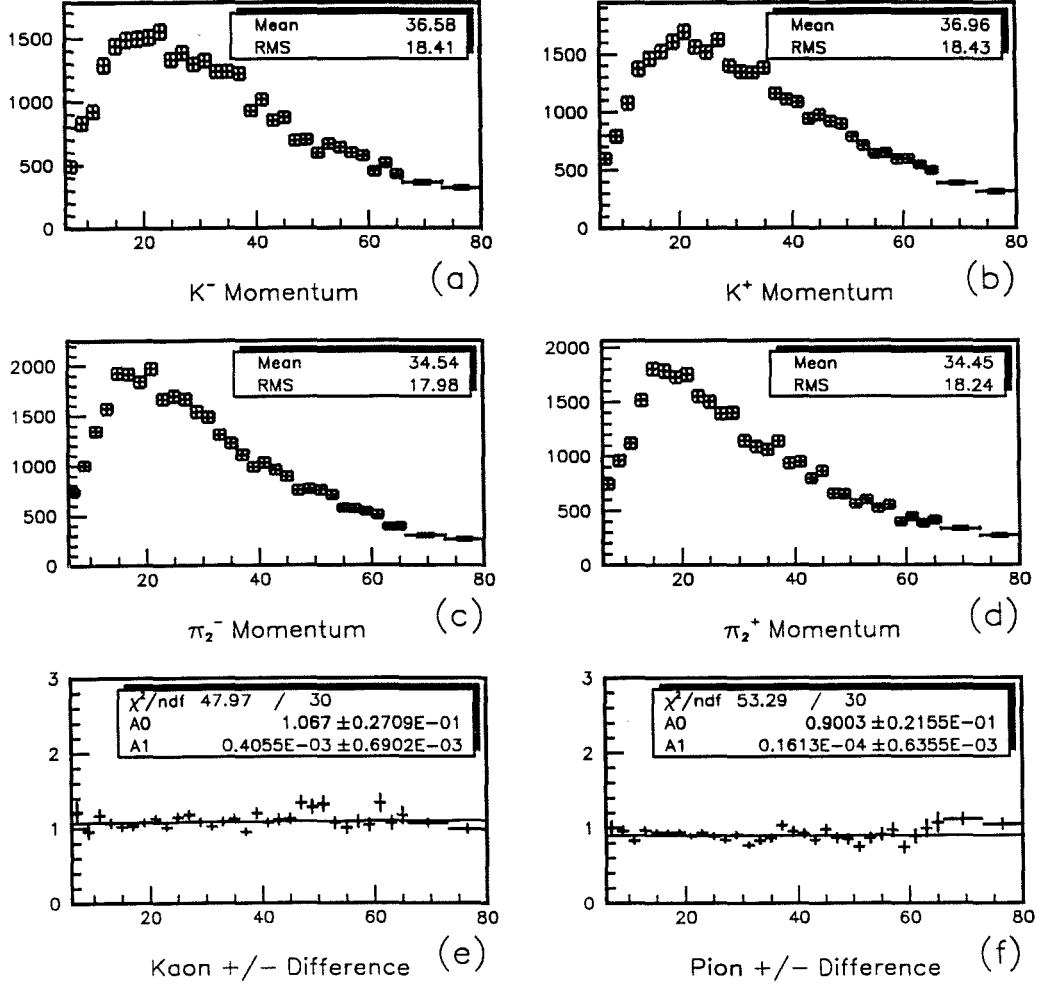
Momentum distribution of $K\pi$ from D^0 

Figure 4.5. Track Momentum Spectra of DATA BG-subtracted $D^0 \rightarrow K^- \pi^+$: Vertical axis is events/bin and horizontal axis is momentum from 6 to 80 GeV/c. Please compare (a), (b), (c), and (d) with Fig. 4.6. (e) and (f) are made by taking the ratios of (b) to (a) and (d) to (c), in order to understand the possible detection bias or the mismatch of the MC simulation. Also compare with Fig. 4.7.

Momentum distribution of $K\pi\pi$ from D^+

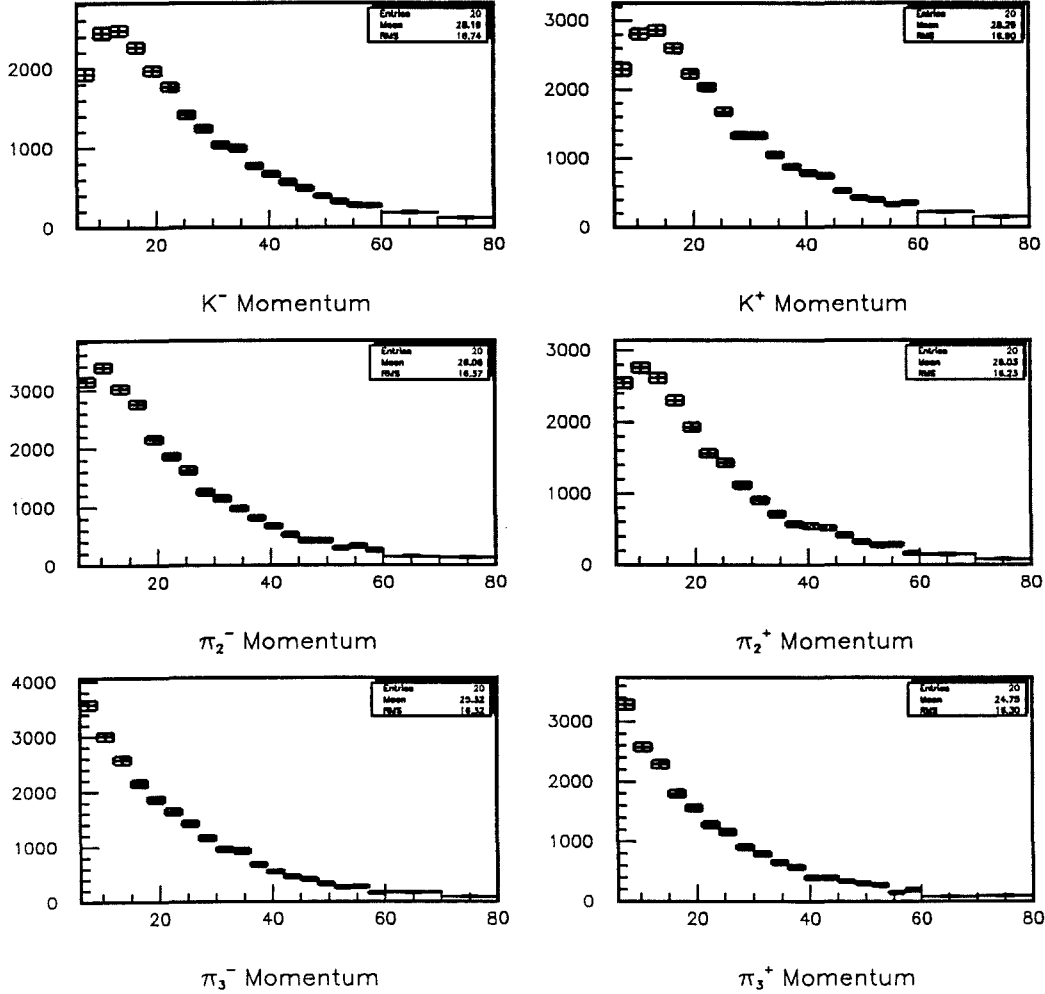


Figure 4.6. Track Momentum Spectra of DATA BG-subtracted $D^+ \rightarrow K^-\pi^+\pi^+$: Vertical axis is events per 3 GeV/c and horizontal axis is momentum from 6 to 80 GeV/c. Please compare with Fig. 4.5 (a), (b), (c), and (d).

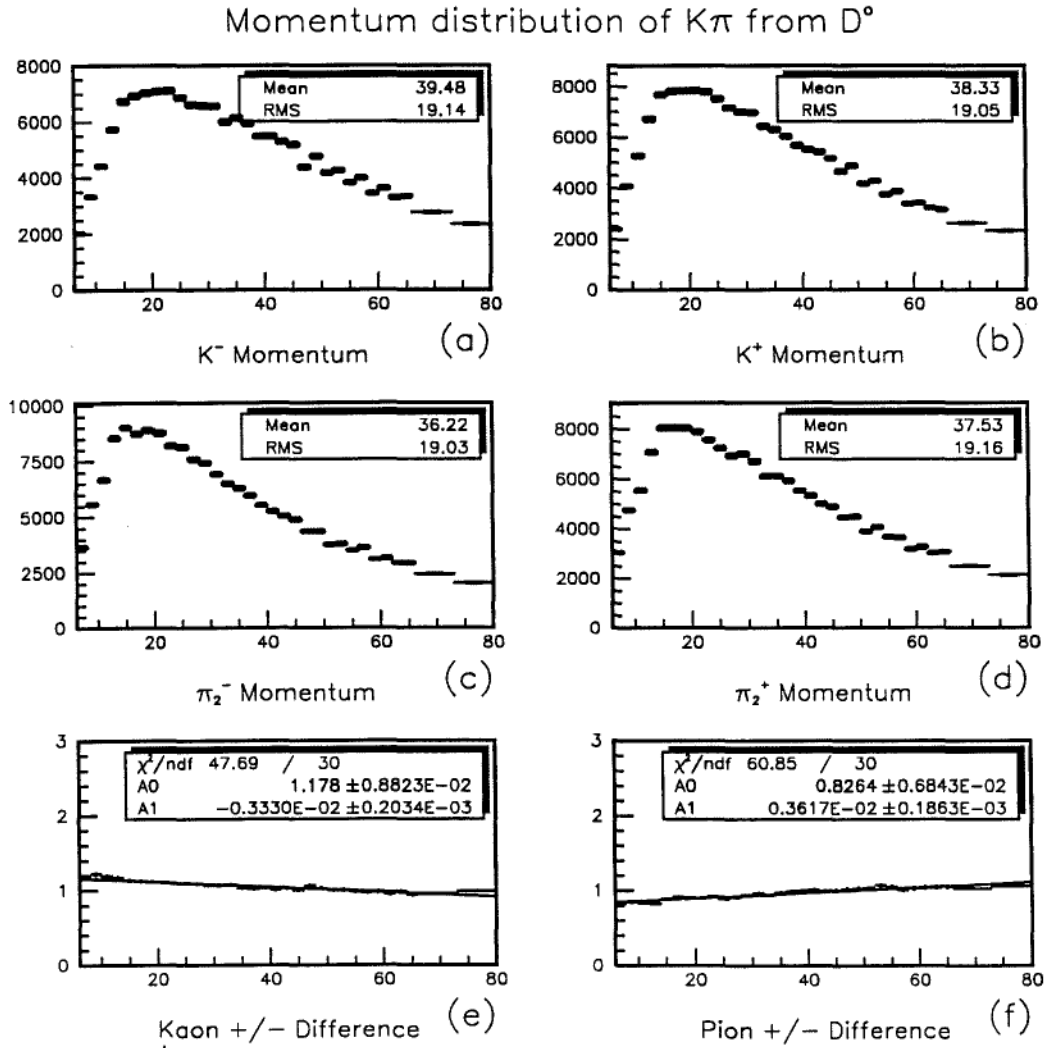


Figure 4.7. Track Momentum Spectra of MC BG-subtracted $D^0 \rightarrow K^- \pi^+$:

Vertical axis is events per 2 GeV/c and horizontal axis is momentum from 6 to 80 GeV/c. (e) and (f) are made by taking the ratios of (b) to (a) and (d) to (c), in order to understand the mismatch of the MC simulation. Compare with Fig. 4.5 to see that the data points in Fig. 4.5 (e) and (f) are merely statistical fluctuations.

Cerenkov Efficiency in Cat = 3,7,15 p = 3 GeV Range from D^0

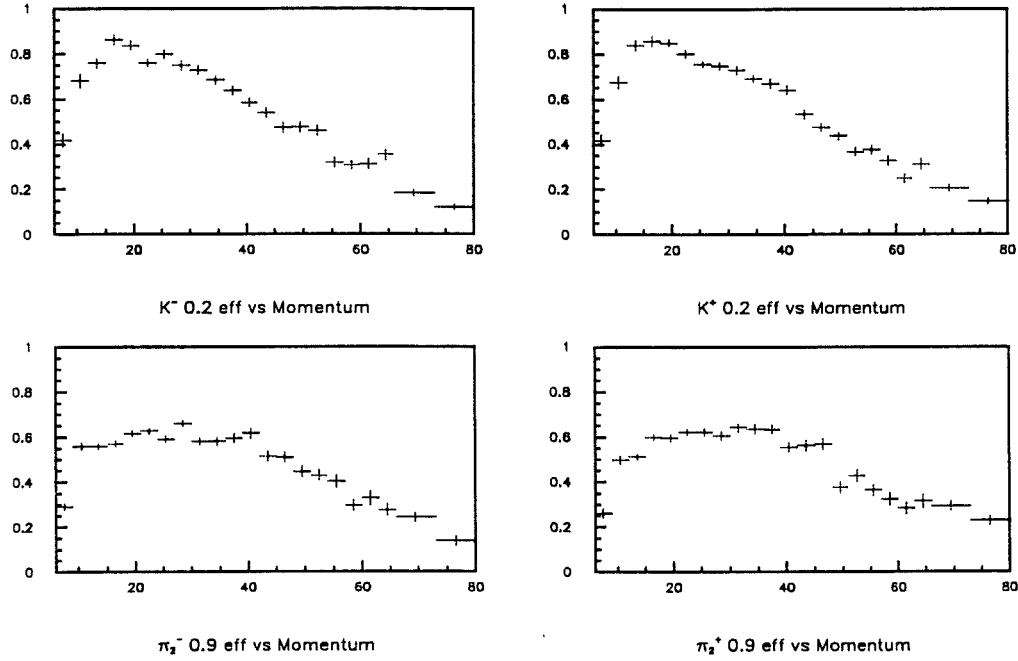


Figure 4.8. Track Čerenkov ID Efficiencies of $D^0 \rightarrow K^- \pi^+$:

Vertical axis is ID cut efficiency and horizontal axis is momentum in the range 6–80 GeV/c. Please compare with Fig. 4.9.

Cerenkov Efficiency in Cat = 3,7,15 p = 3 GeV Range from D^+

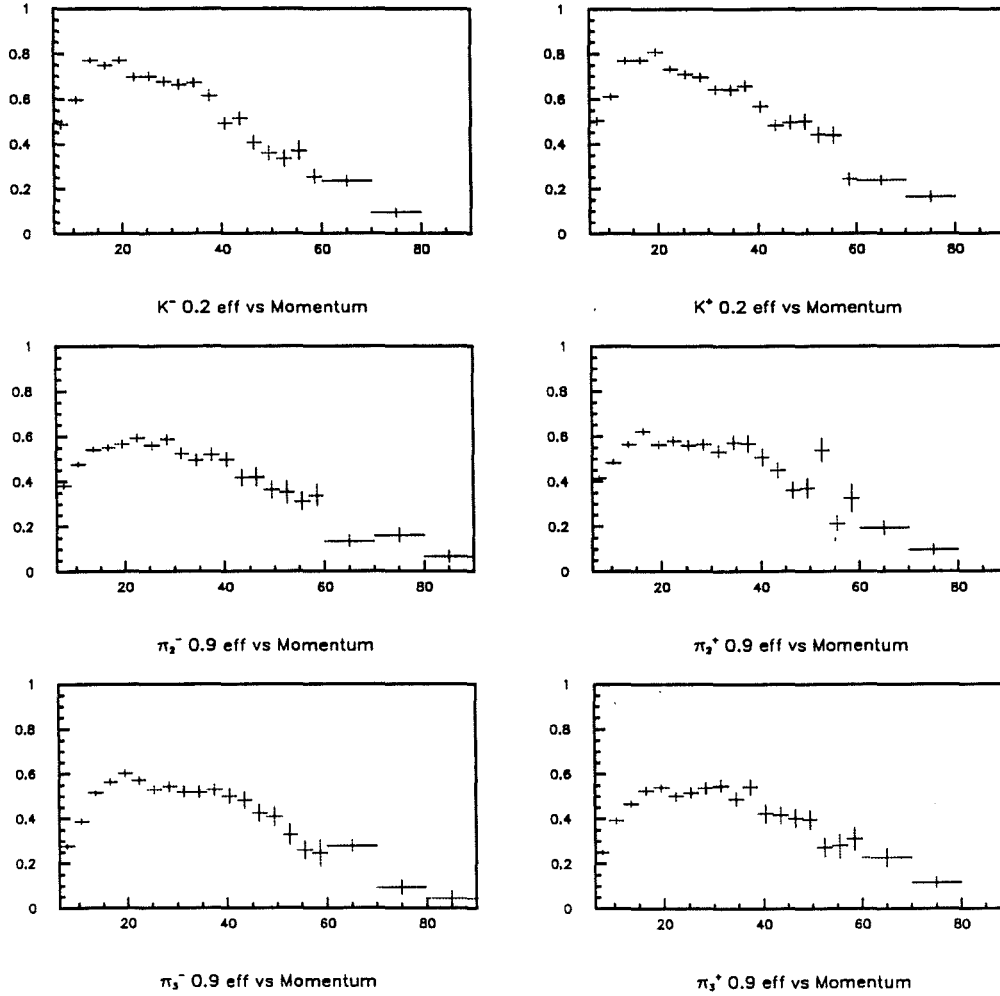


Figure 4.9. Track Čerenkov ID Efficiencies of $D^+ \rightarrow K^- \pi^+ \pi^+$:

Vertical axis is ID cut efficiency and horizontal axis is momentum in GeV/c. Please compare with Fig. 4.8. Also note the difference between π_2 and π_3 of the same charge in low momentum bins, mainly due to the difference of momentum distributions in Fig. 4.6.

Table 4.2. Čerenkov ID Efficiency of Kaon and Pion Identification

Momentum range	$K_{ID} \geq 0.16$ as kaon, $K_{ID} < 0.16$ as pion (from $D^0 \rightarrow K^- \pi^+$ sample)			
	K^-	K^+	π^-	π^+
6 – 8	0.40 ± 0.04	0.38 ± 0.03	0.91 ± 0.02	0.90 ± 0.02
8 – 10	0.58 ± 0.03	0.63 ± 0.04	0.95 ± 0.01	0.96 ± 0.01
10 – 12	0.74 ± 0.03	0.70 ± 0.03	0.94 ± 0.01	0.94 ± 0.02
12 – 14	0.82 ± 0.03	0.85 ± 0.03	0.85 ± 0.01	0.85 ± 0.02
14 – 16	0.79 ± 0.02	0.84 ± 0.02	0.85 ± 0.01	0.83 ± 0.01
16 – 18	0.88 ± 0.02	0.89 ± 0.02	0.90 ± 0.01	0.86 ± 0.02
18 – 20	0.87 ± 0.02	0.88 ± 0.02	0.87 ± 0.01	0.84 ± 0.02
20 – 22	0.80 ± 0.02	0.85 ± 0.02	0.85 ± 0.01	0.84 ± 0.02
22 – 24	0.77 ± 0.02	0.84 ± 0.02	0.89 ± 0.02	0.88 ± 0.02
24 – 26	0.83 ± 0.02	0.82 ± 0.02	0.85 ± 0.02	0.90 ± 0.02
26 – 28	0.80 ± 0.02	0.73 ± 0.02	0.88 ± 0.02	0.89 ± 0.02
28 – 30	0.77 ± 0.02	0.78 ± 0.02	0.85 ± 0.02	0.85 ± 0.02
30 – 32	0.75 ± 0.02	0.75 ± 0.02	0.86 ± 0.02	0.92 ± 0.02
32 – 34	0.78 ± 0.02	0.74 ± 0.02	0.85 ± 0.02	0.93 ± 0.02
34 – 36	0.72 ± 0.02	0.73 ± 0.02	0.84 ± 0.02	0.91 ± 0.02
36 – 38	0.68 ± 0.02	0.74 ± 0.02	0.88 ± 0.02	0.90 ± 0.02
38 – 40	0.68 ± 0.03	0.68 ± 0.02	0.96 ± 0.02	0.90 ± 0.02
40 – 42	0.60 ± 0.02	0.66 ± 0.02	0.91 ± 0.02	0.84 ± 0.02
42 – 44	0.64 ± 0.03	0.62 ± 0.02	0.88 ± 0.02	0.87 ± 0.02
44 – 46	0.56 ± 0.02	0.51 ± 0.02	0.89 ± 0.02	0.92 ± 0.02
46 – 48	0.51 ± 0.03	0.51 ± 0.02	0.84 ± 0.03	0.93 ± 0.02
48 – 50	0.54 ± 0.03	0.49 ± 0.02	0.88 ± 0.02	0.86 ± 0.03
50 – 52	0.53 ± 0.03	0.46 ± 0.02	0.84 ± 0.03	0.91 ± 0.03
52 – 54	0.48 ± 0.03	0.45 ± 0.03	0.88 ± 0.02	0.92 ± 0.03
54 – 56	0.43 ± 0.03	0.45 ± 0.03	0.81 ± 0.03	0.82 ± 0.03
56 – 58	0.41 ± 0.03	0.42 ± 0.03	0.86 ± 0.03	0.93 ± 0.02
58 – 60	0.42 ± 0.03	0.40 ± 0.03	0.81 ± 0.03	0.84 ± 0.03
60 – 62	0.38 ± 0.03	0.35 ± 0.03	0.79 ± 0.03	0.79 ± 0.03
62 – 64	0.41 ± 0.03	0.38 ± 0.03	0.88 ± 0.03	0.82 ± 0.04
64 – 66	0.37 ± 0.03	0.46 ± 0.03	0.76 ± 0.04	0.85 ± 0.04
66 – 73	0.33 ± 0.02	0.35 ± 0.02	0.84 ± 0.02	0.80 ± 0.02
73 – 80	0.28 ± 0.02	0.32 ± 0.02	0.82 ± 0.02	0.81 ± 0.02

4.4 Fitting Invariant Mass Plots

In Fig. 4.10, I show the most likely BG contribution for the $D^0 \rightarrow K^+ K^-$ mass hypotheses. BG are mainly from the reflections of $D^0 \rightarrow K^- \pi^+$ and $D^0 \rightarrow K^- \pi^+ \pi^0$. We see these in MC and data scatter plots. I have also checked some semi-leptonic decay modes and 3-prong modes, and none of them contributes significant BG after our Čerenkov ID cuts.

For $D^0 \rightarrow K^+ K^-$ I fit the SG as a Gaussian (G), the $D^0 \rightarrow K^- \pi^+ \pi^0$ reflection as a broad Breit-Wigner (BW) distribution function the $D^0 \rightarrow K^- \pi^+$ reflection as an asymmetric half-G-half-BW (ASY) — continuous at the peak, and the combinatoric BG as a linear function (L). For the $D^0 \rightarrow \pi^+ \pi^-$ case, I only see the asymmetric reflection of $D^0 \rightarrow K^- \pi^+$ on the low-mass side of the SG, and the combinatoric BG as an exponential function (E).

Thus I fit the mass window of $1.70 - 2.20 \text{ GeV}/c^2$ in $5 \text{ MeV}/c^2$ per bin for $D^0 \rightarrow K^+ K^-$ with $\langle L + BW + G + ASY \rangle$, $D^0 \rightarrow \pi^+ \pi^-$ with $\langle E + ASY + G \rangle$, and $D^0 \rightarrow K^- \pi^+$ and $D^0 \rightarrow K^- \pi^- \pi^+ \pi^+$ with $\langle G + P3 \rangle$. Fig. 4.11 is the result of fitting in the $D^0 \rightarrow K^- \pi^+$, $D^0 \rightarrow K^+ K^-$, $D^0 \rightarrow \pi^+ \pi^-$, and $D^0 \rightarrow K^- \pi^- \pi^+ \pi^+$ modes. Note that I always use (Gaussian peak $\pm 2.5\sigma$) as the SG region, and the Gaussian peak above the crossed BG is BG-subtracted SG. Fig. 4.11 also shows the necessity of applying Čerenkov ID cuts to improve the statistical significance for $D^0 \rightarrow K^+ K^-$ (plot (b)), and fixing SG width to estimate SG for $D^0 \rightarrow \pi^+ \pi^-$ (plot (c)).

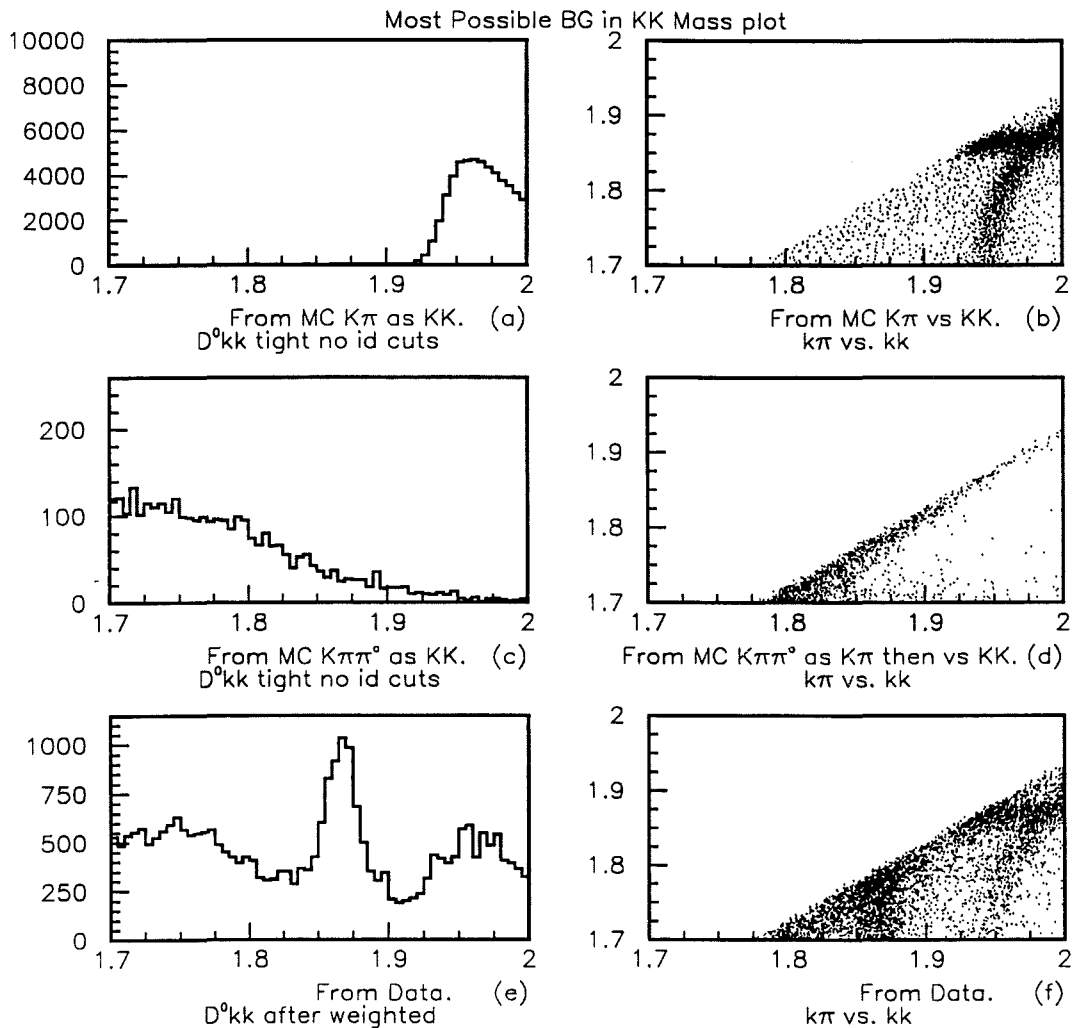


Figure 4.10. Study of Likely BG Under $D^0 \rightarrow K^+ K^-$ Signal:

- (a) From MC, $K\pi$ is misidentified as KK , an asymmetric broad shape.
- (b) From MC $K\pi$, scatter plot of $K\pi$ mass vs. KK mass. The “cross” is from double misidentified $K\pi$ as πK .
- (c) From MC, $K\pi(\pi^0)$ is misidentified as 2-prong KK , and it shows a broad shape.
- (d) From MC $K\pi(\pi^0)$, identified as $K\pi$ mass vs. KK mass. Superimposed (b) and (d) to compare with data (f).
- (e) From Data, KK mass plot with Čerenkov ID cuts.
- (f) From Data, $K\pi$ mass vs. KK mass from the same vertex.

Event Without ID Cuts ==E791==

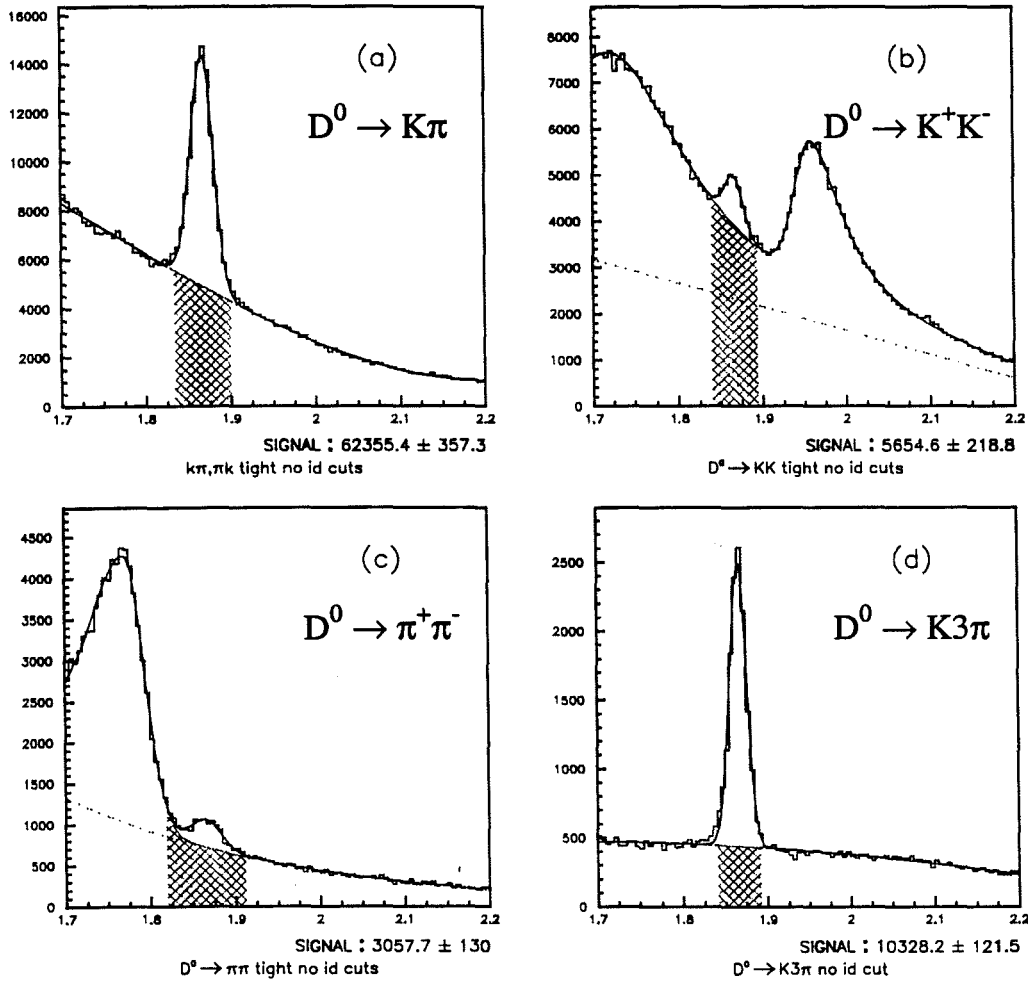


Figure 4.11. The Fitting Functions:

(a) $\langle G + P3 \rangle$ for $K^\mp\pi^\pm$, (b) $\langle L + BW + G + ASY \rangle$ for $K^\pm K^\mp$, (c) $\langle E + ASY + G \rangle$ for $\pi^\pm\pi^\mp$, and (d) $\langle G + P3 \rangle$ for $K3\pi$.

4.5 Reduced Proper Time

The decay proper time t for a particle of invariant mass m_0 and momentum p is defined as

$$\begin{aligned}
 t &= \frac{L_{\text{rest}}}{v} \\
 &= \frac{L_{\text{lab}}/\gamma_E}{v} \\
 &= \frac{L_{\text{lab}} \cdot m_0}{\gamma \cdot m_0 \cdot v} \\
 &= \frac{L_{\text{lab}} \cdot m_0}{p}
 \end{aligned} \tag{4.6}$$

where L is the decay length in the lab or rest frame, v is the velocity, γ_E is the Lorentz energy factor, m_0 is the invariant mass and p is the measured momentum.

The main purpose in adopting reduced proper time is to correct for the loss from our analysis cuts at low proper time without further decreasing the size of the data sample. I can then apply a better (or flatter) acceptance function without huge uncertainties in the low reduced proper time bins.

The basic idea of Reduced Proper Time is to redefine the starting time t_0 in the sample surviving our analysis cuts. There are several ways to define a new reduced proper time. For example, I could define t'_0 to be $\frac{L_{\text{min}} \cdot m_0}{p_{\text{max}}}$, where p_{max} and L_{min} are the maximum momentum and closest approach to the primary vertex under our cuts, and they could be a single value for all events. Then the reduced proper time is $t' = t - t'_0 = \frac{L \cdot m_0}{p} - \frac{L_{\text{min}} \cdot m_0}{p_{\text{max}}}$. But in this case all I really have done is to shift the origin of t , which does not increase the acceptance of low proper time bins. This example illustrates that the lifetime is a unique characteristic of each decayed particle, and it does not matter when you start clocking the particles, since the decay probability is always exponential, i.e. the particle has no “memory” of how long it

has already lived, and it also illustrates that the proper time is a function of length and velocity.

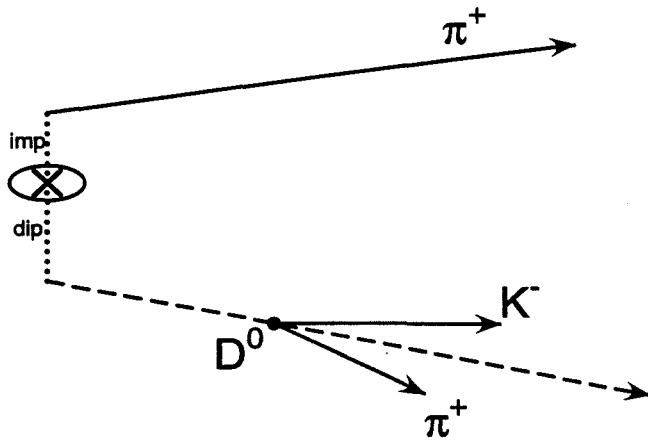
I could also define a new minimum length, L_{min} , as the distance between the point of closest approach to the primary vertex, and the secondary vertex, illustrated in Fig. 4.12 (b). Note that L_{min} cannot be a function of L nor of proper time.

I then define the origin of reduced proper time as $t'_0 = \frac{L_{min} \cdot m_0}{p}$. Note that t'_0 is a function of both reduced length and momentum. For the same value of L_{min} , different values of p will yield different values of t'_0 . However I can separate my sample into different momentum subsamples, and they all share the same lifetime, *i.e.* the reduced proper time is just a coefficient times an exponential distribution, $C_{p_1} \cdot e^{-\frac{t'}{\tau}}$, for each subsample. Then I can combine all the momenta; effectively I am summing all the coefficients but with the same exponential factor of lifetime τ , *i.e.* $[C_{p_1} + C_{p_2} + C_{p_3} + \dots] \cdot e^{-\frac{t'}{\tau}}$. In other words, a momentum-weighting scheme in reduced proper time will not change the exponential character of the decay time spectrum, and our reduced proper time will not change the measured decay lifetime.

So, I define $t' \equiv \frac{(L - L_{min}) \cdot Mass}{P}$, where L_{min} is the maximum of L_{min}^{SDZ} and L_{min}^{PTBAL} . L_{min}^{SDZ} is illustrated in Fig. 4.12, where the basic idea is to “swim back” the D^0 vertex along the line of flight toward the primary vertex. The reconstructed D^0 reaches the point of closest approach at L_{min}^{SDZ} as determined by the SDZ_{cut} value. So from simple trigonometry, we have

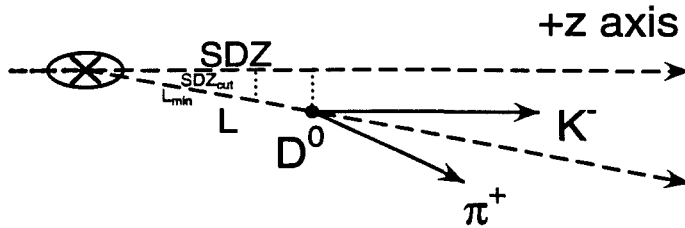
$$L_{min}^{SDZ} = L \cdot \frac{SDZ_{cut}}{SDZ} \quad (4.7)$$

$$L_{min}^{PTBAL} = L \cdot \frac{PTBAL}{PTBAL_{cut}} \quad (4.8)$$



DIP and Impact Parameter.

(a)



$$SDZ / L = SDZ_{cut} / L_{min}$$

L_{min} of SDZ for Reduced Proper Time. (b)

Figure 4.12. Illustrations of (a) DIP and IMPACT Cuts and (b) Reduced Proper Decay Length, L_{min}^{SDZ} .

CHAPTER V

PHYSICS ANALYSIS

5.1 Relative Branching Ratios

The BR's are calculated as follows:

$$\frac{\Gamma(D^0 \rightarrow K^+ K^-)}{\Gamma(D^0 \rightarrow K^- \pi^+)} = \frac{\epsilon_g^{-1}(K^\pm K^\mp) \cdot \{\epsilon_{\check{C}}^{-1}(K^\pm K^\mp) \cdot N_{K^\pm K^\mp}\}}{\epsilon_g^{-1}(K^\mp \pi^\pm) \cdot \{\epsilon_{\check{C}}^{-1}(K^\mp \pi^\pm) \cdot N_{K^\mp \pi^\pm}\}} \quad (5.1)$$

$$\frac{\Gamma(D^0 \rightarrow \pi^+ \pi^-)}{\Gamma(D^0 \rightarrow K^- \pi^+)} = \frac{\epsilon_g^{-1}(\pi^\pm \pi^\mp) \cdot \{\epsilon_{\check{C}}^{-1}(\pi^\pm \pi^\mp) \cdot N_{\pi^\pm \pi^\mp}\}}{\epsilon_g^{-1}(K^\mp \pi^\pm) \cdot \{\epsilon_{\check{C}}^{-1}(K^\mp \pi^\pm) \cdot N_{K^\mp \pi^\pm}\}} \quad (5.2)$$

$$\frac{\Gamma(D^0 \rightarrow K^+ K^-)}{\Gamma(D^0 \rightarrow \pi^+ \pi^-)} = \frac{\epsilon_g^{-1}(K^\pm K^\mp) \cdot \{\epsilon_{\check{C}}^{-1}(K^\pm K^\mp) \cdot N_{K^\pm K^\mp}\}}{\epsilon_g^{-1}(\pi^\pm \pi^\mp) \cdot \{\epsilon_{\check{C}}^{-1}(\pi^\pm \pi^\mp) \cdot N_{\pi^\pm \pi^\mp}\}} \quad (5.3)$$

where ϵ_g^{-1} is the correction from acceptance (geometry and analysis cuts), $\epsilon_{\check{C}}^{-1}$ is the correction from Čerenkov ID cuts, and N is the BG subtracted signal number we observe.

I apply the Čerenkov ID efficiency correction by applying a “weight” to each 2-prong vertex (each track has its own efficiency as a function of its momentum and charge):

$$\text{weight} \pm \Delta w = \frac{1}{[E_{\check{C}}(C_1, p_1) \pm \Delta E_1] \times [E_{\check{C}}(C_2, p_2) \pm \Delta E_2]} \quad (5.4)$$

where C_i and p_i are the charge and the momentum of tracks $i = 1, 2$. The error is propagated from the corresponding efficiency error (refer to Sec. 4.3).

First, I fit the results from the MC study with the same set of cuts as the DATA. I consistently treat Data and MC on the vertex basis. By dividing by the generated MC numbers, I get an acceptance for $D^0 \rightarrow K^- \pi^+$, $D^0 \rightarrow K^+ K^-$, $D^0 \rightarrow \pi^+ \pi^-$, and $D^0 \rightarrow K^- \pi^- \pi^+ \pi^+$ in Fig. 5.1. Second, I fit DATA as illustrated in Fig. 5.2. I fix the widths (by assuming they all have the same ratio of DATA/MC from the

$D^0 \rightarrow K^- \pi^+$ mode) for $D^0 \rightarrow K^+ K^-$ and $D^0 \rightarrow \pi^+ \pi^-$. For example, to obtain the width for $D^0 \rightarrow K^+ K^-$ mode

$$Wid_{Data}(K^\pm K^\mp) = Wid_{MC}(K^\pm K^\mp) \times \frac{Wid_{Data}(K^\mp \pi^\pm)}{Wid_{MC}(K^\mp \pi^\pm)}.$$

Especially in the $D^0 \rightarrow \pi^+ \pi^-$ case, it is necessary to fix the width (refer to Fig. 4.11). I fit unweighted data first in order to determine the fractional errors, then apply these fractional errors to the weighted plots, propagating weighted errors from unweighted fractional errors. Finally, by applying the acceptance correction on each mode, I get the results listed in Table 5.1. Note that $D^0 \rightarrow K^- \pi^- \pi^+ \pi^+$ is our consistency checking mode, and there is no ID cut on $D^0 \rightarrow K^- \pi^- \pi^+ \pi^+$ (but I choose the highest K_{ID} as kaon), so the only correction is from the MC acceptance. $\frac{\Gamma(D^0 \rightarrow K^- \pi^- \pi^+ \pi^+)}{\Gamma(D^0 \rightarrow K^- \pi^+)}$ shows reasonable agreement with the PDG'94 value (2.02 ± 0.11) [PDG94], and this indicates that our MC acceptance is satisfactory.

Table 5.1. Branching Ratios (Statistical Error Only)

Decay Mode	Branching Ratios
$\frac{\Gamma(D^0 \rightarrow K^+ K^-)}{\Gamma(D^0 \rightarrow K^- \pi^+)}$	0.107 ± 0.003
$\frac{\Gamma(D^0 \rightarrow \pi^+ \pi^-)}{\Gamma(D^0 \rightarrow K^- \pi^+)}$	0.040 ± 0.002
$\frac{\Gamma(D^0 \rightarrow K^+ K^-)}{\Gamma(D^0 \rightarrow \pi^+ \pi^-)}$	2.65 ± 0.14
$\frac{\Gamma(D^0 \rightarrow K^- \pi^- \pi^+ \pi^+)}{\Gamma(D^0 \rightarrow K^- \pi^+)}$	2.19 ± 0.03

5.2 Lifetime Difference

Our major 2-prong cuts are

- $SDZ > 8$. — affects the low proper time.
- $PTBAL < .4$ GeV — affects the low proper time.

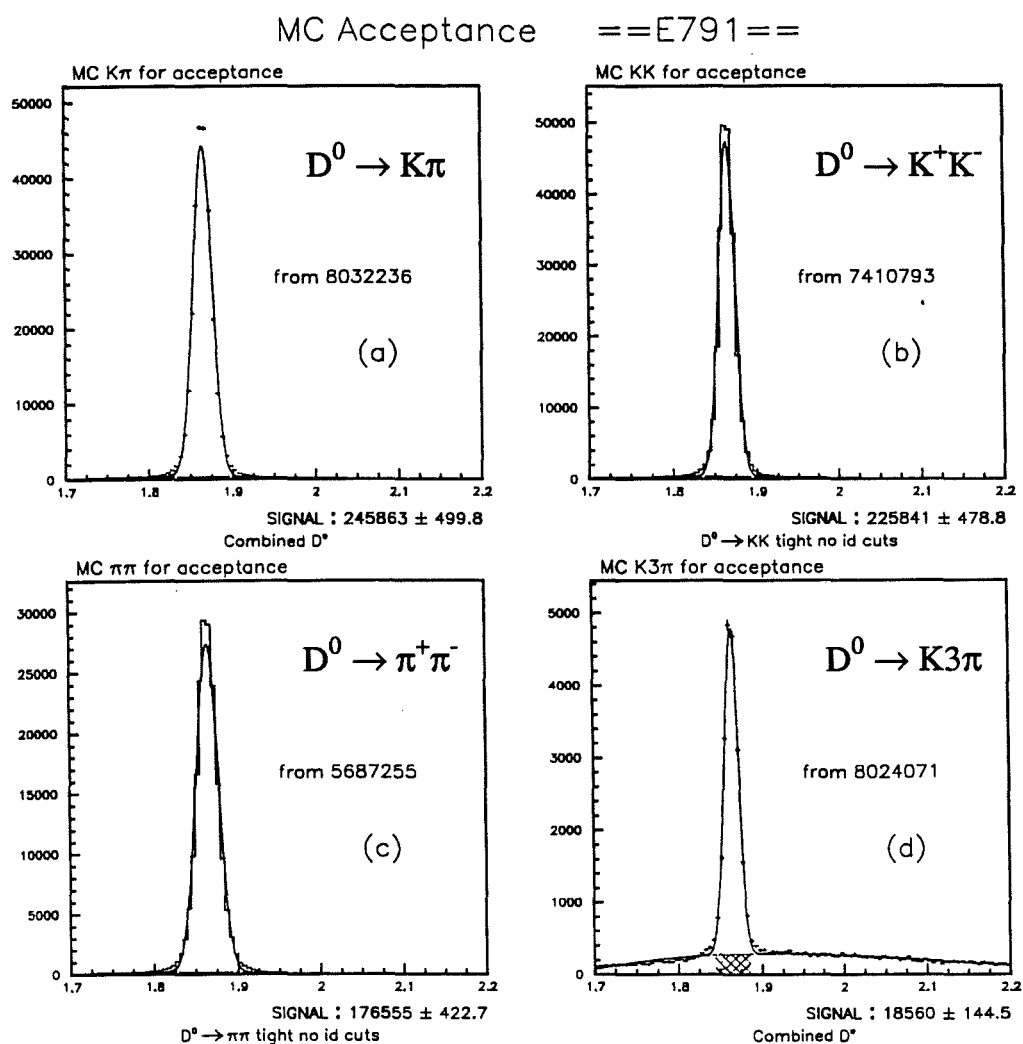


Figure 5.1. MC Acceptance Study for

(a) $K^\mp\pi^\pm$: $(3.062 \pm 0.006)\%$, (b) $K^\pm K^\mp$: $(3.047 \pm 0.006)\%$, (c) $\pi^\pm\pi^\mp$: $(3.087 \pm 0.007)\%$, and (d) $K3\pi$: $(0.231 \pm 0.002)\%$.

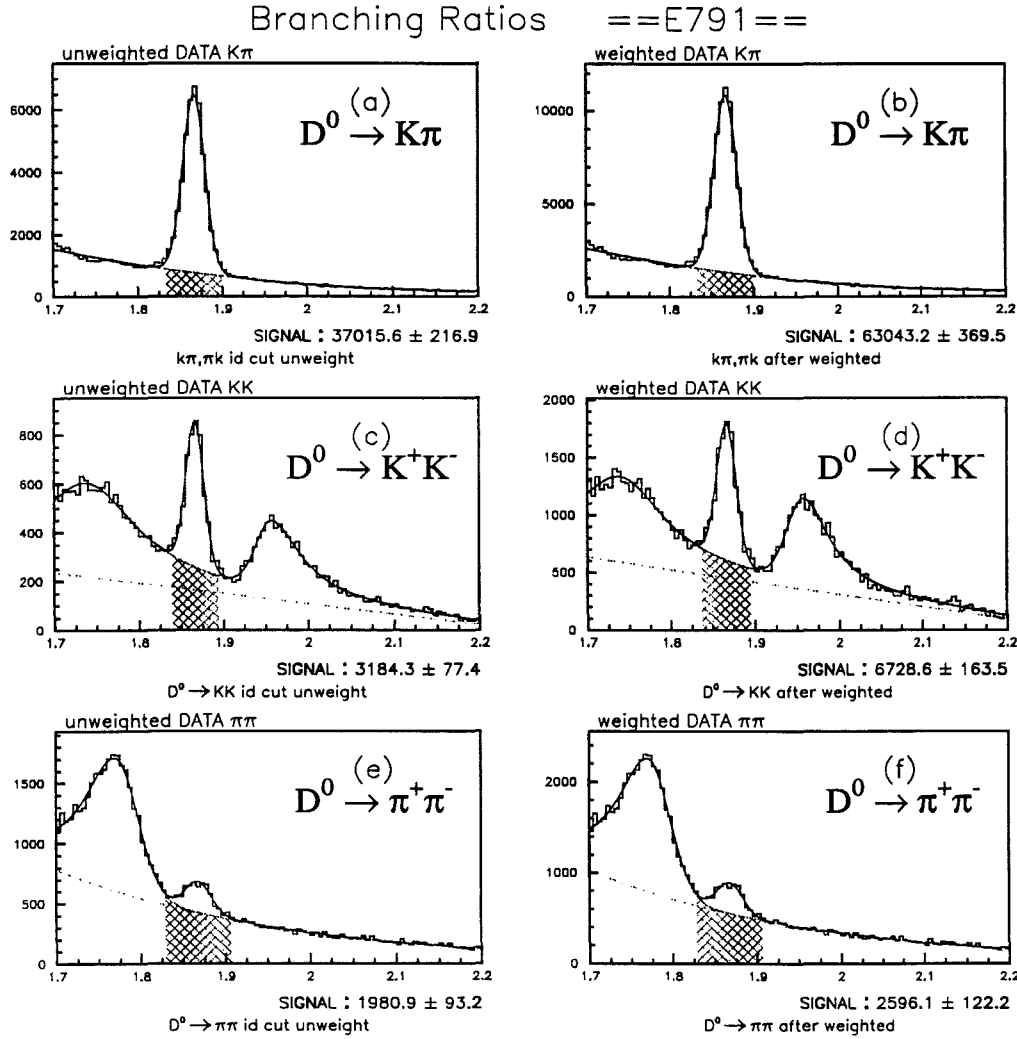


Figure 5.2. The DATA in the left column are the unweighted plots after ID cuts, used to propagate the fractional errors to the right column plots, which are weighted DATA after ID cuts.

To fit the SG numbers of (b), (d), and (f), I fix the widths by comparing DATA and MC.

- Čerenkov ID cuts — alters the momentum spectra and tests the MC's reliability.

The first two items will be corrected by using the reduced proper time. Since we don't have reliable Čerenkov efficiency in the MC, before applying the MC acceptance correction, we apply the Čerenkov correction from the DATA study, described in section 4.3 and Eq. 5.4.

Fig 5.3 illustrates the 2-dimensional view of mass vs. reduced proper time for (a) $K^\pm K^\mp$ and (b) $K^\mp \pi^\pm$. I will slice into 16 bins of reduced proper time for binned method, and also will check the validity by unbinned maximum likelihood fitting on $\tau_{K\pi}$.

5.2.1 Binned Reduced Proper Time Method. Fig. 5.5 ($D^0 \rightarrow K^+ K^-$) and Fig. 5.6 ($D^0 \rightarrow K^- \pi^+$) are from Čerenkov weighted mass plots in 16 reduced proper time bins. I propagate the weighted statistical errors from the unweighted fractional errors of Fig. 5.4, as described in Sec. 5.1.

To fit the SG number in each plot, I fix the SG width in all reduced proper time bins for both modes. Fixing the SG fitting width is reasonable — within the same range of SG region, we are measuring the exponential decay lifetime. This is evidenced by the fact that in the MC of $D^0 \rightarrow K^+ K^-$ (Fig. 5.7) and $D^0 \rightarrow K^- \pi^+$, and the DATA of $D^0 \rightarrow K^- \pi^+$ (Fig. 5.6), one sees similar SG widths throughout the reduced proper time bins. This can be understood from the definition of proper time:

$$t = \frac{L \cdot m_0}{p} \quad (5.5)$$

where L , m_0 , and p are decay length, rest mass, and momentum in the lab frame. The measured momenta are used to get the invariant mass of the hypothesis, so the errors of invariant mass and momentum are correlated.

2D View of Mass vs. Reduced Proper Time ==E791==

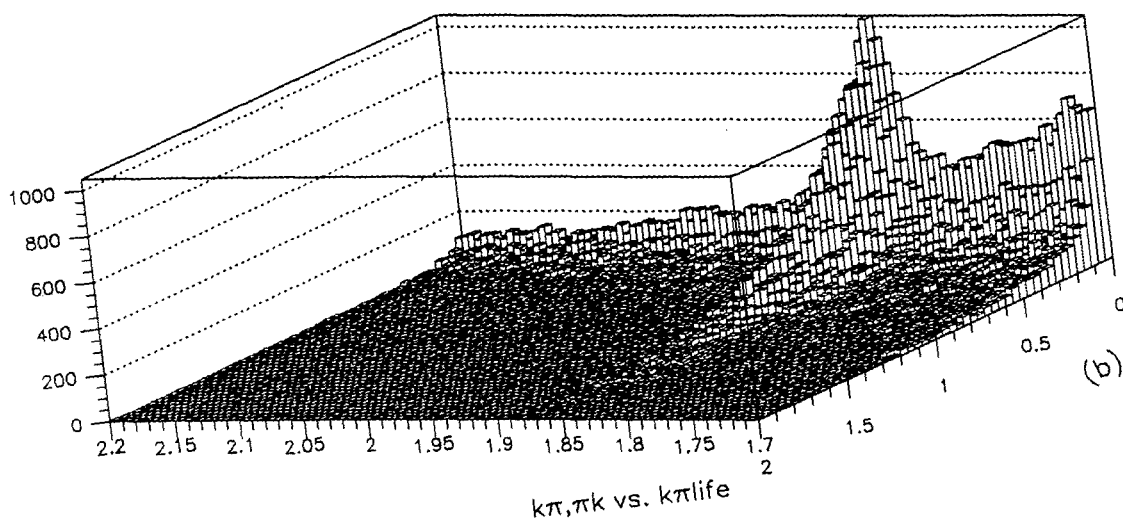
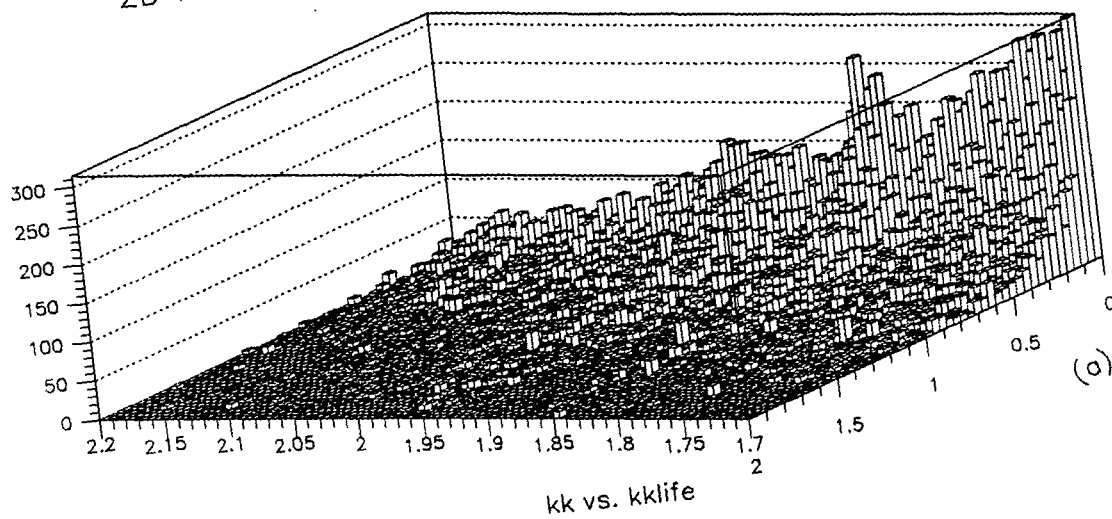


Figure 5.3. 2-Dimensional View of D^0 Mass vs. Reduced Proper Time for (a) $K^\pm K^\mp$ and (b) $K^\mp \pi^\pm$.

Unweighted KK in 16 bins of t' ==E791==

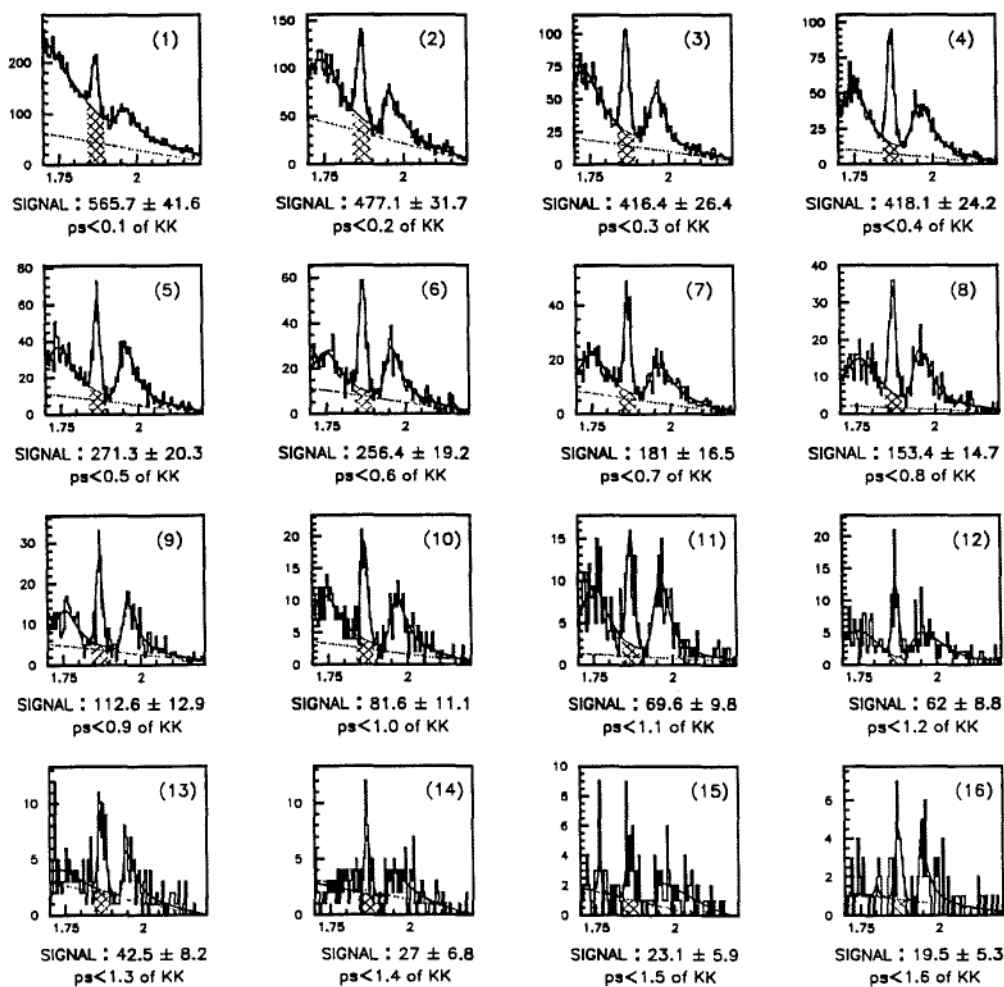


Figure 5.4. $D^0 \rightarrow K^+K^-$ Mass Plots After ID Cut But Unweighted, in 16 Bins of Reduced Proper Time.

Weighted KK in 16 bins of t' ==E791==

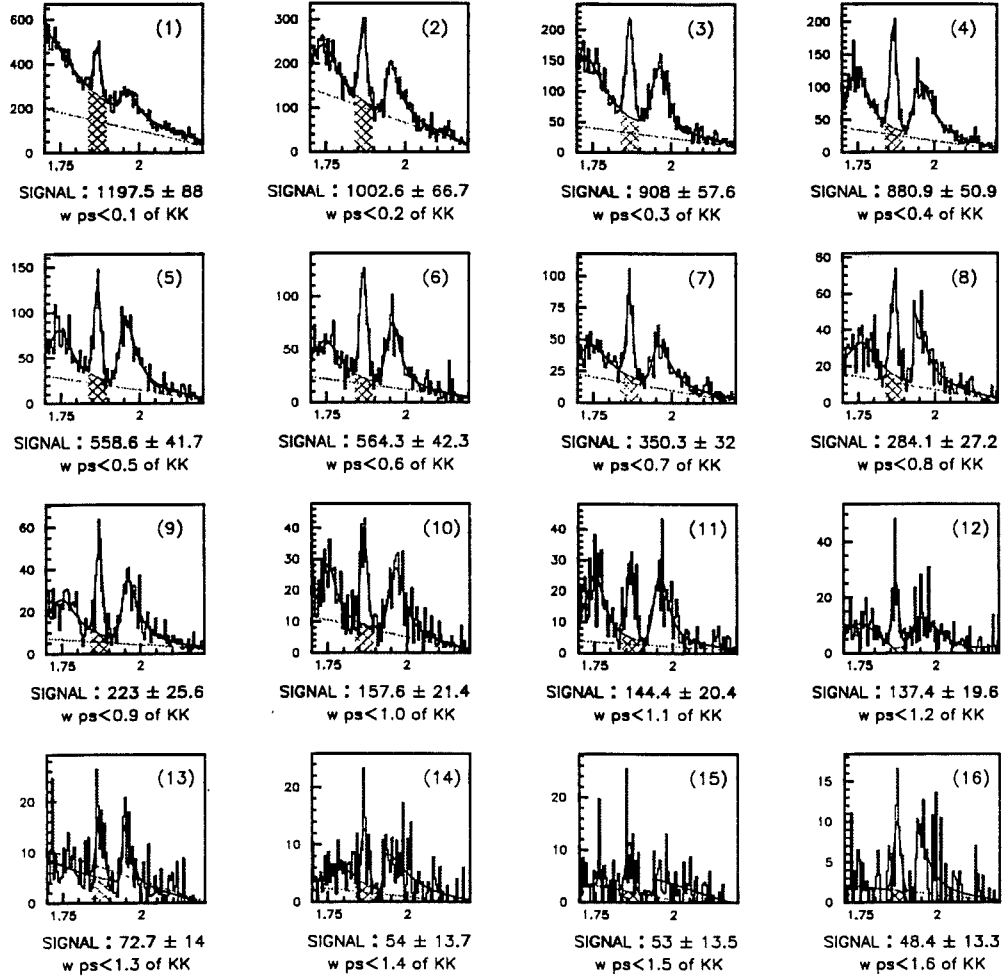


Figure 5.5. BG Subtraction from Čerenkov Corrected (Weighted) $D^0 \rightarrow K^+ K^-$ Mass Plots in 16 Bins of Reduced Proper Time.

Weighted $K\pi$ in 16 bins of t' ==E791==

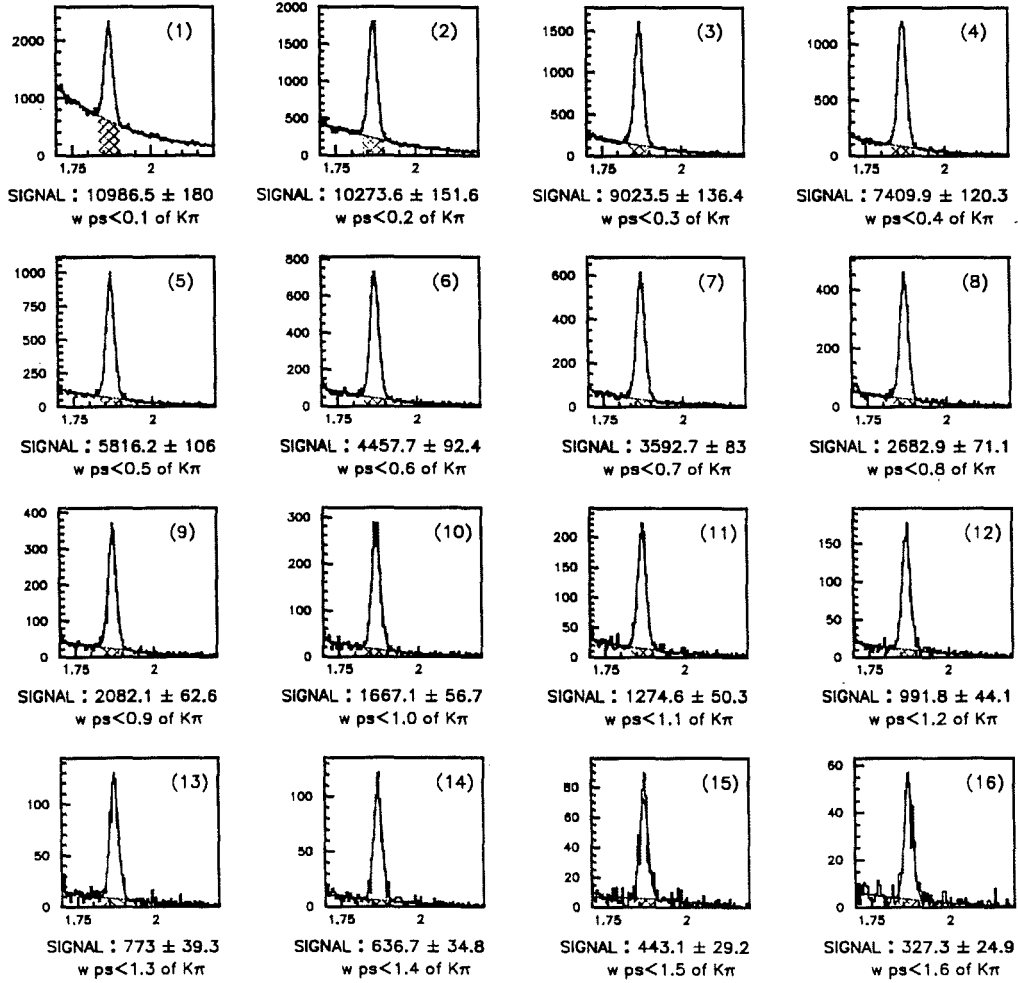


Figure 5.6. BG Subtraction from Čerenkov Corrected $D^0 \rightarrow K^- \pi^+$ Mass Plots in 16 Bins of Reduced Proper Time:

It also illustrates that the widths in each reduced proper time bins are about the same size.

MC $D^0 \rightarrow KK$ in 16 bins of t' ==E791==

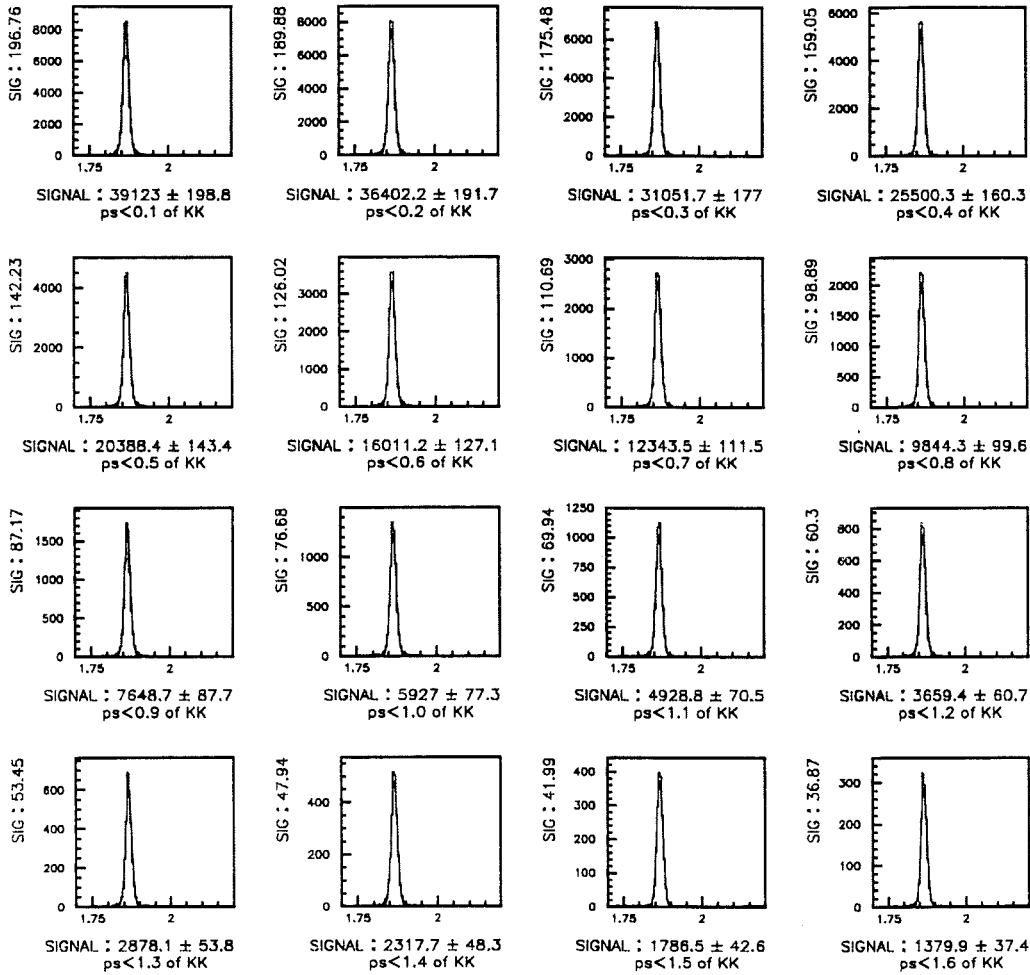


Figure 5.7. BG Subtraction from MC $D^0 \rightarrow K^+ K^-$ Mass Plots in 16 Bins of Reduced Proper Time:

It also illustrates that the widths in each reduced proper time bins are about the same size.

Fig. 5.8 shows the extraction of acceptance functions from the MC studies. Since I have done the Čerenkov ID correction (weighting) in DATA, I apply the same 2-prong cuts, binning the MC into the same 16 reduced proper time bins, but without the Čerenkov ID cuts. I fit the MC from bins 4 to 10 into an exponential shape to get an estimate of heights, and then I use the input MC lifetime (.415 ps) as the slope to draw two straight lines on the semi-log scale, as shown by the dotted lines in Fig. 5.8(a). From the central value of each reduced proper time bin I get the ratios of the fitted MC data points to the exponential inputs. Thus, I get the floating discrete MC acceptance functions (as shown in Fig. 5.8(b)) for the reduced proper time. I consistently use the central value of each bin in DATA and MC, thus eliminating the uncertainty due to the finite binning.

I then apply the MC acceptance corrections on weighted distributions in Fig. 5.5 and Fig. 5.6, and fit the corrected 16 bins with an exponential decay function by log-likelihood maximization. The statistical errors of MC events have been taken into account for each data point. At the same time I also calculate the mean values for $D^0 \rightarrow K^+ K^-$ and $D^0 \rightarrow K^- \pi^+$. Fig. 5.9 presents the fit result from this binned method on a semi-log scale. Fig. 5.10 shows the fitted values and the mean values. Table 5.2 lists the results of the binned lifetime measurement.

Table 5.2. Binned Method Lifetime (Statistical Error Only)

Method	Mode	Binned lifetime measurement
Binned Likelihood	τ_{KK}	0.414 ± 0.012
	$\tau_{K\pi}$	0.409 ± 0.003
Eq. 1.57	$\Delta\gamma_{\text{approx}}$	-0.055 ± 0.148
Eq. 1.55	$\Delta\gamma_{\text{fitted}}$	-0.056 ± 0.149

Decay Mean Value Difference Approaches. Using the method detailed in Appendix A, I also calculate t_{mean} from these 16 bins of BG-subtracted SG. Owing to the complicated BG in $K^\pm K^\mp$ plots, it is difficult to use the unbinned method

Acceptance Function Study from MC $KK, K\pi$ ==791==

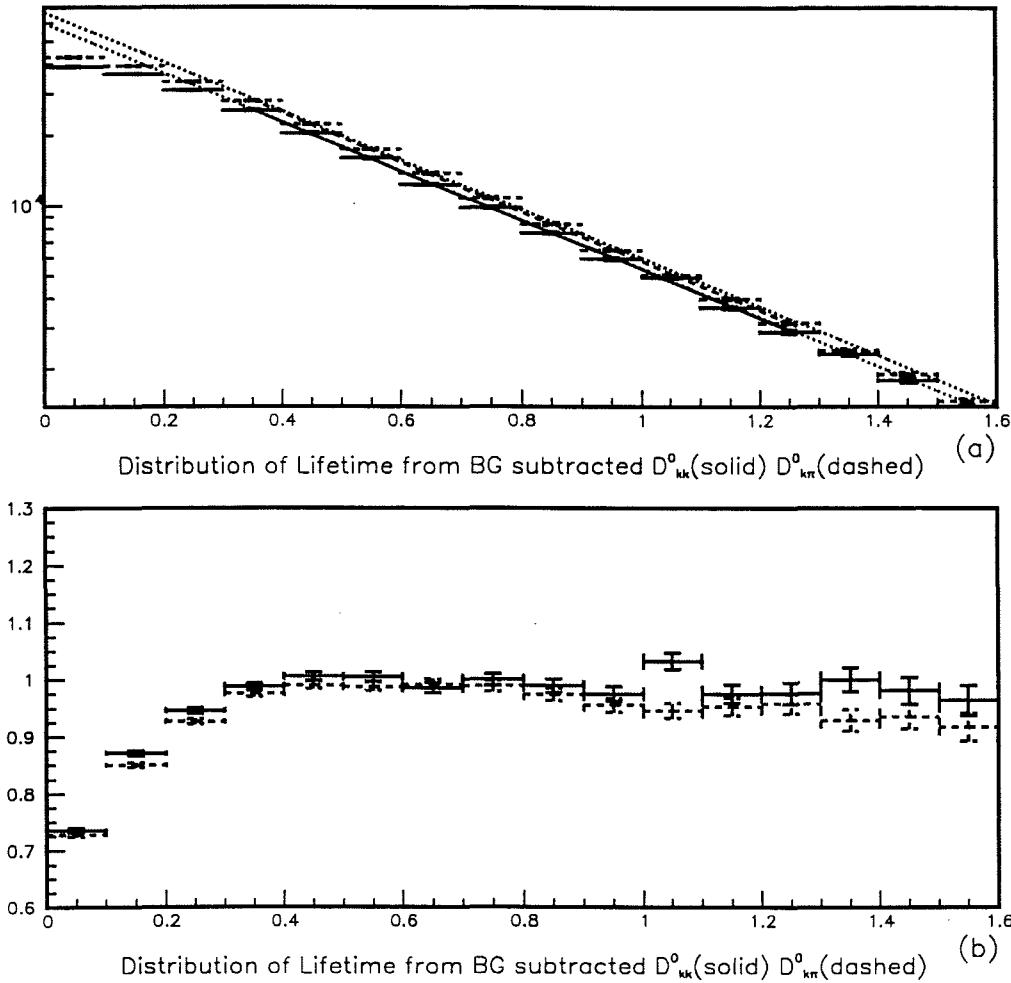


Figure 5.8. The Study of MC Acceptance Functions for the Binned Method:

(a) MC is passed through the same selection criteria as DATA, and separated into the same 16 reduced proper time bins as DATA. The solid line comes from a fit of the 4th bin to the 10th bin in order to get the heights. The dotted slopes are then taken from the MC input lifetimes and the fitted heights.

(b) The ratio of output to input in each bin is my floating discrete acceptance function.

to calculate the mean value, but in the $K^\mp\pi^\pm$ case, it is possible to approximate the linear sideband for an unbinned BG subtraction. I calculate t_{mean} and σ_t (root mean square, RMS) according to their definitions: $\langle t \rangle \equiv \frac{\sum_i t_i \cdot S_i}{\sum_i S_i}$ and $\sigma_t \equiv \sqrt{|\langle t^2 \rangle - \langle t \rangle^2|}$, where S_i and t_i are the BG-subtracted SG number and the central value of the i^{th} bin, respectively. The uncertainty of assigning t_i is only about 0.001 ps in this case. The error of t_{mean} is estimated by $\frac{\sigma_t}{\sqrt{N}}$, where N is the total number of events.

According to Sec. A.1, I use the S_i as the MC acceptance corrected SG number, because Fig. 5.8(b) shows a slight acceptance difference between $K^\pm K^\mp$ and $K^\mp\pi^\pm$. Thus, from Eq. 1.57 and Eq. A.8, I estimate $\Delta\gamma_{\text{mean1}}$ as shown in Fig. 5.10.

I generated the MC with $\tau_{K\pi} = 0.415$ ps [PDG94] (also from Table 5.2, the MC generated lifetime is closer to the measured value of τ_{KK}), so following the discussion in Sec. A.2 and Sec. A.3, I should use Eq. A.19 (not Eq. A.21) to estimate the $\Delta\gamma_{\text{mean2}}$ in Fig. 5.10. Here the S_i and σ_t are not MC acceptance corrected. The correction factor is obtained from the ratios of two MC mean values of the same τ_{KK} lifetime as shown in Eq. A.19. Table 5.3 summarizes the results of the $\Delta\gamma$ approximation by mean value difference methods. The difference between t_{mean1} and t_{mean2} is due to whether the MC acceptance correction is applied or not.

5.2.2 Unbinned 2-Dimensional Maximum Likelihood Fit. In this section, I focus on the $D^0 \rightarrow K^-\pi^+$ case, in order to confirm that the binned reduced proper time method described in Sec. 5.2.1 is adequate.

One can construct the probability distribution function (p.d.f.) for the i^{th} $K^\mp\pi^\pm$ candidate as

$$\begin{aligned} \mathcal{P}(m_i, t_i | \text{par}(1 : 9)) = & \\ & r_0 \cdot \text{Gauss}(m_i, md0, wd0) \cdot \frac{1}{\tau_0} e^{-\frac{t_i}{\tau_0}} + \\ & (1 - r_0) \cdot \text{Lin}(m_i, bgh, bgs) \cdot \text{Lint}(t_i, \tau_{b1}, bgc, \tau_{b2}) \end{aligned} \quad (5.6)$$

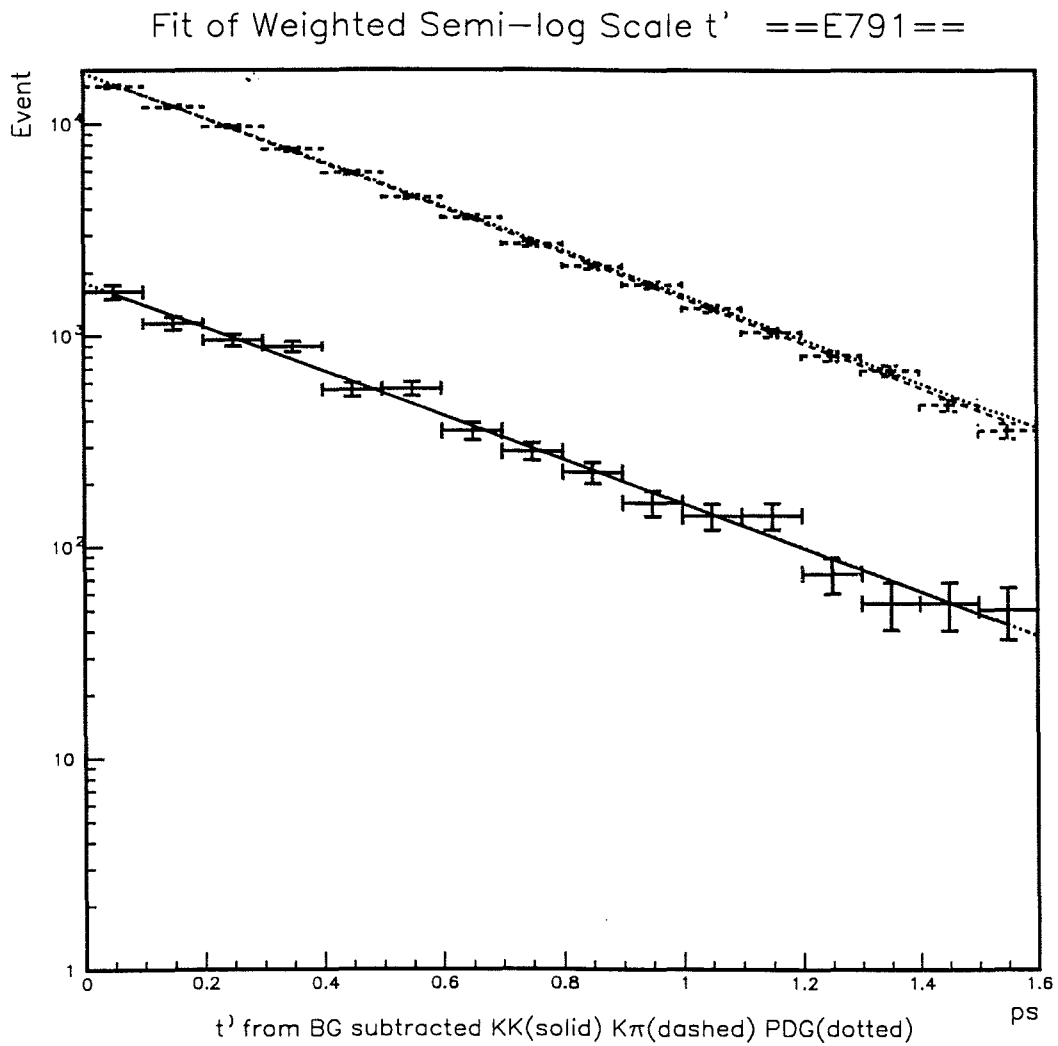


Figure 5.9. A Semi-log Scale Plot of Fig. 5.10:

The solid line is $K^\pm K^\mp$; the dashed line is $K^\mp \pi^\pm$; and the dotted line is from PDG'94 $\tau_{K\pi}$ lifetime.

Fit of ID Weighted and Acceptance Corrected $t' = E791 =$

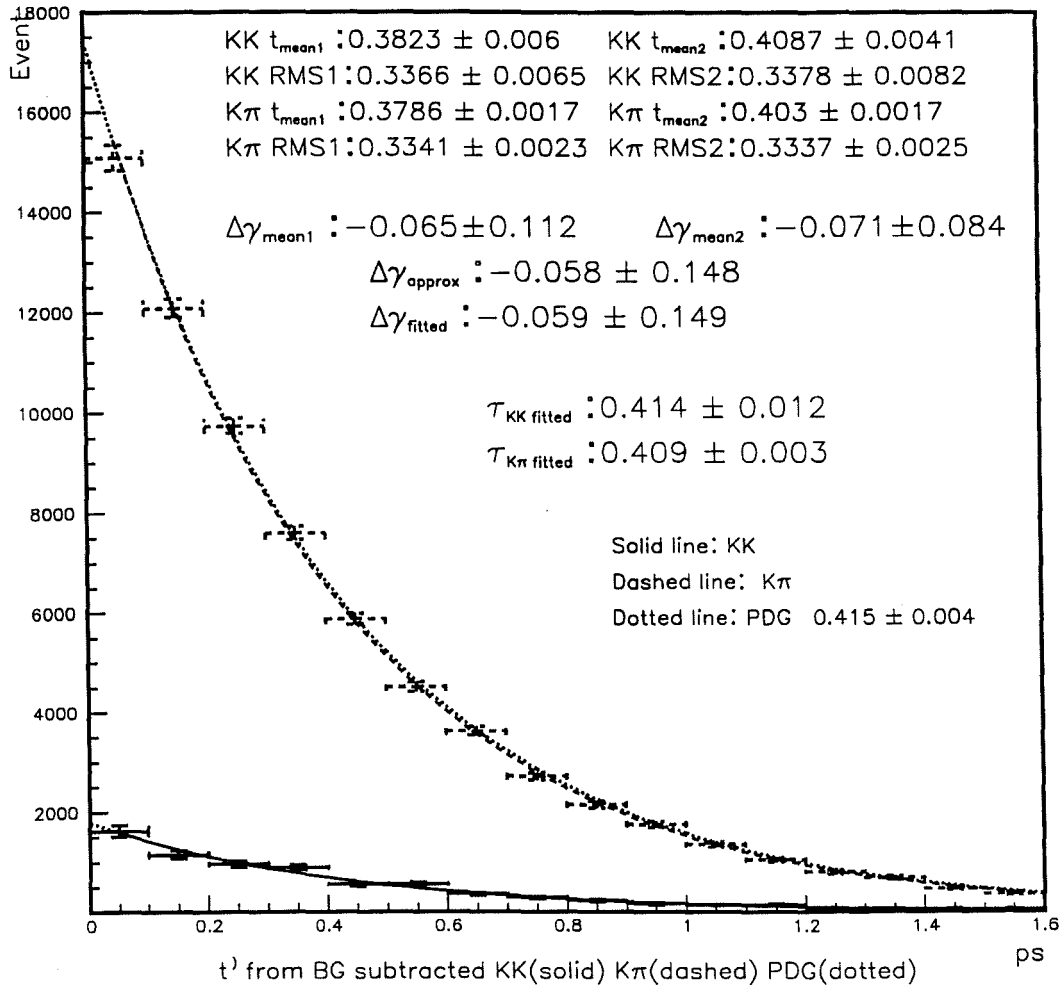


Figure 5.10. Fitting Results for $\Delta\gamma$ Using Different Approaches:

The solid line is $K^\pm K^\mp$; the dashed line is $K^\mp \pi^\pm$; and the dotted line is from PDG'94 $K^\mp \pi^\pm$ lifetime.

t_{mean} shows the mean values described in Appendix A. The left portion of t_{mean} 's are from the method in Sec. A.1, and the right portion is from Sec. A.2. The results of the maximum likelihood fit are shown.

Table 5.3. Binned $\Delta\gamma$ Mean Value (Statistical Error Only)

Method	Value	Mode	E791 Data
Sec. A.1	t_{mean1}	$K^\pm K^\mp$	0.3821 ± 0.0060
		$K^\mp \pi^\pm$	0.3786 ± 0.0017
	RMS1	$K^\pm K^\mp$	0.3362 ± 0.0060
		$K^\mp \pi^\pm$	0.3342 ± 0.0023
	$\Delta\gamma_{\text{mean1}}$	—	-0.063 ± 0.112
Sec. A.2	t_{mean2}	$K^\pm K^\mp$	0.4086 ± 0.0041
		$K^\mp \pi^\pm$	0.4030 ± 0.0017
	RMS2	$K^\pm K^\mp$	0.3374 ± 0.0077
		$K^\mp \pi^\pm$	0.3337 ± 0.0025
	MC correction factor	0.40729/0.40898	
	$\Delta\gamma_{\text{mean2}}$	—	-0.068 ± 0.083

where

$$Gauss(m_i, md0, wd0) = \frac{\frac{1}{wd0\sqrt{2\pi}} e^{-\frac{1}{2}(\frac{m_i - md0}{wd0})^2}}{\int_{m1}^{m2} (\frac{1}{wd0\sqrt{2\pi}} e^{-\frac{1}{2}(\frac{m - md0}{wd0})^2}) dm},$$

$$Lin(m_i, bgh, bgs) = \frac{bgh + bgs \cdot (m_i - 2.0)}{\int_{m1}^{m2} (bgh + bgs \cdot (m - 2.0)) dm},$$

$$Lint(t_i, \tau_{b1}, bgc, \tau_{b2}) = \frac{e^{-\frac{t_i}{\tau_{b1}}} + bgc \cdot e^{-\frac{t_i}{\tau_{b2}}}}{\int_{t1}^{t2} (e^{-\frac{t}{\tau_{b1}}} + bgc \cdot e^{-\frac{t}{\tau_{b2}}}) dt}.$$

Each $\mathcal{P}(m_i, t_i)$ for a single event has 2 contributions: (1) the signal of a Gaussian mass term with a single exponential decay term, and (2) the combinatoric linear term with a double-exponential decay term. Each term is normalized to the mass interval $(m1, m2)$ of $1.77 - 1.95 \text{ GeV}/c^2$ and the time interval $(t1, t2)$ of $0.0 - 1.6 \text{ ps}$.

The 9 parameters are

- $r_0, md0, wd0$, and τ_0 – fraction, Gaussian peak, width and lifetime of the signal,
- $bgh, bgs, \tau_{b1}, \tau_{b2}$, and bgc – height, slope, 1st, 2nd, and coefficients for the two lifetimes of the linear BG.

There is thus a 2-D 9-parameter p.d.f. for each event. Because each observation is independent of the others, the likelihood function (LF), or the joint probability of all observations, is

$$\mathcal{L}(m, t \mid \text{par}(1 : 9)) \equiv \prod_{i=1}^N \mathcal{P}(m_i, t_i \mid \text{par}(1 : 9)). \quad (5.7)$$

But recall that in order to use the MC acceptance function $A(t)$ properly, I need to correct the Čerenkov efficiency by weighting w_i for each event. So the LF is then [Frodesen]

$$\mathcal{L}(m, t \mid \text{par}(1 : 9)) \equiv \prod_{i=1}^N (\mathcal{P}(m_i, t_i \mid \text{par}(1 : 9)))^{w_i}. \quad (5.8)$$

The reason for putting w_i in as a power is that the model of $\mathcal{P}(m, t)$ is based on unbiased prediction and detection (the ideal Gaussian mass term and the ideal exponential decay term), but it is necessary to account for the reciprocal of detection probability due to the Čerenkov ID cut. If at a value of (m_i, t_i) one observes one candidate, there should have been a total of w_i similar candidates, having the same $\mathcal{P}(m_i, t_i)$. The product of all these w_i candidates of $\mathcal{P}(m_i, t_i)$ is equivalent to applying the weight as a power. The Čerenkov efficiency correction does not depend on mass or decay time — SG and BG could have the same Čerenkov efficiency correction (weighting), as described in Sec. 5.2.1.

A similar argument could be applied to the correction of the acceptance function $A(t)$. The LF would be

$$\mathcal{L}(m, t \mid \text{par}(1 : 9)) \equiv \prod_{i=1}^N (\mathcal{P}(m_i, t_i \mid \text{par}(1 : 9)))^{w_i \cdot A^{-1}(t_i)}. \quad (5.9)$$

But I extract the continuous (unbinned) acceptance function from the MC study using a chosen SG region. In other words, I assume that the acceptance function does not depend strongly on mass. It may not be sufficient to assume that the BG

has the same acceptance nor to apply the acceptance correction on both the SG term and the BG term. Thus, I model $A(t)$ into the SG decay function in new $\mathcal{P}'(m, t)$ as

$$\begin{aligned}\mathcal{P}'(m_i, t_i | \text{par}(1 : 9)) = \\ r_0 \cdot \text{Gauss}(m_i, md0, wd0) \cdot AE(t_i, \tau_0) + \\ (1 - r_0) \cdot \text{Lin}(m_i, bgh, bgs) \cdot \text{Lint}(t_i, \tau_{b1}, bgc, \tau_{b2}).\end{aligned}\quad (5.10)$$

where the new normalized SG reduced proper time probability is

$$AE(t_i, \tau_0) = \frac{A(t_i) \cdot e^{-\frac{t_i}{\tau_0}}}{\int_{t1}^{t2} A(t) \cdot e^{-\frac{t}{\tau_0}} dt}.$$

The new LF is then

$$\mathcal{L}'(m, t | \text{par}(1 : 9)) \equiv \prod_{i=1}^N (\mathcal{P}'(m_i, t_i | \text{par}(1 : 9)))^{w_i}. \quad (5.11)$$

Applying the log-likelihood method — the product Π changes into a summation Σ , and the power w_i becomes a coefficient in front of each $(\log \mathcal{P}'(m_i, t_i))$ term; the log-likelihood function (LLF) is:

$$-\log \mathcal{L}'(m, t | \text{par}(1 : 9)) = -\sum_{i=1}^N w_i \cdot \log(\mathcal{P}'(m_i, t_i | \text{par}(1 : 9))). \quad (5.12)$$

where the extra negative sign is necessary for the minimizing program MINUIT [MINUIT].

MINUIT calculates errors by assuming that the LLF is distributed as a Gaussian near the minimum, and that the LLF can be approximated as a parabolic shape. The variance matrix of n parameters is approximated as

$$V(n \times n) = H^{-1}, \quad (5.13)$$

with

$$H_{jk} = -\frac{\partial^2 \log \mathcal{L}}{\partial \theta_j \partial \theta_k}. \quad (5.14)$$

In my weighted LLF, this method obviously underestimates the error, for all $w_i > 1$.

I can reduce every w_i into w'_i by a common factor, e.g. the average weight. Note that rescaling w'_i results in a $\log \mathcal{L}'$ of order similar to the unweighted $\log \mathcal{L}$; each w'_i is just a coefficient in front of $\log(\mathcal{P}'(m_i, t_i))$, so rescaling w'_i does not alter any parameter at the minimum. Then the weighted errors estimated by MINUIT are of the same order as unweighted errors. I can then approximate the rescaled weighted error by multiplying by the “spread” of weights[†],

$$\frac{\sqrt{\sum_i^N w_i^2} / (\sum_i^N w_i)^2}{1/\sqrt{N}}. \quad (5.15)$$

If all the weights were the same, the spread would be 1.

Table 5.4 lists the unbinned maximum likelihood fit results. It shows good agreement with the binned method (refer to Sec. 5.2.1). The small difference could be interpreted as a systematic uncertainty due to the binned method.

5.3 CP Asymmetry

Recall Eq.(1.66) and Eq.(1.67):

$$A_{\text{CP}}^{\text{BR}}(K^\pm K^\mp) = \frac{\frac{N(D^{*+} \rightarrow (D^0 \rightarrow K^+ K^-) \pi^+)}{N(D^{*+} \rightarrow (D^0 \rightarrow K^- \pi^+) \pi^+)} - \frac{N(D^{*-} \rightarrow (\bar{D}^0 \rightarrow K^- K^+) \pi^-)}{N(D^{*-} \rightarrow (\bar{D}^0 \rightarrow K^+ \pi^-) \pi^-)}}{\frac{N(D^{*+} \rightarrow (D^0 \rightarrow K^+ K^-) \pi^+)}{N(D^{*+} \rightarrow (D^0 \rightarrow K^- \pi^+) \pi^+)} + \frac{N(D^{*-} \rightarrow (\bar{D}^0 \rightarrow K^- K^+) \pi^-)}{N(D^{*-} \rightarrow (\bar{D}^0 \rightarrow K^+ \pi^-) \pi^-)}} \\ A_{\text{CP}}^{\text{BR}}(\pi^\pm \pi^\mp) = \frac{\frac{N(D^{*+} \rightarrow (D^0 \rightarrow \pi^+ \pi^-) \pi^+)}{N(D^{*+} \rightarrow (D^0 \rightarrow K^- \pi^+) \pi^+)} - \frac{N(D^{*-} \rightarrow (\bar{D}^0 \rightarrow \pi^- \pi^+) \pi^-)}{N(D^{*-} \rightarrow (\bar{D}^0 \rightarrow K^+ \pi^-) \pi^-)}}{\frac{N(D^{*+} \rightarrow (D^0 \rightarrow \pi^+ \pi^-) \pi^+)}{N(D^{*+} \rightarrow (D^0 \rightarrow K^- \pi^+) \pi^+)} + \frac{N(D^{*-} \rightarrow (\bar{D}^0 \rightarrow \pi^- \pi^+) \pi^-)}{N(D^{*-} \rightarrow (\bar{D}^0 \rightarrow K^+ \pi^-) \pi^-)}}$$

[†]Private communication from Dr. M. Purohit.

Table 5.4. Result of Unbinned 2-D Maximum Likelihood Fit

Number	Parameter	$D^0 \rightarrow K^- \pi^+$ mode
1	md0	1.86668 ± 0.00009
2	wid0	0.01342 ± 0.00009
3	rat0	0.2612 ± 0.0016
4	bgh	0.118 ± 0.0462
5	bgs	-0.84 ± 0.33
* 6 *	τ_0	0.4083 ± 0.0028
7	τ_{b1}	0.3928 ± 0.0025
8	bgc	2.74 ± 0.042
9	τ_{b2}	0.0619 ± 0.0009
Average Weight and Spread for $D^0 \rightarrow K^- \pi^+$ in mass window 1.77 – 1.95 GeV/c ²		
Average Weight		1.614
Weight Spread		1.072

where N stands for the observed SG number after BG-subtraction, decay is assigned to D^0 or \bar{D}^0 by using the charge of the bachelor π^\pm of $D^{*\pm} \rightarrow D^0(\bar{D}^0)\pi^\pm$ tagging, and the normalization to the $D^0 \rightarrow K^- \pi^+$ and $\bar{D}^0 \rightarrow K^+ \pi^-$ modes is necessary to correct for the asymmetry from D^0 and \bar{D}^0 productions. The corrections from geometry and cut efficiency are not necessary in $A_{\text{CP}}^{\text{BR}}$, because they all are cancelled out by the normalization denominators. For instance, the inefficiency of the slow π^+ detection would be cancelled out by $\frac{N(D^{*+} \rightarrow (D^0 \rightarrow K^+ K^-) \pi^+)}{N(D^{*+} \rightarrow (D^0 \rightarrow K^- \pi^+) \pi^+)}$, and the detection bias of charges would be cancelled out by the 2-opposite-charge-pseudoscalar decays. As a check, I also measure the CP asymmetry of the $D^0 \rightarrow K^- \pi^- \pi^+ \pi^+$ mode, which is a CFD, and $A_{\text{CP}}^{\text{BR}}(K3\pi)$ should be consistent with zero if there is no direct CP in CFD. $A_{\text{CP}}^{\text{BR}}(K3\pi)$ is designed to support our measurements on $A_{\text{CP}}^{\text{BR}}(K^\pm K^\mp)$ and $A_{\text{CP}}^{\text{BR}}(\pi^\pm \pi^\mp)$, in case of being non-zero.

In order to carry out proper comparisons between D^0 and \bar{D}^0 , I again fix the same widths for fitting both D^0 and \bar{D}^0 mass plots, using widths from the combined D^0 and \bar{D}^0 mass plots in 4 decay modes. Fig. 5.11 and Fig. 5.12 are the result of fitting mass plots.

CP Asymmetry, $A_{CP}^{BR} = E791$

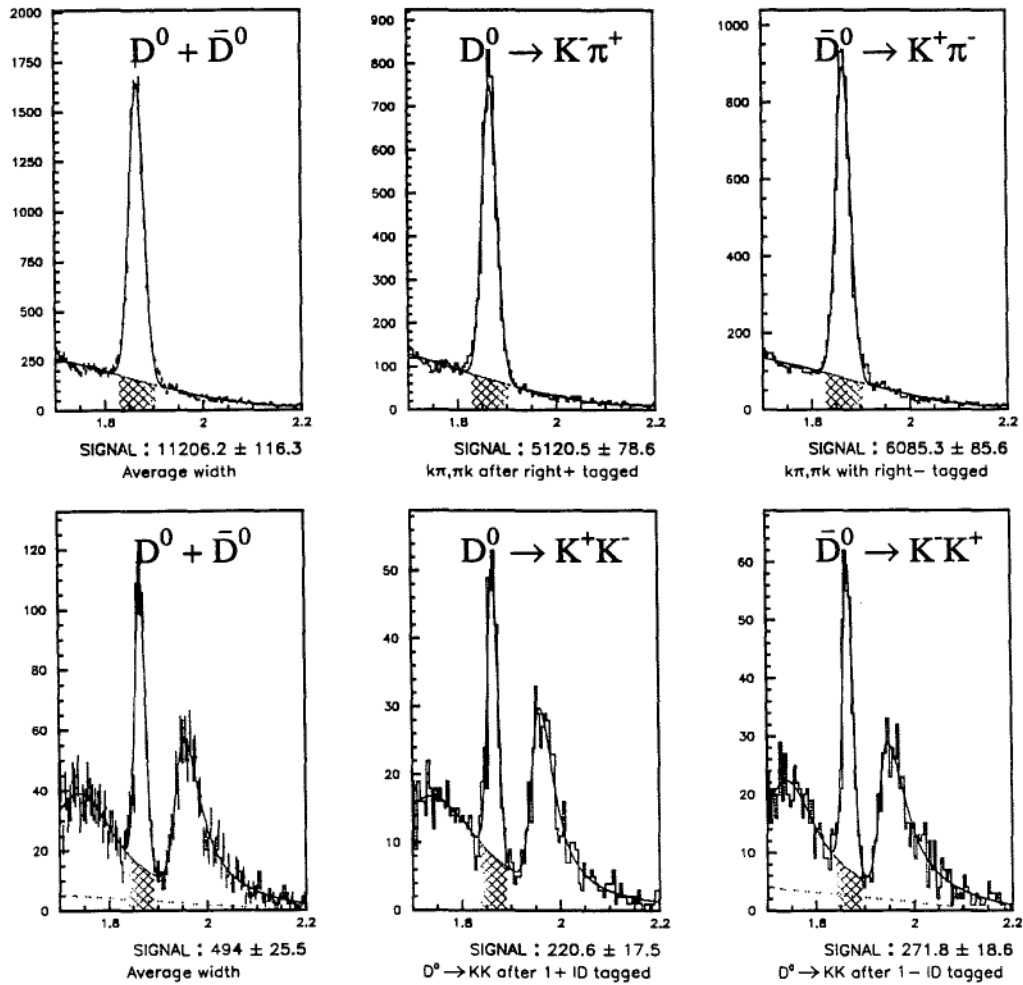


Figure 5.11. A_{CP}^{BR} Study of DATA Plots for $K^\mp \pi^\pm$ and $K^\pm K^\mp$:

Tagged D^0 and \bar{D}^0 are combined to get "average" widths which are later fixed to fit individual D^0 and \bar{D}^0 .

CP Asymmetry, $A_{CP}^{BR} = E791$

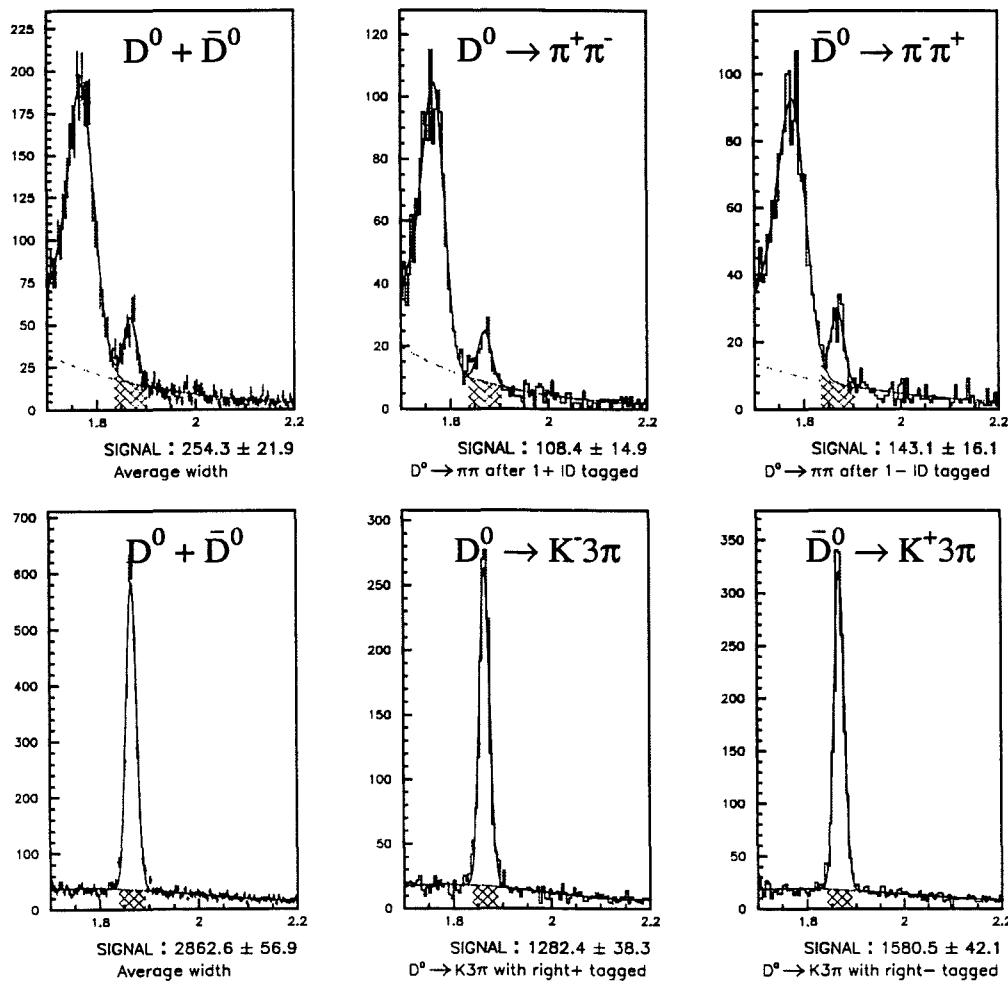


Figure 5.12. A_{CP}^{BR} Study of DATA Plots for $\pi^\pm\pi^\mp$ and $K3\pi$:

Tagged D^0 and \bar{D}^0 are combined to get "average" widths which are later fixed to fit individual D^0 and \bar{D}^0 .

Note that in this CP asymmetry study, there is no MC involved, eliminating any uncertainty due to the MC simulation. Also, because they are all $D^0 \rightarrow PP$ (pseudoscaler), the decay products of D^0 and \bar{D}^0 are isotropic with no polarization in space. Thus, the detector asymmetry between positive charge and negative charge has very little effect on our result. The asymmetry of the bachelor π^+ (π^-) tagging is cancelled out by using $D^0 \rightarrow K^-\pi^+$ ($\bar{D}^0 \rightarrow K^+\pi^-$) for normalization.

Table 5.5 lists the results of $A_{CP}^{BR}(K^\pm K^\mp)$, $A_{CP}^{BR}(\pi^\pm \pi^\mp)$ and $A_{CP}^{BR}(K3\pi)$. Also, I translate the results into 90 % confidence level (C.L.) upper limits[†]. All measurements are consistent with zero.

Table 5.5. A_{CP}^{BR} (Statistical Error Only)

Decay Mode	A_{CP}^{BR}	Upper Limit at 90% Confidence Level
$A_{CP}^{BR}(K^\pm K^\mp)$	-0.018 ± 0.054	$-10.7\% < A_{CP}^{BR} < 7.1\%$
$A_{CP}^{BR}(\pi^\pm \pi^\mp)$	-0.052 ± 0.093	$-20.6\% < A_{CP}^{BR} < 10.1\%$
$A_{CP}^{BR}(K3\pi)$	-0.018 ± 0.023	$-5.6\% < A_{CP}^{BR} < 1.9\%$

[†]By using central value $\pm 1.64 \times$ statistical error

CHAPTER VI

SYSTEMATIC ERROR

In the following sections, I will describe the systematic error arising from the different assumptions or techniques used in the analysis, and the systematic error will be estimated as a fraction relative to the statistical errors.

6.1 Uncertainty Due to Fitting Functions

Some studies from other experiments, such as the study of A_{CP} , rely on a MC to estimate the BG (using the BR from previous measurement), and then do the BG subtraction to eliminate reflections, leading to only a linear BG remaining. But this assumption uses the previous measurement of BR to generate the MC for all possible modes. Obviously, this kind of BG-subtraction is not an appropriate technique for studying BR itself. Instead, I rely on fitting functions to estimate the BG shape. To include the systematic error from the choice of the fitting functions, I have compared several possible choices and choose the function with the lowest χ^2 as my analysis fitting function as described in Sec. 4.4. I estimate the systematic errors from the deviations produced by other fitting functions.

Plot (a) in Fig. 6.1, Fig. 6.2, and Fig. 6.3 is my analysis fitting function. Other fitting functions with larger χ^2 are illustrated as plots (b), (c), and etc.

I conclude that in terms of the statistical error σ , the systematic errors due to the uncertainty of fitting function choices are (1) $\pm 0.50\sigma$ for $N(D^0 \rightarrow \pi^+\pi^-)$, (2) $\pm 0.50\sigma$ for $N(D^0 \rightarrow K^+K^-)$, and (3) $\pm 1.50\sigma$ for $N(D^0 \rightarrow K^-\pi^+)$. These conditions lead to (1) $\pm 0.50\sigma$ for $\frac{\Gamma(D^0 \rightarrow \pi^+\pi^-)}{\Gamma(D^0 \rightarrow K^-\pi^+)}$, (2) $\pm 0.50\sigma$ for $\frac{\Gamma(D^0 \rightarrow K^+K^-)}{\Gamma(D^0 \rightarrow K^-\pi^+)}$, and (3) $\pm 0.40\sigma$ for $\frac{\Gamma(D^0 \rightarrow K^+K^-)}{\Gamma(D^0 \rightarrow \pi^+\pi^-)}$.

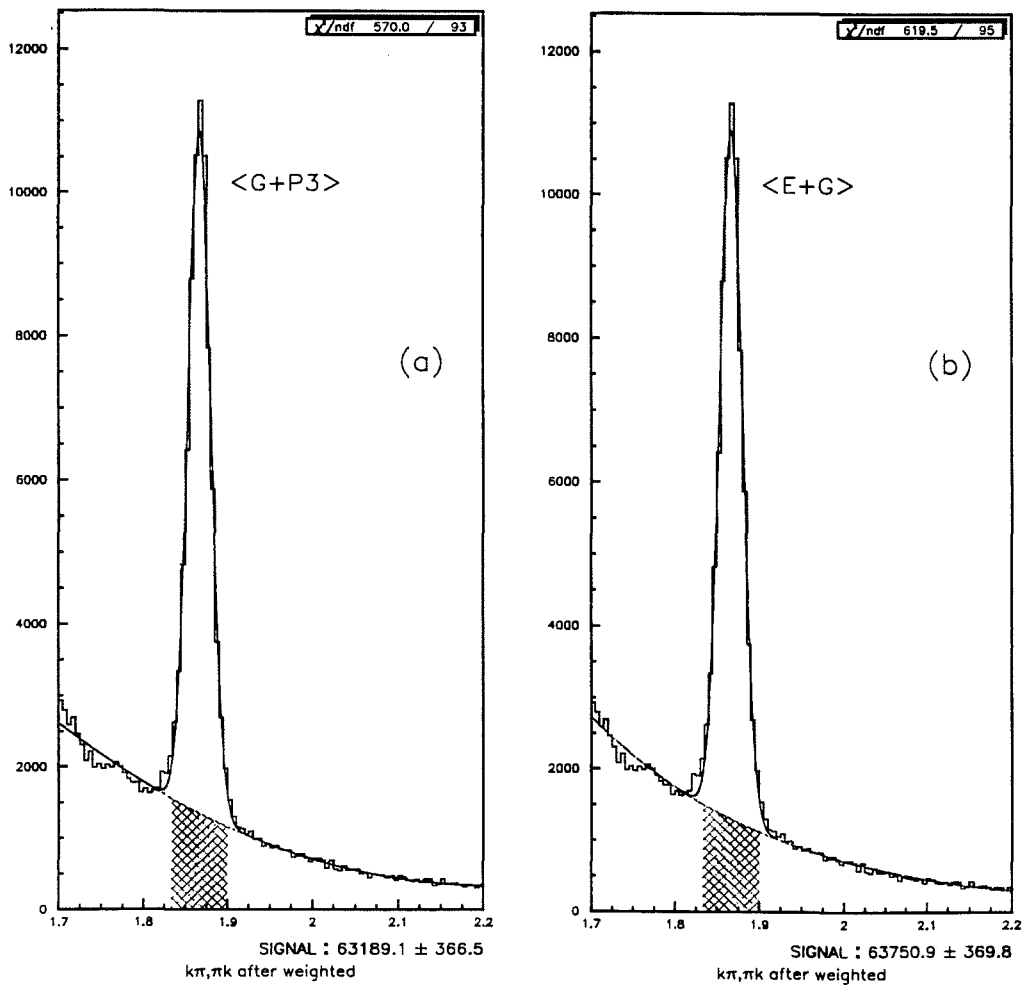
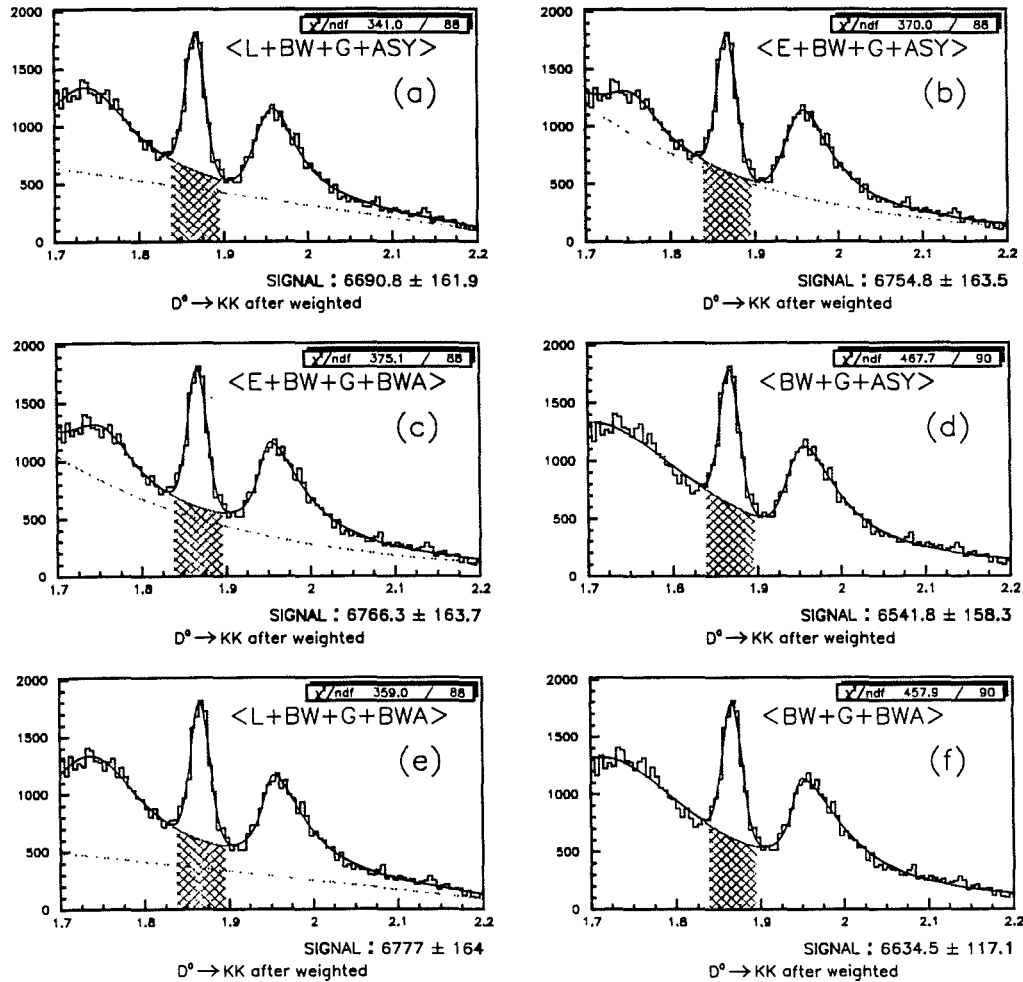
Fitting Function Comparison $K\pi^{\pm} \Rightarrow E791 \Rightarrow$ 

Figure 6.1. Systematic Study of Different Fitting Functions for $K^{\mp}\pi^{\pm}$:
 (a) $\langle G + P3 \rangle$ (Gaussian + 3rd-order-polynomial) with the lower χ^2 ;
 (b) $\langle E+G \rangle$ with an Exponential BG gives $(b)/(a) = 1.01$, which is the systematic error due to the choice of fitting function.

Fitting Function Comparison for $KK \Rightarrow E791 \Rightarrow$ Figure 6.2. Systematic Study of Different Fitting Functions for $K^\pm K^\mp$:

- (a) $\langle L + BW + G + ASY \rangle$ with the lowest χ^2 ;
- (b) $\langle E + BW + G + ASY \rangle$ with an exponential BG, reasonable, and (b)/(a) = 1.01 will be used to estimate the systematic error due to the choice of fitting function;
- (c) $\langle E + BW + G + BWA \rangle$ ($E + BW + G + \text{Half-BW-Half-BW}$) gives (c)/(a) = 1.01;
- (d) $\langle BW + G + ASY \rangle$ is ignored, so is (f); but
- (e) yields (e)/(a) = 1.01.

Fitting Function Comparison for $\pi\pi \Rightarrow E791 \Rightarrow$

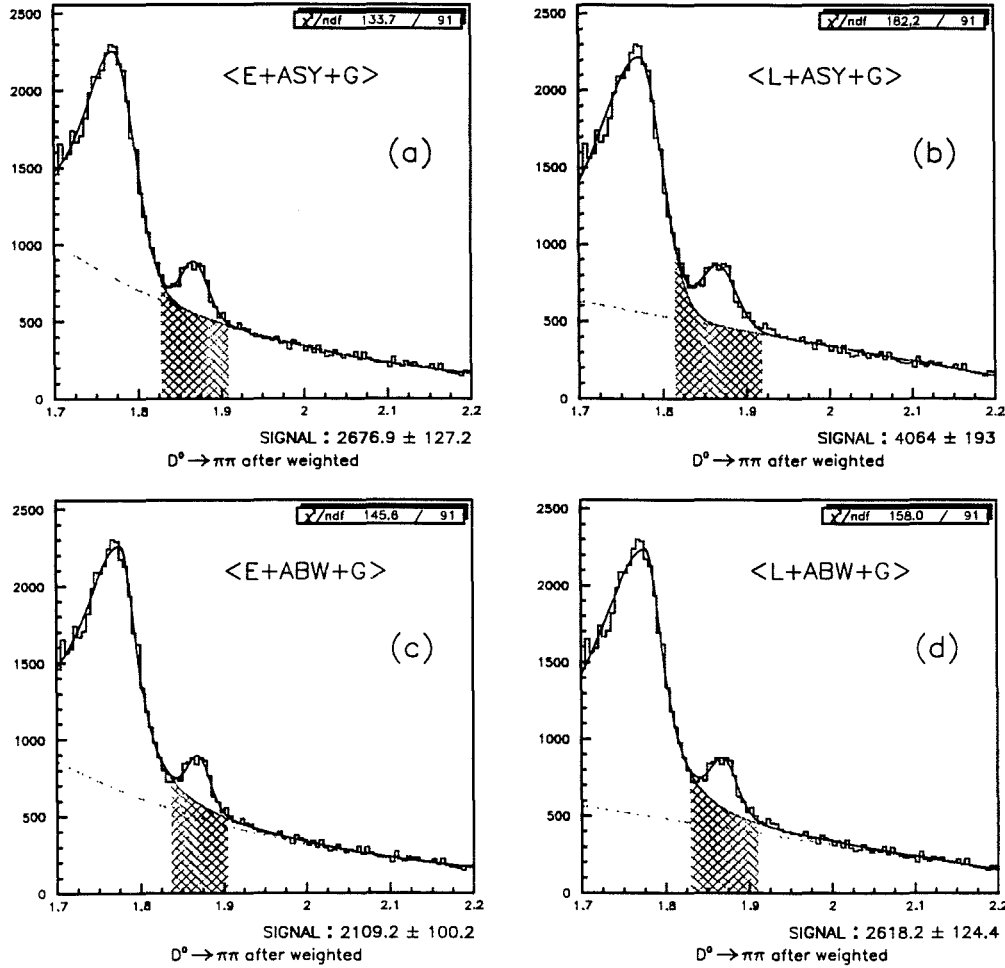


Figure 6.3. Systematic Study of Different Fitting Functions for $\pi^\pm\pi^\mp$:

- (a) $\langle E+ASY+G \rangle$ (Exponential + Half-G-Half-BW + Gaussian) with the lowest χ^2 ;
- (b) $\langle L+ASY+G \rangle$ with linear BG, discarded;
- (c) $\langle E+ABW+G \rangle$ (E + Half-BW-Half-BW + G) unlikely, but (c)/(a) = 0.79;
- (d)/(a) = 0.98 will be used to estimate the systematic error due to the choice of fitting function.

6.2 Uncertainty Due to Weighting

After Čerenkov ID cuts are applied, and in order to correct for the Čerenkov ID cut efficiency, I apply weights to each surviving vertex. I estimate the error of the weight according to Eq. (5.4):

$$w \pm \Delta w = \frac{1}{[E_{\check{C}}(C_1, p_1) \pm \Delta E_1] \times [E_{\check{C}}(C_2, p_2) \pm \Delta E_2]} \quad (6.1)$$

where C_i and p_i are the charge and the momentum of tracks $i = 1, 2$.

But the Δw has not been propagated into the weighted analysis. Therefore I randomly (according to a Gaussian random (\mathcal{GR}) number generator) vary the individual weight as:

$$w' = w + \Delta w \cdot \mathcal{GR}(), \quad (6.2)$$

where $\mathcal{GR}()$ generates a random number from $-\infty$ to ∞ according to the probability of a Gaussian distribution with 0 center and $\sigma = 1$.

The basic idea here is to randomly apply a weight to each candidate entry, then to see the gross variation of the final values, e.g. fitted BG-subtracted SG number. Thus, I define the residual as

$$r_i = \frac{S_i - S_0}{S_0}, \quad (6.3)$$

where S_0 is the SG number without any random weighting, and the S_i is the random weight, $i = 1 - 2000$, in my study.

Each vertex calls $\mathcal{GR}()$ in a loop of 2000 calls to produce high statistics; in other words, the total $\mathcal{GR}()$ calls are (total vertices \times 2000). I calculate r_i by fitting 2000 plots similar to Fig. 5.2 to get 2000 different fitted SG number for each decay mode. Fig. 6.4 shows the distribution of residuals for 3 decay modes. The Gaussian distributed residuals in Fig. 6.4 consist of:

- the uncertainty of random weights on the SG number (*i.e.* the residual Gaussian σ in Fig. 6.4): The small values of the residual σ 's (e.g., Fig. 6.4(a)) arises from the fact that each vertex, SG or BG, can fluctuate the histograms on Fig. 5.2 in the same manner, so that even relatively large variations in random weights (refer to Fig. 4.8) produce a small difference in the fitted distributions.
- the goodness of fit (the offset of the mean from 0): The tiny shift in the residual mean for $\pi^\pm\pi^\mp$ seen in Fig. 6.4(c) may be explained by the observation that fitting an exponential BG is quite unstable, because we only have one sideband for the $\pi^\pm\pi^\mp$ mode (see Fig. 5.2).[†]

I include both the σ 's and mean offsets from Fig. 6.4 as the systematic error due to both weighting and fitting.

I conclude that in terms of the statistical error σ , the systematic errors due to the uncertainty of Čerenkov correction weighting are (1) $\pm 0.069\sigma$ for $N(D^0 \rightarrow \pi^+\pi^-)$, (2) $\pm 0.0118\sigma$ for $N(D^0 \rightarrow K^+K^-)$, and (3) $\pm 0.067\sigma$ for $N(D^0 \rightarrow K^-\pi^+)$. These conditions lead to (1) $\pm 0.05\sigma$ for $\frac{\Gamma(D^0 \rightarrow \pi^+\pi^-)}{\Gamma(D^0 \rightarrow K^-\pi^+)}$, (2) $\pm 0.10\sigma$ for $\frac{\Gamma(D^0 \rightarrow K^+K^-)}{\Gamma(D^0 \rightarrow K^-\pi^+)}$, and (3) $\pm 0.06\sigma$ for $\frac{\Gamma(D^0 \rightarrow K^+K^-)}{\Gamma(D^0 \rightarrow \pi^+\pi^-)}$.

There is no Čerenkov correction in the A_{CP}^{BR} study. For the lifetime difference, I check by fitting two lifetimes without the Čerenkov ID cut.[‡] Fig. 6.5 illustrates $D^0 \rightarrow K^+K^-$ without ID cuts in 16 bins of reduced proper time, and Fig. 6.6 illustrates the semi-log scale of fitting slopes. Table 6.1 lists the results with no ID cut (*i.e.* no weighting).

[†]Keeping all conditions the same, except fixing the same SG Gaussian width for 2000 fits, Fig. 6.4(c) shows a residual plot of double peaks. The fitting condition is the only factor which results in such double peaks.

[‡]The main reason to apply Čerenkov ID cut for the final result is to optimize statistical significance, *i.e.* to minimize fractional error.

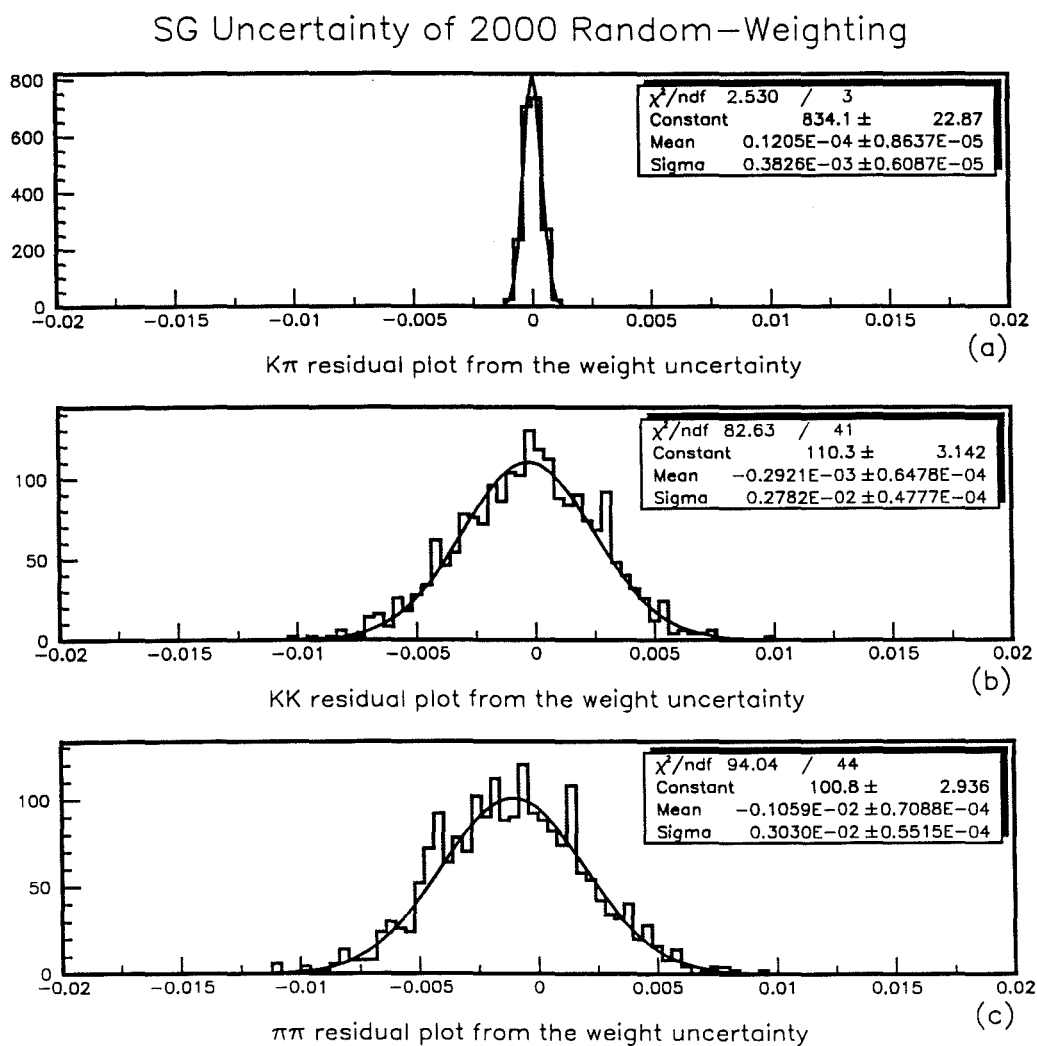


Figure 6.4. The Uncertainty of SG Numbers from Randomized Weighting:

(a) $K^\mp\pi^\pm$, (b) $K^\pm K^\mp$, and (c) $\pi^\pm\pi^\mp$.

The quadrature of offset and Gaussian width is the systematic error due to combined weighting and fitting.

Table 6.1. Binned Method Lifetime (No ID Cut or Weighting)

Method	Mode	Binned lifetime measurement
Binned-likelihood	τ_{KK}	0.417 ± 0.018
	$\tau_{K\pi}$	0.409 ± 0.003
Eq. A.8	$\Delta\gamma_{\text{mean1}}$	-0.123 ± 0.113
Eq. A.19	$\Delta\gamma_{\text{mean2}}$	-0.156 ± 0.087
Eq. 1.57	$\Delta\gamma_{\text{approx}}$	-0.091 ± 0.141
Eq. 1.55	$\Delta\gamma_{\text{fitted}}$	-0.092 ± 0.140

Comparing Table 6.1 with Table 5.2 and Table 5.3, I conclude that in terms of the statistical error σ , the systematic errors due to Čerenkov correction weighting are (1) $\pm 0.25\sigma$ for τ_{KK} , (2) 0.00σ for $\tau_{K\pi}$, (3) $\pm 0.25\sigma$ for $\Delta\gamma_{\text{fitted}}$ and (4) $\pm 0.60\sigma$ and $\pm 1.00\sigma$ for $\Delta\gamma_{\text{mean1}}$ and $\Delta\gamma_{\text{mean2}}$, respectively.

6.3 Uncertainty Due to Cuts

The basic idea here is to vary the cuts and then to see the effect of such variations on the final result, e.g. BR, A_{CP} , and $\Delta\gamma$. Using the analysis cuts arrived at in Chapter V as starting values, I vary each cut one at a time, for example, PT2DK from 0.47 to 0.92. Each varied cut is applied to MC and DATA, and run through the same fitting and analysis procedure. This method thus probes the combined uncertainty of cuts in MC and DATA.

Table 6.2 lists the various cuts numbered with an index used in Fig 6.7 to Fig 6.9:

- 0 is the analysis set of cuts;
- 1 is the value from PDG'94 or previous data for comparison;
- 2–7 demonstrate variations of the ASYM cuts;
- 8–12 demonstrate variations of the DIP cuts;

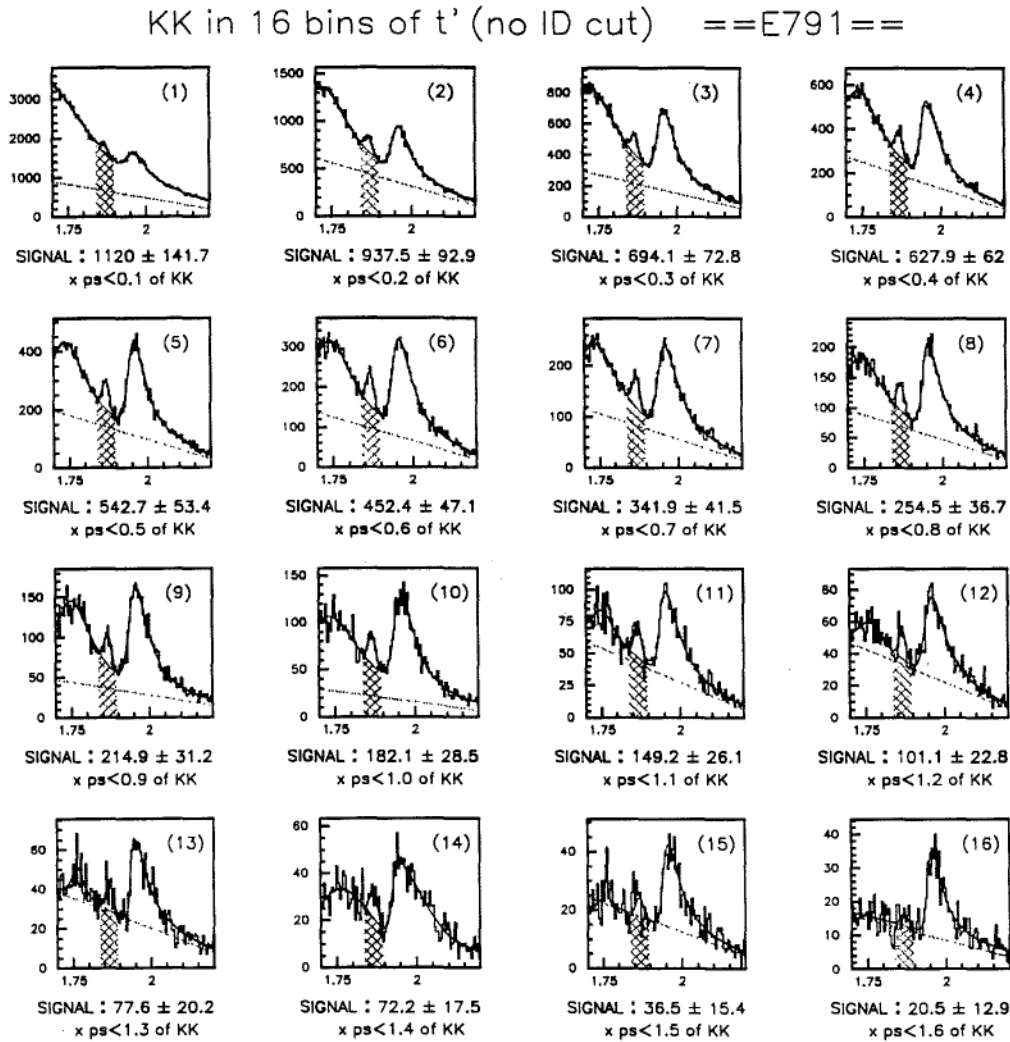


Figure 6.5. BG Subtraction from $D^0 \rightarrow K^+ K^-$ (Without ID Cut) Invariant Mass Plots in 16 Bins of Reduced Proper Time.

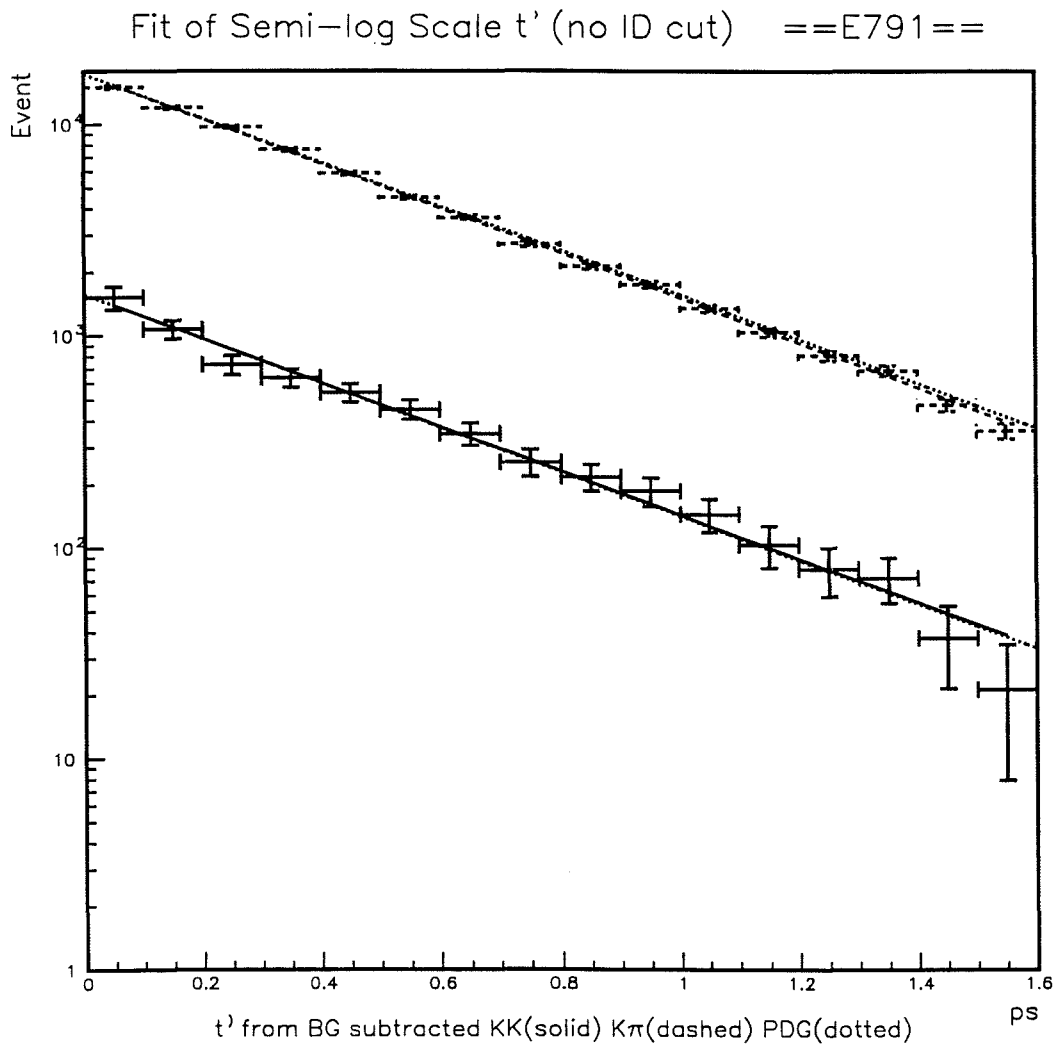


Figure 6.6. A Semi-log Scale Plot of Fitting Lifetimes (Without ID Cuts):
 The solid line is $K^\pm K^\mp$; the dashed line is $K^\mp \pi^\pm$; and the dotted line is from
 PDG'94 $\tau_{K\pi}$ lifetime.

- 13–22 demonstrate variations of the MNCHV cuts;
- 23–32 demonstrate variations of the PT2DK cuts;
- 33–42 demonstrate variations of the PTBAL cuts;
- 43–50 demonstrate variations of the SDZ cuts;
- 51–54 demonstrate variations of the window of Δm in $D^{*\pm} \rightarrow D^0(\bar{D}^0)\pi^\pm$ tagging; and
- 55–61 demonstrate variations of the IMPACT cut of the slow (bachelor) π^\pm in $D^{*\pm} \rightarrow D^0(\bar{D}^0)\pi^\pm$ tagging.

Table 6.2. List of Cut Variations

Item	Cut Variation (* indicates the placement of the starting values)
0	ASYM < 0.8, (No DIP cut), MNCHV > 6, PT2DK > 0.52, PTBAL < 0.4, SDZ < 8, 0.1430 < Δm < 0.1480, IMPACT < 0.008.
1	PDG'94 or Previous Data
2 – 7	ASYM < 0.50, 0.55, 0.60, 0.65, 0.70, 0.75, *
8 – 12	DIP < 0.002, 0.004, 0.006, 0.008, 0.010, (*)
13 – 22	MNCHV > 5.0, 5.5, *, 6.5, 7.0, 7.5, 8.0, 8.5, 9.0, 9.5, 10.0
23 – 32	PT2DK > 0.42, 0.47, *, 0.57, 0.67, ..., 0.87, 0.92
33 – 42	PTBAL < 0.20, 0.22, 0.24, 0.26, 0.28, 0.30, 0.32, 0.34, 0.36, 0.38, *
43 – 50	SDZ > *, 9, 10, 11, 12, 13, 14, 15, 16
51 – 54	Δm in (0.1425, 0.1485), *, (0.1435, 0.1475), (0.1440, 0.1470), (0.1445, 0.1465)
55 – 63	IMPACT < 0.005, 0.006, 0.007, *, 0.009, 0.010, 0.011, 0.012

Some starting values are placed on an end of a range of variation because these cuts are applied on the previous analysis stages (Strip, Micro-Strip, etc.) and I cannot easily recover the stripped data. Fig B.2 shows the mismatch of DIP cuts between MC and DATA. There is no DIP cut in my analysis, but I still vary DIP cuts to probe the reliability of the MC simulation. The results are illustrated in Fig. 6.7 for BR, Fig. 6.8 for lifetime, Fig. 6.9 for $\Delta\gamma$, and Fig. 6.10 for A_{CP}^{BR} .

The shift in lifetime seen in Fig. 6.8 indicates the inaccuracy of our MC, especially for the calculation of reduced proper decay time from SDZ and PTBAL as defined in Eq. 4.7 and Eq. 4.8. We also see evidence of this from the comparison between MC and DATA in Fig. B.8 to Fig. B.11. The systematic cancellation can be seen in Fig. 6.8 (c) and (d), in terms of the difference or the ratio of two lifetimes. The same percentage on systematic error is assigned to $(\tau_{K\pi} - \tau_{KK})$ and $(\tau_{K\pi}/\tau_{KK})$.

On the other hand, the correlations in Fig. 6.9 are evidence for the consistency of the two different approaches:

- (1) $\Delta\gamma$ from individual lifetime fitting, and
- (2) $\Delta\gamma$ from mean values difference (described in Appendix A).

I conclude that in terms of the statistical error σ , the systematic errors due to the uncertainty of the choices of analysis cuts are (1) $\pm 0.90\sigma$ for $\frac{\Gamma(D^0 \rightarrow K^+ K^-)}{\Gamma(D^0 \rightarrow K^- \pi^+)}$, (2) $\pm 1.00\sigma$ for $\frac{\Gamma(D^0 \rightarrow \pi^+ \pi^-)}{\Gamma(D^0 \rightarrow K^- \pi^+)}$, (3) $\pm 0.40\sigma$ for $\frac{\Gamma(D^0 \rightarrow K^+ K^-)}{\Gamma(D^0 \rightarrow \pi^+ \pi^-)}$, (4) $\pm 1.20\sigma$ for $\frac{\Gamma(D^0 \rightarrow K^- \pi^- \pi^+ \pi^+)}{\Gamma(D^0 \rightarrow K^- \pi^+)}$, (5) $\pm 0.50\sigma$ for τ_{KK} , (6) $\pm 1.0\sigma$ for $\tau_{K\pi}$, (7) $\pm 0.50\sigma$ for $(\tau_{K\pi} - \tau_{KK})$ and $(\tau_{K\pi}/\tau_{KK})$, (8) $\pm 0.50\sigma$ for $\Delta\gamma_{\text{fitted}}$, (9) $\pm 0.80\sigma$ and $\pm 1.00\sigma$ for $\Delta\gamma_{\text{mean1}}$ and $\Delta\gamma_{\text{mean2}}$, respectively; (10) $\pm 0.20\sigma$ for $A_{\text{CP}}^{\text{BR}}(K^\pm K^\mp)$, (11) $\pm 0.30\sigma$ for $A_{\text{CP}}^{\text{BR}}(\pi^\pm \pi^\mp)$, and (12) $\pm 0.10\sigma$ for $A_{\text{CP}}^{\text{BR}}(K3\pi)$.

6.4 Uncertainty Due to Fixed Widths

In the analysis (described in Chapter V), I fix the Gaussian widths for fitting SG numbers in order to both simplify the calculation of the BR for $D^0 \rightarrow \pi^+ \pi^-$ (fix the ratio of MC/DATA), and to improve the comparison of the lifetime measurement (fixed in different decay time bins) and $A_{\text{CP}}^{\text{BR}}$ (fixed in both D^0 and \bar{D}^0). Thus varying the common widths is the main technique of this systematic study.

1 PDG, 2-7 ASYM, 8-12 DIP, 13-22 MNCHV, 23-32 PT2DK, 33-42 PTBAL, 43-50 SDZ

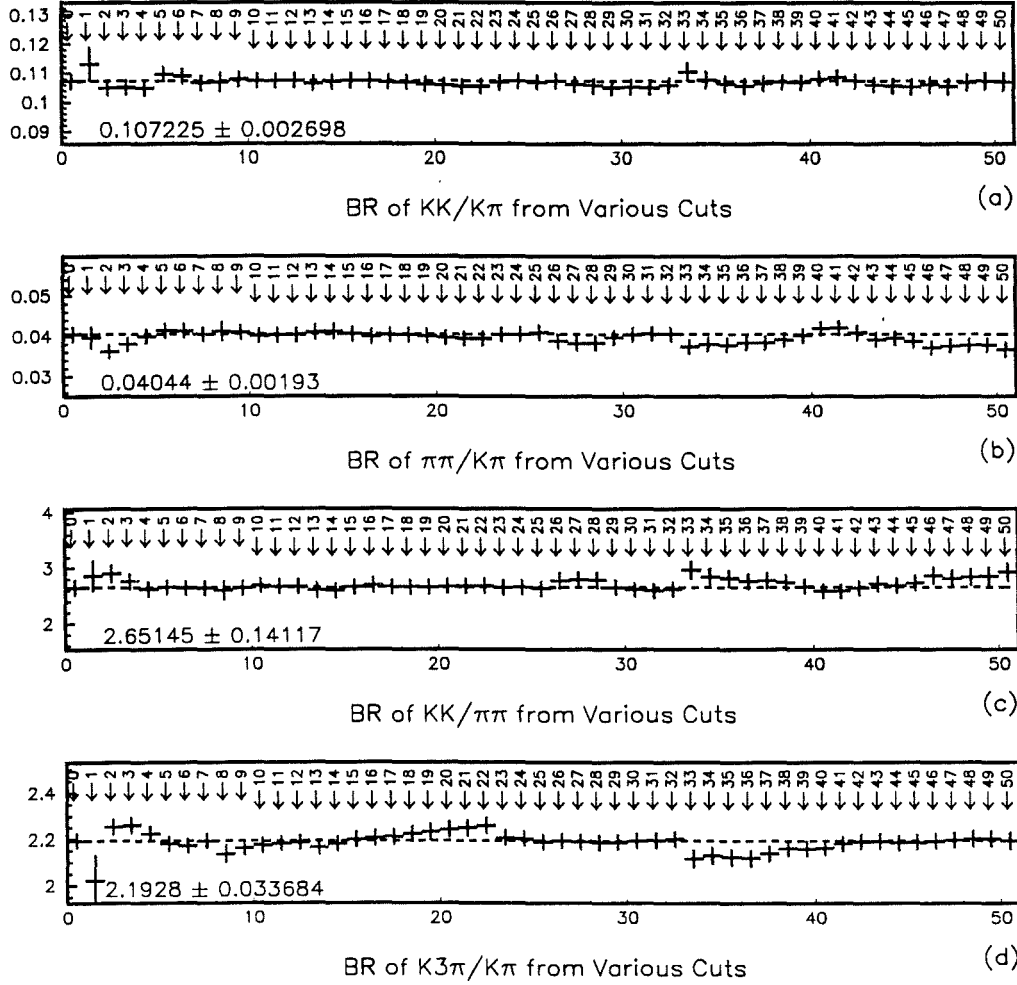


Figure 6.7. Systematic Study of Varying Cuts for BR:

(a) $\frac{\Gamma(D^0 \rightarrow K^+ K^-)}{\Gamma(D^0 \rightarrow K^- \pi^+)}$, (b) $\frac{\Gamma(D^0 \rightarrow \pi^+ \pi^-)}{\Gamma(D^0 \rightarrow K^- \pi^+)}$, (c) $\frac{\Gamma(D^0 \rightarrow K^+ K^-)}{\Gamma(D^0 \rightarrow \pi^+ \pi^-)}$, and (d) $\frac{\Gamma(D^0 \rightarrow K^- \pi^- \pi^+ \pi^+)}{\Gamma(D^0 \rightarrow K^- \pi^+)}$.

Please refer to Table 6.2 for the key.

1 PDG, 2-7 ASYM, 8-12 DIP, 13-22 MNCHV, 23-32 PT2DK, 33-42 PTBAL, 43-50 SDZ

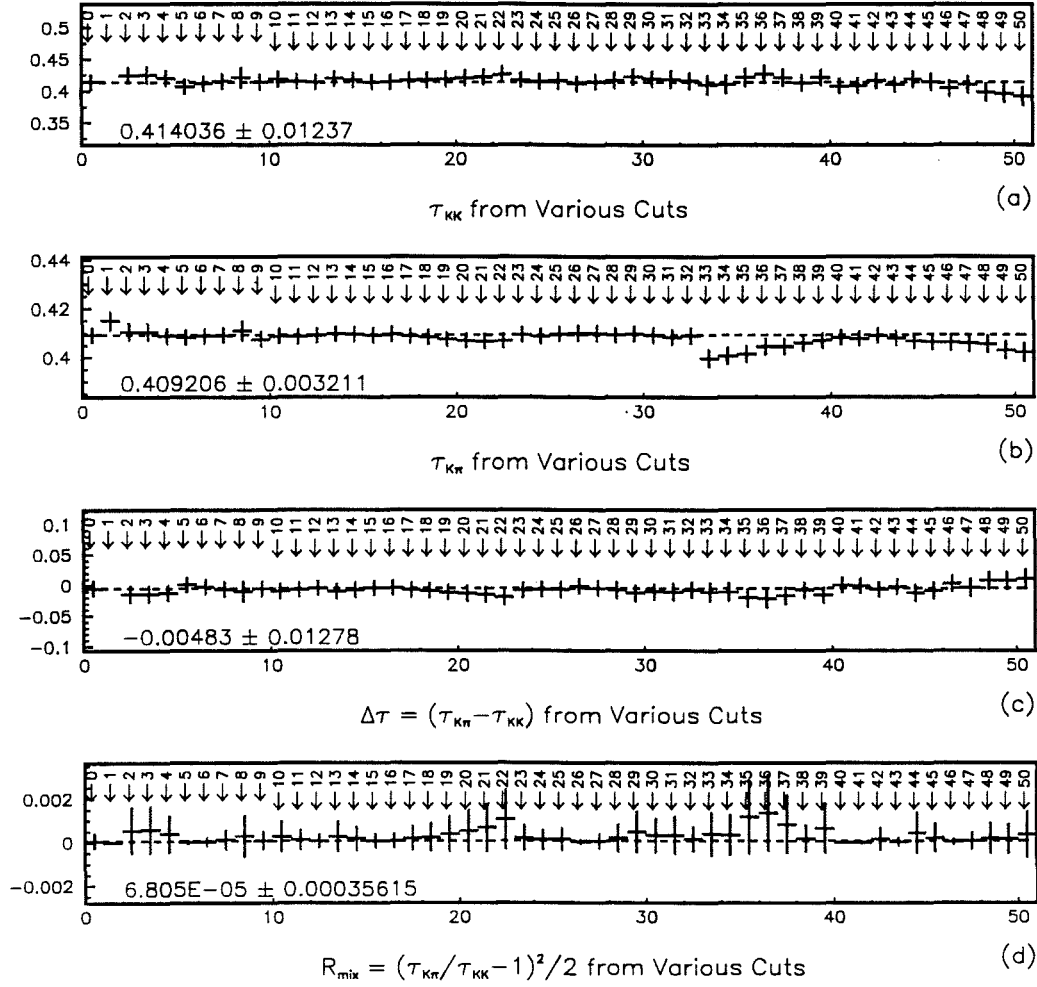


Figure 6.8. Systematic Study of Varying Cuts for
(a) τ_{KK} , (b) $\tau_{K\pi}$, (c) $\Delta\tau (= \tau_{K\pi} - \tau_{KK})$, and (d) $\mathcal{R}_{\text{mix}}^\nu$ due to lifetime difference only.

Please refer to Table 6.2 for the key.

1 PDG, 2-7 ASYM, 8-12 DIP, 13-22 MNCHV, 23-32 PT2DK, 33-42 PTBAL, 43-50 SDZ

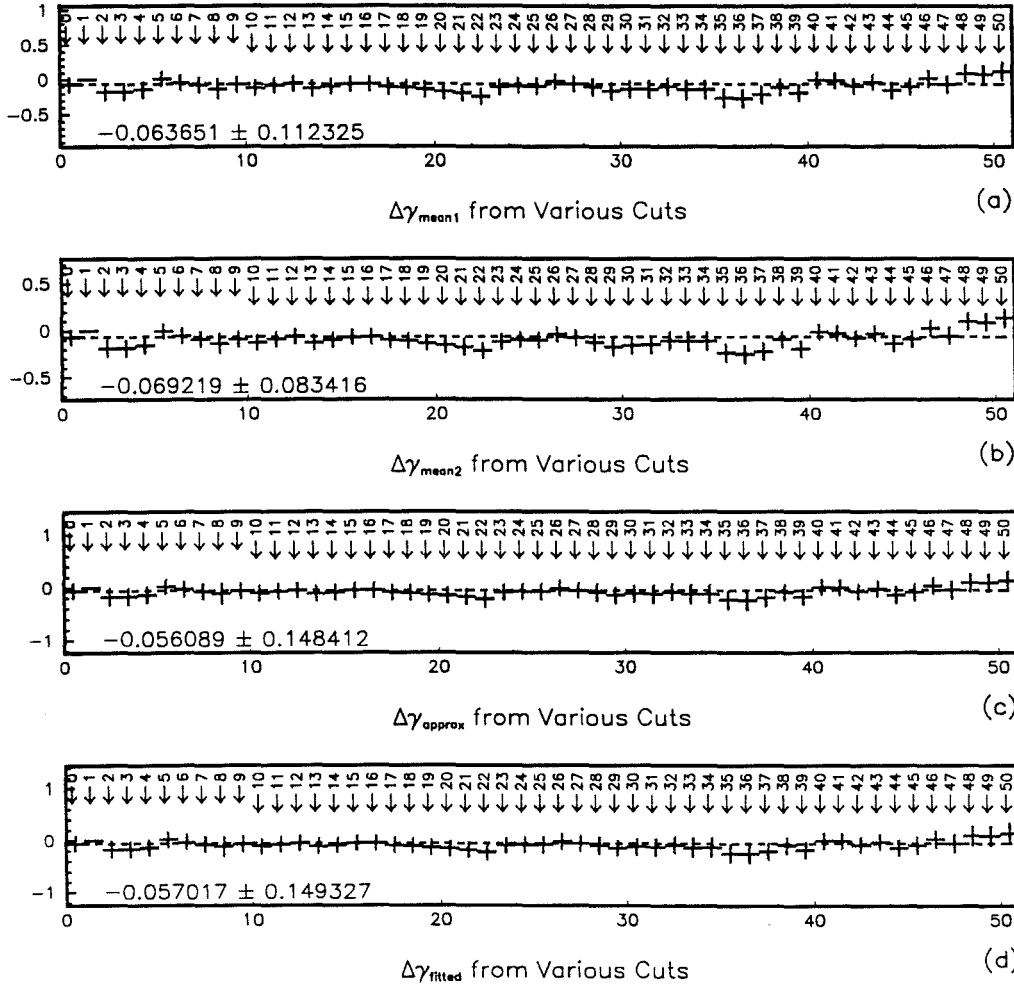


Figure 6.9. Systematic Study of Varying Cuts for

(a) $\Delta\gamma_{\text{mean1}}$, (b) $\Delta\gamma_{\text{mean2}}$, (c) $\Delta\gamma_{\text{approx}}$, and (d) $\Delta\gamma_{\text{fitted}}$.

Please refer to Table 6.2 for the key. The consistency of two approaches — (1) Mean value difference and (2) Fitted lifetime difference — is confirmed.

2-7ASYM,8-12DIP,13-22MNCHV,23-32PT2DK,33-42PTBAL,43-50SDZ,51-54Am,55-61IMPACT

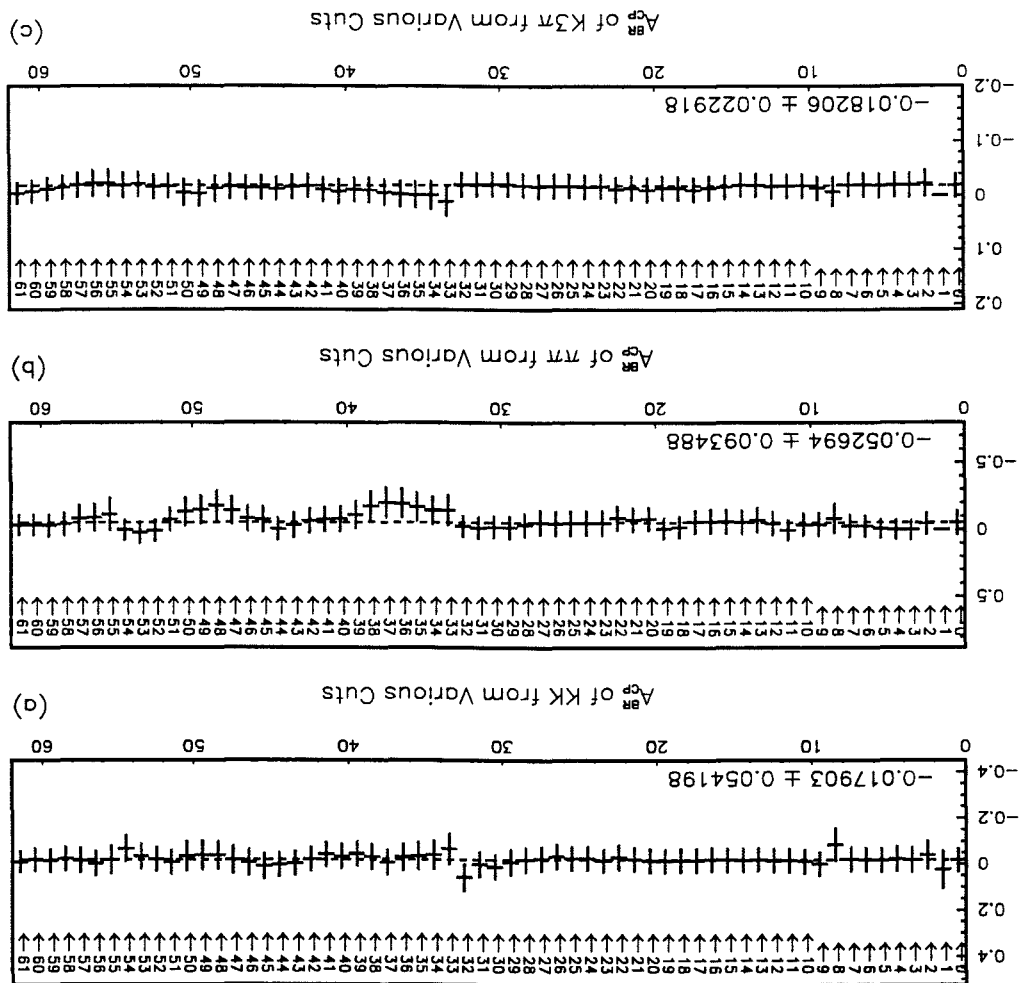


Figure 6.10. Systematic Study of Varying Cuts for A_{BR}^{CP} :
 (a) $K^\pm K^\mp$, (b) $\pi^\pm \pi^\mp$, and (c) $K3\pi$.
 Please refer to Table 6.2 for the key.

In the BR study, I multiply the widths from the MC by a common ratio:

$$Wid_{Data}(K^\pm K^\mp) = Wid_{MC}(K^\pm K^\mp) \times \frac{Wid_{Data}(K^\mp \pi^\pm)}{Wid_{MC}(K^\mp \pi^\pm)}. \quad (6.4)$$

The common ratio is defined as

$$R \pm \sigma_R \equiv \frac{Wid_{Data}(K^\mp \pi^\pm) \pm \sigma_D}{Wid_{MC}(K^\mp \pi^\pm) \pm \sigma_M} \quad (6.5)$$

where σ_D and σ_M are independently deduced from the SG Gaussian fitting errors.

Similarly, in getting the “average” width from combined D^0 and \bar{D}^0 for the A_{CP}^{BR} study or from the combined 16 bins of reduced proper time for lifetime studies, I have the associated fitting error for each “average” width, *i.e.* σ_W .

Taking the increment of σ_R or σ_W , I estimate the 1- σ deviations of the calculated quantities as illustrated in Fig. 6.11 through Fig. 6.15, as measures of the contributions of varying widths to the systematic errors in the SG numbers.

I conclude that in terms of the statistical error σ , the systematic errors due to the uncertainty of fixing SG Gaussian widths are (1) $\pm 0.40\sigma$ for $\frac{\Gamma(D^0 \rightarrow K^+ K^-)}{\Gamma(D^0 \rightarrow K^- \pi^+)}$, (2) $\pm 0.10\sigma$ for $\frac{\Gamma(D^0 \rightarrow \pi^+ \pi^-)}{\Gamma(D^0 \rightarrow K^- \pi^+)}$, (3) $\pm 0.40\sigma$ for $\frac{\Gamma(D^0 \rightarrow K^+ K^-)}{\Gamma(D^0 \rightarrow \pi^+ \pi^-)}$, (4) $\pm 0.15\sigma$ for τ_{KK} , (5) $\pm 0.12\sigma$ for $\tau_{K\pi}$, (6) $\pm 0.20\sigma$ for $\Delta\gamma_{\text{fitted}}$, (7) $\pm 0.24\sigma$ and $\pm 0.32\sigma$ for $\Delta\gamma_{\text{mean1}}$ and $\Delta\gamma_{\text{mean2}}$, respectively; (8) $\pm 0.08\sigma$ for $A_{CP}^{BR}(K^\pm K^\mp)$, (9) $\pm 0.10\sigma$ for $A_{CP}^{BR}(\pi^\pm \pi^\mp)$, and (10) $\pm 0.02\sigma$ for $A_{CP}^{BR}(K3\pi)$.

6.5 Uncertainty Due to Binned Lifetime Fitting

When I fit the lifetimes by the binned method (described in Sec. 5.2.1), I choose 16 bins of reduced proper time and fit them from the first bin to the last one. In this section, I study the uncertainty due to the choices of bins. Table 6.3 lists the results of this study.

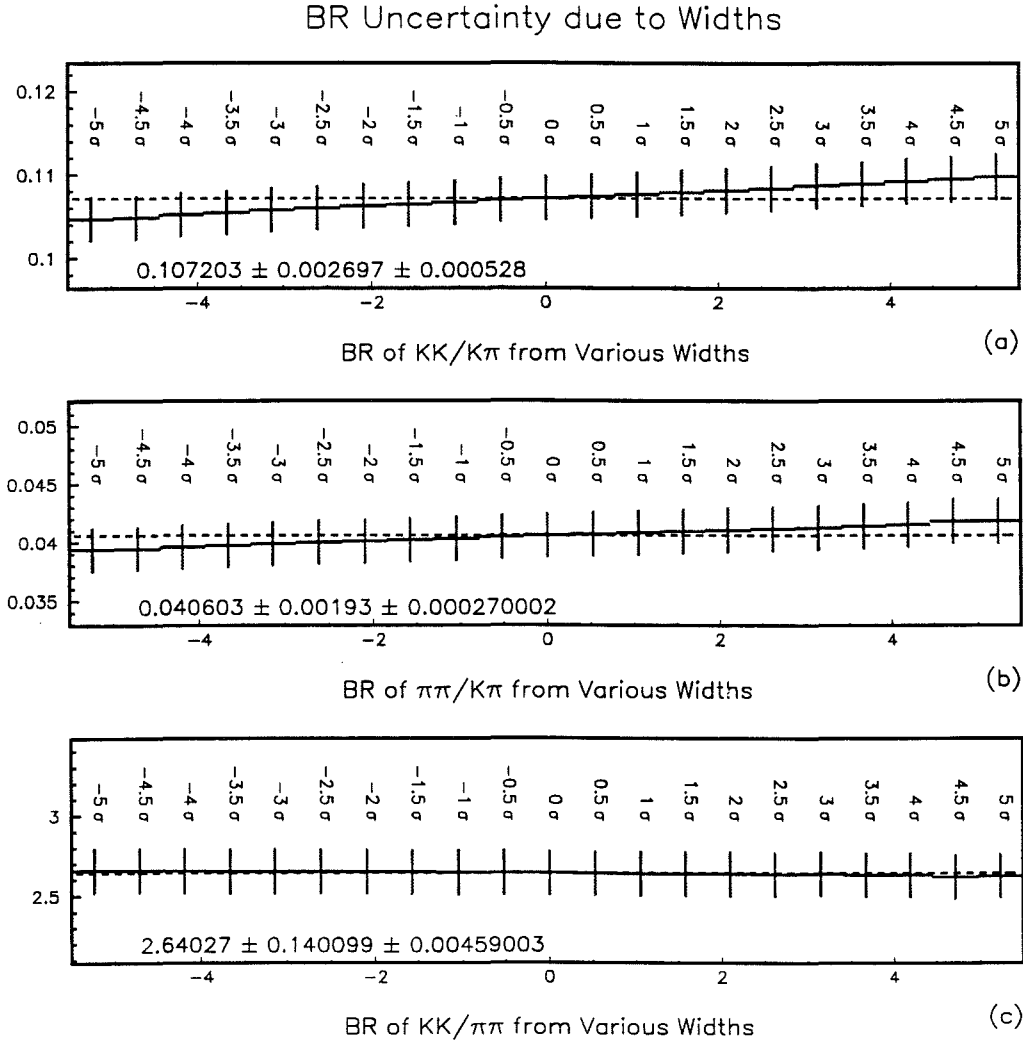


Figure 6.11. Systematic Study of Varying Widths for BR:

(a) $\frac{\Gamma(D^0 \rightarrow K^+ K^-)}{\Gamma(D^0 \rightarrow K^- \pi^+)}$, (b) $\frac{\Gamma(D^0 \rightarrow \pi^+ \pi^-)}{\Gamma(D^0 \rightarrow K^- \pi^+)}$, and (c) $\frac{\Gamma(D^0 \rightarrow K^+ K^-)}{\Gamma(D^0 \rightarrow \pi^+ \pi^-)}$. There is no width fixed in the $\frac{\Gamma(D^0 \rightarrow K^- \pi^- \pi^+ \pi^+)}{\Gamma(D^0 \rightarrow K^- \pi^+)}$ study. The $\pm 1\sigma_R$ deviation is the estimate of the systematic errors. In this figure, it is assumed that changes in the widths are correlated in numerators and denominators. But in Fig. 6.12, each mode has its own systematic error on SG.

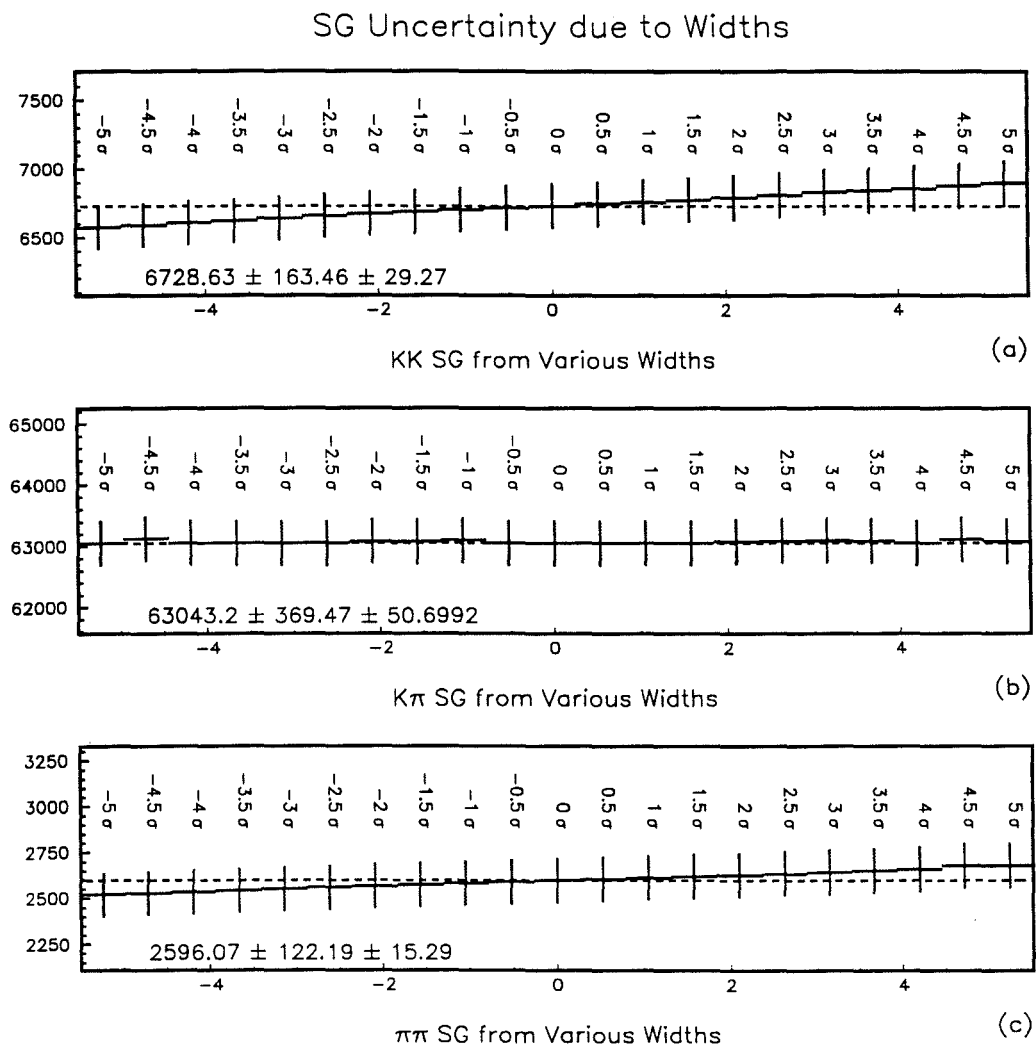


Figure 6.12. Systematic Study of Varying Widths for SG:

(a) $K^\pm K^\mp$, (b) $K^\mp \pi^\pm$, and (c) $\pi^\pm \pi^\mp$. There is no width fixed in $K3\pi$ study. The $\pm 1\sigma_w$ deviation is the estimate of the systematic errors.

Lifetime Uncertainty due to Widths

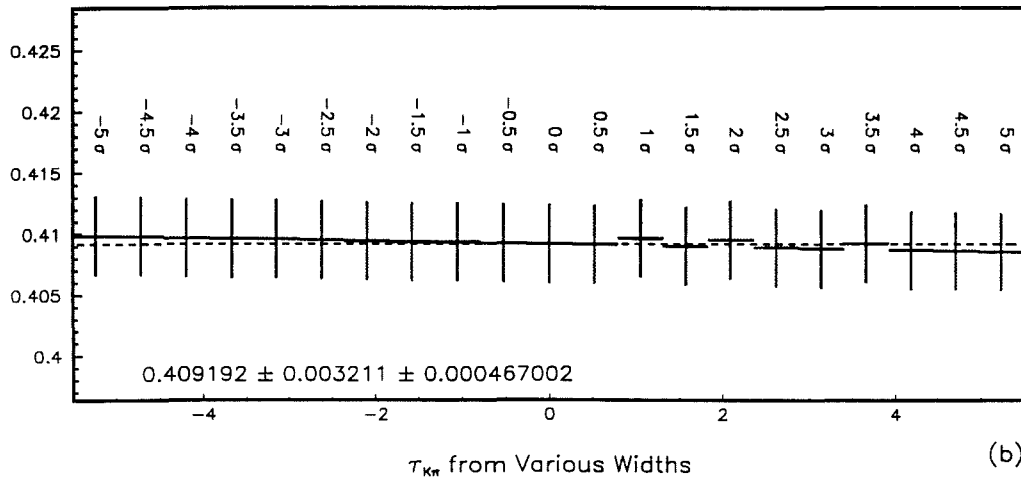
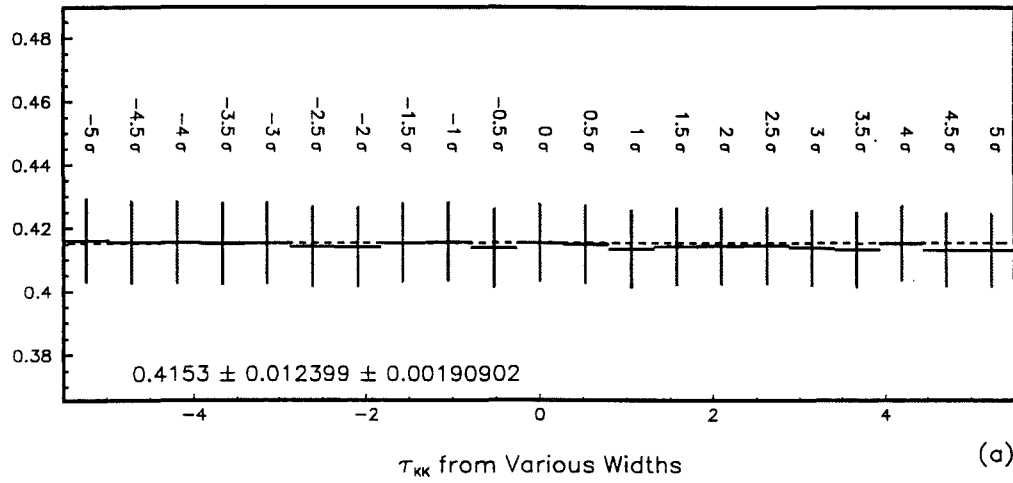


Figure 6.13. Systematic Study of Varying widths For (a) τ_{KK} and (b) $\tau_{K\pi}$. The $\pm 1\sigma_w$ deviation is the estimate of the systematic errors.

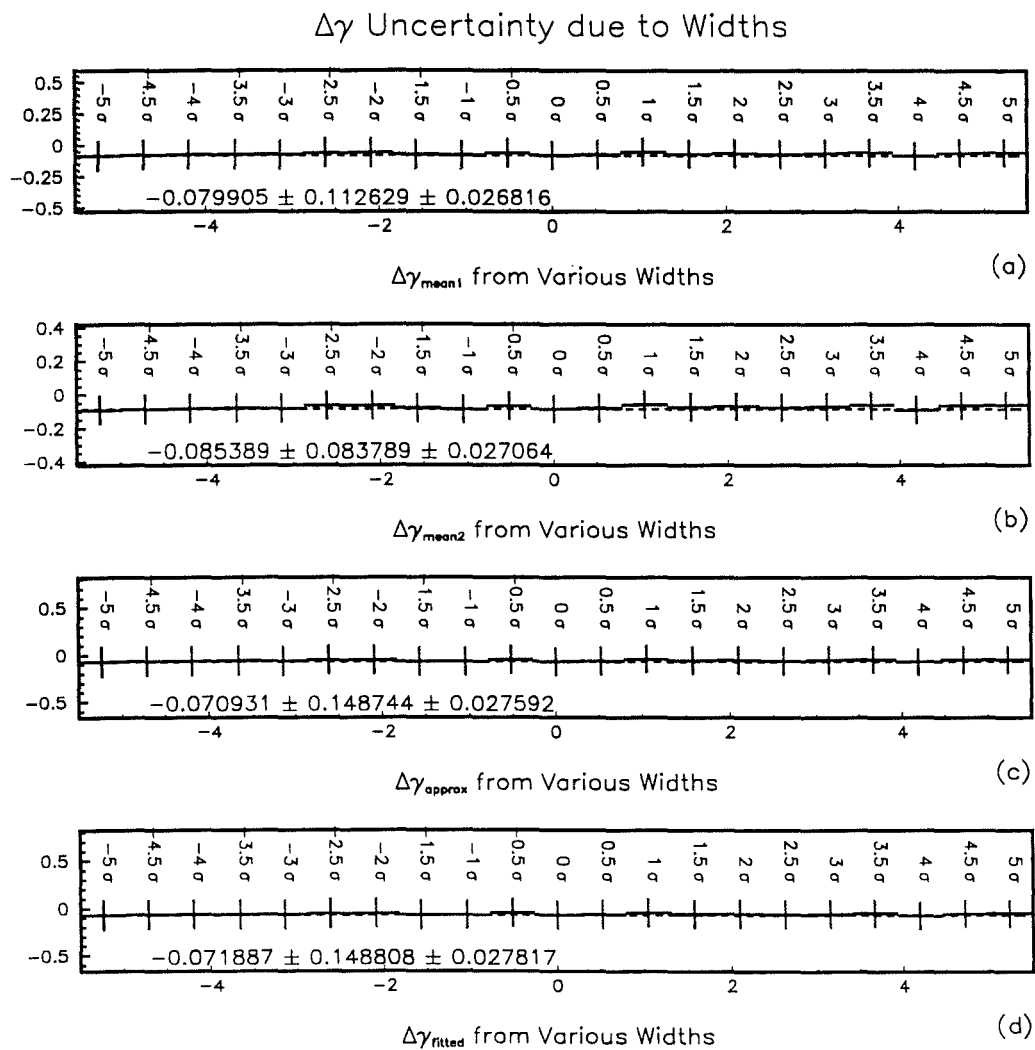


Figure 6.14. Systematic Study of Varying Widths for
 (a) $\Delta\gamma_{\text{mean1}}$, (b) $\Delta\gamma_{\text{mean2}}$, (c) $\Delta\gamma_{\text{approx}}$, and (d) $\Delta\gamma_{\text{fitted}}$.
 The $\pm 1\sigma_W$ deviation is the estimate of the systematic errors.

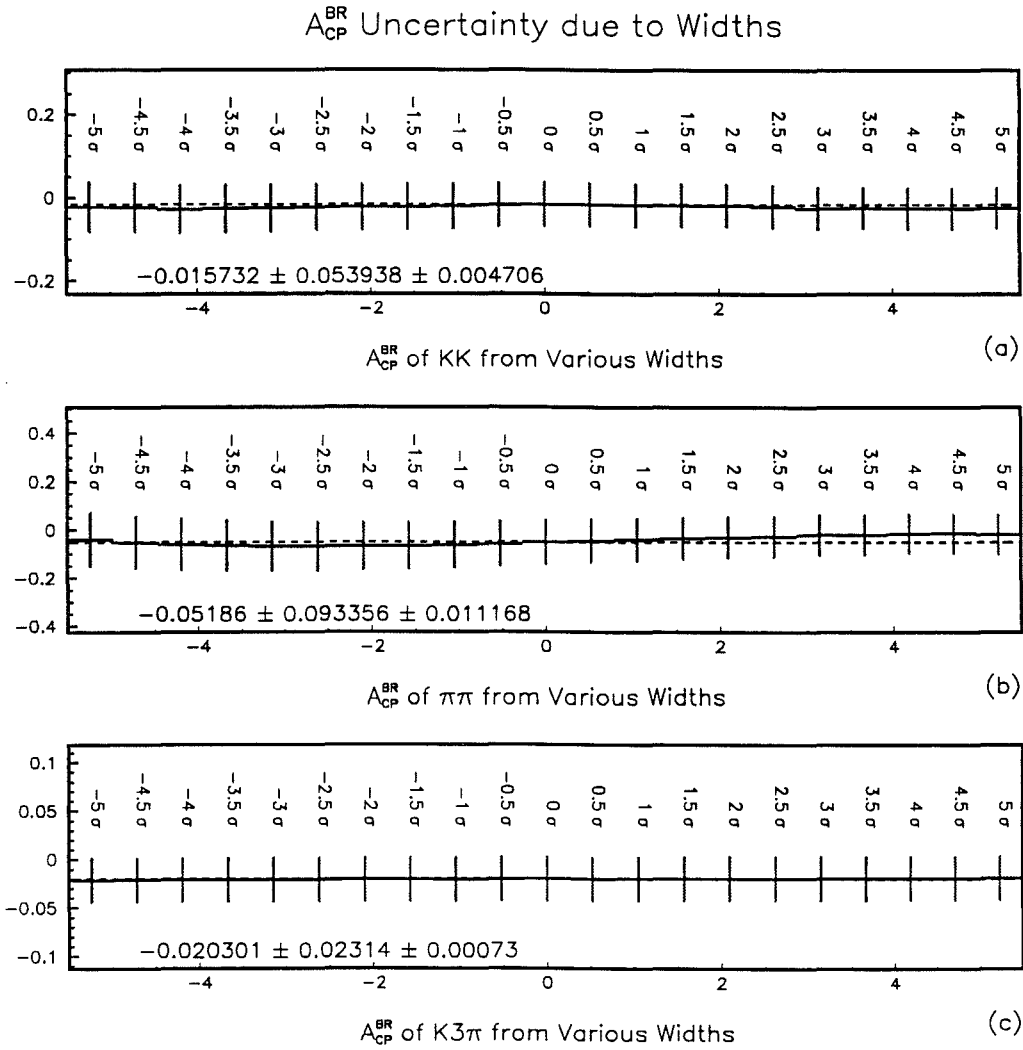


Figure 6.15. Systematic Study of Varying Widths for A_{CP}^{BR} :

(a) $K^\pm K^\mp$, (b) $\pi^\pm \pi^\mp$, and (c) $K3\pi$.

The $\pm 1\sigma_W$ deviation is the estimate of the systematic errors.

Table 6.3. List of Different Bins Fitting

Start, End	τ_{KK}	$\tau_{K\pi}$	$\Delta\gamma_{\text{fitted}}$
* 1, 16 *	0.4121 ± 0.0123	0.4091 ± 0.0032	-0.0365 ± 0.1498
1, 15	0.4118 ± 0.0127	0.4101 ± 0.0033	-0.0200 ± 0.1553
1, 14	0.4121 ± 0.0133	0.4109 ± 0.0035	-0.0142 ± 0.1620
1, 13	0.4161 ± 0.0142	0.4101 ± 0.0037	-0.0700 ± 0.1695
1, 12	0.4206 ± 0.0153	0.4107 ± 0.0039	-0.1139 ± 0.1788
2, 16	0.4146 ± 0.0145	0.4054 ± 0.0037	-0.1085 ± 0.1747
2, 15	0.4143 ± 0.0151	0.4066 ± 0.0039	-0.0922 ± 0.1823
2, 14	0.4149 ± 0.0159	0.4073 ± 0.0041	-0.0902 ± 0.1913
2, 13	0.4203 ± 0.0172	0.4059 ± 0.0043	-0.1694 ± 0.2018

I conclude that in terms of the statistical error σ , the systematic errors due to the uncertainty of binning fits are (1) $\pm 0.25\sigma$ for τ_{KK} , (2) $\pm 0.80\sigma$ for $\tau_{K\pi}$, and (3) $\pm 0.25\sigma$ for $\Delta\gamma_{\text{fitted}}$, $\Delta\gamma_{\text{mean1}}$, and $\Delta\gamma_{\text{mean2}}$.

6.6 Uncertainty Due to MC Production Distribution

The E791 MC has been tuned to match the DATA production asymmetry. The MC for my final analysis results are generated with charm quark mass (c_m) $1.7 \text{ GeV}/c^2$ and primordial transverse momenta (K_T) of the incoming partons as $1.0 \text{ GeV}/c$. I also have studied a MC sample generated using the values distributed with Version 5.7 of Pythia [Pythia]: $c_m = 1.35 \text{ GeV}/c^2$ and $K_T = 0.44 \text{ GeV}/c$. After identical analysis procedures, the results from two MC samples are consistent with each other within statistical errors. So, I conservatively conclude the systematic errors due to MC production are[‡] (1) $\pm 0.30\sigma$ for $\frac{\Gamma(D^0 \rightarrow K^+ K^-)}{\Gamma(D^0 \rightarrow K^- \pi^+)} \{0.104\}$, (2) $\pm 0.30\sigma$ for $\frac{\Gamma(D^0 \rightarrow \pi^+ \pi^-)}{\Gamma(D^0 \rightarrow K^- \pi^+)} \{0.039\}$, (3) $\pm 0.20\sigma$ for $\frac{\Gamma(D^0 \rightarrow K^+ K^-)}{\Gamma(D^0 \rightarrow \pi^+ \pi^-)} \{2.67\}$, (4) $\pm 1.00\sigma$ for $\frac{\Gamma(D^0 \rightarrow K^- \pi^- \pi^+ \pi^+)}{\Gamma(D^0 \rightarrow K^- \pi^+)} \{2.01\}$, (5) $\pm 1.00\sigma$ for $\tau_{KK} \{0.423\}$, (6) $\pm 0.50\sigma$ for $\tau_{K\pi} \{0.412\}$, (7) $\pm 0.25\sigma$ for $(\tau_{K\pi} - \tau_{KK}) \{0.011\}$, (8) $\pm 0.80\sigma$ for $\Delta\gamma_{\text{fitted}} \{-0.141\}$, (9) $\pm 0.80\sigma$ and $\pm 0.80\sigma$ for $\Delta\gamma_{\text{mean1}} \{-0.151\}$ and $\Delta\gamma_{\text{mean2}} \{-0.162\}$, respectively.

[‡]The values in the braces { } are the results using a different MC production distribution.

6.7 Uncertainty Due to Detection Bias on $A_{\text{CP}}^{\text{BR}}$

Recall the definition of $A_{\text{CP}}^{\text{BR}}(K^\pm K^\mp)$ in Eq. 1.66. The detection bias of slow π^\pm in $D^{*\pm} \rightarrow D^0(\bar{D}^0)\pi^\pm$ tagging can be compensated by the normalization. For pseudoscalars, since $K^\pm K^\mp$ are the same final states of D^0 and \bar{D}^0 , any detector bias will be cancelled out. So, I only need to worry about the detection bias between $D^0 \rightarrow K^-\pi^+$ and $\bar{D}^0 \rightarrow K^+\pi^-$.

Let me divide detector efficiency into two geometrical parts: longitudinal efficiency and transverse efficiency.

- For longitudinal efficiency, Fig. 4.5 shows K^+ and K^- or π^+ and π^- have very similar momentum spectra after detection. Fig. 4.5 and Fig. 4.6 illustrate that there is no longitudinal efficiency bias.
- For transverse efficiency, to form a D^0 or \bar{D}^0 requires two tracks (one positive-charged and one negative-charged), so charge detection inefficiency is not a problem here. Fig. 4.5 (e) and (f) show that K^+/K^- and π^+/π^- have flat slopes, indicating our detection along the direction low-momentum to high-momentum on the transverse plane is smooth (also compare Fig. 4.7 of MC).

Of course, I assume that the direct CP asymmetry between $D^0 \rightarrow K^-\pi^+$ and $\bar{D}^0 \rightarrow K^+\pi^-$ is minimal, otherwise the above discussion is incomplete because any detection bias may be hidden by CP asymmetry. In such a case, we return to our original intention: measure the CP asymmetry of $K^\pm K^\mp$ and $\pi^\pm \pi^\mp$, since Fig. 4.5 proves there is no net asymmetry in the normalization mode.

CHAPTER VII

COMPARISONS AND CONCLUSIONS

In this chapter, I present the comparisons of my measurements with previous experimental data. I include here the systematic errors discussed in Chapter VI. I also emphasize the meanings of my measurements to Theoretical predictions.

7.1 Comparison with Previous Measurements

The comparison of BR measurements are listed in Table 7.1 and Table 7.2, and illustrated in Fig. 7.1 and Fig. 7.2. E791 has better measurements than the previous world averages.

Table 7.1. Comparison of BR Measurements

Year	Group	$\frac{\Gamma(D^0 \rightarrow K^+ K^-)}{\Gamma(D^0 \rightarrow K^- \pi^+)}$	$\frac{\Gamma(D^0 \rightarrow \pi^+ \pi^-)}{\Gamma(D^0 \rightarrow K^- \pi^+)}$	$\frac{\Gamma(D^0 \rightarrow K^+ K^-)}{\Gamma(D^0 \rightarrow \pi^+ \pi^-)}$
1979	Mark II[mark-79]	0.113 ± 0.030	0.033 ± 0.015	3.4 ± 1.8
1984	Mark III[mark-85]	$0.122 \pm 0.018 \pm 0.012$	$0.033 \pm 0.010 \pm 0.006$	3.7 ± 1.3
1989	ARGUS[argu-90]	$0.10 \pm 0.02 \pm 0.01$	$0.040 \pm 0.007 \pm 0.006$	2.5 ± 0.7
1990	CLEO[cleo-90]	$0.117 \pm 0.010 \pm 0.007$	$0.050 \pm 0.007 \pm 0.005$	$2.35 \pm 0.37 \pm 0.28$
1991	E691[e691-91]	$0.107 \pm 0.010 \pm 0.009$	$0.055 \pm 0.008 \pm 0.005$	$1.95 \pm 0.34 \pm 0.22$
1992	WA82[wa82-92]	$0.107 \pm 0.029 \pm 0.015$	$0.048 \pm 0.013 \pm 0.008$	$2.23 \pm 0.81 \pm 0.46$
1993	CLEO[cleo-93]		$0.0348 \pm 0.0030 \pm 0.0023$	
1994	E687[e687-94]	$0.109 \pm 0.007 \pm 0.009$	$0.043 \pm 0.007 \pm 0.003$	$2.53 \pm 0.46 \pm 0.19$
1994	PDG [PDG94]	0.113 ± 0.006	0.0396 ± 0.0027	2.86 ± 0.28
1995	E791	$0.107 \pm 0.003 \pm 0.003$	$0.040 \pm 0.002 \pm 0.002$	$2.65 \pm 0.14 \pm 0.13$

The comparison of lifetime measurements is listed in Table 7.3 and illustrated in Fig. 7.3(a).

The comparison of CP asymmetry measurements is listed in Table 7.4 and illustrated in Fig. 7.3(b).

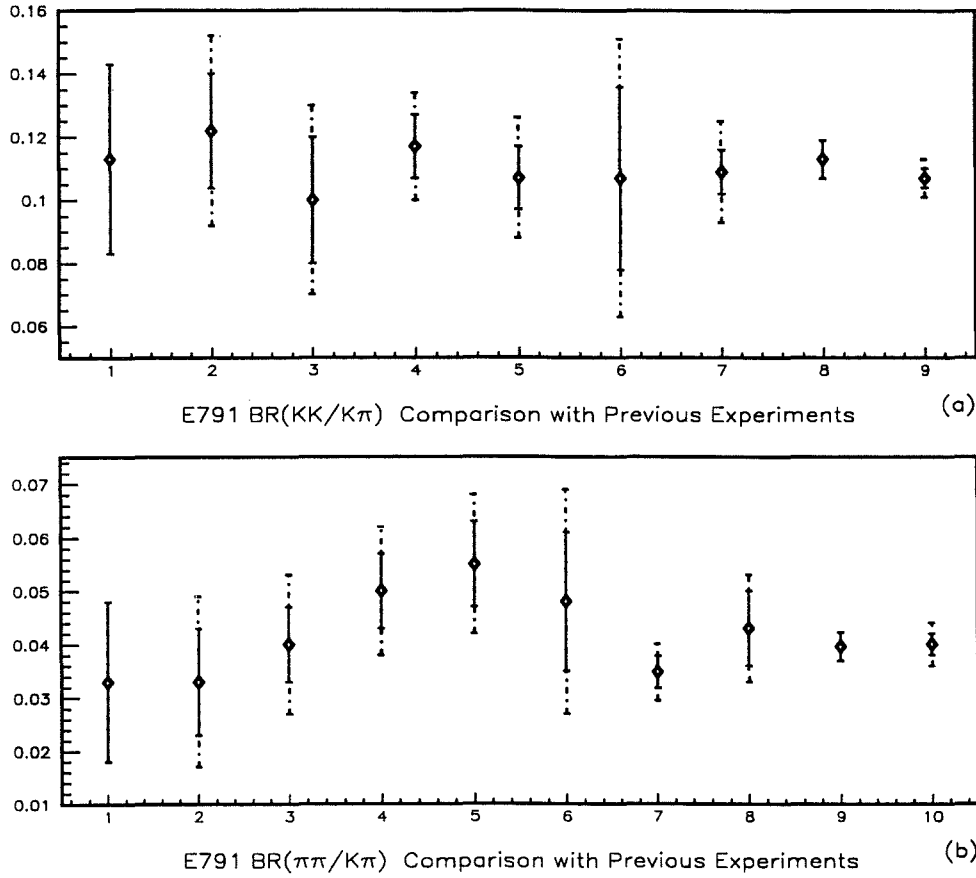


Figure 7.1. E791 BR's Comparison with Previous Experiments:

(a) The comparison of $\frac{\Gamma(D^0 \rightarrow K^+ K^-)}{\Gamma(D^0 \rightarrow K^- \pi^+)}$ from 1) 1979 Mark II, 2) 1984 Mark III, 3) 1989 ARGUS, 4) 1990 CLEO, 5) 1991 E691, 6) 1992 WA82, 7) 1994 E687, 8) 1994 PDG, 9) This experiment.

(b) The comparison of $\frac{\Gamma(D^0 \rightarrow \pi^+ \pi^-)}{\Gamma(D^0 \rightarrow K^- \pi^+)}$ from 1) 1979 Mark II, 2) 1984 Mark III, 3) 1989 ARGUS, 4) 1990 CLEO, 5) 1991 E691, 6) 1992 WA82, 7) 1993 CLEO II, 8) 1994 E687, 9) 1994 PDG, 10) This experiment (with the better error than the world average).

The solid error bars include only the statistical errors, and the dashed error bars represent the systematic errors added to statistical errors.

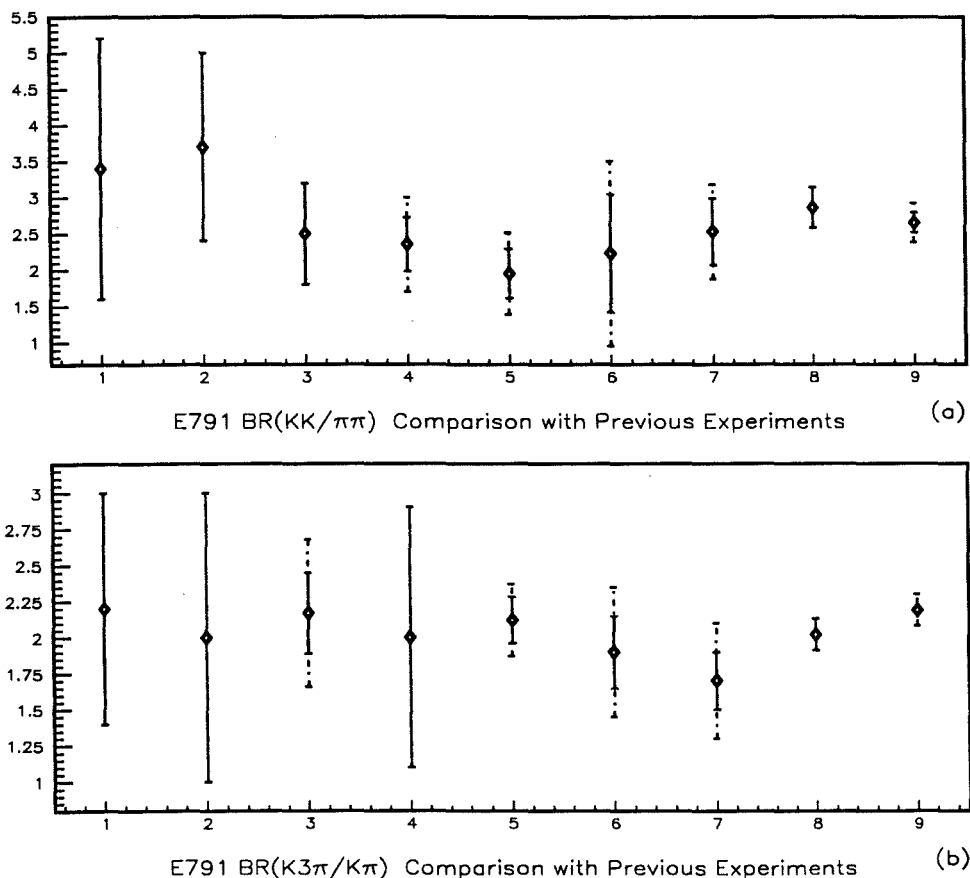


Figure 7.2. E791 BR's Comparison with Previous Experiments:

(a) The comparison of $\frac{\Gamma(D^0 \rightarrow K^+ K^-)}{\Gamma(D^0 \rightarrow \pi^+ \pi^-)}$ from 1) 1979 Mark II, 2) 1984 Mark III, 3) 1989 ARGUS, 4) 1990 CLEO, 5) 1991 E691, 6) 1992 WA82, 7) 1994 E687, 8) 1994 PDG, 9) This experiment.

(b) The comparison of $\frac{\Gamma(D^0 \rightarrow K^- \pi^- \pi^+ \pi^+)}{\Gamma(D^0 \rightarrow K^- \pi^+)}$ from 1) 1977 Mark I, 2) 1984 SPEC, 3) 1985 ARGUS, 4) 1986 ACCM, 5) 1988 CLEO, 6) 1991 NA14, 7) 1992 NA14, 8) 1994 PDG, 9) This experiment.

The solid error bars include only the statistical errors, and the dashed error bars represent the systematic errors added to statistical errors.

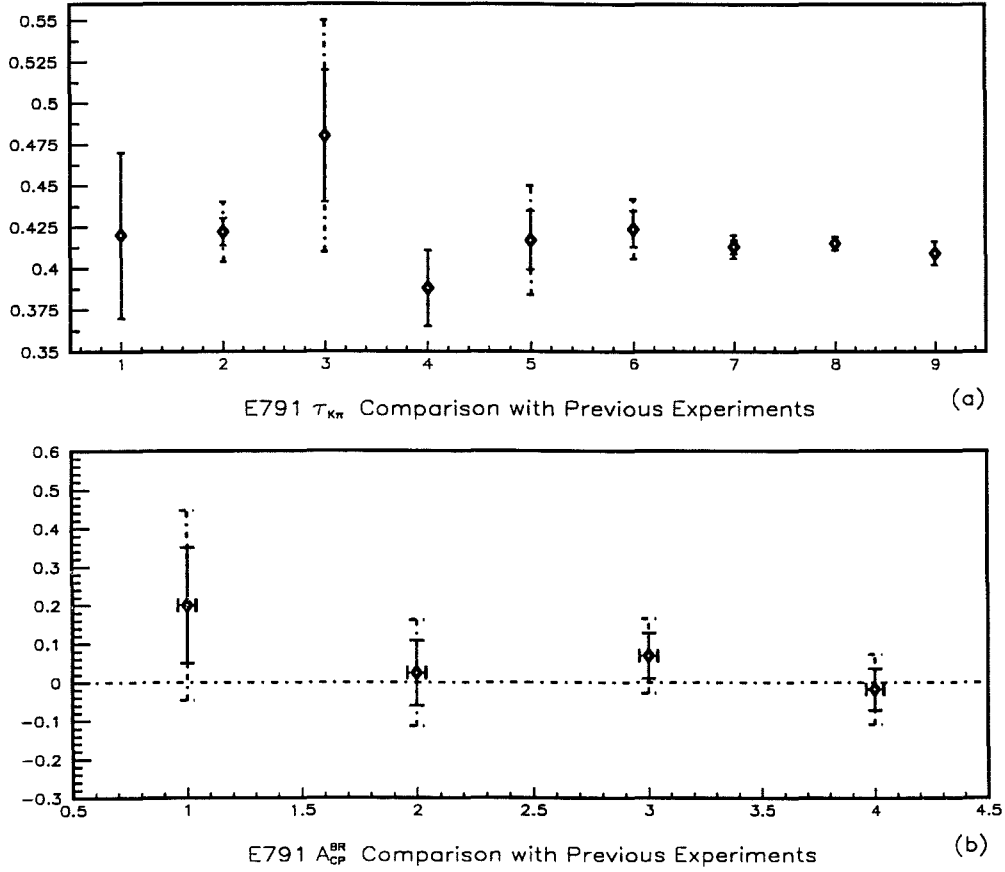


Figure 7.3. E791 $\tau_{K\pi}$ and $A_{CP}^{BR}(K^{\pm}K^{\mp})$ Comparison with Previous Experiments:
 (a) The comparison of $\tau_{K\pi}$ from 1) 1987 ACCM, 2) 1988 E691, 3) 1988 ARGUS, 4) 1990 ACCM, 5) 1990 NA14, 6) 1991 E687, 7) 1994 E687, 8) 1994 PDG, 9) This experiment.

(a) The comparison of $A_{CP}^{BR}(K^{\pm}K^{\mp})$ from 1) 1991 E691, 2) 1994 E687, 3) 1995 CLEO II, 4) This experiment.

The solid error bars include only the statistical errors, and the dashed error bars represent the 90% C.L. interval.

Table 7.2. Comparison of BR $K3\pi$ Measurements

Year	Group	$\frac{\Gamma(D^0 \rightarrow K^- \pi^- \pi^+ \pi^+)}{\Gamma(D^0 \rightarrow K^- \pi^+)}$
1977	Mark I [mark-77]	2.2 ± 0.8
1983	SPEC [accm-83]	2.0 ± 1.0
1985	ARGUS [argu-85]	$2.17 \pm 0.28 \pm 0.23$
1986	ACCM [accm-86]	2.0 ± 0.9
1988	CLEO [cleo-88]	$2.12 \pm 0.16 \pm 0.09$
1991	NA14 [na14-902]	$1.90 \pm 0.25 \pm 0.20$
1992	E691 [e691-92]	$1.7 \pm 0.2 \pm 0.2$
1994	PDG [PDG94]	2.02 ± 0.11
1995	E791	$2.19 \pm 0.03 \pm 0.08$

Table 7.3. Comparison of Lifetime Measurements

Year	Group	Decay Mode	Mean Lifetime (ps)
1987	ACCM [accm-872]	$D^0 \rightarrow K^- \pi^+$	0.42 ± 0.05
1988	E691 [e691-882]	$D^0 \rightarrow K^- \pi^+$	$0.422 \pm 0.008 \pm 0.010$
1988	ARGUS [argu-882]	$D^0 \rightarrow K^- \pi^+$	$0.48 \pm 0.04 \pm 0.03$
1990	ACCM [accm-902]	$D^0 \rightarrow K^- \pi^+$	0.388 ± 0.022
1990	NA14 [na14-902]	$D^0 \rightarrow K^- \pi^+$	$0.417 \pm 0.018 \pm 0.015$
1991	E687 [e687-912]	$D^0 \rightarrow K^- \pi^+$	$0.424 \pm 0.011 \pm 0.007$
1994	E687 [e687-942]	$D^0 \rightarrow K^- \pi^+, K3\pi$	$0.413 \pm 0.004 \pm 0.003$
1994	PDG [PDG94]	CFD	0.415 ± 0.004
1995	E791	$D^0 \rightarrow K^- \pi^+$	$0.409 \pm 0.003 \pm 0.004$
		$D^0 \rightarrow K^+ K^-$	$0.414 \pm 0.012 \pm 0.014$
1995	E791	$(\tau_{K\pi} - \tau_{KK})$	$-0.005 \pm 0.012 \pm 0.013$

Table 7.4. Comparison of CP Asymmetry Measurements

Year	Group & Mode	A_{CP} of $D^0 - \bar{D}^0$	Upper Limit at C.L. 90% [†]
1991	E691 $A_{CP}^{BR}(K^\pm K^\mp)$	0.20 ± 0.15	$A_{CP}^{BR} < 45\%$ [e691-91]
1994	E687 $A_{CP}^{BR}(K^\pm K^\mp)$	0.024 ± 0.084	$-11\% < A_{CP}^{BR} < 16\%$ [e687-943]
1995	CLEO $A_{CP}(K^\pm K^\mp)$	0.069 ± 0.059	$-2.8\% < A_{CP} < 16.6\%$ [cleo-953]
1995	E791 $A_{CP}^{BR}(K^\pm K^\mp)$	$-0.018 \pm 0.054 \pm 0.012$	$-10.8\% < A_{CP}^{BR} < 7.2\%$
1995	E791 $A_{CP}^{BR}(\pi^\pm \pi^\mp)$	$-0.052 \pm 0.093 \pm 0.029$	$-21.2\% < A_{CP}^{BR} < 10.6\%$
1995	E791 $A_{CP}^{BR}(K3\pi)$	$-0.018 \pm 0.023 \pm 0.002$	$-5.5\% < A_{CP}^{BR} < 1.9\%$

[†]By using central value $\pm 1.64 \times$ combined error

7.2 Conclusions

Branching Ratio. In the past, there were many theoretical models developed to explain $\frac{\Gamma(D^0 \rightarrow K^+ K^-)}{\Gamma(D^0 \rightarrow \pi^+ \pi^-)}$ alone, but not all models survived the global fit to all the 2-body decay BR's of D mesons. The current $\frac{\Gamma(D^0 \rightarrow K^+ K^-)}{\Gamma(D^0 \rightarrow \pi^+ \pi^-)}$ measurement is consistent with previous experimental data (see Fig. 7.1 and Fig. 7.2) as well as theoretical explanations — SU(3) symmetry breaking and coupled channel final state interactions. These E791 measurements provide data for phenomenological studies of other decay modes.

Decay Mode	E791 Branching Ratios
$\frac{\Gamma(D^0 \rightarrow K^+ K^-)}{\Gamma(D^0 \rightarrow K^- \pi^+)}$	$0.107 \pm 0.003 \pm 0.003$
$\frac{\Gamma(D^0 \rightarrow \pi^+ \pi^-)}{\Gamma(D^0 \rightarrow K^- \pi^+)}$	$0.040 \pm 0.002 \pm 0.002$
$\frac{\Gamma(D^0 \rightarrow K^+ K^-)}{\Gamma(D^0 \rightarrow \pi^+ \pi^-)}$	$2.65 \pm 0.14 \pm 0.13$
$\frac{\Gamma(D^0 \rightarrow K^- \pi^- \pi^+ \pi^+)}{\Gamma(D^0 \rightarrow K^- \pi^+)}$	$2.19 \pm 0.03 \pm 0.08$

All the BR measurements are consistent with previous measurements, and yield smaller errors than the previous world average values.

Lifetime Difference. This work reports the first measurement of $\Delta\gamma$ and y using the lifetime difference ($\tau_{K\pi} - \tau_{KK}$) and lifetime ratio ($\tau_{K\pi}/\tau_{KK} - 1$), respectively. In addition to directly measuring two exponential decay lifetimes, I also approximate the lifetime difference in terms of the difference of two mean decay times (described in Appendix. A), so that I have a parallel approach to confirm the measurement.

E791 Measurements			
τ_{KK}	$D^0 \rightarrow K^+ K^-$	0.414	$\pm 0.012 \pm 0.014$
$\tau_{K\pi}$	$D^0 \rightarrow K^- \pi^+$	0.409	$\pm 0.003 \pm 0.004$
$\Delta\tau$	$(\tau_{K\pi} - \tau_{KK})$	-0.005	$\pm 0.013 \pm 0.013$
$\Delta\gamma$	(CP invariance)	-0.06	$\pm 0.15 \pm 0.15$
y	$(\tau_{K\pi}/\tau_{KK} - 1)$	-0.0121	± 0.0483 (combined error)

With the CP invariance assumption, $\Delta\tau$, $\Delta\gamma$, and y are the first estimate of the D^0 - \bar{D}^0 Mixing due to the lifetime difference. According to Eq. 1.58, $\mathcal{R}_{\text{mix}}^y \equiv y^2/2 = 0.000073 \pm 0.000438^\dagger$ due to lifetime difference, which gives an upper limit of 0.00079 at 90% C.L. All measurements are consistent with the Standard Model prediction of very small Mixing effects in the D^0 - \bar{D}^0 system.

CP Asymmetry. In Sec. 1.3.2, I emphasized that $D^0 \rightarrow K^+ K^-$ (or $D^0 \rightarrow \pi^+ \pi^-$) is not a good system in which to measure pure Direct CP asymmetry, due to interference with possible Indirect CP asymmetry arising from D^0 - \bar{D}^0 Mixing. The interference of direct-indirect CP asymmetry cannot be cancelled by the normalization of $D^{*\pm} \rightarrow (D^0 \rightarrow K^\mp \pi^\pm) \pi^\pm$. But any non-zero result of our measurements would indicate Direct or Indirect CP asymmetry, or both. In addition, $A_{\text{CP}}^{\text{BR}}(K^\pm K^\mp) = 0$ is no longer a guarantee of CP invariance (see Eq. 1.81). The current measurements are consistent with zero, but it is still appropriate to estimate the upper limits for $A_{\text{CP}}^{\text{BR}}$ being non-zero at the 90% confidence level. Although $A_{\text{CP}}^{\text{BR}}(K3\pi)$ has been used in this work as a consistency checking mode, it can also be interpreted as a measurement of a direct CP asymmetry arising from interference between the sector of beyond the Standard Model and the sector of the Standard Model (see Sec. 1.3.1).

Decay Mode	$A_{\text{CP}}^{\text{BR}}$ of D^0 - \bar{D}^0	90% C.L. Upper Limit
$K^\pm K^\mp$	$-0.018 \pm 0.054 \pm 0.012$	$-10.8 \% < A_{\text{CP}}^{\text{BR}} < 7.2 \%$
$\pi^\pm \pi^\mp$	$-0.052 \pm 0.093 \pm 0.029$	$-21.2 \% < A_{\text{CP}}^{\text{BR}} < 10.6 \%$
$K3\pi$	$-0.018 \pm 0.023 \pm 0.002$	$-5.5\% < A_{\text{CP}}^{\text{BR}} < 1.9 \%$

$A_{\text{CP}}^{\text{BR}}(\frac{\pi^\pm \pi^\mp}{K^\pm K^\mp}) = -0.034 \pm 0.106$, as described at the end of Chapter I, can also be interpreted as an indication of direct CP asymmetry. It too is consistent with zero.

[†]I assign the same magnitude of statistical error as systematic error, then combine them in quadrature for an estimated error in y .

The $A_{\text{CP}}^{\text{BR}}$ measurements are currently the best CP asymmetry measurements in the $D^0\text{-}\bar{D}^0$ system, and are consistent with the predictions of the Standard Model. In future high statistics charm experiments, it may be possible to measure the time-evolution of the CP asymmetry parameter, $A_{\text{CP}}(t)$ as described in Sec. 1.3.2, and to do the multiple-parameter fit for Direct CP asymmetry, Indirect CP asymmetry, and the Mass Mixing parameters.

APPENDIX A

LIFETIME DIFFERENCE VS. MEAN DECAY TIME DIFFERENCE

A.1 $\Delta\tau$ in the Case of Equal Acceptance

If the acceptance for D^0 decays in both modes is identical, then the lifetime difference can easily be measured using the observed mean lifetimes as follows.[†]

Let us define the mean and sigma of the observed time distribution as t_1 and σ . Higher moments of the observed distribution will be called t_n . Thus,

$$t_1 \equiv \frac{\int t \cdot e^{-t/\tau} \cdot A(t) dt}{\int e^{-t/\tau} \cdot A(t) dt} = \frac{N}{D} \quad (\text{A.1})$$

where $A(t)$ is the acceptance as a function of time and τ is the lifetime of the particle. N and D simply stand for numerator and denominator respectively.

Similarly,

$$t_n \equiv \frac{\int t^n \cdot e^{-t/\tau} \cdot A(t) dt}{\int e^{-t/\tau} \cdot A(t) dt}. \quad (\text{A.2})$$

Recall that σ is related to the moments simply by

$$\sigma^2 = t_2 - t_1^2. \quad (\text{A.3})$$

Now, we see that

$$\frac{\partial t_1}{\partial \tau} = \frac{1}{D} \frac{\partial N}{\partial \tau} - \frac{N}{D^2} \frac{\partial D}{\partial \tau} \quad (\text{A.4})$$

$$= \frac{1}{D} \int t \cdot A(t) \cdot e^{-t/\tau} \left(\frac{t}{\tau^2} \right) dt - \frac{N}{D^2} \int A(t) \cdot e^{-t/\tau} \left(\frac{t}{\tau^2} \right) dt \quad (\text{A.5})$$

$$= \frac{t_2 - t_1^2}{\tau^2} \quad (\text{A.6})$$

$$= \frac{\sigma^2}{\tau^2} \quad (\text{A.7})$$

Thus, the lifetime difference in the two modes can be obtained from the difference in measured mean lifetime:

$$\Delta\tau = \frac{\tau^2}{\sigma^2} \Delta t_1. \quad (\text{A.8})$$

[†]Developed by Dr. M. Purohit.

A.2 $\Delta\tau$ in the Case of Unequal Acceptance

In the previous section we assumed that $A(t)$ is the same for both modes. However, we know that there could be differences in the acceptance for the two modes. For instance, there is less phase space in the $K^\pm K^\mp$ mode so the lab frame opening angle may be smaller leading to somewhat different acceptance. This may be a bigger effect at higher momenta. Similarly, due to differences in Čerenkov cuts the acceptance could be different in the two modes. Again, this could be a momentum dependent effect. So we must think about how to measure $\Delta\tau$ in spite of differences in acceptance.[†]

One important fact is that the acceptance is really a function of the lab frame attributes of the decay particles. After integrating over those variables, we may think of the acceptance as a function of the lab frame D^0 variables: t , p_z , and p_T . Since the D^0 is spinless, it is sufficient to consider the acceptance as $A(t, \vec{p})$, but the argument is the same regardless of how many variables A depends on. Take the vector \vec{p} to denote “all D^0 variables.” Note that $A(t)$ does not depend on lifetime τ , but on decay time t .

Let us then call the acceptance in the two modes as $_{KK}A(t, \vec{p})$ and $_{K\pi}A(t, \vec{p})$ and the density of D^0 's to be $f(\vec{p})$. The mean measured decay time in the two modes will be given by

$$_{KK}t_1 \equiv \frac{\int dt \, t \, \exp(-t/\tau_{KK}) \int d\vec{p} \, f(\vec{p}) \, _{KK}A(t, \vec{p})}{\int dt \, \exp(-t/\tau_{KK}) \int d\vec{p} \, f(\vec{p}) \, _{KK}A(t, \vec{p})}. \quad (\text{A.9})$$

Similarly, for the $K^\mp \pi^\pm$ mode

$$_{K\pi}t_1 \equiv \frac{\int dt \, t \, \exp(-t/\tau_{K\pi}) \int d\vec{p} \, f(\vec{p}) \, _{K\pi}A(t, \vec{p})}{\int dt \, \exp(-t/\tau_{K\pi}) \int d\vec{p} \, f(\vec{p}) \, _{K\pi}A(t, \vec{p})}. \quad (\text{A.10})$$

[†]Developed by Dr. M. Purohit.

Defining the acceptance integrated over everything except the proper time t as

$${}_{KK}A(t) \equiv \int d\vec{p} f(\vec{p}) {}_{KK}A(t, \vec{p})$$

and

$${}_{K\pi}A(t) \equiv \int d\vec{p} f(\vec{p}) {}_{K\pi}A(t, \vec{p}).$$

We see that

$${}_{KK}t_1 \equiv \frac{\int dt t \exp(-t/\tau_{KK}) {}_{KK}A(t)}{\int dt \exp(-t/\tau_{KK}) {}_{KK}A(t)} \quad (\text{A.11})$$

and

$${}_{K\pi}t_1 \equiv \frac{\int dt t \exp(-t/\tau_{K\pi}) {}_{K\pi}A(t)}{\int dt \exp(-t/\tau_{K\pi}) {}_{K\pi}A(t)}. \quad (\text{A.12})$$

It is conceivable that ${}_{KK}A(t)$ will be different from ${}_{K\pi}A(t)$ despite the fact that momentum and t are uncorrelated. In general, these are different functions and we can write without loss of generality

$${}_{KK}A(t) = g(t) \cdot {}_{K\pi}A(t) \quad (\text{A.13})$$

where $g(t)$ is some function of t which can be determined from MC. We will see below that we do not actually need to determine $g(t)$.

Now,

$$\begin{aligned} {}_{KK}t_1 &\equiv \frac{\int dt t \exp(-t/\tau_{KK}) {}_{KK}A(t)}{\int dt \exp(-t/\tau_{KK}) {}_{KK}A(t)} \\ &= \frac{\int dt t \exp(-t/\tau_{KK}) g(t) {}_{K\pi}A(t)}{\int dt \exp(-t/\tau_{KK}) g(t) {}_{K\pi}A(t)} \\ &= \frac{g_1 \int dt t \exp(-t/\tau_{K\pi}) {}_{K\pi}A(t)}{g_0 \int dt \exp(-t/\tau_{K\pi}) {}_{K\pi}A(t)} \end{aligned} \quad (\text{A.14})$$

where we have introduced two constants g_1 and g_0 defined by

$$g_1 \equiv \frac{\int dt t \exp(-t/\tau_{KK}) {}_{KK}A(t)}{\int dt t \exp(-t/\tau_{KK}) {}_{K\pi}A(t)} \quad (\text{A.15})$$

and

$$g_0 \equiv \frac{\int dt \exp(-t/\tau_{KK}) {}_{KK}A(t)}{\int dt \exp(-t/\tau_{KK}) {}_{K\pi}A(t)}. \quad (\text{A.16})$$

We see immediately that

$$\frac{g_1}{g_0} = \frac{{}_{KK}t_1^{MC}}{{}_{K\pi}t_1^{MC}} \quad (\text{A.17})$$

where ${}_{KK}t_1^{MC}$ and ${}_{K\pi}t_1^{MC}$ are defined as the mean accepted time for MC events in the KK and $K\pi$ modes respectively where both MC are generated using the same lifetime τ_{KK} .

We can rewrite Eq. A.14 as

$${}_{KK}t_1 = \frac{g_1}{g_0} {}_{KK}t_1^{K\pi} \quad (\text{A.18})$$

where ${}_{KK}t_1^{K\pi}$ stands for the mean measured decay time in the KK mode if the acceptance for the KK mode were the same as the more copious $K\pi$ mode. We know from the Eq. A.8 that

$$\begin{aligned} (\tau_{K\pi} - \tau_{KK}) &= \frac{\tau^2}{\sigma^2} \left({}_{K\pi}t_1 - \frac{g_0}{g_1} {}_{KK}t_1 \right) \\ &= \frac{\tau^2}{\sigma^2} \left[{}_{K\pi}t_1 - \left(\frac{{}_{K\pi}t_1^{MC\tau_{KK}}}{{}_{KK}t_1^{MC\tau_{KK}}} \right) {}_{KK}t_1 \right]. \end{aligned} \quad (\text{A.19})$$

The advantage of Eq. A.19 is obvious: we do not need to know the details of the difference in the acceptance in the two modes. We only need to know from MC the ratio $\frac{{}_{K\pi}t_1^{MC\tau_{KK}}}{{}_{KK}t_1^{MC\tau_{KK}}}$ which can be more easily determined to sufficient precision. Note again that the two MC samples should be generated with the same parameter τ_{KK} .

A.3 Comments

Eq. A.8 can only be used for a small lifetime difference due to the approximation from (in a single decay mode)

$$\frac{\partial t_1}{\partial \tau} = \frac{\sigma^2}{\tau^2}$$

to (between two decay modes)

$$\frac{\Delta t_1}{\Delta \tau} = \frac{\sigma^2}{\tau^2}.$$

Following Sec. A.1, to make acceptance corrections in each decay time bin for each mode, requires adequate MC statistics for each bin. Alternatively, Sec. A.2 shows a method of determining a gross MC acceptance correction. Ideally, we would expect that if we generate MC with the same τ_{KK} for $K^\pm K^\mp$ and $K^\mp \pi^\pm$ then it does not matter how accurate the MC τ_{KK} is, as long as it is the same for the $K^\pm K^\mp$ and $K^\mp \pi^\pm$ samples. But if we simply reverse Eq. A.13 as

$$_{K\pi}A(t) = g(t) \cdot _{KK}A(t) \quad (\text{A.20})$$

then we get

$$\begin{aligned} (\tau_{K\pi} - \tau_{KK}) &= \frac{\tau^2}{\sigma^2} \left(\frac{g_0}{g_1} _{K\pi}t_1 - _{KK}t_1 \right) \\ &= \frac{\tau^2}{\sigma^2} \left[\left(\frac{_{KK}t_1^{MC\tau_{K\pi}}}{_{K\pi}t_1^{MC\tau_{K\pi}}} \right) _{K\pi}t_1 - _{KK}t_1 \right]. \end{aligned} \quad (\text{A.21})$$

This requires that we generate the same MC $\tau_{K\pi}$ for $K^\pm K^\mp$ and $K^\mp \pi^\pm$.

Since both τ_{KK} and $\tau_{K\pi}$ are unknown, and we expect that $\Delta\tau$ is small compared with γ , the method in Eq. A.19 or Eq. A.21 is not sufficient to detect $\Delta\tau$ alone.

However I measure the separate τ_{KK} and $\tau_{K\pi}$ (described in Sec. 5.2), and I can thus use the measured τ_{KK} to generate two MC samples ($K^\pm K^\mp$ and $K^\mp \pi^\pm$) to find $\Delta\tau$ according to Eq. A.19. Similarly, I can use the measured $\tau_{K\pi}$ to generate two MC samples ($K^\pm K^\mp$ and $K^\mp \pi^\pm$) to find $\Delta\tau$ according to Eq. A.21. Both of these should give the same $\Delta\tau$, and I have then examined the measured τ_{KK} and $\tau_{K\pi}$.

APPENDIX B

CUT COMPARISONS OF MC AND DATA

In this Appendix, I use the sidebands of $D^0 \rightarrow K^- \pi^+$ to represent the BG under SG peak, and to produce the continuous cut distributions of SG by BG subtraction. Thus, it is very important to understand the BG distributions. Each figure in Appendix B has 3 rows (e.g. Fig. B.1). The first row is produced without any Čerenkov ID selection criteria; for data (the right column), I try both $K\pi$ and πK hypotheses on each vertex, so I double-count BG (but without double-counting in the SG peak) and create charm-like or double misidentified BG in the sidebands. In the second row, I apply loose Čerenkov criteria choosing the track with higher K_{ID} as the kaon. There is then no double-counting in BG, but still some charm-like or double misidentified events in the sidebands. In the third row, I apply Čerenkov criteria ($K_{ID} \geq .16$ as kaons and $K_{ID} < .16$ as pions), thus eliminating any double-counting or misidentification, but the inefficiency of the MC ID cuts has to be accounted for. I concentrate on the comparison of the second rows, but use the top and bottom rows as references and comparisons (e.g. Fig. B.6). the SG region is defined to be in the interval of MC(1.8345, 1.8945) and DATA(1.837, 1.897); the low sideband BG is MC(1.7245, 1.7845) and DATA(1.727, 1.787), and the high sideband BG is MC(1.9445, 2.0045) and DATA(1.947, 2.007). The results are not sensitive to the choice of sideband regions.

These comparisons serve two purpose:

- In order to choose a “matched” set of cuts for tuning the cuts, described in Sec. 4.2;
- To understand the systematic errors due to the MC inefficiency, described in Chapter VI.

The guideline is the comparison of the shapes and peak values between the distribution of MC SG and DATA SG (BG-subtracted).

For example, Fig. B.2 and Fig. B.3 show shifts in MC (the solid line) compared to DATA (the dotted line) in the left columns, and thus I avoid using DIP and PISO cuts in my analysis. Fig. B.6 shows no peak shift, and the slight mismatch can be accounted for by the difficulty in deducing the BG-subtraction from the DATA sidebands. Fig. B.13 indicates the failure of the MC production model to accurately reproduce the D^0 momentum spectrum. The bottom left plots of Fig. B.14 and Fig. B.15 indicate the inefficiency of the Čerenkov identification in the MC.

Cuts comparison for MC and DATA of mkpi2422

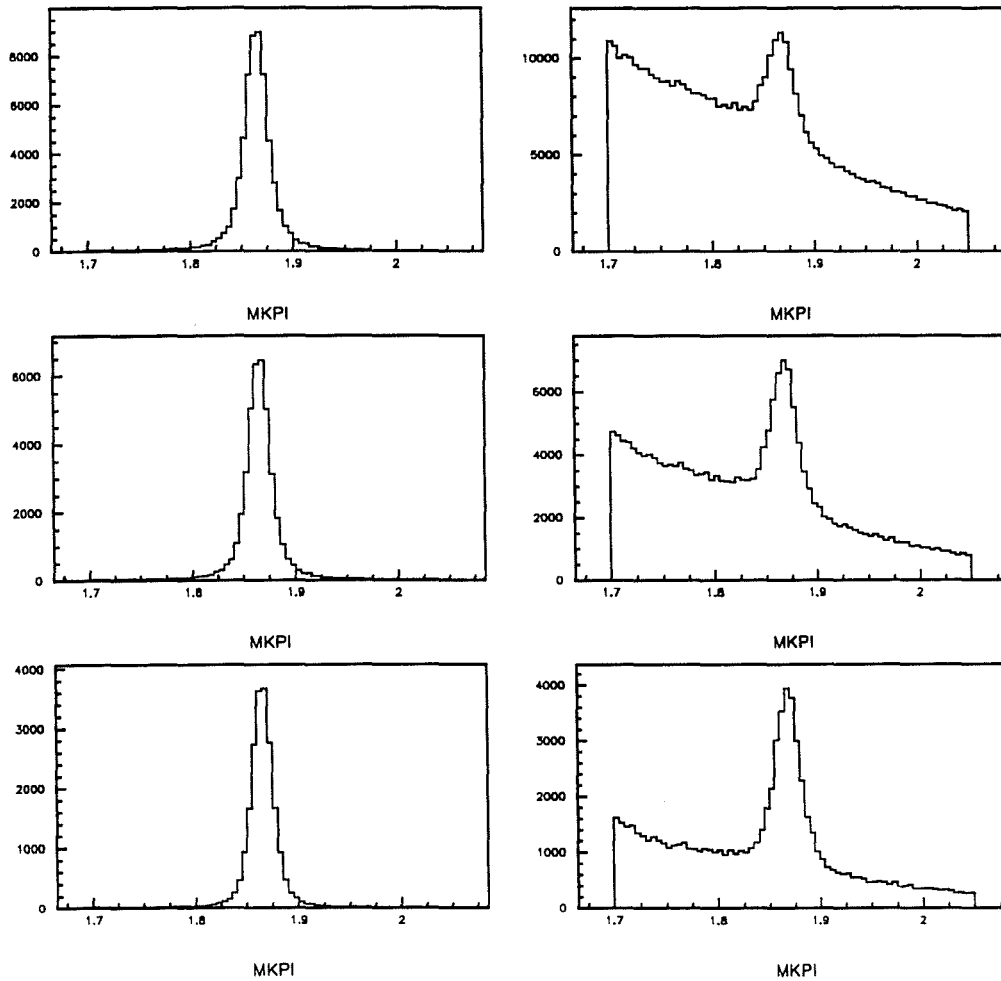


Figure B.1. Mass plots in the left column are from MC in 3 stages:
 (1) try both $K\pi$ and πK hypothesis (no ID cuts, but double-counting in BG);
 (2) choose higher kaon ID as kaon (loose ID cuts, no double-counting);
 (3) $K_{ID} \geq .16$ as kaon, and $K_{ID} < .16$ as pion (tight ID cut, to reduce BG).
 The plots in the right column are from DATA in the equivalent 3 stages.

Cuts comparison for MC and DATA of mkpi2422

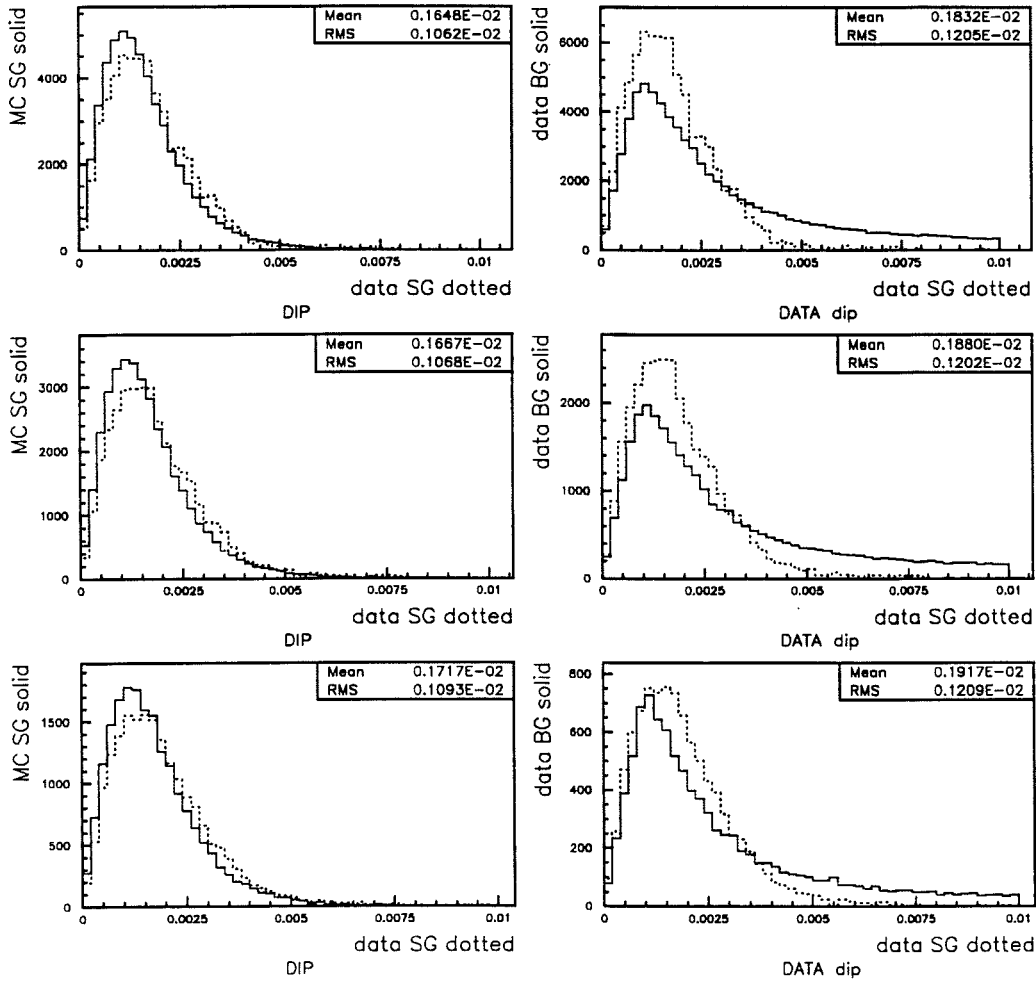


Figure B.2. DIP cut distribution comparisons are done in 3 stages in order to understand the BG subtraction in DATA:

Solid lines in the left column are from MC SG, the solid lines in the right are from normalized DATA BG, and the dotted line in both columns are from normalized BG-subtracted DATA SG (left dotted lines are normalized to MC SG numbers and right dotted line to the height). The mean and rms values in the left column are for MC SG, and the values in the right are for DATA SG.

Cuts comparison for MC and DATA of mkpi2422

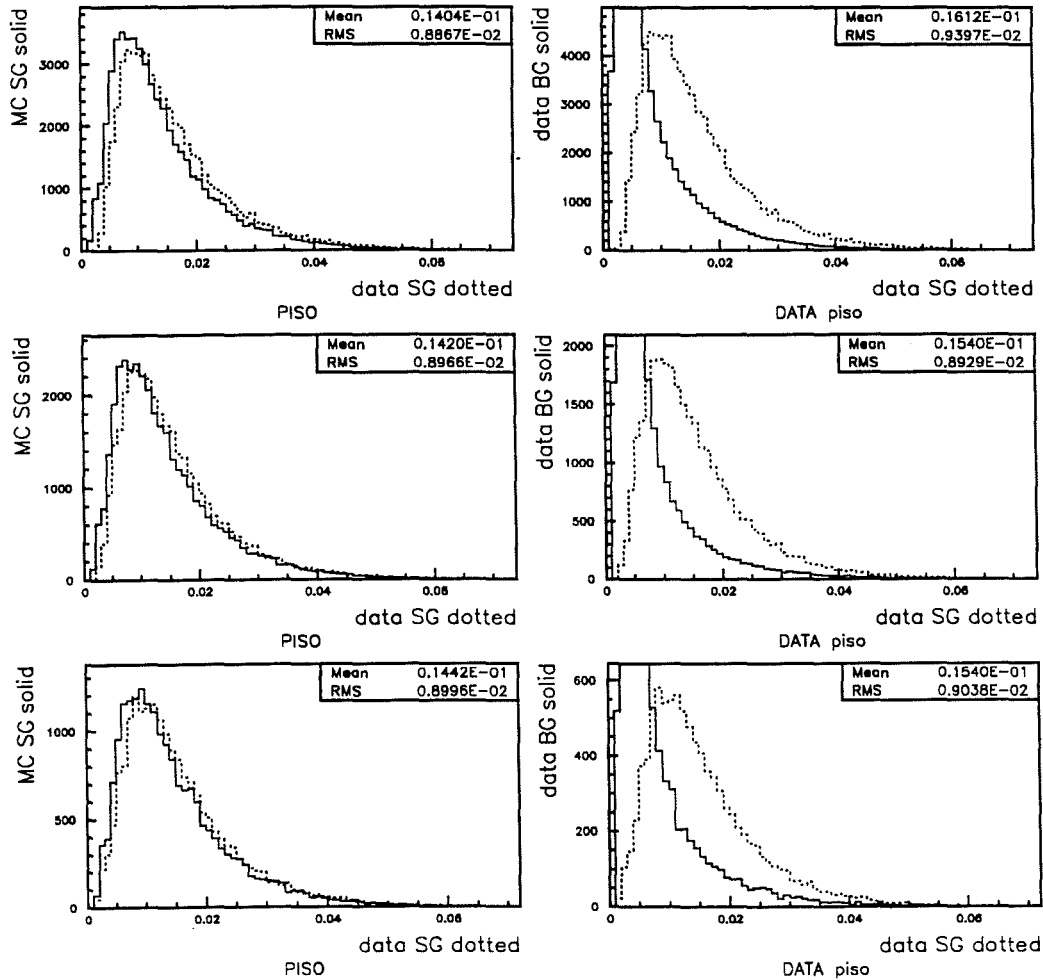


Figure B.3. PISO cut distribution comparisons are done in 3 stages in order to understand the BG subtraction in DATA:

Solid lines in the left column are from MC SG, the solid lines in the right are from normalized DATA BG, and the dotted line in both columns are from normalized BG-subtracted DATA SG (left dotted lines are normalized to MC SG numbers and right dotted line to the height). The mean and rms values in the left column are for MC SG, and the values in the right are for DATA SG.

Cuts comparison for MC and DATA of mkpi2422

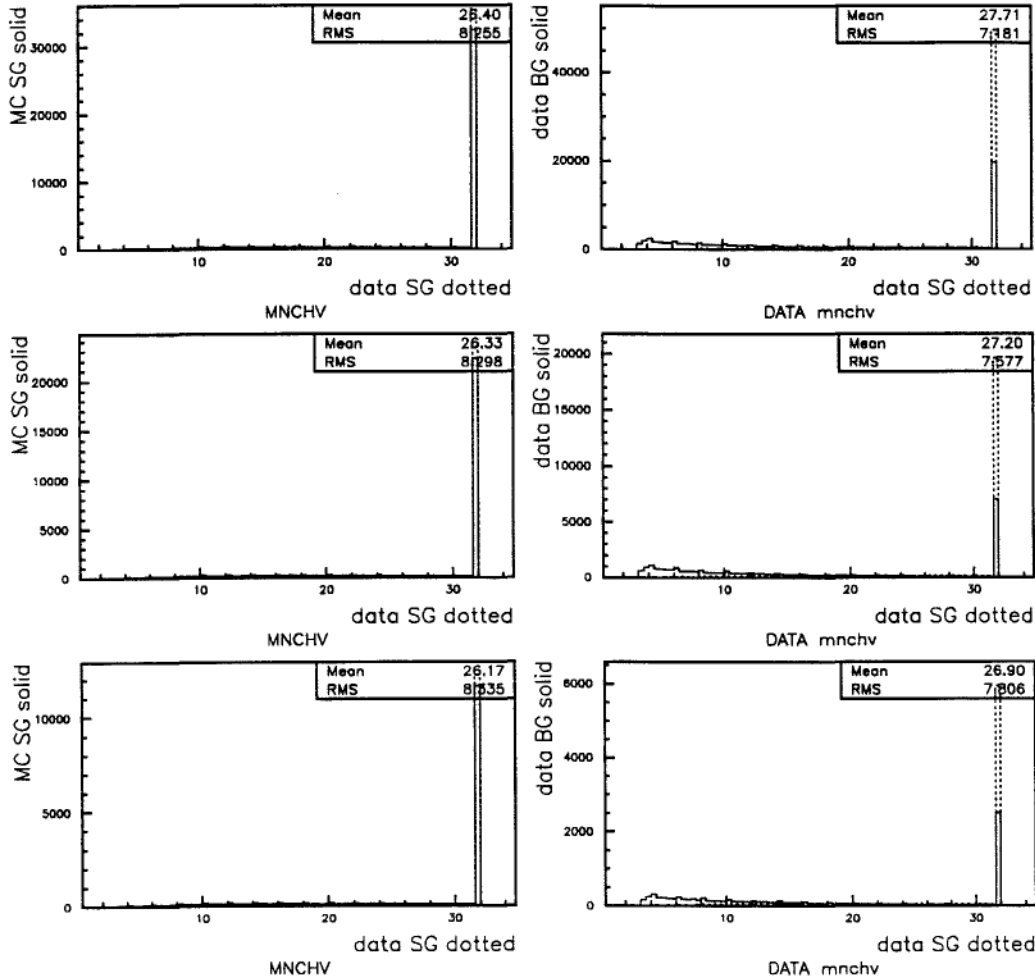


Figure B.4. MNCHV cut distribution comparisons are done in 3 stages in order to understand the BG subtraction in DATA:

Solid lines in the left column are from MC SG, the solid lines in the right are from normalized DATA BG, and the dotted line in both columns are from normalized BG-subtracted DATA SG (left dotted lines are normalized to MC SG numbers and right dotted line to the height). The mean and rms values in the left column are for MC SG, and the values in the right are for DATA SG.

Cuts comparison for MC and DATA of mkpi2422

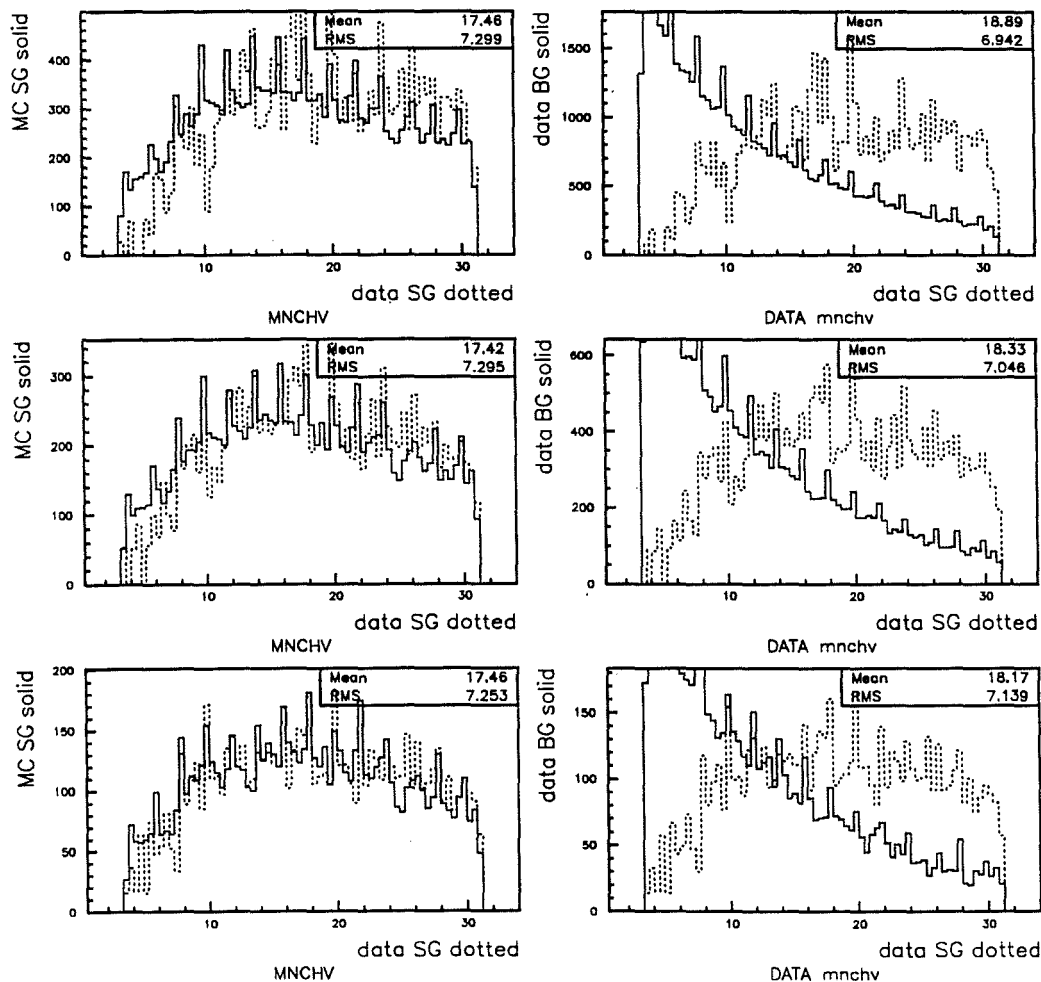


Figure B.5. MNCHV (without 32) cut comparisons are done in 3 stages in order to understand the BG subtraction in DATA:

Solid lines in the left column are from MC SG, the solid lines in the right are from normalized DATA BG, and the dotted line in both columns are from normalized BG-subtracted DATA SG (left dotted lines are normalized to MC SG numbers and right dotted line to the height). The mean and rms values in the left column are for MC SG, and the values in the right are for DATA SG.

Cuts comparison for MC and DATA of mkpi2422

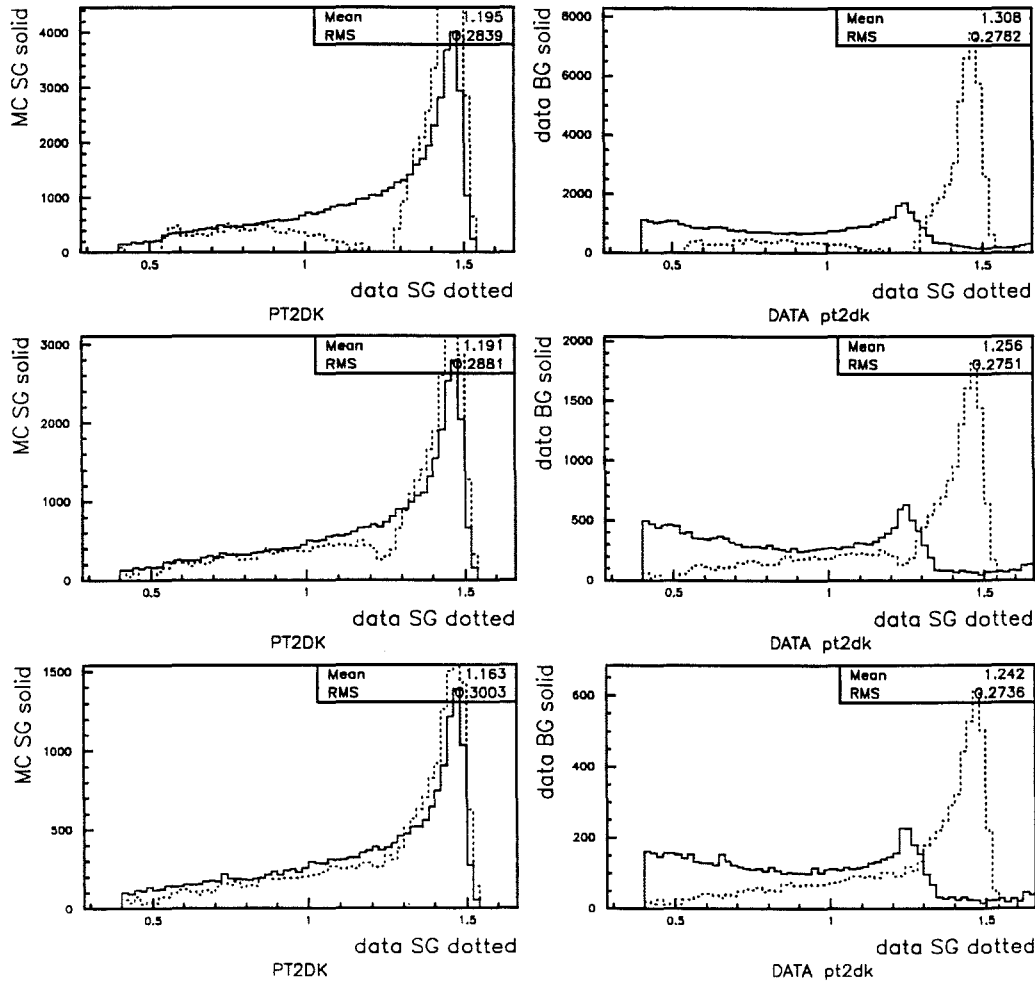


Figure B.6. PT2DK cut distribution comparisons are done in 3 stages in order to understand the BG subtraction in DATA:

Solid lines in the left column are from MC SG, the solid lines in the right are from normalized DATA BG, and the dotted line in both columns are from normalized BG-subtracted DATA SG (left dotted lines are normalized to MC SG numbers and right dotted line to the height). The mean and rms values in the left column are for MC SG, and the values in the right are for DATA SG.

Cuts comparison for MC and DATA of mkpi2422

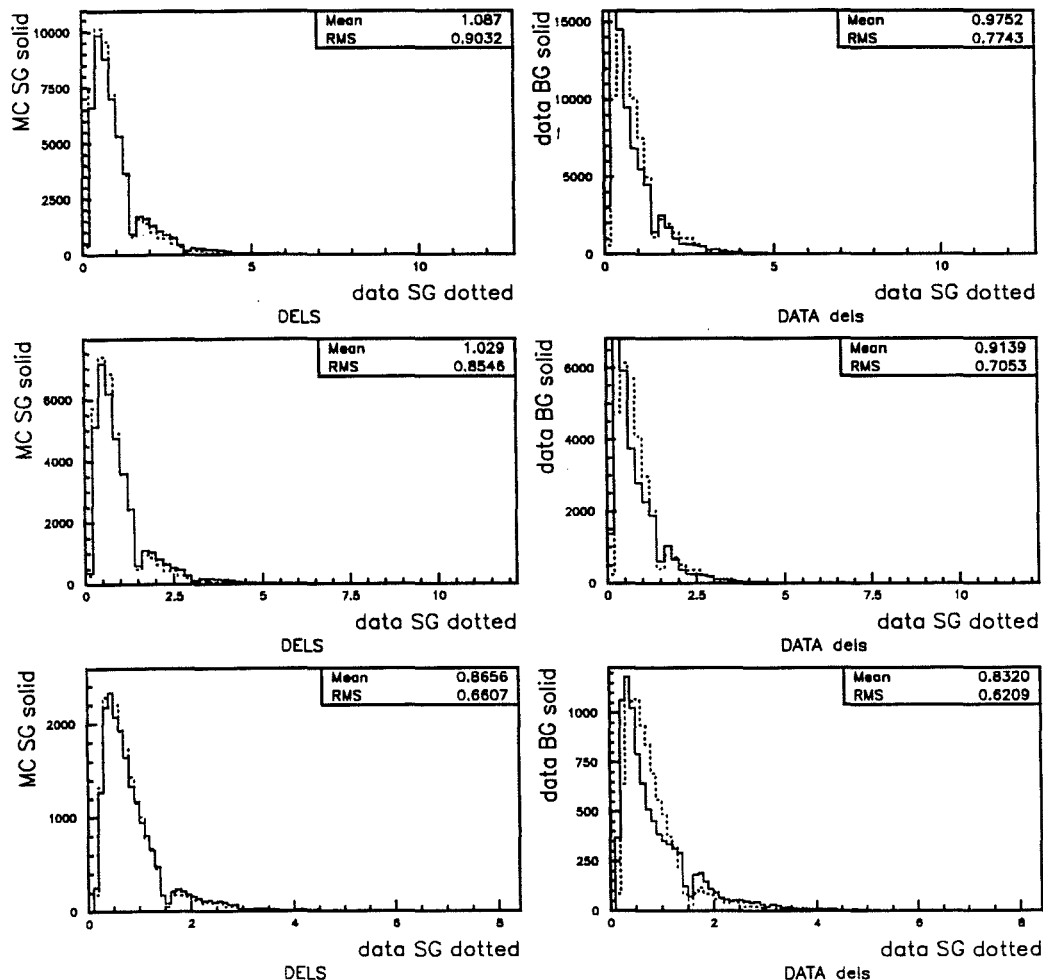


Figure B.7. Decay Distance distribution comparisons are done in 3 stages in order to understand the BG subtraction in DATA:

Solid lines in the left column are from MC SG, the solid lines in the right are from normalized DATA BG, and the dotted line in both columns are from normalized BG-subtracted DATA SG (left dotted lines are normalized to MC SG numbers and right dotted line to the height). The mean and rms values in the left column are for MC SG, and the values in the right are for DATA SG.

Cuts comparison for MC and DATA of mkpi2422

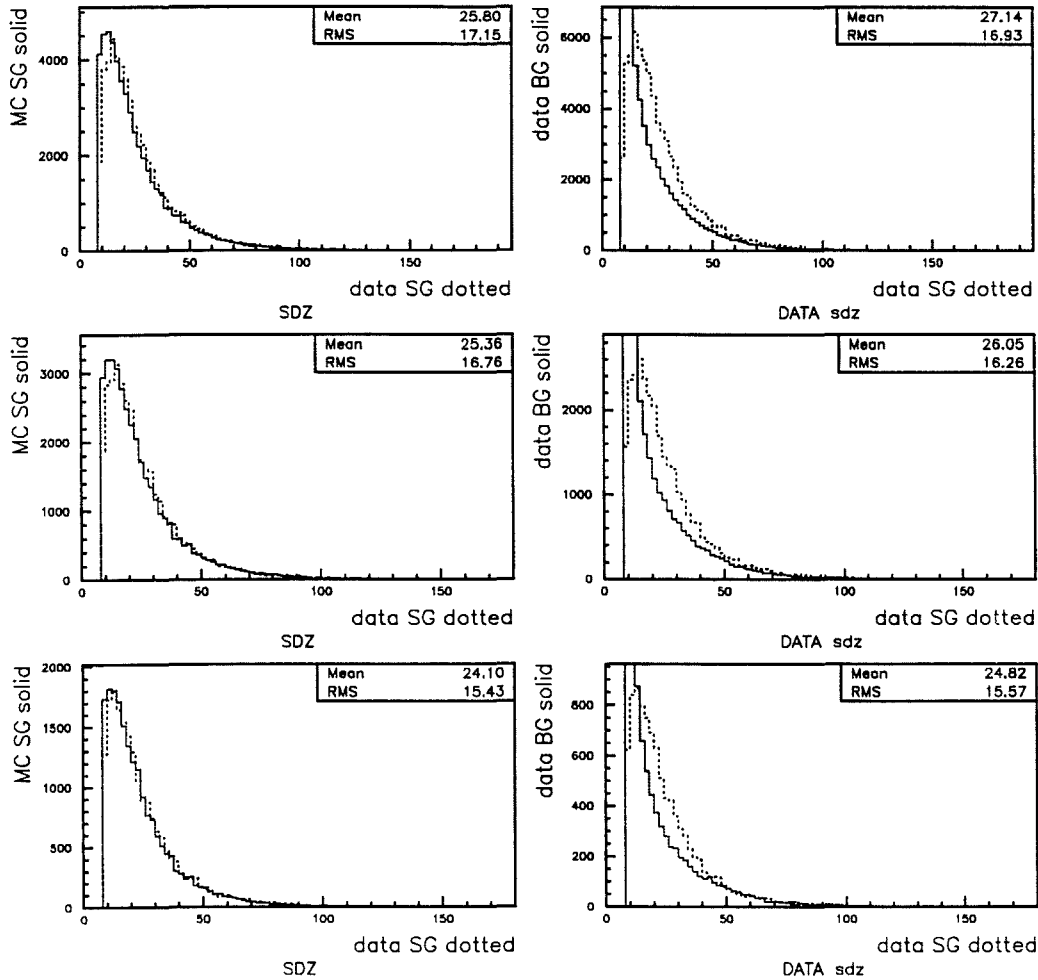


Figure B.8. SDZ cut distribution comparisons are done in 3 stages in order to understand the BG subtraction in DATA:

Solid lines in the left column are from MC SG, the solid lines in the right are from normalized DATA BG, and the dotted line in both columns are from normalized BG-subtracted DATA SG (left dotted lines are normalized to MC SG numbers and right dotted line to the height). The mean and rms values in the left column are for MC SG, and the values in the right are for DATA SG.

Cuts comparison for MC and DATA of mkpi2422

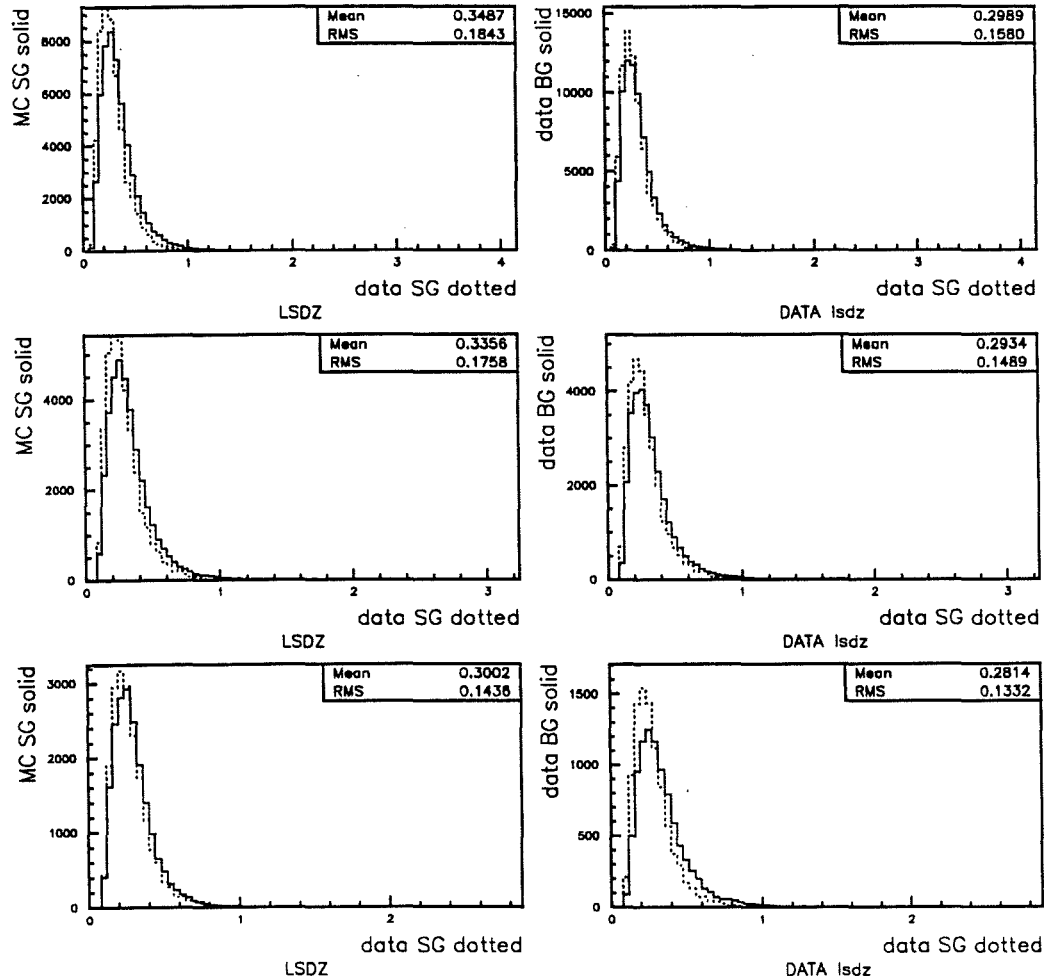


Figure B.9. L_{SDZ}^{min} distribution comparisons are done in 3 stages in order to understand the BG subtraction in DATA:

Solid lines in the left column are from MC SG, the solid lines in the right are from normalized DATA BG, and the dotted line in both columns are from normalized BG-subtracted DATA SG (left dotted lines are normalized to MC SG numbers and right dotted line to the height). The mean and rms values in the left column are for MC SG, and the values in the right are for DATA SG.

Cuts comparison for MC and DATA of mkpi2422

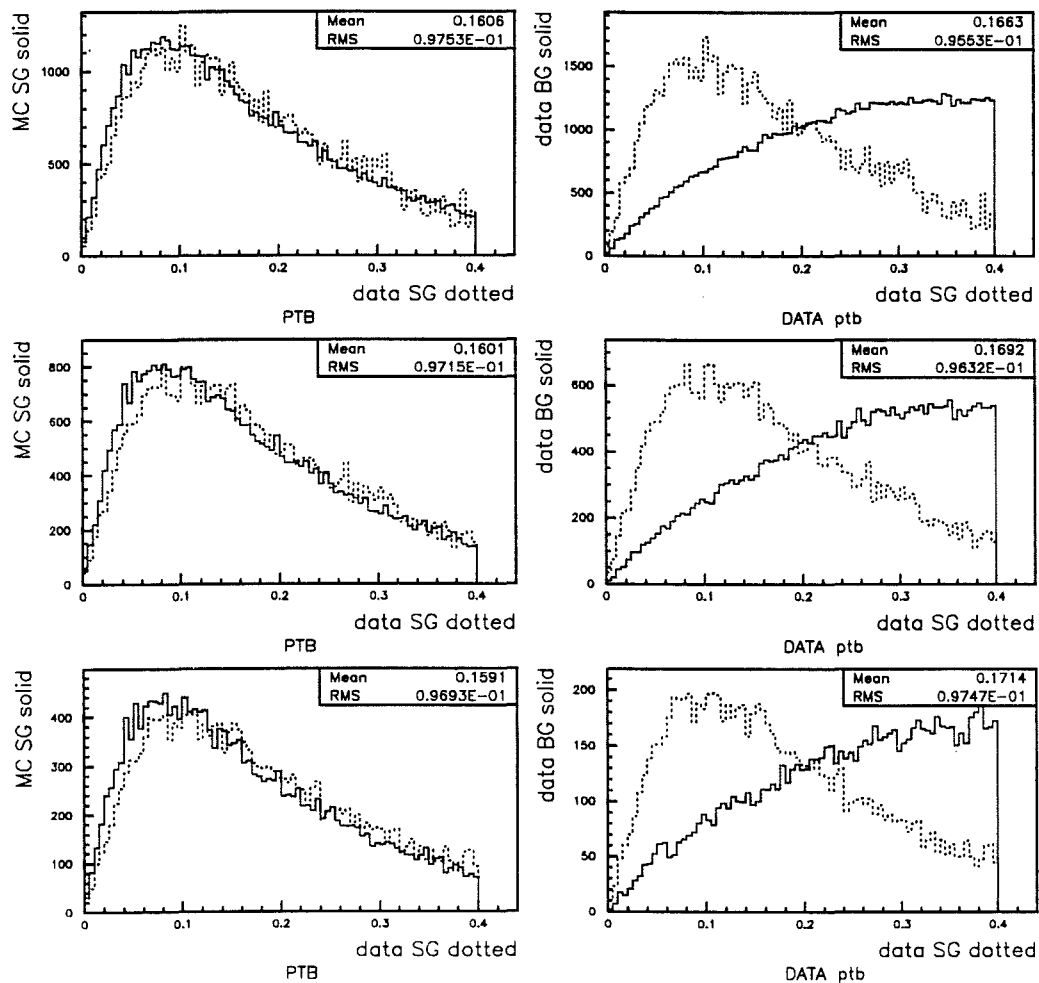


Figure B.10. PTBAL cut distribution comparisons are done in 3 stages in order to understand the BG subtraction in DATA:

Solid lines in the left column are from MC SG, the solid lines in the right are from normalized DATA BG, and the dotted line in both columns are from normalized BG-subtracted DATA SG (left dotted lines are normalized to MC SG numbers and right dotted line to the height). The mean and rms values in the left column are for MC SG, and the values in the right are for DATA SG.

Cuts comparison for MC and DATA of mkpi2422

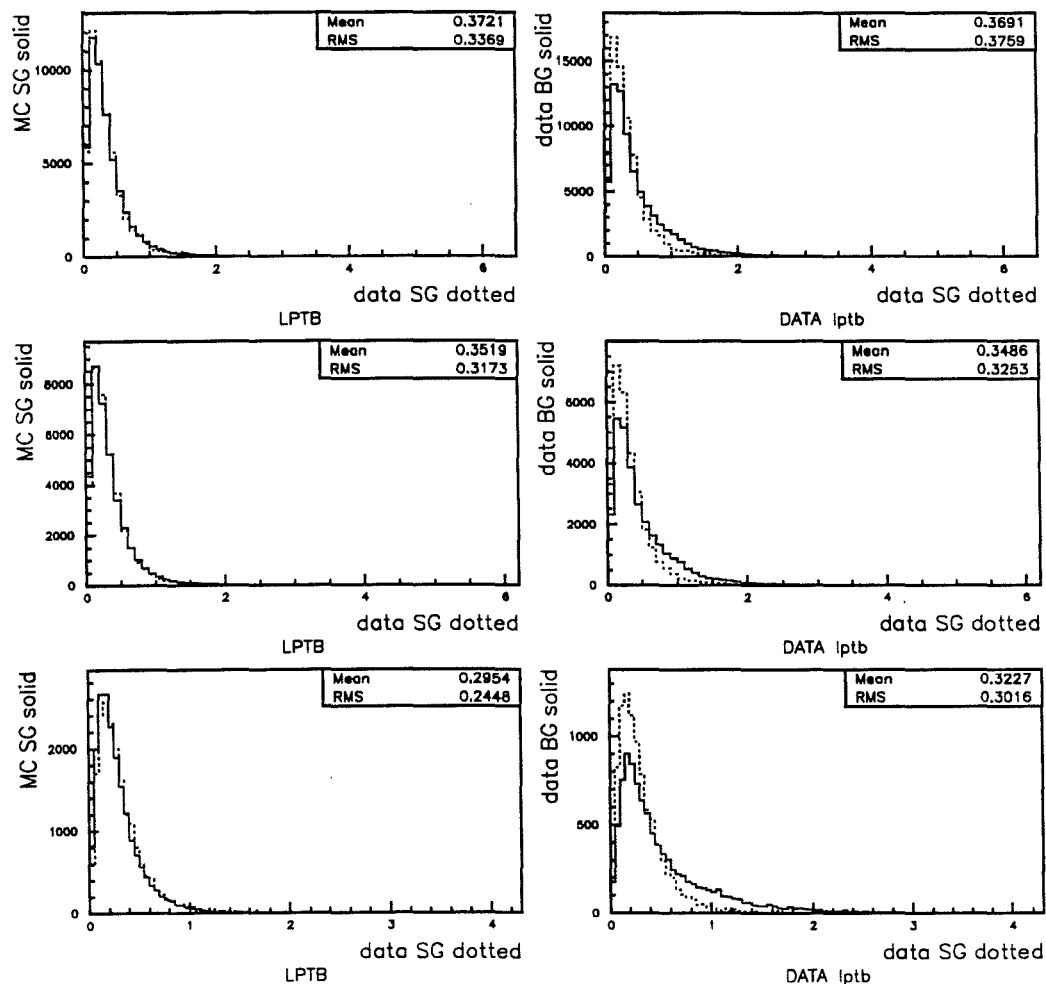


Figure B.11. L_{min}^{PTBAL} distribution comparisons are done in 3 stages in order to understand the BG subtraction in DATA:

Solid lines in the left column are from MC SG, the solid lines in the right are from normalized DATA BG, and the dotted line in both columns are from normalized BG-subtracted DATA SG (left dotted lines are normalized to MC SG numbers and right dotted line to the height). The mean and rms values in the left column are for MC SG, and the values in the right are for DATA SG.

Cuts comparison for MC and DATA of mkpi2422

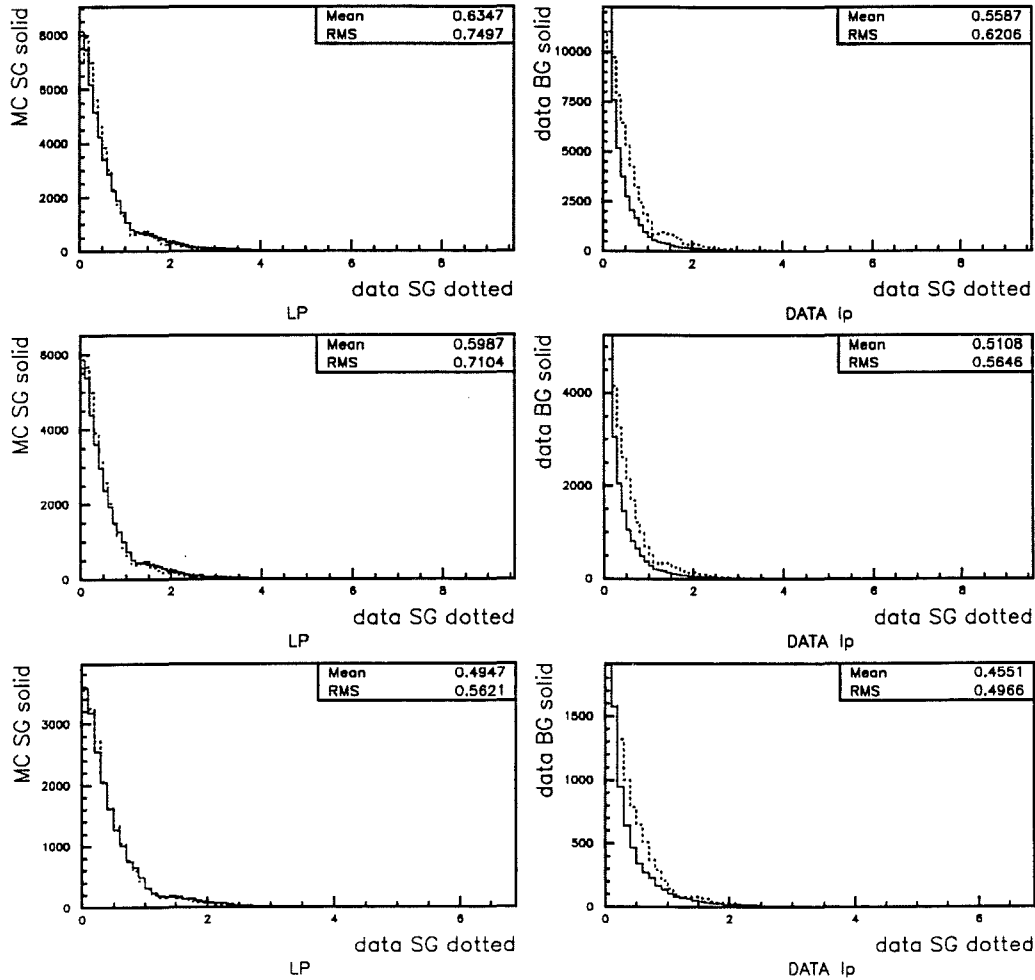


Figure B.12. Reduced Length distribution comparisons are done in 3 stages in order to understand the BG subtraction in DATA:

Solid lines in the left column are from MC SG, the solid lines in the right are from normalized DATA BG, and the dotted line in both columns are from normalized BG-subtracted DATA SG (left dotted lines are normalized to MC SG numbers and right dotted line to the height). The mean and rms values in the left column are for MC SG, and the values in the right are for DATA SG.

Cuts comparison for MC and DATA of mkpi2422

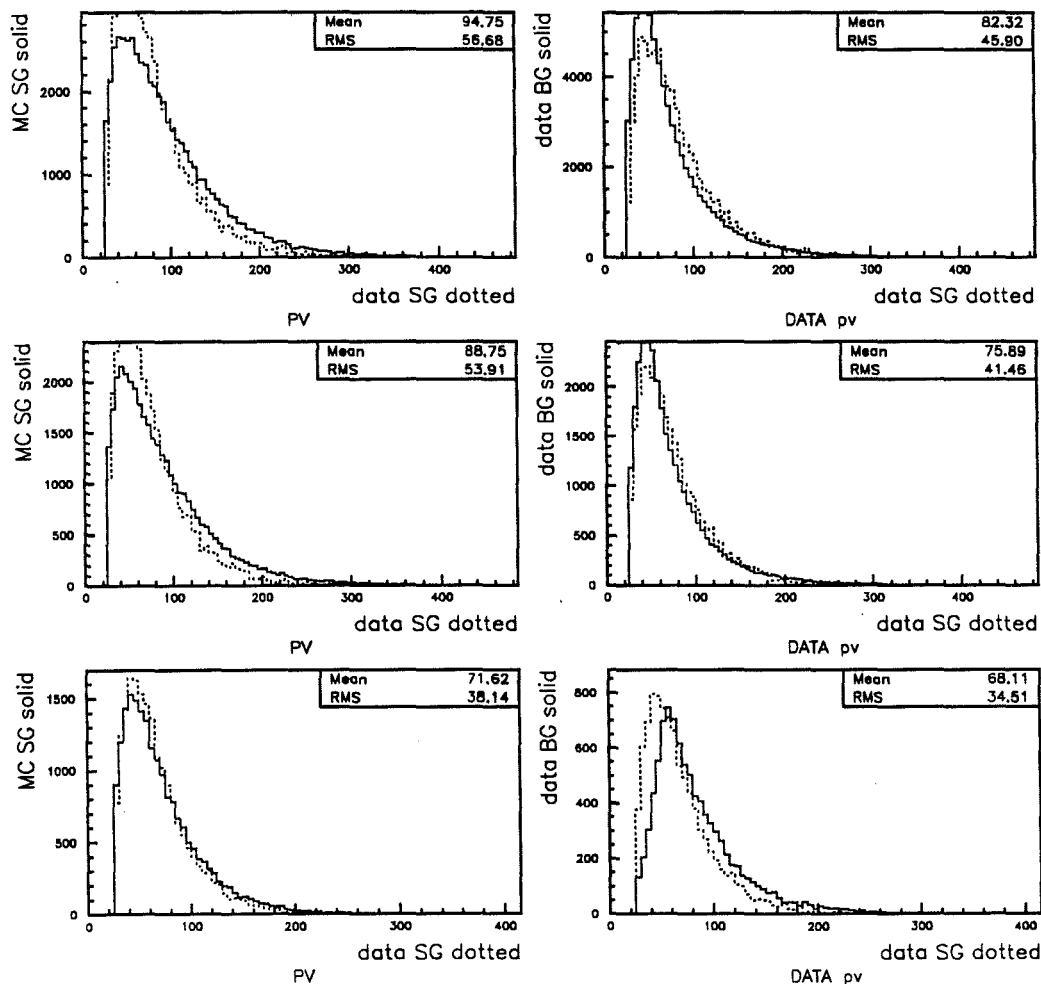


Figure B.13. D^0 Momentum distribution comparisons are done in 3 stages in order to understand the BG subtraction in DATA:

Solid lines in the left column are from MC SG, the solid lines in the right are from normalized DATA BG, and the dotted line in both columns are from normalized BG-subtracted DATA SG (left dotted lines are normalized to MC SG numbers and right dotted line to the height). The mean and rms values in the left column are for MC SG, and the values in the right are for DATA SG.

Cuts comparison for MC and DATA of mkpi2422

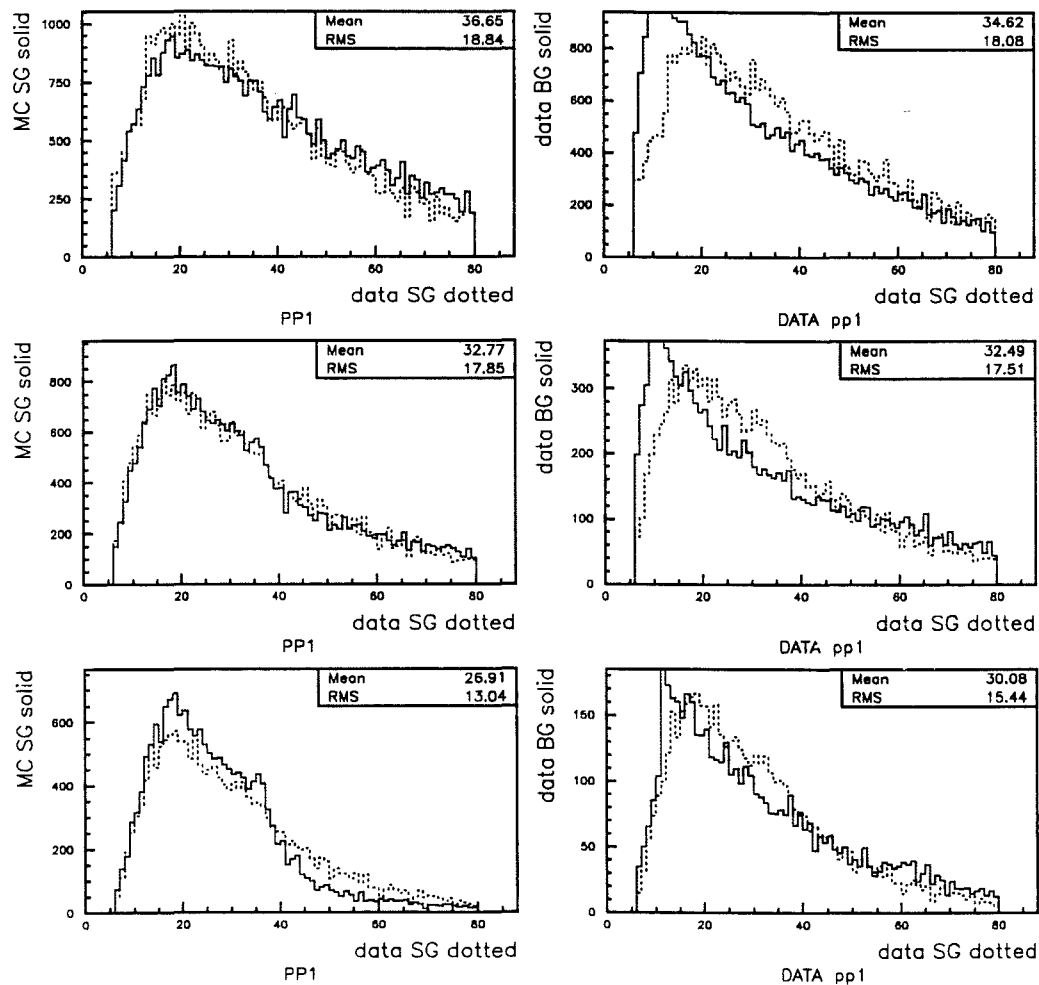


Figure B.14. K^- Momentum distribution comparisons are done in 3 stages in order to understand the BG subtraction in DATA:

Solid lines in the left column are from MC SG, the solid lines in the right are from normalized DATA BG, and the dotted line in both columns are from normalized BG-subtracted DATA SG (left dotted lines are normalized to MC SG numbers and right dotted line to the height). The mean and rms values in the left column are for MC SG, and the values in the right are for DATA SG.

Cuts comparison for MC and DATA of mkpi2422

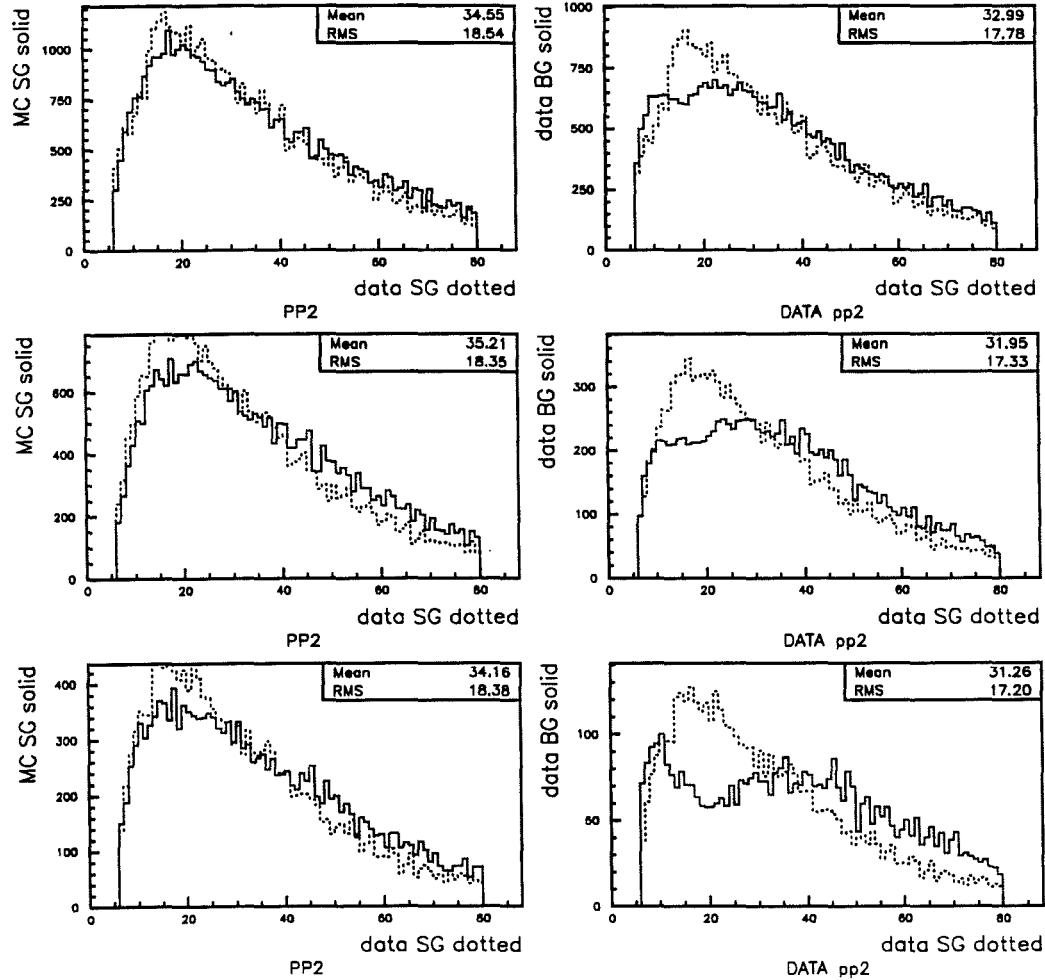


Figure B.15. π^+ Momentum distribution comparisons are done in 3 stages in order to understand the BG subtraction in DATA:

Solid lines in the left column are from MC SG, the solid lines in the right are from normalized DATA BG, and the dotted line in both columns are from normalized BG-subtracted DATA SG (left dotted lines are normalized to MC SG numbers and right dotted line to the height). The mean and rms values in the left column are for MC SG, and the values in the right are for DATA SG.

Cuts comparison for MC and DATA of mkpi2422

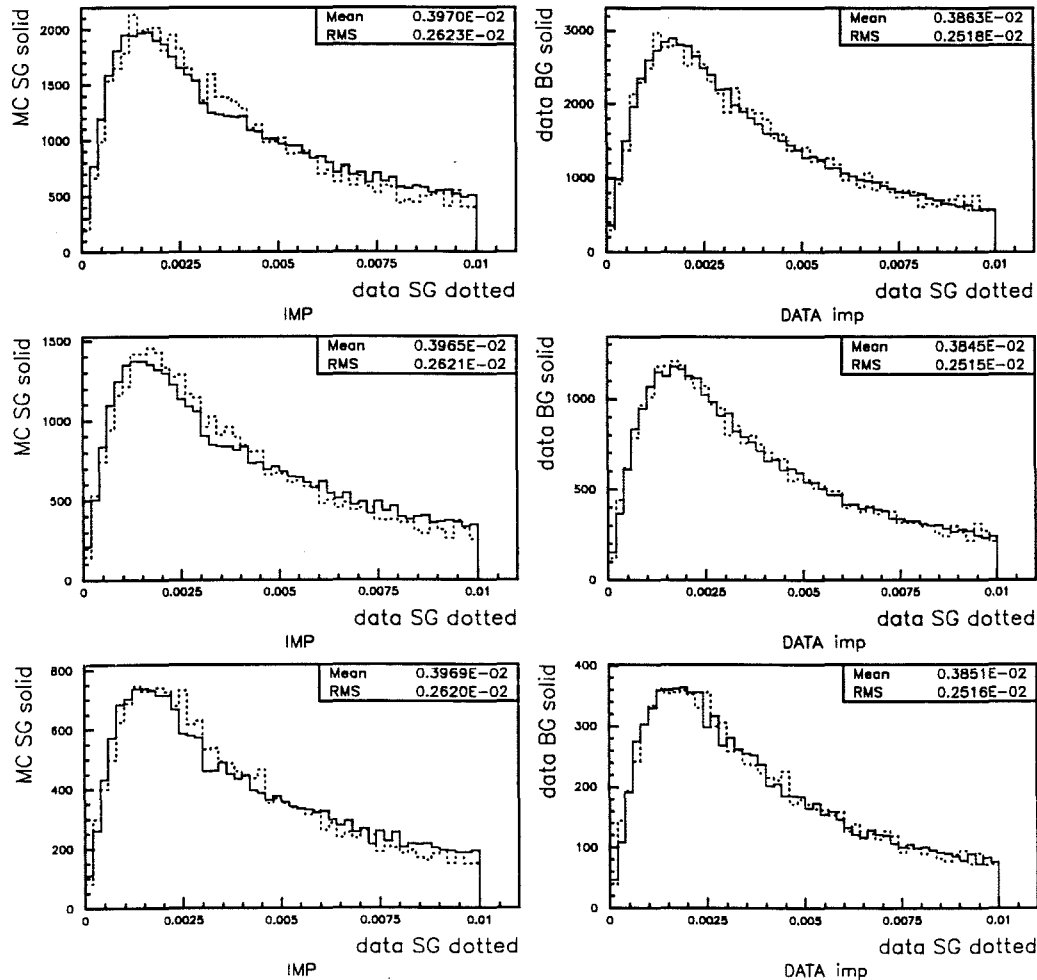


Figure B.16. IMPACT cut distribution comparisons are done in 3 stages in order to understand the BG subtraction in DATA:

Solid lines in the left column are from MC SG, the solid lines in the right are from normalized DATA BG, and the dotted line in both columns are from normalized BG-subtracted DATA SG (left dotted lines are normalized to MC SG numbers and right dotted line to the height). The mean and rms values in the left column are for MC SG, and the values in the right are for DATA SG.

REFERENCES

- [BS85] M. Bauer and B. Stech, "Exclusive D-Decays," Phys. Lett. B 152 (1985) pp. 380-384.
- [BSW85] M. Wirbel, B. Stech, and M. Bauer, "Exclusive Semileptonic Decays of Heavy Mesons," Z. Phys. C 29 (1985) pp. 637-642.
- [BSW87] M. Bauer, B. Stech, and M. Wirbel, "Exclusive Non-Leptonic Decays of D^- , D_s^- and B -Mesons," Z. Phys. C 34 (1987) p. 103.
- [BaPa79] V. Barger and S. Pakvasa, "Two-body Hadronic Decays of D Mesons," Phys. Rev. Lett. 43 (1979) pp. 812-815.
- [BeJa81] J. Bernabeu and C. Jarlskog, "CP Violation in Decay Rates of Charged Bottom Mesons," Z. Phys. C 8 (1981) pp. 233-238.
- [BiSa81] I.I. Bigi and A.I. Sanda, "Notes on the Observability of CP Violations in B Decays," Nucl. Phys. B 193 (1981) pp. 85-108.
- [BiSa86] I.I. Bigi and A.I. Sanda, "On D^0 - \bar{D}^0 Mixing and CP Violation," Phys. Lett. B 171 (1986) pp. 320-324.
- [BuLu93] F. Buccella *et al.*, "CP Violating Asymmetries in Charged D Meson decays," Phys. Lett. B 302 (1993) pp. 319-325.
- [Bur86] A.J. Buras, J.-M. Gerard, and R. Rückl, "1/N Expansion for Exclusive and Inclusive Charm Decays," Nucl. Phys. B 268 (1986) pp. 16-48.
- [CaSa81] A.B. Carter and A.I. Sanda, "CP Violation in B-meson Decay," Phys. Rev. D v 23 (1981) pp. 1567-1579.
- [ChCh84] L.L. Chau and H.Y. Cheng, "CP Nonconservation in the Partial Decay Rates of Charm and Beauty Mesons," Phys. Rev. Lett. 53 (1984) pp. 1037-1040.
- [ChCh85] L.L. Chau and H.Y. Cheng, "CP Violation in Decay Rates of Neutral B Mesons," Phys. Lett. B 165 (1985) pp. 429-433.
- [ChCh86] L.L. Chau and H.Y. Cheng, "Quark-Diagram Analysis of Two-Body Charm Decays," Phys. Rev. Lett. 56 (1986) p. 1655.
- [ChCh87] L.L. Chau and H.Y. Cheng, "Analysis of Two-body Decays of Charm Mesons Using the Quark-diagram Scheme," Phys. Rev. D v 36 pp. 137-153.
- [ChCh891] L.L. Chau and H.Y. Cheng, "Analysis of Two-Body Decays of Charm Mesons Using the Quark-Diagram Scheme: Addendum on Hairpin Diagrams," Phys. Rev. D 39 (1989) pp. 2788-2791.

- [ChCh892] L.L. Chau and H.Y. Cheng, "Analysis of the Recent Data of Exclusive Two-Body Charm Decays," Phys. Lett. B 222 (1989) pp. 285-292.
- [ChCh90] L.L. Chau and H.Y. Cheng, "Predictions for the Quark-Mixing Doubly Suppressed Decays of Charmed Mesons," Phys. Rev. D 42 (1990) pp. 1837-1840.
- [ChCh92] L.L. Chau and H.Y. Cheng, "Final-state-interaction and SU(3)-breaking Effects in $D^0 \rightarrow \pi^+ \pi^-$, $K \bar{K}$," Phys. Lett. B 280 (1992) pp. 281-286.
- [ChCh94] L.L. Chau and H.Y. Cheng, "SU(3) Breaking Effects in Charmed Meson Decays," Phys. Lett. B 333 (1994) pp. 514-518.
- [Chau79] L.L. Chau, Phys. Rev. Lett. 43 (1979) p. 816.
- [Chen94] H.Y. Cheng, "Nonfactorizable Contributions to Nonleptonic Weak Decays of Heavy Mesons," Phys. Lett. B 335 (1994) pp. 428-435.
- [Commins] E. D. Commins and P. H. Bucksbaum, Weak Interaction of Leptons and Quarks, Cambridge University Press (1983).
- [Du88] I. Dunietz, "Rephase Invariance of KM Matrices and CP Violation," Ann. Phys., 184 (1988) pp. 350-410.
- [EiQu75] M.B. Einhorn and C. Quigg, "Nonleptonic Decays of Charmed Mesons: Implications for e^+e^- Annihilation," Phys. Rev. D 12 (1975) pp. 2015-2030.
- [Finj81] J. Finjord, "The Magnitude of Annihilation and Penguin Contributions to Charm-meson Decays," Nucl. Phys. B 181(1981) pp. 74-90.
- [FrMi80] H. Fritzsch and p. Minkowski, Nucl. Phys. B 171 (1980) p. 413.
- [Frodesen] A.G. Frodesen, O. Skjeggstad, and H. Tofte, Probability and Statistics in Particle Physics, (1979), pp. 252-254.
- [Gluc79] M. Clück, "Cabibbo Suppressed Two-Body Hadronic Decays of D-Mesons," Phys. Lett. B 88 (1979) pp. 145-146.
- [GoGr89] M. Golden and B. Grinstein, "Enhanced CP Violations in Hadronic Charm Decays," Phys. Lett. B 222 (1989) pp. 501-506.
- [KaCo81] A. N. Kamal and E. D. Cooper, "Hadronic Interaction Correction to Two Body D^0 -Decays," Z. Phys. C 8 (1981) p. 67.
- [KaPh941] A. N. Kamal and T. N. Pham, "Test of Factorization in $D^0 \rightarrow \pi\pi$ and $K \bar{K}$ Decays," Phys. Rev. D 50 (1994) pp. 1832-1835.

- [KaPh942] A. N. Kamal and T. N. Pham, "Test of Factorization in Cabibbo-favored Two-body Decays of D Mesons," Phys. Rev. D 50 (1994) pp. 6849-6854.
- [KaSi87] A. N. Kamal and R. Sinha, "Coupled-Channel Treatment of Cabibbo-angle-suppressed $(D, D_s^+) \rightarrow PP$ Decays," Phys. Rev. D 36 (1987) pp. 3510-3513.
- [KaVe87] A. N. Kamal and R. C. Verma, "Analysis of Charm $\rightarrow PP$ Based on SU(3) Symmetry and Final-state Interactions," Phys. Rev. D 35 (1987) pp. 3515-3518.
- [KaXu92] A. Czarnecki, A. N. Kamal and Q. Xu, "On $D^0 \rightarrow \pi\pi$ and $K\bar{K}$ Decays," Z. Phys. C 54 (1992) pp. 411-417.
- [Kane88] G. Kane, "Modern Elementary Particle Physics." Addison-Wesley Publishing Company (1988).
- [Liu94] T. Liu, Harvard University Report No. HUTP-94/E201.
- [Liu95] T. Liu, Princeton University Report No. hep-ph/9508415.
- [MINUIT] MINUIT, version 94.1, p. 40.
- [Na94] T. Nakada, "Review on CP Violation"
Lepton and Photon Interactions, (AIP, NY, 1994) pp. 425-463.
- [PDG94] Physical Review D Particles and Fields, August 1994.
- [PaWu95] W. F. Palmer and Y. L. Wu, "Rephase-invariant CP-violating observables and mixings in the B^0 -, D^0 - and K^0 -systems," Phys. Lett. B 350 (1995) pp. 245-251.
- [Pham86] X. Y. Pham, "Desperately Seeking Penguin or Non Local Effect in the CHarm Sector," Mod. Phys. Lett. v 1 No.11 (1986) pp. 619-629.
- [Pythia] T. Sjöstrand, Pythia 5.7 and Jetset 7.4, (1993).
- [Solnitz] F. Solnitz, "Analysis of Experiments in Particle Physics," Ann. Rev. Nucl. Sci. v 14, p. 375 (1964).
- [Wolf95] L. Wolfenstein, "CP Violation in D^0 - \bar{D}^0 Mixing," Phys. Rev. Lett. 75 (1995) pp. 2460-2461.
- [YOR92] A. Le Yaouance, L. Oliver and J.-C. Raynal, "CP Violation Beyond the Standard Model and Final State Interaction phases in D Mesons," Phys. Lett. B 292 (1992) pp. 353-363.
- [accm-83] R. Bailey *et al.*, "Production and Decay Properties of D and D^* Mesons in π^- Be Interaction," Phys. Lett. B 132 (1983) pp. 237-240.

- [accm-86] R. Bailey *et al.*, "measurement of D Meson Production in 200 GeV π^- -Be Interactions," Z. Phys. C 30 (1986) pp. 51-63.
- [accm-872] S. Barlag *et al.*, "Lifetimes of Charged and Neutral D Mesons," Z. Phys. C 37 (1987) pp. 17-23.
- [accm-902] S. Barlag *et al.*, "Measurement of the masses and lifetimes of the charmed mesons D^0 , D^+ , and D_s^+ ," Z. Phys. C 46 (1990) pp. 563-567.
- [argu-882] H. Albrecht *et al.*, "Lifetimes of Charmed Mesons," Phys. Lett. B 210 (1988) pp. 267-272.
- [argu-85] H. Albrecht *et al.*, "Production and Decay of the Charged D^* Meson in e^+e^- Annihilation at 10 GeV Centre-of-mass Energy," Phys. Lett. B 150 (1985) pp. 235-241.
- [argu-90] H. Albrecht *et al.*, "A study of Cabibbo-suppressed D^0 Decays," Z. Phys. C 46 (1990) pp. 9-14.
- [cleo-88] D. Bortoletto *et al.*, "Charm Production in Nonresonant e^+e^- annihilation at $\sqrt{s} = 10.55$ GeV," Phys. Rev. D 37 (1988) pp. 1719-1743.
- [cleo-90] J. Alexander *et al.*, "Study of the Decays $D^0 \rightarrow K\bar{K}, \pi\bar{\pi}$," Phys. Rev. Lett. v 65 (1990) pp. 1184-1187.
- [cleo-93] M. Selen *et al.*, "Measurement of the $D \rightarrow \pi\pi$ Branching Fractions," Phys. Rev. Lett. v 71 (1993) pp. 1973-1977.
- [cleo-953] J. Bartelt *et al.*, "Search for CP violation in D^0 decay," Cornell preprint, CLNS 95/1333 (1995).
- [e687-912] P. L. Frabetti *et al.*, "A Measurement of the D^0 and D^+ Lifetimes," Phys. Lett. B 263 (1991) pp. 584-590.
- [e687-94] P. L. Frabetti *et al.*, "A Measurement of the Cabibbo-Suppressed Decays $D^0 \rightarrow \pi^+\pi^-$ and $D^0 \rightarrow K^+K^-$," Phys. Lett. B 321 (1994) pp. 295-302.
- [e687-942] P. L. Frabetti *et al.*, "Precise Measurements of the D^0 and D^+ Meson Lifetimes," Phys. Lett. B 323 (1994) pp. 459-466.
- [e687-943] P. L. Frabetti *et al.*, "Search for CP Violation in Charm Meson Decay," Phys. Rev. D 50 (1994) pp. R2953-R2956.
- [e691-882] J. R. Raab *et al.*, "Measurement of the D^0 , D^+ , and D_s^+ Lifetimes," Phys. Rev. D 37 (1988) pp. 2391-2402.
- [e691-91] J. C. Anjos *et al.*, "Measurement of the decays $D^0 \rightarrow \pi^+\pi^-$ and $D^0 \rightarrow K^+K^-$," Phys. Rev. D 44 (1991) pp. R3371-R3374.

- [e691-92] J. C. Anjos *et al.*, "Study of the Decays $D \rightarrow K3\pi$," Phys. Rev. D 46 (1992) 1941-1950.
- [mark-77] M. Piccolo *et al.*, "D Meson Production and Decay in e^+e^- Annihilation at 4.03 and 4.41 GeV C.M. Energy," Phys. Lett. B 70 (1977) pp. 260-264.
- [mark-79] G. S. Abrams *et al.*, "Observation of Cabibbo-Suppressed Decay $D^0 \rightarrow \pi^+\pi^-$ and $D^0 \rightarrow K^+K^-$," Phys. Rev. Lett. v 43 (1979) pp. 481-483.
- [mark-85] R. M. Baltrusaitis *et al.*, "Measurements of Cabibbo-Suppressed Hadronic Decays of Charmed D^+ and D^0 Mesons," Phys. Rev. Lett. v 55 (1985) pp. 150-153.
- [na14-902] M. P. Alvarez *et al.*, "Lifetime measurements of the D^+ , D^0 , D_s^+ , and Λ_c^+ charmed particles," Z. Phys. C 47 (1990) pp. 539-545.
- [wa82-92] M. Adamovich *et al.*, "Measurement of relative Branching Fractions of D^0 Cabibbo-suppressed Decays," Phys. Lett. B 280 (1992) 163-168.

